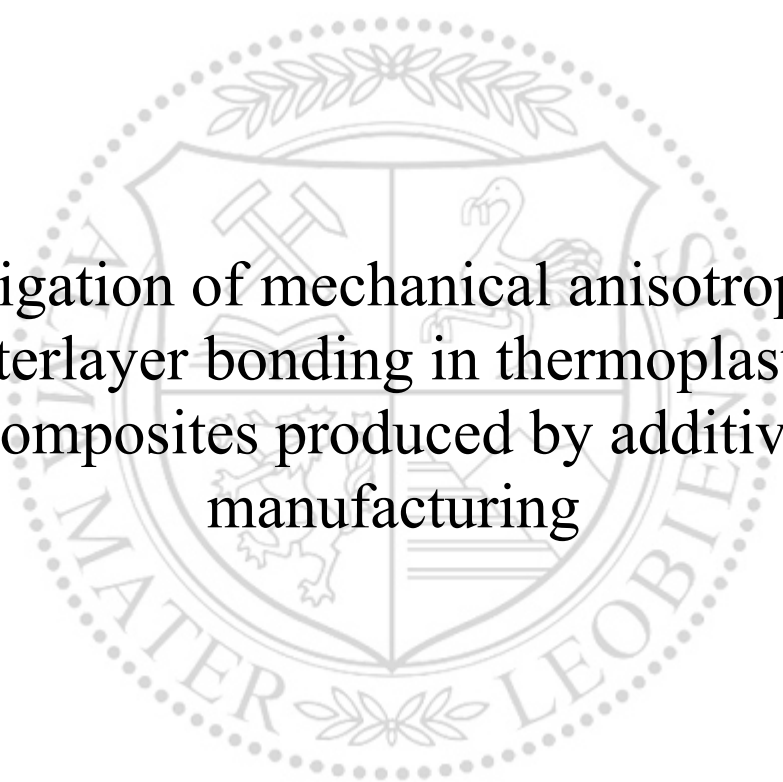




Chair of Materials Science and Testing of Polymers

Doctoral Thesis



Investigation of mechanical anisotropy and  
interlayer bonding in thermoplastic  
composites produced by additive  
manufacturing

Anastasiia Khudiakova

December 2020

## Affidavit

I declare on oath that I wrote this thesis independently, did not use other than the specified sources and aids, and did not otherwise use any unauthorised aids.

I declare that I have read, understood, and complied with the guidelines of the senate of the Montanuniversitaet Leoben for "Good Scientific Practice".

Furthermore, I declare that the electronic and printed version of the submitted thesis are identical, both, formally and with regard to content.

Leoben, .....

Date

.....

Signature

The research work was performed within the COMET project VI-2.06, 'New strategies towards laser assisted manufacturing of fibre reinforced thermoplastic composites,' at the Polymer Competence Center Leoben GmbH (PCCL, Austria) within the framework of the Federal Ministry for Climate Action, Environment, Energy, Mobility, Innovation and Technology and the Federal Ministry for Digital and Economic Affairs with contributions by Technical University of Munich (Institute for Carbon Composites) and Montanuniversitaet Leoben (Institute of Material Science and Testing of Polymers) as scientific partners and AFPT and Cevotec as company partners. The PCCL is funded by the Austrian Government and the State Governments of Styria, Lower Austria and Upper Austria.

## Acknowledgements

I would like to express my deepest appreciation to the following people who have helped me to undertake this research:

Firstly, I would like to thank my group and project leader, DI Dr. Markus Wolfahrt, who gave me the opportunity to complete this thesis and has profoundly supported me over the last four years. I am grateful for his invaluable help during the difficult times of the project. I also wish to thank DI Dr. Michael Berer for his support and for letting me be part of his projects, which have significantly broadened my knowledge of additive manufacturing.

I would like to extend my gratitude to my academic supervisor, Professor Pinter, for his unwavering guidance and active involvement in my thesis. The meetings and conversations with him have always motivated me to delve deeper into fracture mechanics keeping a positive attitude. I would also like to thank my mentor DI Dr. Damir Godec for his supervision and helpful contribution to this thesis.

Thanks should also go to all project partners as well as all co-authors of the papers included in this thesis for a rewarding experience to work with them. I am particularly grateful to Dr. Andreas J Brunner for his valuable advice and discussions in the field of fracture mechanics.

My sincere thanks are also extended to Sebastian Maar and Valerie Grasser, for their assistance in the laboratory, and to DI Dr. Florian Röper, for his help and support.

I wish to acknowledge the help provided by the WPK team from the University of Leoben, especially DI Dr. Florian Arbeiter, for giving valuable advice and practical suggestions during my research; Jürgen Grosser and Jürgen Föttinger, for their assistance with operating the test machines; and Franz Grasser, for his valuable help with specimen preparation.

The completion of my dissertation would not have been possible without the support of my family. I am extremely grateful to my dad, mum and sister for always being there for me in spite of the thousand kilometres between us. I must also thank my first school physics teacher, Zaboreva Olga Mikhailovna, whose talent sparked my interest in this subject and with whom my academic journey began in classroom No. 317. I also thank my friends for their support and the incredible moments we have shared together during these years.

Finally, I wish to express my gratitude to my beloved Simon, whom I was fortunate to meet during this study. I am sincerely grateful for his constant support and encouragement and for all these happy days we have spent with each other over the past years.

# Investigation of mechanical anisotropy and interlayer bonding in thermoplastic composites produced by additive manufacturing

## Abstract

Additive manufacturing (AM) methods are a promising alternative to conventional manufacturing processes in the production of carbon fibre (CF) reinforced thermoplastic composites. These composites are lightweight and show outstanding mechanical performance and are therefore of great interest to many industries, such as aerospace, automotive, sports and medical. A major drawback of AM constitutes the layer-by-layer manufacturing approach, inevitably leading to direction-dependent properties of the parts and the accumulation of defects between the layers, which undermines their load-bearing capacity. This crucial topic demands more in-depth research, which is why the present thesis is devoted to the characterisation of mechanical anisotropy and interlayer bonding of parts produced by AM.

The topic of mechanical anisotropy was addressed by the systematic analysis of short CF reinforced polyamide 1212 tensile bars produced by selective laser sintering (SLS), which revealed the presence of a preferable fibre orientation. X-ray tomography analysis showed that more than half of the fibres were oriented along the travel direction of the roller distributing the powder. This effect led to highly direction-dependent mechanical properties of the parts that consequently exhibited the highest tensile strength and tensile modulus upon loading along the fibre direction.

Further, the anisotropic behaviour of neat and short CF reinforced polylactic acid (PLA) specimens produced by fused filament fabrication (FFF) was characterised by means of tensile testing and digital image correlation (DIC). Specimens were printed with 0°, 45° and 90° raster angles. For both materials, the complete sets of engineering constants could be successfully acquired under the assumption of transverse isotropy. In addition, multi-material parts were produced by direct printing of neat PLA on CF-PLA. Interlayer bonding between the materials was characterised by fracture mechanics tests, namely mode I double cantilever beam (DCB) and cracked round bar tests. The results obtained confirmed that the interlayer bonding of PLA/CF-PLA was at least as strong as that of CF-PLA/CF-PLA.

Fracture mechanics tests, namely quasi-static and fatigue mode I DCB tests, were also applied to characterise the effect of manufacturing parameters on the interlayer bonding of unidirectional (UD) CF reinforced polyphenylene sulphide laminates produced by automated tape placement with in-situ consolidation (ATPisc). Regardless of the manufacturing parameters used, all laminates exhibited a complex delamination behaviour with multiple cracking. Different approaches for data reduction and data representation were employed for the quantitative assessment of the laminate quality.

In order to make the mode I DCB test less labour-intensive and less dependent on visual crack length measurements, DIC was applied. In the framework of this approach, two data reduction methods were developed to determine the crack length based on either the high strain concentration at the crack tip or the crack tip opening displacement. The methods developed yielded data consistent with those of the top surface analysis method known from literature. Ultimately, it was shown that DIC is a suitable alternative to conventional optical measuring tools, enabling the automated tracking of crack propagation.

Besides fracture toughness, the interlayer bonding was characterised in terms of shear strength. For this purpose, compression shear tests (CST) were performed on UD CF/PA6 and steel-CF/PA6 hybrid

samples, produced using ATPisc. As a result, CST was revealed to be a simple and straightforward test method that requires only a small sample size and can therefore be recommended for a first qualitative assessment of the interlayer bonding in AM parts.

# Untersuchung der mechanischen Anisotropie und Zwischenschichthaftung in thermoplastischen Verbundwerkstoffen hergestellt durch additive Fertigung

## Zusammenfassung

Additive Fertigungsverfahren sind eine attraktive Alternative zu konventionellen Fertigungsverfahren in der Herstellung von kohlenstofffaserverstärkten thermoplastischen Verbundwerkstoffen. Letztere weisen hervorragende mechanische Eigenschaften bei geringem Gewicht auf, weshalb sie für viele Industrien von großem Interesse sind. Das schichtweise Arbeitsprinzip additiver Fertigungsverfahren bringt jedoch einen erheblichen Nachteil mit sich, denn es führt zwangsläufig zu richtungsabhängigen Eigenschaften der Teile und zur Anhäufung von Defekten zwischen den Schichten, was wiederum deren Belastbarkeit nachteilig beeinflusst. Deswegen widmet sich die vorliegende Arbeit der Charakterisierung der mechanischen Anisotropie und Zwischenschichthaftung von additiv gefertigten Bauteilen.

Die Studien zur mechanischen Anisotropie erfolgten anhand der Untersuchung von mit kurzen Kohlenstofffasern (KF) verstärkten Polyamid 1212 Zugstäben, die durch selektives Lasersintern hergestellt wurden. Die Ergebnisse wiesen auf eine bevorzugte Faserorientierung hin und röntgentomographische Analysen bestätigten, dass mehr als die Hälfte der KF entlang der Laufrichtung der Walze ausgerichtet waren. Dieser Effekt resultierte in richtungsabhängigen mechanischen Eigenschaften.

Weiterhin wurde das anisotrope Verhalten von reinen und mit kurzen KF verstärkten Polymilchsäure (PLA)-Proben mittels Zugversuche und Digital Image Correlation (DIC) studiert. Die Probenherstellung erfolgte durch Fused Filament Fabrication und unter Variation des Rasterwinkels. Unter Annahme transversaler Isotropie konnten für beide Materialien die vollständigen Sätze der technischen Konstanten erfasst werden. Zusätzlich wurden Mehrkomponententeile durch direktes Drucken von reiner PLA auf mit kurzen KF verstärkter PLA (KF-PLA) hergestellt. Die Zwischenschichthaftung dieser Materialien wurde anschließend durch bruchmechanische Tests charakterisiert, nämlich anhand von Mode I Double Cantilever Beam (DCB) und Cracked Round Bar Tests. Die Ergebnisse bestätigten, dass die Zwischenschichthaftung von PLA/KF-PLA mindestens so gut ist wie diejenige von KF-PLA/KF-PLA.

Aus der Gruppe bruchmechanischer Tests wurde weiterhin der Mode I DCB-Test unter quasistatischer sowie Ermüdungsbelastung angewandt, um den Einfluss der Herstellungsparameter auf die Zwischenschichthaftung von unidirektionalen (UD) KF verstärkten Polyphenylsulfid-Laminaten zu charakterisieren. Die Produktion erfolgte durch Automated Tape Placement mit In-situ-Konsolidierung (ATPisc) und unabhängig von den verwendeten Herstellungsparametern wiesen alle Lamine ein komplexes Delaminationsverhalten mit Mehrfachrissbildung auf. Für die quantitative Bewertung der Laminatqualität wurden verschiedene Ansätze zur Datenreduktion und -darstellung verwendet.

Um den Mode I DCB-Test weniger arbeitsintensiv zu machen und die Abhängigkeit von visuellen Risslängenmessungen zu verringern wurde DIC eingesetzt. Im Rahmen dieses Konzepts erfolgte die Entwicklung zweier Datenreduktionsmethoden, um die Risslänge entweder anhand der hohen Dehnungskonzentration an der Risspitze oder der Verschiebung der Rissspitzenöffnung zu bestimmen. Die erhaltenen Daten waren in Übereinstimmung mit den Resultaten der literaturbekannten Top Surface-Analyse. So konnte demonstriert werden, dass DIC eine geeignete Alternative zu konventionellen optischen Messwerkzeugen darstellt und darüber hinaus eine automatisierte Verfolgung der Rissausbreitung ermöglicht.

Neben der Bruchzähigkeit war die Charakterisierung der Zwischenschichthaftung hinsichtlich der Scherfestigkeit von Interesse. Zu diesem Zweck wurden Druck-Scherversuche an UD-KF/PA6- und Stahl-KF/PA6-Hybridmaterialien, die mittels ATPisc hergestellt wurden, durchgeführt. Diese erwiesen sich als geeignete und leicht durchführbare Prüfmethode, die somit für eine erste qualitative Bewertung der Zwischenschichthaftung in additiv gefertigten Bauteilen empfohlen werden kann.



# Table of contents

Chapter 1.	Introduction and Scope .....	1
1.1.	Motivation .....	1
1.2.	Objectives .....	3
1.3.	Structure of the thesis .....	4
1.4.	References .....	5
Chapter 2.	Theoretical Background.....	8
2.1.	Additive manufacturing of thermoplastic composites.....	8
2.2.	Basic principles of the selected additive manufacturing methods .....	9
2.3.	Mechanical anisotropy in additive manufacturing.....	13
2.3.1.	Printing with neat thermoplastics .....	13
2.3.2.	Printing with reinforced thermoplastics .....	15
2.4.	Experimental methods for interlayer bonding characterisation.....	18
2.4.1.	Fracture mechanics testing .....	18
2.4.2.	Interlaminar shear testing.....	26
2.5.	References .....	26
Chapter 3.	Characterisation of Mechanical Anisotropy in AM .....	37
3.1.	Systematic analysis of the mechanical anisotropy of fibre-reinforced polymer specimens produced by laser sintering.....	37
3.1.1.	Bibliographic information.....	37
3.1.2.	Abstract .....	38
3.1.3.	Introduction.....	38
3.1.4.	Experimental .....	39
3.1.5.	Results and discussion .....	42
3.1.6.	Conclusion .....	57
3.1.7.	References.....	59
3.2.	Interlayer bonding characterisation between materials with different degrees of stiffness processed by fused filament fabrication.....	63
3.2.1.	Bibliographic information.....	63
3.2.2.	Abstract .....	64
3.2.3.	Introduction.....	64
3.2.4.	Experimental .....	66
3.2.5.	Results and discussion .....	72
3.2.6.	Conclusion .....	79
3.2.7.	References.....	80
Chapter 4.	Characterisation of Interlayer Bonding in AM.....	84

4.1.	On the investigation of quasi-static and fatigue crack resistance of thermoplastic tape layered composites with multiple delaminations: Approaches for quantification.....	84
4.1.1.	Bibliographic information.....	84
4.1.2.	Abstract .....	85
4.1.3.	Introduction.....	85
4.1.4.	Materials and methods .....	86
4.1.5.	Data analysis techniques .....	89
4.1.6.	Results and discussion.....	91
4.1.7.	Conclusion .....	113
4.1.8.	References.....	115
4.2.	Automated monitoring of the crack propagation in mode I testing of thermoplastic composites by means of digital image correlation .....	119
4.2.1.	Bibliographic information.....	119
4.2.2.	Abstract .....	120
4.2.3.	Introduction.....	120
4.2.4.	Experimental .....	121
4.2.5.	Data reduction methods.....	124
4.2.6.	Results and discussions .....	127
4.2.7.	Conclusion .....	132
4.2.8.	References.....	133
4.3.	A comparative study for shear testing of thermoplastic-based composites and metal-composite hybrids .....	136
4.3.1.	Bibliographic information.....	136
4.3.2.	Abstract .....	137
4.3.3.	Introduction.....	137
4.3.4.	Materials and testing methods .....	139
4.3.5.	Results and discussion.....	141
4.3.6.	Summary and conclusion .....	143
4.3.7.	References.....	144
Chapter 5.	Summary and Outlook.....	146

## Chapter 1. Introduction and Scope

### 1.1. Motivation

In this age of growing technology, industries more than ever demand fast, high-quality and cost-efficient production. In addition, one of the most important requirements today is the environmental friendliness of products [1]. Therefore, the use of lightweight components, which leads to fuel savings and lower CO<sub>2</sub> emissions, has always been of interest to global industries, such as automotive and aerospace [2–5]. To meet this demand, fibre reinforced polymer composites have been implemented [6]. They are known for their high strength-to-weight and stiffness-to-weight ratios, giving them an edge over traditional metal parts [7,8]. Composites with thermoplastic matrices are the most attractive for industry sectors because of their outstanding fracture toughness, high temperature resistance and recyclability [9,10]. Moreover, thermoplastics exhibit the unique ability to solidify upon cooling from the melting temperature without undergoing chemical crosslinking [11]. Therefore, thermoplastic composites usually do not require post-processing, such as heat or pressure, which leads to lower production costs and significant energy savings. However, it has to be noted that, especially for high performance thermoplastic matrix materials, these savings are offset by higher material costs.

Technologies to process composite materials are constantly evolving, since new material and engineering capabilities emerge. About forty years ago, a new era of additive manufacturing (AM) techniques began [12–14]. Nowadays, AM enables a cost and energy efficient manufacturing of structures from different materials and of different shapes in a completely new manner compared to conventional manufacturing (CM), such as thermoforming, injection moulding and blow moulding [15–17]. It has been estimated that manufacturing components using AM only demands 1/3 to 1/2 of the energy required to produce them using CM [18]. Of the various AM techniques, fused filament fabrication (FFF), selective laser sintering (SLS) and automated tape placement with in-situ consolidation (ATPisc) can process fibre reinforced thermoplastics [17,19–21]. More precisely, ATPisc can continuously process endless fibre reinforced thermoplastics, SLS – short fibre reinforced thermoplastics, and FFF – both endless and short fibre reinforced thermoplastics [19–21]. These AM methods rely on different operation principles which involve different systems of material feeding, heating, cooling, etc. [19]. It is noteworthy that they also have different production scales. For instance, ATPisc allows large composite panels to be produced in fairly short times [22], while FFF and SLS are more limited in both production size and speed. These methods have one thing in common – a layer-wise manner of manufacturing that brings forth problems with the quality of AM parts [17,19].

The sequential creating of objects layer by layer makes the material properties different within- and out-of-layer directions. Temperature gradients and contraction of the polymer matrix upon cooling cause thermal residual stresses. In addition, the fibre reinforcement influences the morphology and mechanical properties of composites. All of these factors lead to high anisotropy in parts produced by AM, which must be thoroughly investigated in order to predict their mechanical performance. Another critical issue in AM parts is the interlayer adhesion due to the accumulation of defects, e.g. porosity between layers [23–25]. It is therefore important to analyse the interlayer performance of AM parts in order to ensure their reliability.

In AM, numerous manufacturing parameters can be varied that influence the final mechanical properties [19]. Therefore, it is imperative to define test methods which would provide a fast way to decide whether the manufacturing parameters used affect the interlayer bonding negatively or positively. Such test methods are particularly necessary in the first phase of research to obtain a qualitative assessment of the laminates. One of the possible tests that can solve this problem is the compression shear test [26]. This test requires a relatively small sample size and it is easy to perform. Thus, the first stages of research can begin with the determination of the most appropriate manufacturing parameters that yield the highest interlayer shear strength. Afterwards, the parts can be further examined using more sophisticated fracture mechanics (FM) tests.

For linear elastic materials, fracture toughness obtained using FM tests can be defined in terms of the stress intensity factor or strain energy release rate [27]. Once these characteristics are known, it is possible not only to evaluate the quality of the interlayer bonding, but also to predict the load range that can be applied to a particular structural component containing a crack without causing its growth under both quasi-static and fatigue loadings [28]. The knowledge of the delamination resistance under cyclic loading is of special importance and should be considered in the safety design of structural components. It has been shown that a part containing a crack can withstand a certain load range under quasi-static loading; however, this range may be sufficient to cause a fracture under cyclic loading. [29]. This is especially true for laminates produced by ATPisc, which are frequently used in aircraft construction [22]. ATPisc is a complex non-isothermal manufacturing process with numerous manufacturing parameters, which can be varied by the machine operator. The use of suboptimal manufacturing parameters for the processing of a certain material adversely affects the laminate quality, in particular the interlayer adhesion. The presence of interlayer defects can lead to the development of delamination under operational loads, which in turn causes a decrease in stiffness and undermines the ability of the laminate to withstand the loads. To date, all available studies have focused on the influence of manufacturing parameters on the quasi-static fracture toughness of ATPisc laminates [30–34]. In contrast, the crack resistance of ATPisc laminates under cyclic loading has not yet been studied and therefore requires intensive research.

In FM tests, in particular the mode I double cantilever beam (DCB) test, it can take a lot of time to propagate a crack to the required length in accordance with the test standards [35,36]. For that reason, automated crack length measuring methods would be required to mitigate these difficulties. One possible solution might be digital image correlation (DIC). In literature, there are several studies that have successfully applied DIC to track crack propagation during FM tests of composites performed under both quasi-static [37–41] and fatigue [41,42] loadings. However, this method is not yet well-established and requires further research.

To sum up, anisotropy of mechanical and morphological properties of parts produced by AM requires a more thorough investigation. A comprehensive analysis of fracture processes occurring in AM parts is indispensable. It is especially important to characterise the interlayer bonding, which is a vulnerability of AM, using both quasi-static and fatigue loading regimes. It is essential to understand the mechanical performance of parts produced by AM in order to ensure their reliable use as load-bearing structural components.

## 1.2. Objectives

To address the issues pointed out above, the present study focuses on the investigation of the anisotropic mechanical behaviour and the interlayer bonding in thermoplastic composites produced by AM methods, namely FFF, SLS and ATPisc. The objectives pursued in the present study were formulated as follows:

- Definition of the desired materials, type of reinforcement and stacking sequences
- Assessment of the degree of anisotropy and inhomogeneity in neat and carbon fibre reinforced parts produced by FFF and SLS
  - Definition of specimen orientation and printing direction in the building volume
  - Mechanical characterisation of specimens by means of tensile testing
  - Analysis of the material morphology using image analysis techniques (e.g. light microscopy, scanning electron microscopy (SEM), X-ray tomography)
- Interlayer bonding characterisation in terms of both fracture toughness and shear strength
  - Fracture mechanics characterisation of interlayer bonding between two materials of different stiffness processed by FFF
  - Application of the compression shear test to characterise the interlayer shear strength in composites produced by ATPisc
- Investigation of the delamination resistance in laminates produced by ATPisc
  - Definition of optimal processing parameters and building approaches of laminates
  - Mode I DCB testing of unidirectional laminates under both quasi-static and fatigue loading
  - Quantitative assessment of the laminate quality
- Development of a reliable and straightforward methodology for automated tracking of crack development in mode I DCB testing
  - Application of DIC in mode I DCB testing
  - Development of new reduction methods and criteria to localise the crack tip position from the DIC data
  - Validation of the methods developed by comparison with methods established in literature

### 1.3. Structure of the thesis

The objectives listed above were addressed and fulfilled in the course of a consistent work summarised in five peer-reviewed scientific publications, which are presented below. The thesis is organised according to the following outline:

1. Introduction and scope
2. Theoretical background
3. Investigation of the mechanical anisotropy of AM parts
4. Characterisation of the interlayer bonding of AM parts
5. Summary and outlook

**Chapter 1** presents the motivation and objectives of the present thesis.

**Chapter 2** includes the theoretical background of the topics covered in this thesis. In particular, it provides brief descriptions of FFF, SLS and ATPisc, all used in this thesis. Furthermore, problems with layer-wise manufacturing, such as anisotropy and vulnerable interlayer bonding, are addressed. Finally, test methods characterising interlayer bonding in terms of fracture toughness and shear strength are presented.

**Chapter 3** focuses on the problem of the anisotropic material behaviour of parts produced by AM. **Publication 1** investigates the anisotropic behaviour of neat and short carbon fibre reinforced polyamide specimens manufactured by SLS. Mechanical tests, microscopy analyses and computer tomography were performed to confirm the presence of a preferable fibre orientation in the composite parts. Most of the fibres were found to be aligned along the travel direction of the roller that distributes the powder over the building platform. **Publication 2** addresses the anisotropic behaviour of neat and carbon fibre (CF) reinforced PLA processed by means of FFF. The complete sets of engineering constants were obtained for both materials considering them transversely isotropic. DIC was applied to follow strains on the front and side surfaces of the tensile specimens. This resulted in the determination of the Poisson's ratio in the  $xz$ - and  $yz$ -planes, which are usually missing in literature. Additionally, the bonding strength between neat PLA printed on top of carbon fibre reinforced PLA was characterised by fracture mechanics tests, namely mode I double cantilever beam and cracked round bar tests.

**Chapter 4** is devoted to the characterisation of interlayer bonding in parts produced by AM. The interlayer bonding of unidirectional CF reinforced polyphenylene sulphide laminates produced by ATPisc was characterised using both quasi-static and fatigue mode I DCB tests in **Publication 3**. The specimens exhibited a complex crack propagation behaviour, which included fibre bridging and multiple cracking. Different approaches were followed to quantitatively estimate the degree of damage in the laminates. **Publication 4** presents a novel methodology for tracking crack propagation in mode I DCB testing using DIC. Two reduction methods were developed to obtain the crack length, relying on either the displacement or strain DIC data. The results were in good agreement with the top surface analysis known from literature. It was shown that DIC is an appropriate alternative to conventional crack length measurement methods. **Publication 5** focuses on the investigation of interlayer shear strength in hybrid steel/PA6 composites produced by means of ATPisc. A compression shear device was used to assess the effect of different laser texturing of metal surfaces on the bonding with PA6. It was shown that the compression shear test yields the results consistent with the standard

single lap shear test and can therefore be used for the characterisation of the interlayer bonding strength in AM parts.

**Chapter 5** summarises and concludes the main results obtained and also provides some recommendations for further research.

The publications mentioned above have the following titles:

**Publication 1:** Systematic analysis of the mechanical anisotropy of fibre-reinforced polymer specimens produced by laser sintering

**Publication 2:** Inter-layer bonding characterisation between materials with different degrees of stiffness processed by fused filament fabrication

**Publication 3:** On the investigation of quasi-static and fatigue crack resistance of thermoplastic tape layered composites with multiple delaminations: Approaches for quantification

**Publication 4:** Automated monitoring of the crack propagation in mode I testing of thermoplastic composites by means of digital image correlation

**Publication 5:** A comparative study for shear testing of thermoplastic-based composites and metal-composite hybrids

One bachelor thesis has been completed in the course of this research by Valerie Grasser: 'Development of a methodology to measure delamination length in fracture toughness tests by means of digital image correlation', 2019, MU Leoben.

#### 1.4. References

- [1] Ashby MF. *Materials and the Environment: Eco-informed Material Choice*. 1st ed. s.l.: Elsevier professional; 2009.
- [2] Beardmore P JCF. The potential for composites in structural automotive applications. *Compos Sci Technol* 1986;26(4):251–81.
- [3] Pervaiz M, Panthapulakkal S, KC B, Sain M, Tjong J. Emerging Trends in Automotive Lightweighting through Novel Composite Materials. *MSA* 2016;07(01):26–38.
- [4] McIlhagger A, Archer E, McIlhagger R. Manufacturing processes for composite materials and components for aerospace applications. In: Irving PE, Soutis C, editors. *Polymer composites in the aerospace industry*. Oxford: Woodhead Publishing; 2019, p. 59–81.
- [5] Barile C, Casavola C, Cillis F de. Mechanical comparison of new composite materials for aerospace applications. *Compos B Eng* 2019;162:122–8.
- [6] Clyne TW HD. *An introduction to composite materials*: Cambridge university press; 2019.
- [7] Abrate S WDA. Machining of composite materials. Part I: Traditional methods. *Composites Manufacturing* 1992;3(2):75–83.
- [8] Liao K, Schultesiz CR, Hunston DL, Brinson LC. Long-term durability of fiber-reinforced polymer-matrix composite materials for infrastructure applications: a review. *Journal of advanced materials* 1998;1(30).
- [9] Offringa A. R. Thermoplastic composites—rapid processing applications. *Compos Part A Appl Sci Manuf* 1996;27(4):329–36.

- [10] Costa AP, Botelho EC, Costa ML, Narita NE, Tarpani JR. A review of welding technologies for thermoplastic composites in aerospace applications. *Journal of Aerospace Technology and Management* 2012;4(3):255–65.
- [11] Campbell FC. *Structural composite materials*. Materials Park Ohio: ASM International; 2010.
- [12] Bourell, D. L., et al. (ed.). *A brief history of additive manufacturing and the 2009 roadmap for additive manufacturing: looking back and looking ahead*; 2009.
- [13] Wohlers T GT. *History of additive manufacturing*. Wohlers report 2014;24:118.
- [14] Urhal P, Weightman A, Diver C, Bartolo P. Robot assisted additive manufacturing: A review. *Robotics and Computer-Integrated Manufacturing* 2019;59:335–45.
- [15] Valino AD, Dizon JRC, Espera AH, Chen Q, Messman J, Advincula RC. Advances in 3D printing of thermoplastic polymer composites and nanocomposites. *Progress in Polymer Science* 2019;98:101162.
- [16] Ford S, Despeisse M. Additive manufacturing and sustainability: An exploratory study of the advantages and challenges. *J Clean Prod* 2016;137:1573–87.
- [17] Kumar S, Kruth J-P. Composites by rapid prototyping technology. *Mater. Des.* 2010;31(2):850–6.
- [18] Huang R, Riddle M, Graziano D, Warren J, Das S, Nimbalkar S et al. Energy and emissions saving potential of additive manufacturing: The case of lightweight aircraft components. *J Clean Prod* 2016;135:1559–70.
- [19] Gibson I, Rosen D, Stucker B. *Additive Manufacturing Technologies*. New York, NY: Springer New York; 2015.
- [20] Frketic J, Dickens T, Ramakrishnan S. Automated manufacturing and processing of fiber-reinforced polymer (FRP) composites: An additive review of contemporary and modern techniques for advanced materials manufacturing. *Additive Manufacturing* 2017;14:69–86.
- [21] Yassin K, Hojjati M. Processing of thermoplastic matrix composites through automated fiber placement and tape laying methods. *Journal of Thermoplastic Composite Materials* 2018;31(12):1676–725.
- [22] Grimshaw, Grant, Diaz. Advanced Technology Tape Laying For Affordable Manufacturing Of Large Composite Structures. In: *International sampe symposium and exhibition, SAMPE, 1999*, p. 2484–2494.
- [23] Aliheidari N, Christ J, Tripuraneni R, Nadimpalli S, Ameli A. Interlayer adhesion and fracture resistance of polymers printed through melt extrusion additive manufacturing process. *Mater. Des.* 2018;156:351–61.
- [24] Grouve WJB, Warnet LL, Rietman B, Visser HA, Akkerman R. Optimization of the tape placement process parameters for carbon–PPS composites. *Compos. Part A Appl. Sci. Manuf.* 2013;50:44–53.
- [25] Pilipović A, Valentan B, Brajljić T, Haramina T, Balić J, Kodvanj J, Šercer M, Drstvenšek I. Influence of laser sintering parameters on mechanical properties of polymer products. In: *Proceedings of 3rd International Conference on Additive Technologies, 2010*.
- [26] Schneider, K., B. Lauke, and W. Beckert. Compression shear test (CST)—a convenient apparatus for the estimation of apparent shear strength of composite materials. *Applied Composite Materials* 2001;8(1):43–62.
- [27] Anderson TL. *Fracture Mechanics: Fundamentals and Applications*: CRC press; 2017.
- [28] C.T. Sun, Z.-H. Jin. *Fracture mechanics*: Elsevier; 2012.
- [29] Schön J, Nyman T, Blom A, Ansell H. A numerical and experimental investigation of delamination behaviour in the DCB specimen. *Compos Sci Technol* 2000;60(2):173–84.
- [30] Ray D, Comer AJ, Lyons J, Obande W, Jones D, Higgins RMO et al. Fracture toughness of carbon fiber/polyether ether ketone composites manufactured by autoclave and laser-assisted automated tape placement. *J. Appl. Polym. Sci.* 2014;132(11).



- [31] Modi, D; Comer, A; O'Higgins, R.M.O; McCarthy, M. A. Thermoplastic composites: in-situ consolidation or in-situ welding; 2013.
- [32] Qureshi Z, Swait T, Scaife R, El-Dessouky HM. In situ consolidation of thermoplastic prepreg tape using automated tape placement technology: Potential and possibilities. *Compos B Eng* 2014;66:255–67.
- [33] Bandaru, A.K; Clancy, G.J; Peeters, D; O'Higgins, R; Weaver, P.M. Interface characterization of thermoplastic skin-stiffener composite manufactured using laser-assisted tape placement; 2018.
- [34] Sacchetti F, Grouve WJB, Warnet LL, Villegas IF. Effect of cooling rate on the interlaminar fracture toughness of unidirectional Carbon/PPS laminates. *Eng. Fract. Mech.* 2018;203:126–36.
- [35] ASTM D5528-13, Standard Test Method for Mode I Interlaminar Fracture Toughness of Unidirectional Fiber-Reinforced Polymer Matrix Composites.
- [36] ISO15024: 2001. Fibre-reinforced Plastic Composites: Determination of Mode I Interlaminar Fracture Toughness, GIC, for Unidirectionally Reinforced Materials.: International Organization for Standardization; 2001.
- [37] Reiner J, Torres JP, Veidt M. A novel Top Surface Analysis method for Mode I interface characterisation using Digital Image Correlation. *Eng Fract Mech* 2017;173:107–17.
- [38] Mogadpalli GP, Parameswaran V. Determination of Stress Intensity Factor for Cracks in Orthotropic Composite Materials using Digital Image Correlation. *Strain* 2008;44(6):446–52.
- [39] Grabois TM, Neggens J, Ponson L, Hild F, Toledo Filho RD. On the validation of integrated DIC with tapered double cantilever beam tests. *Engineering Fracture Mechanics* 2018;191:311–23.
- [40] Merzkirch M, Ahure Powell L, Foecke T. Measurements of Mode I Interlaminar Properties of Carbon Fiber Reinforced Polymers Using Digital Image Correlation. *KEM* 2017;742:652–9.
- [41] Murray BR, Fonteyn S, Carrella-Payan D, Kalteremidou KA, Cernescu A, Van Hemelrijck D, Pyl L. Crack tip monitoring of mode I and mode II delamination in CF/Epoxyes under static and dynamic loading conditions using digital image correlation. *Multidisciplinary Digital Publishing Institute Proceedings* 2018;8(2):389.
- [42] Zhu M, Gorbatiikh L, Fonteyn S, Pyl L, van Hemelrijck D, Carrella-Payan D et al. Digital Image Correlation Measurements of Mode I Fatigue Delamination in Laminated Composites. *Proceedings* 2018;2(8):430.

## Chapter 2. Theoretical Background

### 2.1. Additive manufacturing of thermoplastic composites

Additive manufacturing, also referred to as 3D printing, describes the construction process of 3D objects by depositing material in a layer-wise manner [1]. As the name suggests, AM produces parts additively, as opposed to subtractive manufacturing, which is based on material removal. AM is considered the more economical method, since the material is only placed where it is needed. In the first phase, AM requires a digital model created using computer-aided design (CAD) software. This model is then digitally sliced into thin parallel sections that are laid on top of each other one by one by an AM machine until the object is completed. Due to the ability to produce complex parts without the necessity of moulds and the wide range of available materials, AM has changed ‘design for manufacturing’ and ‘design for assembly’ concepts, which are used in conventional manufacturing, to ‘design for function’ concepts. AM permits the processing of neat and reinforced polymers, ceramics, and metals in the forms of filament, pellets, powder or liquids. With regard to polymer matrices, reinforcement can be in the form of nanofibers, short fibres, and continuous fibres [2–4]. The present study focuses on AM methods, specifically FFF, SLS and ATPisc that can process short and continuous carbon fibre reinforced thermoplastic composites, which have received increased attention in the industry in recent decades as an alternative to thermoset composites [5,6].

One of the main reasons for this trend is the ability of thermoplastic composites to be processed more quickly. Thermoplastics consist of long linear polymer chains of high molecular weight that interact through relatively weak, non-covalent forces [7]. Upon heating, these physical bonds break down, leading to a viscous behaviour of the materials and the possibility to process (e.g. mould) them. Upon cooling, thermoplastics solidify without the formation of chemical crosslinks, which are present in thermosets (Fig. 1) [6]. Thus, unlike thermosets, thermoplastics do not require long curing times at elevated temperatures, which would theoretically lead to energy savings [8]. The absence of crosslinks also makes thermoplastics tougher and more resistant to impact in comparison with thermosets. Moreover, thermoplastics display an unlimited shelf life. With regard to safety issues, it is more convenient to work with thermoplastics as they are completely reacted polymers. Most importantly, due to only physical interactions between the polymer chains, they can be (re)processed and reshaped multiple times when heated above the respective glass transition temperature  $T_g$  for amorphous or melting temperature  $T_m$  for semi-crystalline matrices [9].

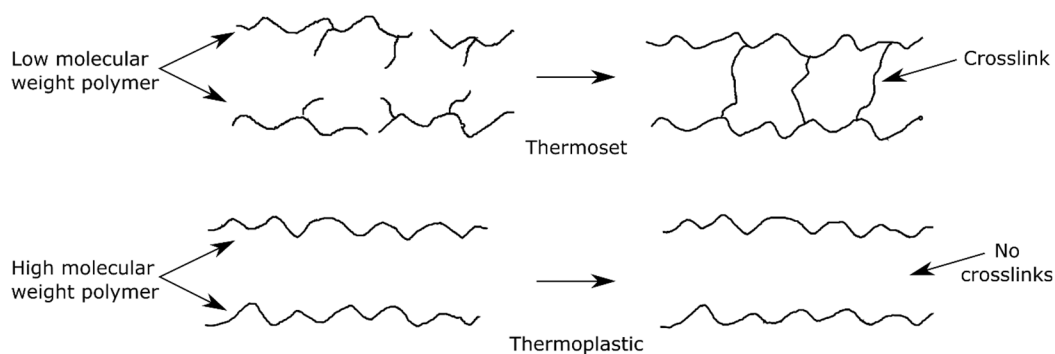


**Fig. 1.** Schematic illustration of the molecular chain structures of thermosets (top) and thermoplastics (bottom). Scheme adopted from [6].

Among all thermoplastic composites, industries such as aerospace, automotive, biomedical, sport, etc. are most interested in composites with high-performance thermoplastic (HPTP) matrices (e.g. PEEK, PPS, PEI), which stand out for their superlative mechanical characteristics [10]. They have higher  $T_g$  and therefore higher operation temperatures than conventional thermoplastics (e.g. PP, PE, ABS). In addition, HPTPs exhibit better toughness properties, which yield improved fracture resistance. However, the processing of HPTPs requires relatively high temperature inputs. For instance, processing temperatures of PEEK are in the range of 360-400 °C, of PPS – 330-345 °C and of PEI – 315-360 °C [6]. This makes processing thermoplastics costly in terms of the required equipment. It should have a large power capacity and be resistant to high operating temperatures. Additive manufacturing methods have such capacities, making them attractive for the industry.

## 2.2. Basic principles of the selected additive manufacturing methods

### Fused filament fabrication

Fused filament fabrication (FFF), also referred to as fused deposition modelling (FDM), was developed by Scott Crump and patented in 1992 [11]. In this method, a thermoplastic polymer in the form of a filament is fed to a print head where it is heated up to the molten state. Afterwards, it is extruded through a print nozzle onto a printing bed, which is usually heated up slightly above  $T_g$  of a material to ensure better bonding with the first printed layer [12]. The final 3D object is created by continuous printing layer by layer (Fig. 2) [1]. A single stripe of filament printed on the printing bed is called a bead, and bonding between adjacent beads and layers is realised through neck formation between them (Fig. 3) [13,14]. The neck formation occurs as a result of fusion of molten filaments, governed by wetting mechanisms driven by surface area reduction and free energy minimisation [14,15]. When two molten beads come into contact with each other, inter-diffusion of polymer chains occurs through the adjoining interfaces. The inter-diffusion depends on the thermal energy supplied to the material and the time that the material needs to cool from melting to ambient temperature. Longer times at higher temperatures favour a better distribution of polymer chains across the interface. However, the polymer chains lose their mobility with decreasing temperature [16].

Every layer can have a different orientation of beads, which is called a raster angle. For example, a stacking layer sequence can be 0°/90°, +45°/-45° or any other, including unidirectional 0°. Nowadays, the most commonly used materials in FFF are thermoplastics [17]. This includes neat thermoplastics and thermoplastics reinforced with either nanofibers, short fibres or continuous fibres [18]. FFF printers can have multiple print nozzles, enabling continuous printing with different materials. The printing with materials of different degrees of stiffness on top of each other enables the production of locally reinforced parts [19–21]. FFF allows printing parts of complex shapes, placing the filament only where it is needed, which leads to comparatively low processing costs. However, printing objects with overhangs requires the additional printing of support structures, which can be removed mechanically or chemically at the end of printing. To date, FFF has mainly been used for prototyping, educational or domestic purposes, but not yet for manufacturing high-performance structural parts [22]. This is largely attributed to a pronounced anisotropy and an improper interlayer bonding.

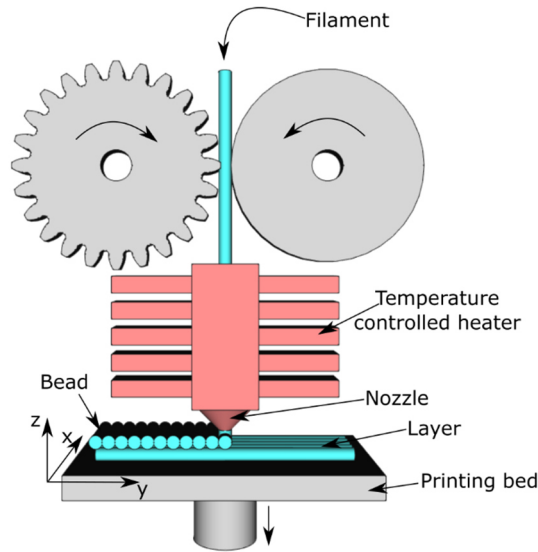


**Fig. 2.** Schematic drawing of fused filament fabrication (FFF).

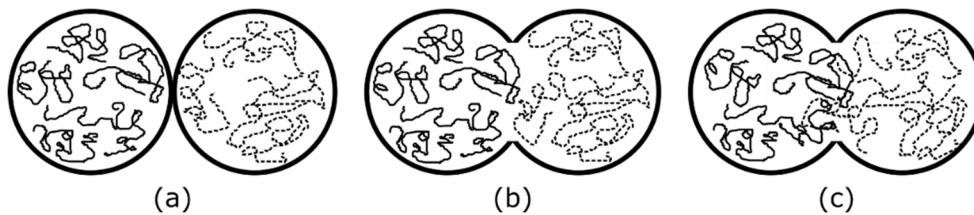


**Fig. 3.** Schematic illustration of the bond formation between two adjacent filaments: surface contacting (a), neck growth (b), and inter-diffusion and randomisation of polymer chains (c). Scheme adopted from [14].

### Selective laser sintering

Selective laser sintering (SLS) of polymers is an additive manufacturing process in which a 3D object is built from powder materials through layer by layer sintering with a laser (e.g. CO<sub>2</sub> laser) [23,24]. After the first powder layer is sintered, the printing platform is shifted down by the width of one layer and the roller or rake spreads a new layer of the powder over the platform and the sintering process is repeated (Fig. 4) [25]. The binding mechanism of polymer powder particles occurs through solid state sintering, which involves a neck growth between the adjacent particles without their complete melting (Fig. 5) [1,26]. The fusion of the powder particles occurs at temperatures between  $T_m/2$  and  $T_m$  and is governed by the minimisation of their total free energy as a result of the reduction of the total surface area upon fusion. Thus, higher temperatures and longer sintering times lead to the smallest total surface area, which means to the smallest size of pores entrapped between fused particles. However, porosity cannot be completely excluded from SLS parts due to the high laser scanning speeds ( $\approx 3000$  mm/s [27]), which deteriorate the final mechanical properties. In order to reduce temperature gradients during manufacturing and increase the diffusion rate of molecular chains, preheating of the building chamber is performed [26]. Compared to FFF, SLS does not require any additional support material because the protruding elements sintered are supported by the non-sintered powder around them. In addition, SLS parts exhibit a higher accuracy and better surface finish than FFF parts due to the use of material in powder form [28]. SLS can process neat thermoplastic

powders as well as thermoplastic powders reinforced with, for instance, beads, nanofibers and short fibres [24].

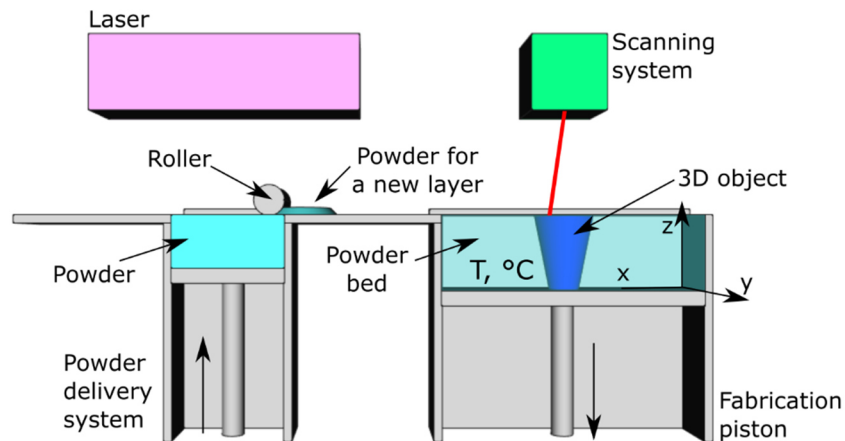


**Fig. 4.** Schematic drawing of the selective laser sintering (SLS) process. Scheme adopted from [29].

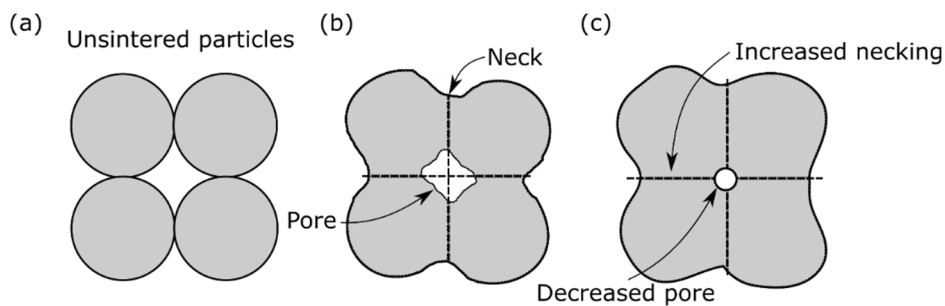


**Fig. 5.** Schematic illustration of solid state sintering in the SLS process: particles before sintering (a), neck formation between adjacent particles at temperatures of one half above the absolute melting temperature (b), and neck growth and consequent decrease in pore size during sintering (c). Scheme adopted from [1].

### Automated tape placement with in-situ consolidation

Automated tape placement with in-situ consolidation (ATPisc) is an additive manufacturing process that has been successfully implemented to build complex and large composite structures [30]. In ATPisc, a mould that can be either at room temperature or preheated to a certain temperature is automatically covered with a continuous fibre tape pre-impregnated with a thermoplastic matrix (Fig. 6). The incoming tape is heated up to  $T_m$  of the matrix by means of a heating source, for instance a  $\text{CO}_2$  laser, a diode laser or a hot gas torch to activate the tack of the tape. The tape placement head deposits one strip of the tape next to another, creating a laminate layer by layer. The adhesion between the layers is ensured by the pressure applied by the consolidation roller, which creates an intimate contact between the incoming tape and the substrate (Fig. 7) [31,32]. The close loop control provides the link between the laser angle and laser power that should be adjusted considering temperature fluctuations caused by heat convection into the ambient environment and heat conduction to the laminate and the mould. This is ensured by an infrared camera that measures the temperature at the nip-point, providing automatic adjustment of the laser power and the laser bias angle to keep the incoming tape and the substrate at the same temperature [33].

The adhesion between adjacent layers is realised by means of a process called autohesion or healing (Fig. 8) [34]. This process only occurs when the intimate contact between the incoming tape and the substrate has been established. In fact, the tape surface is not perfectly flat but exhibits asperities. When the tape and the substrate are heated up to  $T_m$ , the respective materials start to flow, developing a contact with each other and thereby smoothing the asperities under the compaction roller. Subsequently, the polymer chains exchange across the interface created between the incoming tape and the substrate at temperatures above  $T_g$  of the matrix [6,34–36,9]. To describe the degree of bonding, the corresponding models involving two sub-problems – the intimate contact and the healing problem – have been developed [37–40]. The parameters included in these analytical problems are viscosity, temperature, pressure and time [9,41]. Manufacturing parameters such as placement speed, compaction force, processing temperature and cooling rate essentially influence the degree of bonding in ATPisc. Regarding materials, ATPisc enables the manufacturing of thermoplastic composites with different layups without the need for an autoclave, as they consolidate upon cooling to ambient temperature directly in the building process [42]. For those reasons, ATP is considered as an out-of-autoclave (OOA) process with *in-situ* consolidation [8].

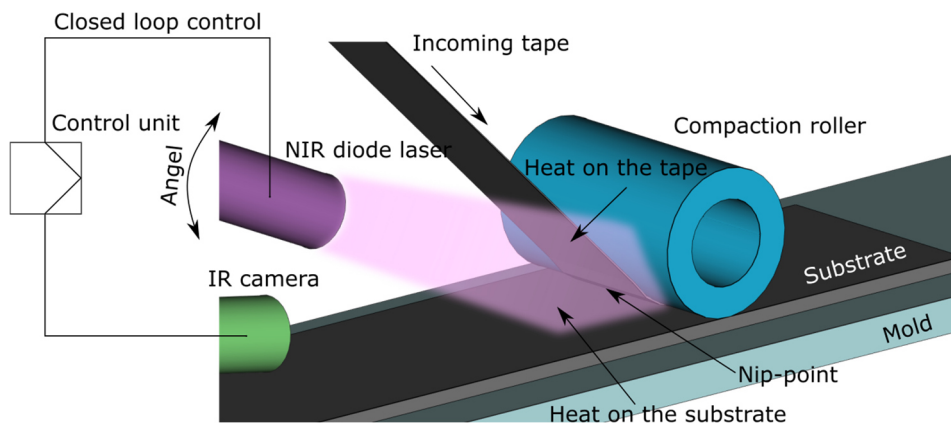


**Fig. 6.** Schematic drawing of the automated tape placement (ATP) process.

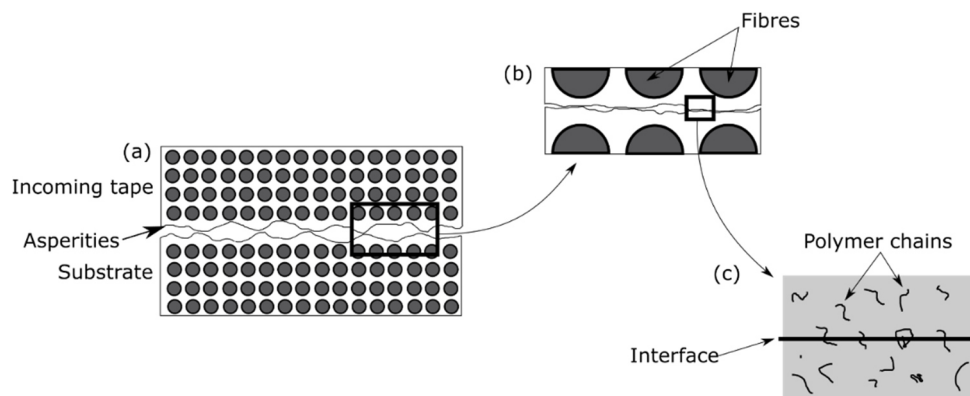


**Fig. 7.** Schematic illustration of autohesion in the ATP process: incoming tape is placed on the substrate (a), development of the intimate contact (b), and interdiffusion of polymer chains (c). Scheme adopted from [43].

### 2.3. Mechanical anisotropy in additive manufacturing

Additive manufacturing constitutes a production method for creating 3D objects by sequential placement of one material layer upon another, which inevitably leads to their anisotropic nature with direction-dependent mechanical properties upon the application of forces, such as tensile, compression, flexural and impact. Layer-by-layer manufacturing provokes the formation of interfaces between the materials placed/sintered, whose adhesion strength can be deteriorated by non-uniform and improper fusion. More precisely, incomplete fusion causes an inhomogeneous material structure with uneven density and intra- and interlayer voids, hindering the mechanical performance of the final object. The degree of anisotropy is also influenced by fibre reinforcement in the case of composites. On the one hand, the addition of stiff carbon fibres to the matrix improves the mechanical and thermal properties and reduces distortion of the part during printing [44–46]. On the other hand, the fact that carbon fibres are much stronger in the longitudinal than transverse direction makes the mechanical properties even more direction-dependent.

#### 2.3.1. Printing with neat thermoplastics

##### **Fused filament fabrication**

In fused filament fabrication (FFF), the material beads placed do not have a perfectly round but rather ellipsoid shape, which facilitates the formation of voids between their edges [13,47–49]. The void content between the beads placed in an individual layer is expected to be less than that of adjacent layers [50,51]. This is explained by the fact that the time required to place two adjacent beads in one layer is significantly shorter than the time required to place two adjacent layers. Consequently, the temperature of the interface created between the incoming bead and the neighbouring bead placed right before is higher than the temperature at the interface to the bead from the lower layer, which has cooled down for a longer time. Naturally, the higher temperature of the interface between two neighbouring beads in the same layer leads to a better fusion of them, which is governed by inter-diffusion of polymer chains. In this context, Ahn et al. [52] have recommended the use of a negative gap, meaning that material beads are placed in such a way that they partially overlap. The positive impact on both tensile strength and stiffness was highlighted. It has to be noted that too large negative gaps can cause excessive material accumulation on the extruder nozzle, which impairs the appearance and accuracy of the final part [53].

Since FFF printers are not perfectly isolated from the environment, FFF is a non-isothermal process in which thermal energy dissipates by means of convection and radiation. The energy dissipates not only into the environment, but also through adjacent beads, layers and voids [54]. This leads to temperature gradients throughout the part thickness and a complex thermal history of the printed parts, directly affecting the bonding quality [55]. Moreover, non-uniform temperature distribution causes uneven material shrinkage upon cooling and warpage of the part [56–59]. This is especially noticeable for semi-crystalline thermoplastics, where crystalline regions contract the amorphous regions upon slow cooling, resulting in local residual stresses [60]. The nozzle and chamber temperatures, printing speed, bead height and width and also printing path influence the mechanical characteristics of parts printed by FFF such as tensile [49,51,52,60–69], flexural [13,51,61–64,66,67] and compression [51,61–64,66,67,70]. This is due to the fact that these printing parameters influence the inter-diffusion of polymer chains and the material solidification. More details with regard to the fundamental modelling of these effects can be found in [71–73].

The formation of interfaces between beads affects the load-bearing capacity of the specimens. Several studies have shown that FFF specimens exhibit both the highest tensile strength and tensile modulus when loaded in the axial direction of the beads [49,52,61,68]. The authors have also reported that the tensile properties gradually decrease from a raster angle of 45° and reach the lowest values for 90°. The same was highlighted for the flexural properties [51,61]. This clearly implies that bead-to-bead bonding is a critical issue of FFF. The building orientation of specimens also influences their mechanical properties. Specimens printed lying in the horizontal  $xy$ -plane of the printing platform exhibit higher tensile strength than those printed standing vertically along the  $z$ -axis. This is due to the fact that in the case of vertical specimens, the load is carried through layer-by-layer bonding, containing defects [51,64,74]. Furthermore, Bellini et al. [51] have shown that FFF parts can by no means be considered isotropic, since pseudo-isotropic specimens printed in different building directions showed different mechanical responses to both tensile and compression loadings. In addition to tensile, bending, compression and impact tests have been employed for the characterisation of the anisotropic behaviour of FFF parts [61–63]. It has been demonstrated that the specimens printed with the raster orientation of 0° absorbed higher energy prior to fracture compared to those with 90° [61].

In order to predict the stress-strain behaviour of FFF parts using Hooke's law, the engineering parameters in the material's principle planes should be known [75]. Depending on the symmetry of a material's microstructure, the number of independent parameters in the stiffness matrix varies from 21 for anisotropic to 3 for isotropic materials. Some publications indicate that FFF parts behave like an orthotropic material [51,74,76], which requires the determination of 9 independent material constants. Kulkarni et al. [50] considered the FFF part to be a fibre reinforced laminate consisting of multiple unidirectional laminae stacked in different directions. Thus, every individual layer was treated as a lamina and the voids as fibres. Based on this consideration, the laminate theory [75] was applied to analyse the stiffness properties, where every individual layer was considered transversely isotropic. The laminate theory was also applied in [48,77], with the difference that every individual unidirectional layer was considered orthotropic. There was a good agreement between the experimental and modelling results, implying that the laminate theory can be applied to describe the mechanical behaviour of FFF parts. An interesting study has been carried out by Spoerk et al. [78], who showed that the meso-structure of PLA parts is homogeneous when printed at extremely high temperatures, exceeding the melting point of PLA by 100 °C. In a follow-up study, Arbeiter et al. [79] demonstrated that specimens printed with 0° and 0°/90° raster orientation have nearly the same fracture toughness, which suggests that material isotropy can indeed be obtained by the careful optimisation of printing parameters.

### **Selective laser sintering**

In SLS parts anisotropy is mainly the result of an inhomogeneous density distribution. One of the reasons for this phenomenon is porosity formed between powder particles that are not completely sintered with each other [80,81]. Improper sintering can be caused by insufficient heat input [82–85], too large powder particle size [86], and low powder bed density [87]. The heat energy supplied to the powder is described by the Andrew number  $A_n$  [ $J/mm^2$ ], which is a product of the laser power  $P$  times the inverse scanning speed  $V^{-1}$  and the inverse hatch distance  $d^{-1}$  [88]. Thus, these parameters should be thoroughly adjusted to the particular material to achieve the highest possible part quality. Higher energy inputs tend to result in enhanced tensile [82–84,89,90] and flexural [91,92] properties,



which can be attributed to an increased material density. However, the use of too high temperatures can lead to material degradation and deterioration of the mechanical properties [91–93].

During SLS printing, the area around the powder that was exposed to laser radiation can be heated up to temperatures as high as the melting point. This leads to partial sintering of these powder particles with each other, and as a consequence, to an increase in the average powder particle size [94]. The powder that has not been directly exposed to laser heat is usually reused in the following SLS prints, which means that the average powder particle size increases with every reuse [1,95]. Particle size and layer thickness play an important role in the final mechanical characteristics and surface appearance of SLS parts [96–98]. If the particles are too large, they cannot be fused properly, firstly because of the large surface area and secondly because of the rapid fusion process. Naturally, larger particles require higher energy inputs; otherwise, the particle cores remain unmelted, leading to an uneven density distribution [99]. The same applies to the layer thickness that should be as thin as possible, since thicker layers need more energy for proper sintering [84,91,97]. Another reason for the non-uniform material densification is the formation of a highly porous 'skin' from passively heated powder particles located around the main printed part exposed to the laser. The presence of porosity between powder particles, especially between sintered layers, leads to the dependency of the mechanical properties on the printing orientation [100–102,84]. The printed parts are therefore most vulnerable to tensile loads applied in the transverse direction to fused cross-sections [82,103,89]. For material modelling of SLS parts, the transversely isotropic behaviour with isotropic properties in planes perpendicular to the building axis can be assumed [104,105].

### 2.3.2. Printing with reinforced thermoplastics

#### **Fused filament fabrication and selective laser sintering**

It has been shown that FFF specimens printed from short carbon fibre reinforced thermoplastics exhibited both enhanced longitudinal tensile strength and flexural strength in comparison with neat specimens [106–108]. This was attributed to the fact that most of the fibres aligned along the filament axis due to the material flow in the molten state, signifying that the load was partially carried by the fibres. Consequently, the strength of FFF composites depends on the fibre-matrix interfacial bonding and the fibre content. It has been demonstrated that while a rise in fibre content reduces the void content between the placed filaments, the void content within the filament itself increases [108]. Ning et al. [44] have investigated the effect of fibre length and fibre content on tensile, flexural and toughness properties of carbon fibre reinforced ABS. Fibres with a length of 150  $\mu\text{m}$  yielded a higher tensile strength and Young's modulus than fibres with a length of 100  $\mu\text{m}$ , whereas the latter favoured better toughness. Fibre contents of 3-7.5 wt% gave higher tensile strength; however, a further increase to 10 and 15 wt% resulted in tensile strengths close to neat ABS. For material modelling, short carbon fibre reinforced parts produced by FFF have been considered orthotropic in [107,109].

The presence of carbon fibres in SLS has a significant impact on the thermal history of the parts during manufacturing, since they absorb more energy and provide a better heat transfer and heat storage within the powder [3]. The processing parameters should be optimised accordingly for the application of carbon fibre reinforced powders. Yan et al. [27] have investigated the effect of the fibre content on the tensile and flexural properties of PEEK specimens. Fibre content of 5-10 wt% was found to be optimal to achieve the highest tensile and flexural strength, while 15 and 20 wt% resulted in values lower than those for neat PEEK. A higher fibre content also led to higher porosity concentrated

mainly between adjacent layers due to a low melting depth. Jing et al. [110] have shown that tensile strength and tensile modulus of carbon fibre reinforced polyamide 12 (PA12) SLS specimens increased by 60% and 323% compared to neat PA12, respectively. Their flexural strength and flexural modulus increased by 108% and 298%, respectively. Similar to FFF, the presence of a preferable fibre orientation has been mentioned in studies of SLS [3,111]. Micrograph analysis revealed a partial alignment of the fibres along the travel direction of the rake, spreading the powder over the printing platform in the SLS machine (Fig. 8). The effect gave a higher tensile strength for specimens printed along this direction. An assumption of the orthotropic material behaviour has also been used for modelling of short fibre reinforced polymers processed by SLS, for example, in [112].

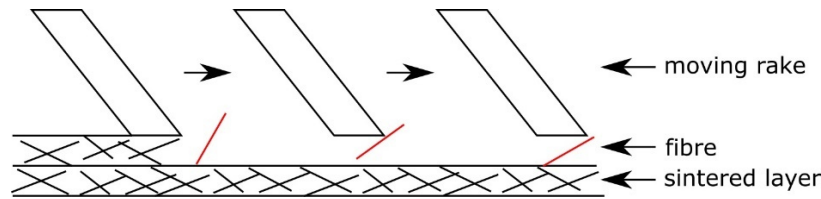


**Fig. 8.** Schematic representation of the fibre alignment process in SLS adopted from [111].

### Automated tape placement with in-situ consolidation

ATPisc enables the processing of unidirectional carbon fibre reinforced thermoplastic tapes, which can be used to create laminates with different lay-ups. Depending on the layer stacking sequence, the final mechanical properties can vary from quasi-isotropic to fully anisotropic. To predict the stress-strain behaviour of ATPisc laminates, the laminate theory can be applied [75]. It is apparent that unidirectional (UD) laminates exhibit much higher tensile strength when loaded along than across the fibre direction. However, it is a challenging task to print a flat laminate using ATPisc due to the pronounced residual stresses that accumulate during manufacturing.

The residual stresses built up in continuous fibre reinforced thermoplastics can be categorised into three levels [113,114]. The first level is the micromechanical level, describing residual stresses that are caused by a greater shrinkage of the matrix than the fibres upon cooling down from  $T_m$ . This is caused by a mismatch of the coefficients of thermal expansion (CTE) of the matrix and the fibres [113,114]. A difference in the shrinkage behaviour is also observed for amorphous and semi-crystalline matrices [114]. Semi-crystalline thermoplastics tend to shrink to a greater extent than amorphous ones due to the higher densification when lamellae fold [6]. The second level of residual stress accumulation is the macro-mechanical level, which refers to the layer-to-layer connection. Residual stresses build-up on this level due to the difference in CTE in the longitudinal and transverse directions. For instance, in a  $[0/90]$  laminate, a  $0^\circ$  layer contracts a  $90^\circ$  layer along the fibres, while a  $90^\circ$  layer contracts a  $0^\circ$  layer across the fibres, causing laminate distortion [114]. The third level of residual stress is the global level, which is associated with the accumulation of residual stresses through the laminate thickness, resulting in the parabolic curvature of the laminates [113,114]. Figure 9 illustrates the mechanism of accumulation of residual stresses using the example of a unidirectional carbon fibre reinforced laminate.

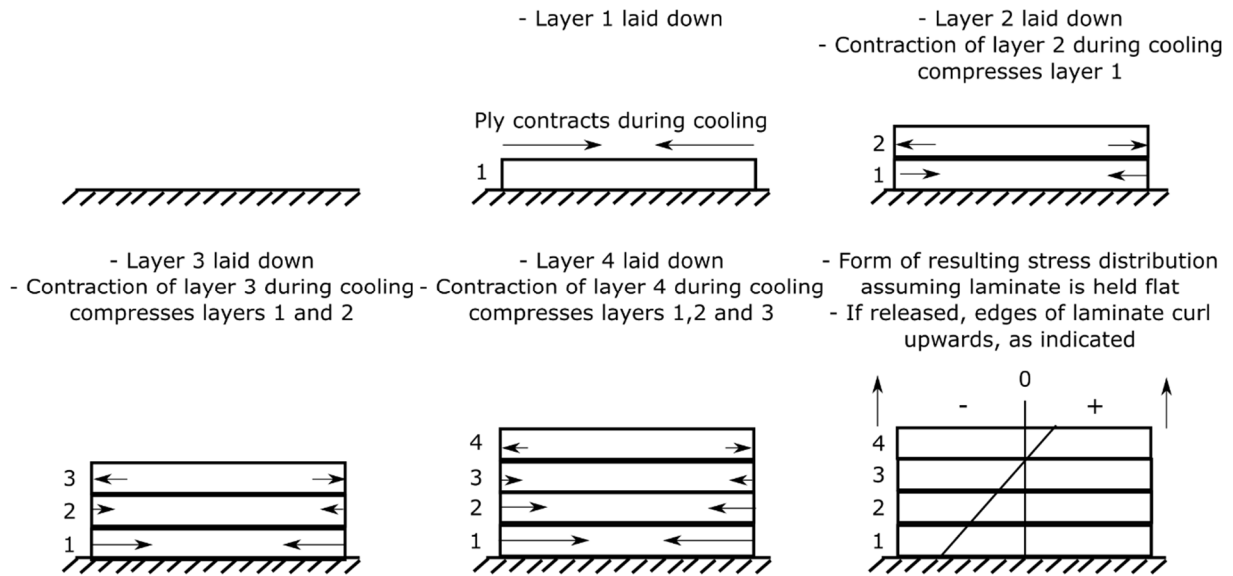


**Fig. 9.** Schematic illustration of accumulation of residual stresses on the global level in a unidirectional carbon fibre reinforced laminate produced by ATPisc adopted from [59].

A further parameter with a significant impact on residual stresses in thermoplastic composites produced by ATPisc is the cooling rate used during manufacturing. Slow cooling of laminates results in lower residual stresses on the global level because the material has more time to ‘relax’. To address this issue, thermoplastic composites comprising thermal residual stresses after fabrication can be annealed with a prolonged cooling time from  $T_m$  to  $T_g$  [115,116]. Another factor inducing residual stresses on the global level is the non-uniform cooling of the laminate. The laminate’s bottom layers cool down and solidify earlier than the upper layers. Thus, the already solidified layers have a restraining effect on the not yet solidified layers, bringing about laminate curvature [114]. Excessive residual stresses occurring during manufacturing can even result in premature cracks and delamination between the laminate layers.

The cooling rate also strongly affects the degree of crystallinity, which in turn influences the mechanical characteristics and interlayer bonding in thermoplastic composites produced by ATPisc [117]. It has been shown that higher cooling rates lead to better fracture toughness properties [117–120], whereas tensile strength, stiffness and shear strength are adversely affected [16,42,121–124]. Therefore, manufacturing parameters (e.g. processing temperature, placement speed, cooling rate) and laminate characteristics (e.g. geometric dimensions, thermal conductivity, insulating properties of the material) that affect the thermal history should be carefully optimised for every print in order to achieve the best laminate quality in terms of interlayer bonding and flatness [40].

Another critical issue of ATPisc laminates is the presence of voids between layers. The fact is that the incoming tape always has a certain number of inherent voids that get squeezed by the compaction roller [125,126]. As soon as the roller pressure ceases, the voids entrapped between the layers expand due to the high inner pressure and the low viscosity of the matrix, resulting in impaired interlayer bonding [125,127,128]. Khan et al. [125] have investigated the influence of a series of manufacturing parameters (e.g. placement speed, roller diameter, consolidation force, mould temperature, laminate thickness) on the laminate quality, assessed in terms of the degree of bonding and porosity content. The authors showed that laminate production with a higher consolidation force has a positive effect on both the porosity content and the degree of bonding. While faster placement speed and lower tool temperature also favour a lower porosity, the degree of bonding deteriorates.

Tierney et al. [127] have pointed out that multiple passes with the compaction roller can reduce the number of entrapped voids between layers, thereby improving the mechanical properties of laminates. Besides the inherent void content, Gruber et al. [126] have also highlighted the issue of fibre-rich areas in the tapes that constrain the roller from pressing out the voids.

## 2.4. Experimental methods for interlayer bonding characterisation

The layer-by-layer building approach of additive manufacturing makes the interlayer bonding a critical aspect for thermoplastic composites. The interface between adjacent layers is a potential site for voids and non-uniform adhesion that promote crack formation and expose the entire structure to a high risk of catastrophic failure. It is therefore of utmost importance to thoroughly characterise the bonding quality in order to be able to predict the fracture behaviour of parts produced by AM.

### 2.4.1. Fracture mechanics testing

One of the terms which can be used to characterise interlayer bonding in neat and fibre reinforced polymers is the fracture toughness. This is a material property that describes the material's resistance to crack propagation and can be used to characterise the quality of interlayer adhesion. According to the linear elastic fracture mechanics (LEFM), where the material is considered linear elastic almost without nonlinear effects, the fracture toughness is described by means of stress intensity factor (SIF) and strain energy release rate (ERR). SIF, designated as  $K$ , is derived from the crack tip stress field approach and explains the stress, strain and displacement field in the vicinity of the crack tip. The stress field  $\sigma_{ij}$  at the point with polar coordinates  $(r, \theta)$  is described by Eq. 1 [129].

$$\sigma_{ij}(r, \theta) = \frac{K}{\sqrt{2\pi r}} f_{ij}(\theta) + \text{other terms} \quad (1)$$

The strain energy release rate (SERR), denoted as  $G$ , expresses the crack propagation based on the energy balance approach and is defined as the amount of potential energy  $d\Pi$  released per newly created crack area  $dA$  (Eq. 2).

$$G = -\frac{d\Pi}{dA} = \left[ \frac{J}{m^2} \right] \quad (2)$$

Crack advancement can occur following either one of the main three fracture modes or a combination thereof (mixed-mode) with the corresponding  $K$  and  $G$  values (Fig. 10). When  $K_{(I,II,III)}$  or  $G_{(I,II,III)}$  exceed a certain critical value  $K_c$  or  $G_c$ , crack growth occurs and the respective crack growth criterion is described with Eq. 3 [129]. For linear elastic materials, the relationship between  $G$  and  $K$  is explained with Eq. 4 [129].

$$K_{(I,II,III)} \geq K_{(I,II,III)c} \text{ or } G_{(I,II,III)} \geq G_{(I,II,III)c} \quad (3)$$

$$G = \frac{K_I^2}{E'} + \frac{K_{II}^2}{E'} + \frac{K_{III}^2}{2\mu} \quad (4)$$

$$E' = E \text{ for plane stress; } E' = \frac{E}{1-\vartheta} \text{ for plane strain}$$

where  $E$  is Young's modulus,  $\vartheta$  is Poisson's ratio, and  $\mu$  is shear modulus.

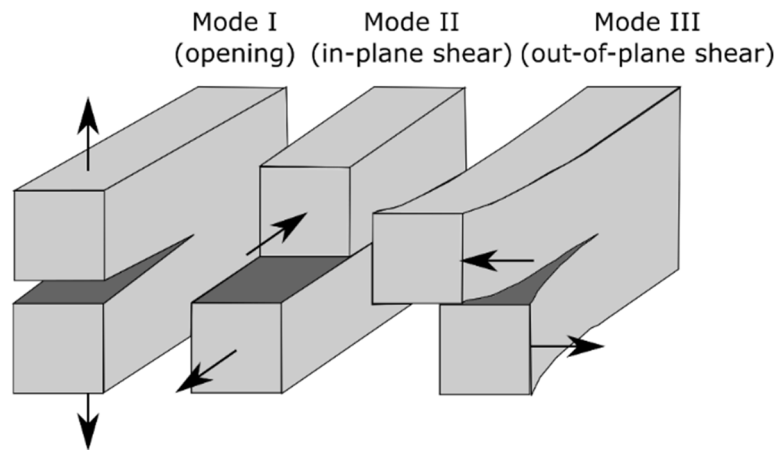


**Fig. 10.** Schematic illustration of the three basic fracture modes of crack propagation. Adopted from [129].

Each of the fracture modes requires a certain test setup and an appropriate test procedure. Generally, studies begin with the mode I fracture, where the crack growth occurs in the mid-plane perpendicular to the loading axis. Table 1 summarises studies that have applied the mode I FM tests to characterise the fracture toughness of polymers processed by FFF, SLS and ATPisc. It can be seen from Table 1 that the single edge notched bend (SENB) test and the compact tension (CT) test are used for the determination of fracture toughness of FFF and SLS parts. While the double cantilever beam (DCB) test is used to characterise FFF and ATPisc, but not SLS parts. This is due to the fact that DCB testing is applied to the laminates with a distinguished layer structure, which is typical for FFF and ATPisc parts. Whereas SLS parts have a more homogeneous material structure. It can also be concluded from Table 1 that SENB is used mostly for testing neat thermoplastics, while the CT and DCB tests can be employed for testing both neat and fibre reinforced thermoplastics. At the same time, DCB mode I test is a common test to characterise interlayer bonding in UD laminates produced by ATPisc. It should also be noted that besides the tests mentioned in Table 1, the crack round bar (CRB) test seems to be a promising test method to characterise the adhesion between two adjacent layers. This test was employed, for example, by Watschke et al. [130] for multi-material FFF parts. However, the authors did not characterise the interlayer bonding in terms of FM.

### Quasi-static mode I DCB testing

To date, there are no FM test procedures standardised exclusively for AM parts. Thus, the standards available for FM testing of polymers and polymer composites are applied in the field of AM. The National Institute of Standards and Technology (NIST, USA) has published a report, containing the test standards applicable for the characterisation of AM parts [131]. In this report, ISO 15024 [132] and ASTM D 5528 [133] are recommended for the characterisation of the mode I fracture toughness of fibre reinforced polymers processed by AM (within the framework of LFM) [131]. The quasi-static DCB mode I test described in these standards is a common test method applied to evaluate the fracture toughness of both neat and fibre reinforced polymer laminates [134]. During quasi-static mode I DCB test, the delamination length  $a$  is recorded together with the corresponding load  $P$  and displacement  $\delta$ , which are subsequently used for the calculation of  $G_I$  using either the beam theory (BT), the modified beam theory (MBT), compliance calibration (CC) or modified compliance calibration (MCC).

The formulas of these methods can be found in both ISO 15024 [132] and ASTM D 5528 [133]. In general,  $G_I$  of a DCB specimen with a width  $B$  can be calculated using Eq. 5.

$$G_I = \frac{1}{2 * B} P^2 \frac{dC}{da} \quad (5)$$

where  $P$  is the load and  $C = \delta/P$  is the compliance.

**Table 1.** Studies that have used fracture mechanics testing for the characterisation of interlayer bonding in laminates produced by FFF, SLS and ATPisc.

Test	Author	Material
<b>Fused filament fabrication</b>		
<b>Single edge notched bend (SENB) test</b>	Hart et al. [135]	ABS
	Song et al. [136]	PLA
	Ahmed et al. [137]	PLA
	Arbeiter et al. [79]	PLA
<b>Compact tension (CT) fracture test</b>	Torres et al. [138]	PLA
	McLouth et al. [139]	ABS
	Arif et al. [140]	PEEK
	Ahmed et al. [137]	PLA
	Gardan et al. [141]	ABS
	Arbeiter et al. [79]	PLA
	Papon et al. [142]	PLA, short CF-PLA
	<b>Double cantilever beam (DCB) mode I test</b>	Aliheidari et al. [17]
	Spoerk et al. [78]	PLA
	Young et al. [143]	ABS, short CF-ABS
	Barile et al. [144]	ABS
	Park et al. [145]	ABS
	Fonseca et al. [146]	PA12, short CF-PA12
<b>Selective laser sintering</b>		
<b>Single edge notched bend (SENB) test</b>	Linul et al. [147]	PA2200
	Stoia et al. [148]	PA2200
<b>Compact tension (CT) fracture test</b>	Cano et al. [149]	PA12
	Brugo et al. [150]	PA2200
	Salazar et al. [151]	PA11, PA12
	Salazar et al. [152]	PA12, short CF-PA12
	Blattmeier et al. [153]	PA12
<b>Automated tape placement with in-situ consolidation</b>		
<b>Double cantilever beam (DCB) mode I test</b>	Ray et al. [117]	UD CF/PEEK
	Modi et al. [154]	UD CF/PEEK
	Qureshi et al. [4]	UD CF/PEEK
	Bandaru et al. [155]	UD CF/PEEK

The delamination resistance is presented using R-curves (resistance curves) by plotting  $G_{Ic}$  versus the delamination length  $a$ . The R-curves enable the determination of (i) the initiation value of  $G_{Ic}$  required to start the crack growth and the propagation value of  $G_{Ic}$  required for its further propagation, of (ii) the instability of crack behaviour (e.g. the R-curve with a saw-tooth shape intimates the stick-slip behaviour of crack propagation (Fig. 11) [156,157]), and of (iii) the presence of additional

damage processes (e.g. rising R-curves indicate the presence of fibre bridging, which is a net of fibres pulled out from the beams upon crack opening [158]).

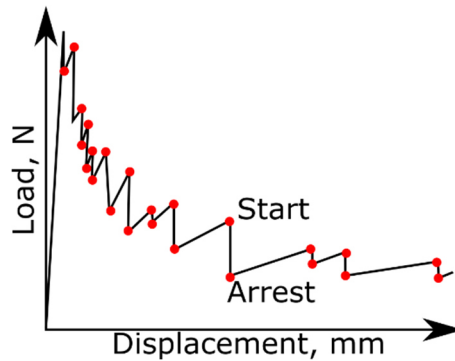


**Fig. 11.** Schematic presentation of the load-displacement curve of a DCB specimen, exhibiting the stick-slip behaviour during mode I quasi-static testing. The labels ‘start’ and ‘arrest’ refer to the start of the crack growth and to the arrest of the crack, respectively.

As already mentioned, in the quasi-static mode I DCB test, the crack length is monitored as a function of the corresponding load and displacement. Both ISO 15024 [132] and ASTM D 5528 [133] suggest using a traveling microscope or an equivalent magnifying device to follow the crack tip, while an action button in the test machine software enables the extraction of force and displacement values at every crack increment. As a result, the measurements are highly dependent on the reaction and carefulness of the machine operator. In addition, the test can take a long time to propagate the crack to a certain length (at least 45 mm are required according to the standards for loading rates of 1-5 mm/min), making testing multiple specimens labour intensive. To make the measurements easier and less dependent on the visual measurement made by the machine operator, several studies have employed digital image correlation (DIC) [159–164]. It has been demonstrated that the results acquired using DIC were in good agreement with both a method based on compliance variations [161–163] and the conventional visual measurements [159,162]. Moreover, Zhu et al. [164] highlighted that DIC enables the crack length determination with a higher accuracy compared with microscopic observations. The working principle of DIC is the tracking of changes in images that were taken during testing. Prior to testing, a contrast stochastic dot pattern is applied to the specimen surface. A calibrated optical system with either one camera for 2D measurements [165] or two cameras for 3D measurements [166] is employed to take images of the specimen surface throughout the test. The correlation of the actual coordinates of speckles with their initial coordinates enables the calculation of displacement and strain fields by a comparison of grey intensity inside the subsets that are created virtually on the images [167]. Deeper insights into the theory of the working principle of DIC can be found, for example, in [168] and recommendations on specimen preparation and DIC analysis in [169].

The quasi-static mode I DCB test has been employed for testing of neat and short carbon fibre reinforced thermoplastic DCB specimens printed by FFF in [17,78,143,146] (Table 1). However, in these studies, the specimens were printed deliberately 3-5 times thicker than the standard thickness of 3-5 mm in order to avoid plastic deformation of the beams under excessive crack opening. Mode I DCB testing of ABS specimens printed using FFF has revealed that higher processing temperatures and a smaller layer height have a positive impact on fracture toughness [17]. Young et al. [143] have highlighted the importance of a careful adjustment of printing parameters for every material. The authors found out that the fracture toughness of short carbon fibre reinforced ABS specimens was smaller than that of neat ABS specimens. It was explained by poor wetting of the chopped carbon

fibres that caused a formation of intra-layer voids. However, Fonseca et al. [146] have shown that carbon fibres enhanced the fracture toughness of PA12 specimens printed using FFF. Regarding ATPisc, Ray et al. [117] have demonstrated that ATPisc laminates exhibited higher  $G_{IC}$  than those produced using autoclave processing. The difference was explained by a lower degree of crystallinity and more pronounced plastic deformations of the matrix in the case of ATPisc specimens.

### Mode I fatigue testing

In addition to the characterisation of crack propagation under quasi-static loading, it is necessary to investigate that under fatigue loading, which dramatically affects the service-life of structural parts. For characterisation of the fatigue delamination resistance of parts produced by AM, NIST [131] has recommended to use ISO 15850 [170] and ASTM D 6115 [171].

ISO 15850 describes a test procedure to determine the tension-tension fatigue crack propagation in polymers in the framework of LEFM using the compact tension (CT) specimens. In general, CT specimens have been used in many studies to characterise the fatigue behaviour of AM parts. For example, they were used by Arbeiter et al. [79] to investigate the effect of raster orientations on the fatigue lifetime of PLA processed by FFF. The authors showed that regardless of the raster angle ( $0^\circ$ ,  $90^\circ$  and  $0^\circ/90^\circ$ ), the specimens exhibited nearly the same fatigue life. Blattmeier et al. [172] showed that PA12 CT specimens produced by SLS have longer fatigue life compared to those produced by injection moulding. Salazar et al. [151] investigated the impact of different ambient conditions on the fatigue crack propagation in PA11 and PA12 CT specimens produced by SLS. The specimens were tested in a dry environment at  $23^\circ\text{C}$  and  $50^\circ\text{C}$ , and in a wet environment at  $23^\circ\text{C}$ . Independently of the ambient conditions, PA11 specimens showed higher fatigue delamination resistance than PA12 specimens. The effect of short carbon fibre on the fatigue crack propagation in PA12 CT specimens produced by SLS was addressed by Salazar et al. [152]. It was shown that the fibres improve the fatigue life of specimens significantly when tested in a dry environment at  $-50^\circ\text{C}$ . Cano et al. [149] examined the fatigue crack propagation in PA12 CT specimens. The authors demonstrated that the fatigue delamination resistance depends on the loading direction of specimens with respect to the orientation of the sintered layers.

ASTM D 6115 provides a test procedure to determine the mode I fatigue delamination growth onset of unidirectional (UD) fibre reinforced polymer composites. This standard could potentially be applied to ATPisc laminates, but all studies available in literature have investigated the fracture resistance of ATPisc laminates under quasi-static loading (Table 1), while that under fatigue loading has not yet been studied. Moreover, ASTM D 6115 is limited to the determination of the fatigue delamination growth onset, but not propagation. This problem has been addressed by the European Structural Integrity Society Technical Committee 4 (ESIS TC4), who proposed a test protocol for mode I fatigue testing developed over the course of the round-robin testing of UD fibre reinforced laminates [173].

### Fatigue mode I DCB testing

According to the ESIS TC4 protocol [173], a DCB specimen is subjected to cyclic loading at 3, 5 or 10 Hz either under load control with a constant R-ratio =  $P_{min}/P_{max}$  or under displacement control with a constant  $R_\delta$ -ratio =  $\delta_{min}/\delta_{max}$ . It is recommended that testing be performed under displacement control for a stable delamination growth, since in this case, both the crack growth rate and the energy release rate decrease with crack propagation, whereas for load control, the opposite



is observed [174]. The recommended  $R_\delta$ -ratio is 0.1 [173]. For the calculations of  $G_{I_{max}}$  and  $G_{I_{min}}$ , the mid-plane delamination length  $a$  is recorded together with the corresponding number of cycles  $N$ , peak values of load  $P_{max}$ ,  $P_{min}$  and displacement  $\delta_{max}$ ,  $\delta_{min}$ . When the crack growth rate slows down to  $10^{-6}$  mm per cycle, the corresponding SERR is taken as a threshold value, below which no delamination propagation is expected. The threshold value can be further used in a safe-life assessment of a structure. The importance of considering the fatigue delamination resistance in safety design has been demonstrated, for instance, by Schoen et al. [175]. The authors showed that the threshold SERR obtained from fatigue tests was 1.7 times smaller than  $G_{Ic}$  derived from quasi-static tests. This data implies that while delamination might not start to grow under certain static loading conditions, it could be started during fatigue loading, possibly leading to unexpected failure. Brunner et al. [176] have highlighted that the threshold values obtained for mode I fatigue crack growth in UD carbon fibre reinforced epoxy laminates are very low. For the safety design, thresholds go down to about  $30 \text{ J/m}^2$ . Such low values impose significant design limitations on the structural components. In their other work on the development of a standardised procedure for mode I DCB fatigue testing, Brunner et al. [177] have reported that threshold values could not be determined even after 22 days of cyclic loading at 10 Hz under displacement control; the crack growth rate did not slow down to  $10^{-6}$  mm/cycle. This also indicates very low fatigue delamination thresholds.

There are several ways to represent fatigue delamination resistance data [178]. One of them is using a Paris relation based method by plotting the crack growth rate  $da/dN$  versus a function of SERR. (Eq. 6)

$$\frac{da}{dN} = A * f(G)^m \quad (6)$$

where  $A$  and  $m$  are constants defined as the Y-intercepts and the slopes of the linear regressions fitted to the linear regions of the curves, respectively. In earlier studies,  $da/dN$  was plotted versus either  $f(G) = G_{I_{max}}$  or  $f(G) = \Delta G = (G_{I_{max}} - G_{I_{min}})$ . It has been pointed out that the original Paris-Erdogan equation was derived for metals and alloys using SIF, which is proportional to the square root of SERR [179]. Thus, it was highlighted that Eq. 6 should be a function of either  $\sqrt{G_{I_{max}}}$  or  $\Delta\sqrt{G} = \sqrt{G_{I_{max}}} - \sqrt{G_{I_{min}}}$ . A comprehensive review of this topic can be found in [178].

Another approach that enables the representation of fatigue delamination resistance is a Hartman-Schijve based approach, proposed by Jones et al. [180] for mode I and II delamination growth. This approach implies the use of the modified Hartman-Schijve equation, which is also referred to as the Hartman-Schijve variant of the NASGRO equation [179]. According to this equation, the fatigue crack growth rate  $da/dN$  can be expressed in the form of Eq. 7.

$$\frac{da}{dN} = D * \left[ \frac{\Delta\sqrt{G} - \Delta\sqrt{G_{thr}}}{\sqrt{\left\{ 1 - \sqrt{\frac{G_{max}}{A}} \right\}}} \right]^n \quad (7)$$

where  $\Delta\sqrt{G_{thr}} = \sqrt{G_{I_{max,thr}}} - \sqrt{G_{I_{min,thr}}}$ ,  $A, D, n$  are constants.  $\Delta\sqrt{G_{thr}}$  and  $A$  are chosen so that the plot of Eq. 7 becomes virtually linear [181–183]. It is stated that  $A$  can be first estimated to be about of the critical quasi-static SERR, which can be further refined in order to achieve the best linear fit [181].  $G_{thr}$  relates to the threshold SERR,  $G_{th}$ , in Eq. 8, associated with a crack growth rate of  $10^{-10}$  m/cycle.

$$10^{-10} = D * \left[ \frac{\Delta\sqrt{G_{th}} - \Delta\sqrt{G_{thr}}}{\sqrt{\left\{ 1 - \sqrt{\frac{G_{max}}{A}} \right\}}} \right]^n \quad (8)$$

The crack propagation in carbon fibre reinforced laminates is often not a single damage process, but accompanied by fibre bridging, multiple cracking, void growth, etc. [184]. Additional damage processes affect the real threshold value of crack growth onset, which leads to wrong life-cycle estimations. The formation of multiple cracking overestimates SERR by an extra energy release per newly created fracture surface and additional secondary fracture modes [185]. Fibre bridging significantly retards the fatigue crack growth rate, which also increases the effective SERR [158]. It is worth noting that the extent of fibre bridging depends on the crack length, which questions the adequacy of the threshold SERR obtained from a single resistance curve based on a certain pre-crack length. This problem has been addressed by Yao et al. [158]. The authors showed that a longer crack length promotes the development of fibre bridging, which leads to a shift in the fatigue resistance curves from left to right along the X-axis in a plot displaying  $da/dN$  as a function of  $\Delta\sqrt{G}$  (Fig. 12). It was found that the curves no longer shift to the right from a certain delamination length, indicating that a state of fully developed fibre bridging was achieved ( $da_5$  in Fig. 12). It was also demonstrated that the extent of fibre bridging developed in quasi-static and fatigue testing is different. The fatigue resistance curve of a specimen with a pre-crack introduced under quasi-static loading was more to the right than the curve of a specimen with a pre-crack of the same length, but introduced under fatigue loading. This indicated that fibre bridging developed under fatigue loading is less pronounced than that of quasi-static loading.

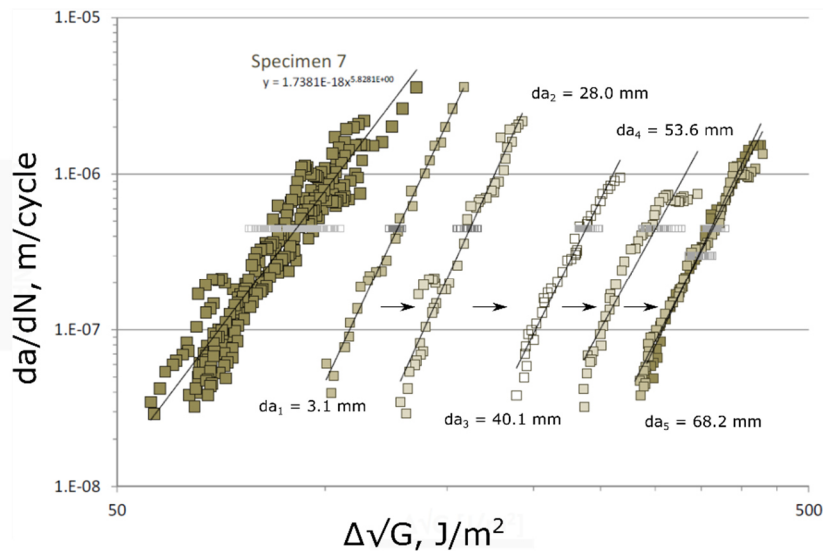


**Fig. 12.** Six crack growth curves obtained from sequential fatigue tests performed on one specimen by Yao et al. [186]. The curves shift to the right until a certain crack length is reached, where they start to overlap. The leftmost curve refers to the so-called ‘zero-bridging’ curve obtained from the regression analysis of all curves. Figure adopted from [186].

The methodology to exclude the influence of fibre bridging on the fatigue crack growth based on the findings described above was developed and presented by Alderliesten et al. [186]. According to this methodology, a series of sequential fatigue loading cycles is performed on one specimen. At the beginning, the first pre-crack is created using quasi-static loading yielding  $\delta_{max}$ , which is used in the

following fatigue loading with a constant  $R_\delta$ -ratio of 0.1. The fatigue test is interrupted when the crack growth rate slows down to about  $10^{-11}$  mm/min. After that, the same specimen is loaded under quasi-static conditions to further propagate the crack of about 1-3 mm, yielding new  $\delta_{max}$ . Next, another fatigue loading cycle is started using this value of  $\delta_{max}$ . The procedure is repeated until the fatigue resistance curves stop shifting to the right and start overlapping (Fig. 12). The overlapping of the curves corresponds to the full development of fibre bridging. Subsequently, regression analysis of the entire data obtained is performed, in order to get a single 'zero-bridging growth' curve for the unambiguous determination of  $\Delta\sqrt{G_{th}}$  from it (see the leftmost curve in Fig. 12). So, the 'zero-bridging growth' approach can be used to present fatigue delamination resistance.

Fatigue delamination resistance can also be described using an energy-based approach, relying on the energy dissipation occurring upon fatigue crack extension. Accordingly,  $da/dN$  can be plotted versus  $dU/dN$ , where  $U$  is the applied energy (Eq. 9, Fig. 13) [174,187]. The total energy release  $dU/dN$  in a DCB specimen exhibiting fibre bridging under fatigue loading consists of the energy released upon the crack increment  $dU_a/dN$  and the energy released upon fibre bridging  $dU_{br}/dN$  (Eq. 10) [187]. It has been shown that the contribution of  $dU_{br}/dN$  to the total energy is much smaller in comparison with  $dU_a/dN$ , which was demonstrated by the overlap of curves of different pre-crack lengths in a single curve (Fig. 13) [174,187]. This was attributed to the fact that the change in the applied energy was mainly governed by crack propagation rather than fibre bridging. It was stated that bridging fibres periodically store and release strain energy upon loading and unloading during fatigue testing and thus only contribute to the effective energy release in the event of failure [174]. It was demonstrated that the energy-based approach can be used to assess the extent of fibre bridging in laminates.

$$U = \frac{1}{2} P_{max} \delta_{max} \quad (9)$$

$$\frac{dU}{dN} = \frac{dU}{da} \frac{da}{dN} = \left( \frac{dU_a}{da} + \frac{dU_{br}}{da} \right) \frac{da}{dN} \quad (10)$$

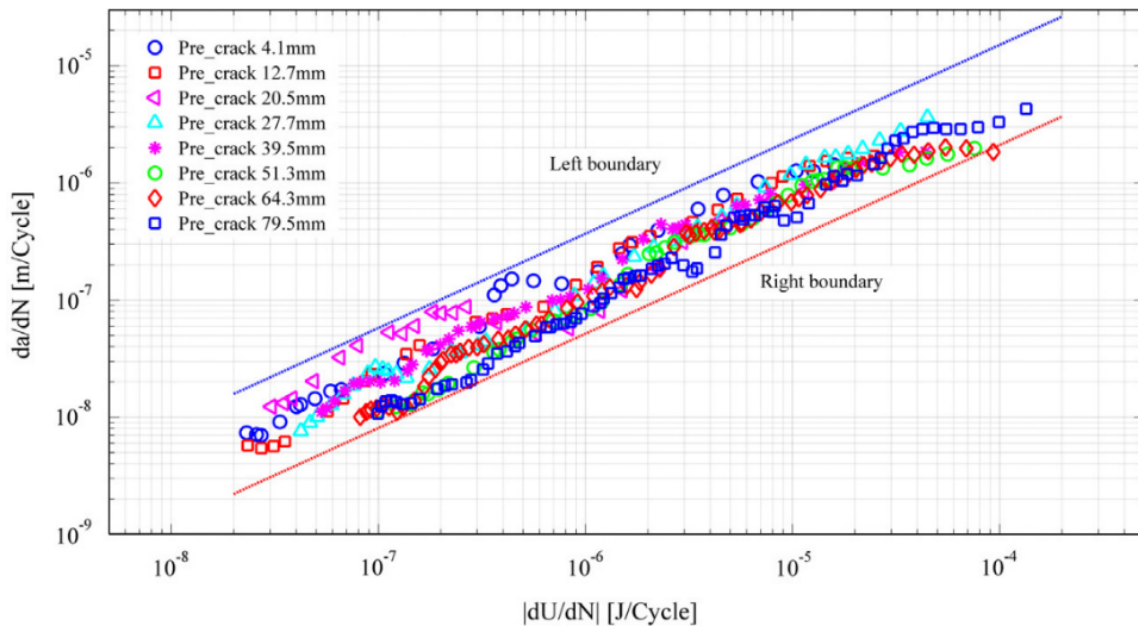


**Fig. 13.** Example of fatigue data representation of specimens with different pre-crack lengths using the energy approach, where  $da/dN$  is plotted versus  $|dU/dN|$ . Figure reprinted from [174].

### 2.4.2. Interlaminar shear testing

Interlayer bonding can also be characterised by shear tests under tensile (single and double lap shear tests), compression (Iosipescu shear test, shear test between metal plates, single lap compression shear test) or bending (short-beam strength test) [188] loading conditions. As a rule, the short-beam strength (SBS) test is applied to obtain the interlayer shear strength (ILSS) due to the simplicity of this test [189]. SBS is an easy-to-perform test that requires relatively small specimens to be loaded in three-point-bending. According to the test standard [189], the specimen thickness can be up to 6 mm and the maximum specimen length and width can reach 36 and 12 mm, respectively. Despite the above described simplicity of the SBS procedure, it has been shown that this test does not yield a pure shear state in thermoplastic matrix composites. It was demonstrated that interlayer delamination does not occur in shear, but that the specimen fails under a mixture of compression and shear loads in the upper part [188,190]. To overcome these limitations, Rosselli and Santare [191] used a compression shear device which had first been proposed by Lauke et al. [192]. This device consists of one stationary and one loading block. A rectangular sample is placed between the blocks in such a way that a vertical axis virtually drawn through the centre of the sample is at an equidistance from the stationary and loading noses. The sample size recommended is conveniently small, amounting to a width of  $\leq 20$  mm, length of  $\leq 20$  mm and thickness of  $\leq 1.5 \cdot \text{length}$  [188]. The finite element analysis performed in [191] proved that the compression shear test (CST) gives a shear stress state closer to pure shear and also less complex in comparison with SBS.

In the field of AM, the topic of true interlaminar shear strength has been addressed, for example, by Dutra et al. [193]. The authors characterised the interlaminar shear strength of continuous carbon fibre reinforced composites produced by FFF using SBS. It was shown that the specimens failed either under interlaminar shear or under compression. CST was recommended to avoid uncertainties in failure modes in future studies. However, some authors have limited their studies to SBS and employed it for quality control reasons only. For instance, Caminero et al. [21] used SBS to characterise thermoplastic composites FFF printed using different material configurations and layer thicknesses. SBS was also used in [4,39,155,194] for the characterisation of the interlaminar shear strength in laminates produced by ATP without checking whether the failure modes were valid. The issue of the characterisation of the true interlaminar shear strength in AM parts requires further research with the determination of an appropriate test method to obtain it.

## 2.5. References

- [1] Gibson I, Rosen D, Stucker B. Additive Manufacturing Technologies. New York, NY: Springer New York; 2015.
- [2] Blok LG, Longana ML, Yu H, Woods BKS. An investigation into 3D printing of fibre reinforced thermoplastic composites. *Addit. Manuf.* 2018;22:176–86.
- [3] Yan C, Hao L, Xu L, Shi Y. Preparation, characterisation and processing of carbon fibre/polyamide-12 composites for selective laser sintering. *Compos Sci Technol* 2011;71(16):1834–41.
- [4] Qureshi Z, Swait T, Scaife R, El-Dessouky HM. In situ consolidation of thermoplastic prepreg tape using automated tape placement technology: Potential and possibilities. *Compos B Eng* 2014;66:255–67.
- [5] Offringa A. R. Thermoplastic composites—rapid processing applications. *Compos Part A Appl Sci Manuf* 1996;27(4):329–36.

- [6] Campbell FC. Structural composite materials. Materials Park Ohio: ASM International; 2010.
- [7] Askeland DR, Fulay PP. Essentials of materials science and engineering. 2nd ed. Australia, United States: Cengage Learning; 2009.
- [8] Dave Hauber, Zachary August, Graham Ostrander, John Michasiow (eds.). Recent developments in automated fiber placement of thermoplastic composites; 2014.
- [9] Stokes-Griffin CM, Compston P. Investigation of sub-melt temperature bonding of carbon-fibre/PEEK in an automated laser tape placement process. *Compos Part A Appl Sci Manuf* 2016;84:17–25.
- [10] Vidya Kishore, Xun Chen, Christine Ajinjeru, Ahmed Arabi Hassen, John Lindahl, Jordan Failla, Vlastimil Kunc, Chad Duty. Additive Manufacturing of High Performance Semicrystalline Thermoplastics and Their Composites.
- [11] Crump SS. Apparatus and method for creating three-dimensional objects: U.S.(5,121,329); 1992.
- [12] Spoerk M, Gonzalez-Gutierrez J, Sapkota J, Schuschnigg S, Holzer C. Effect of the printing bed temperature on the adhesion of parts produced by fused filament fabrication. *Plast Rubber Compos* 2017;47(1):17–24.
- [13] Sun Q, Rizvi GM, Bellehumeur CT, Gu P. Effect of processing conditions on the bonding quality of FDM polymer filaments. *Rapid Prototyp J* 2008;14(2):72–80.
- [14] Bellehumeur C, Li L, Sun Q, Gu P. Modeling of Bond Formation Between Polymer Filaments in the Fused Deposition Modeling Process. *Journal of Manufacturing Processes* 2004;6(2):170–8.
- [15] Pavan Kumar Gurralla, Srinivasa Prakash Regalla. Part strength evolution with bonding between filaments in fused deposition modelling. This paper studies how coalescence of filaments contributes to the strength of final FDM part.
- [16] Batista NL, Olivier P, Bernhart G, Rezende MC, Botelho EC. Correlation between degree of crystallinity, morphology and mechanical properties of PPS/carbon fiber laminates. *Mat. Res.* 2016;19(1):195–201.
- [17] Aliheidari N, Tripuraneni R, Ameli A, Nadimpalli S. Fracture resistance measurement of fused deposition modeling 3D printed polymers. *Polym Test* 2017;60:94–101.
- [18] Brenken B, Barocio E, Favalaro A, Kunc V, Pipes RB. Fused filament fabrication of fiber-reinforced polymers: A review. *Additive Manufacturing* 2018;21:1–16.
- [19] Dickson AN, Barry JN, McDonnell KA, Dowling DP. Fabrication of continuous carbon, glass and Kevlar fibre reinforced polymer composites using additive manufacturing. *Addit. Manuf.* 2017;16:146–52.
- [20] Caminero MA, Chacón JM, García-Moreno I, Rodríguez GP. Impact damage resistance of 3D printed continuous fibre reinforced thermoplastic composites using fused deposition modelling. *Compos B Eng* 2018;148:93–103.
- [21] Caminero MA, Chacón JM, García-Moreno I, Reverte JM. Interlaminar bonding performance of 3D printed continuous fibre reinforced thermoplastic composites using fused deposition modelling. *Polym Test* 2018;68:415–23.
- [22] Ćwikła G, Grabowik C, Kalinowski K, Paprocka I, Ociepka P. The influence of printing parameters on selected mechanical properties of FDM/FFF 3D-printed parts. *IOP Conf. Ser.: Mater. Sci. Eng.* 2017;227:12033.
- [23] Kumar S. Selective Laser Sintering: A Qualitative and Objective Approach.
- [24] Kruth JP, Wang X, Laoui T, Froyen L. Lasers and materials in selective laser sintering. *Assembly Autom* 2003;23(4):357–71.
- [25] Schmidt M, Pohle D, Rechtenwald T. Selective Laser Sintering of PEEK. *CIRP Annals - Manufacturing Technology* 2007;56(1):205–8.
- [26] Kruth J-P, Mercelis P, van Vaerenbergh J, Froyen L, Rombouts M. Binding mechanisms in selective laser sintering and selective laser melting. *Rapid Prototyp J* 2005;11(1):26–36.

- [27] M. Yan, X. Tian, G. Peng, D. Li, X. Zhang. High temperature rheological behavior and sintering kinetics of CF/PEEK composites during selective laser sintering. *Compos Sci Technol* 2018;165:140–7.
- [28] Mahesh M, Wong YS, Fuh JYH, Loh HT. Benchmarking for comparative evaluation of RP systems and processes. *Rapid Prototyp J* 2004;10(2):123–35.
- [29] Sohrabpoor H, Negi S, Shaiesteh H, Ahad I, Brabazon D. Optimizing selective laser sintering process by grey relational analysis and soft computing techniques. *Optik* 2018;174:185–94.
- [30] Dell'Anno G, Partridge I, Cartié D, Hamlyn A, Chehura E, James S et al. Automated manufacture of 3D reinforced aerospace composite structures. *Int Jnl of Struct Integrity* 2012;3(1):22–40.
- [31] Narnhofer M, Schledjewski R, Mitschang P, Perko L. Simulation of the Tape-Laying Process for Thermoplastic Matrix Composites. *Adv. Polym. Technol.* 2013;32(S1):E705-E713.
- [32] Zhang L, Wang X, Pei J, Zhou Y. Review of automated fibre placement and its prospects for advanced composites. *J Mater Sci* 2020;39(2):25.
- [33] Höck, B., Regnet, M., Bickelmaier, S., Henne, F., Sause, M., Schmidt, T. and Geiss, G. (ed.). Innovative and efficient manufacturing technologies for highly advanced composite pressure vessels; 2014.
- [34] Stokes-Griffin CM, Compston P. An inverse model for optimisation of laser heat flux distributions in an automated laser tape placement process for carbon-fibre/PEEK. *Compos Part A Appl Sci Manuf* 2016;88:190–7.
- [35] Stokes-Griffin CM, Compston P. A combined optical-thermal model for near-infrared laser heating of thermoplastic composites in an automated tape placement process. *Compos Part A Appl Sci Manuf* 2015;75:104–15.
- [36] Stokes-Griffin CM, Compston P. The effect of processing temperature and placement rate on the short beam strength of carbon fibre–PEEK manufactured using a laser tape placement process. *Compos Part A Appl Sci Manuf* 2015;78:274–83.
- [37] Mantell SC, Springer GS. Manufacturing Process Models for Thermoplastic Composites. *J. Compos. Mater* 1992;26(16):2348–77.
- [38] Yang F, Pitchumani R. A fractal Cantor set based description of interlaminar contact evolution during thermoplastic composites processing. *J. Mater. Sci.* 2001;36:4661–71.
- [39] Tierney J, Gillespie JW. Modeling of In Situ Strength Development for the Thermoplastic Composite Tow Placement Process. *J. Compos. Mater.* 2006;40(16):1487–506.
- [40] Khan MA, Mitschang P, Schledjewski R. Identification of some optimal parameters to achieve higher laminate quality through tape placement process. *Adv. Polym. Technol.* 2010;29(2):98–111.
- [41] Levy, A; Heider, D; Tierney, J; Gillespie, Jr J.W; Lefebure, P; Lang, D; IW–CT, E.A.D.S; du Chaffault, C. Simulation and optimization of the thermoplastic Automated Tape Placement (ATP) process; 2012.
- [42] Comer AJ, Ray D, Obande WO, Jones D, Lyons J, Rosca I et al. Mechanical characterisation of carbon fibre–PEEK manufactured by laser-assisted automated-tape-placement and autoclave. *Compos Part A Appl Sci Manuf* 2015;69:10–20.
- [43] Groupe WJB, Warnet LL, Rietman B, Visser HA, Akkerman R. Optimization of the tape placement process parameters for carbon–PPS composites. *Compos. Part A Appl. Sci. Manuf.* 2013;50:44–53.
- [44] Ning F, Cong W, Qiu J, Wei J, Wang S. Additive manufacturing of carbon fiber reinforced thermoplastic composites using fused deposition modeling. *Compos B Eng* 2015;80:369–78.
- [45] Love LJ, Kunc V, Rios O, Duty CE, Elliott AM, Post BK et al. The importance of carbon fiber to polymer additive manufacturing. *J. Mater. Res.* 2014;29(17):1893–8.

- [46] Pistor CM, Yardimci MA, Güçeri SI. On-line consolidation of thermoplastic composites using laser scanning. *Compos Part A Appl Sci Manuf* 1999;30(10):1149–57.
- [47] Koch C, van Hulle L, Rudolph N. Investigation of mechanical anisotropy of the fused filament fabrication process via customized tool path generation. *Addit. Manuf.* 2017;16:138–45.
- [48] Li, Longmei, et al. (ed.). *Composite modeling and analysis of FDM prototypes for design and fabrication of functionally graded parts*; 2001.
- [49] Rodríguez JF, Thomas JP, Renaud JE. Mechanical behavior of acrylonitrile butadiene styrene (ABS) fused deposition materials. Experimental investigation. *Rapid Prototyp J* 2001;7(3):148–58.
- [50] Kulkarni P DD. Deposition Strategies and Resulting Part Stiffnesses in Fused Deposition Modeling 1999:93–103.
- [51] Bellini A, Güçeri S. Mechanical characterization of parts fabricated using fused deposition modeling. *Rapid Prototyp J* 2003;9(4):252–64.
- [52] Ahn S-H, Montero M, Odell D, Roundy S, Wright PK. Anisotropic material properties of fused deposition modeling ABS. *Rapid Prototyp J* 2002;8(4):248–57.
- [53] Montero, Michael, et al. Material Characterization of Fused Deposition Modeling (FDM) ABS by Designed Experiments. *Society of Manufacturing Engineers* 2001;10:1–21.
- [54] Costa SF, Duarte FM, Covas JA. Thermal conditions affecting heat transfer in FDM/FFE: a contribution towards the numerical modelling of the process. *Virtual and Physical Prototyping* 2015;10(1):35–46.
- [55] Li L., Sun Q., Bellehumeur C., Gu P. Investigation of Bond Formation in FDM Process. *Solid freeform fabrication proceedings* 2002;403.
- [56] Carneiro OS, Silva AF, Gomes R. Fused deposition modeling with polypropylene. *Mater. Des.* 2015;83:768–76.
- [57] Lee C-Y, Liu C-Y. The influence of forced-air cooling on a 3D printed PLA part manufactured by fused filament fabrication. *Addit. Manuf.* 2019;25:196–203.
- [58] Galantucci LM, Bodi I, Kacani J, Lavecchia F. Analysis of Dimensional Performance for a 3D Open-source Printer Based on Fused Deposition Modeling Technique. *Procedia CIRP* 2015;28:82–7.
- [59] Spoerk M, Sapkota J, Weingrill G, Fischinger T, Arbeiter F, Holzer C. Shrinkage and Warpage Optimization of Expanded-Perlite-Filled Polypropylene Composites in Extrusion-Based Additive Manufacturing. *Macromol. Mater. Eng.* 2017;302(10):1700143.
- [60] Onwubolu GC, Rayegani F. Characterization and Optimization of Mechanical Properties of ABS Parts Manufactured by the Fused Deposition Modelling Process. *International Journal of Manufacturing Engineering* 2014;2014:1–13.
- [61] Es-Said OS, Foyos J, Noorani R, Mendelson M, Marloth R, Pregger BA. Effect of Layer Orientation on Mechanical Properties of Rapid Prototyped Samples. *Materials and Manufacturing Processes* 2000;15(1):107–22.
- [62] Panda SK. Optimization of Fused Deposition Modelling (FDM) Process Parameters Using Bacterial Foraging Technique. *IIM* 2009;01(02):89–97.
- [63] Sood AK, Ohdar RK, Mahapatra SS. Parametric appraisal of mechanical property of fused deposition modelling processed parts. *Mater. Des.* 2010;31(1):287–95.
- [64] Durgun I, Ertan R. Experimental investigation of FDM process for improvement of mechanical properties and production cost. *Rapid Prototyp J* 2014;20(3):228–35.
- [65] Tymrak BM, Kreiger M, Pearce JM. Mechanical properties of components fabricated with open-source 3-D printers under realistic environmental conditions. *Mater. Des.* 2014;58:242–6.
- [66] Rahman KM, Todd Letcher, Riley Reese. Mechanical Properties of Additively Manufactured PEEK Components Using Fused Filament Fabrication. In: *ASME 2015 International Mechanical Engineering Congress and Exposition*, 2015.

- [67] Wu W, Geng P, Li G, Di Zhao, Zhang H, Zhao J. Influence of Layer Thickness and Raster Angle on the Mechanical Properties of 3D-Printed PEEK and a Comparative Mechanical Study between PEEK and ABS. *Materials* 2015;8(9):5834–46.
- [68] Riddick JC, Haile MA, Wahlde RV, Cole DP, Bamiduro O, Johnson TE. Fractographic analysis of tensile failure of acrylonitrile-butadiene-styrene fabricated by fused deposition modeling. *Additive Manufacturing* 2016;11:49–59.
- [69] Cantrell, Jason, et al. Experimental Characterization of the Mechanical Properties of 3D-Printed ABS and Polycarbonate Parts. *Rapid Prototyp J* 2017;23(4):811–24.
- [70] Lee CS, Kim SG, Kim HJ, Ahn SH. Measurement of anisotropic compressive strength of rapid prototyping parts. *Journal of Materials Processing Technology* 2007;187-188:627–30.
- [71] Coogan TJ, Kazmer DO. Prediction of interlayer strength in material extrusion additive manufacturing. *Addit. Manuf.* 2020;35:101368.
- [72] Petersmann S, Spoerk-Erdely P, Feuchter M, Wieme T, Arbeiter F, Spoerk M. Process-induced morphological features in material extrusion-based additive manufacturing of polypropylene. *Addit. Manuf.* 2020;35:101384.
- [73] Yuan Y, Abeykoon C, Mirihanage W, Fernando A, Kao Y-C, Harings JAW. Prediction of temperature and crystal growth evolution during 3D printing of polymeric materials via extrusion. *Mater. Des.* 2020;196:109121.
- [74] Bertoldi M., Yardimci M. A., Pistor C. M., Güçeri S. I., Sala G. (eds.). *Mechanical Characterization of Parts Processed via Fused Deposition*; 1998.
- [75] Jones RM. *Mechanics of composite materials*: CRC press; 1998.
- [76] Rodríguez JF, Thomas JP, Renaud JE. Mechanical behavior of acrylonitrile butadiene styrene fused deposition materials modeling. *Rapid Prototyp J* 2003;9(4):219–30.
- [77] Somireddy M CA. Mechanical Characterization of Additively Manufactured Parts by FE Modeling of Mesostructure. *JMMP* 2017;1(2):18.
- [78] Spoerk M, Arbeiter F, Cajner H, Sapkota J, Holzer C. Parametric optimization of intra- and inter-layer strengths in parts produced by extrusion-based additive manufacturing of poly(lactic acid). *J. Appl. Polym. Sci.* 2017;134(41):45401.
- [79] Arbeiter F, Spoerk M, Wiener J, Gosch A, Pinter G. Fracture mechanical characterization and lifetime estimation of near-homogeneous components produced by fused filament fabrication. *Polym Test* 2018;66:105–13.
- [80] Flodberg G, Pettersson H, Yang L. Pore analysis and mechanical performance of selective laser sintered objects. *Additive Manufacturing* 2018;24:307–15.
- [81] Stichel T, Frick T, Laumer T, Tenner F, Hausotte T, Merklein M et al. A Round Robin study for Selective Laser Sintering of polyamide 12: Microstructural origin of the mechanical properties. *Optics & Laser Technology* 2017;89:31–40.
- [82] Caulfield B, McHugh PE, Lohfeld S. Dependence of mechanical properties of polyamide components on build parameters in the SLS process. *Journal of Materials Processing Technology* 2007;182(1-3):477–88.
- [83] Ho HCH, Gibson I, Cheung WL. Effects of energy density on morphology and properties of selective laser sintered polycarbonate. *Journal of Materials Processing Technology* 1999;89-90:204–10.
- [84] Gibson I. SD. Material properties and fabrication parameters in selective laser sintering process. *Rapid Prototyp J*;1997.
- [85] Franco A, Romoli L. Characterization of laser energy consumption in sintering of polymer based powders. *Journal of Materials Processing Technology* 2012;212(4):917–26.
- [86] Shi Y, Chen J, Wang Y, Li Z, Huang S. Study of the selective laser sintering of polycarbonate and postprocess for parts reinforcement. *Proceedings of the Institution of Mechanical Engineers, Part L: Journal of Materials: Design and Applications* 2007;221(1):37–42.



- [87] Childs THC, Berzins M, Ryder GR, Tontowi A. Selective laser sintering of an amorphous polymer—simulations and experiments. *Proceedings of the Institution of Mechanical Engineers, Part B: Journal of Engineering Manufacture* 1999;213(4):333–49.
- [88] Schmid M. *Laser Sintering with Plastics: Technology, Processes, and Materials*: Carl Hanser Verlag GmbH & Co. KG; 2018.
- [89] Hofland EC, Baran I, Wismeijer DA. Correlation of Process Parameters with Mechanical Properties of Laser Sintered PA12 Parts. *Advances in Materials Science and Engineering* 2017;2017(5):1–11.
- [90] Gill, T. J., and K. K. B. Hon (ed.). *Experimental investigation into the selective laser sintering of silicon carbide polyamide composites*; 2004.
- [91] Pilipović A, Valentan B, Brajlilić T, Haramina T, Balič J, Kodvanj J, Šercer M, Drstvenšek I. Influence of laser sintering parameters on mechanical properties of polymer products. In: *Proceedings of 3rd International Conference on Additive Technologies*, 2010.
- [92] Williams JD, Deckard CR. Advances in modeling the effects of selected parameters on the SLS process. *Rapid Prototyp J* 1998;4(2):90–100.
- [93] Wudy K, Drummer D, Kühnlein F, Drexler M. Influence of degradation behavior of polyamide 12 powders in laser sintering process on produced parts. In: *American Institute of Physics*; 2014, p. 691–695.
- [94] Dadbakhsh S, Verbelen L, Verkinderen O, Strobbe D, van Puyvelde P, Kruth J-P. Effect of PA12 powder reuse on coalescence behaviour and microstructure of SLS parts. *European Polymer Journal* 2017;92:250–62.
- [95] Anurag Katta, Berer M. *Analysis of PA6 powder ageing during the selective laser sintering process*. Master thesis, Hochschule Aalen; 2019.
- [96] Bacchewar PB, Singhal SK, Pandey PM. Statistical modelling and optimization of surface roughness in the selective laser sintering process. *Proceedings of the Institution of Mechanical Engineers, Part B: Journal of Engineering Manufacture* 2007;221(1):35–52.
- [97] Sindinger S-L, Kralovec C, Tasch D, Schagerl M. Thickness dependent anisotropy of mechanical properties and inhomogeneous porosity characteristics in laser-sintered polyamide 12 specimens. *Additive Manufacturing* 2020;33:101141.
- [98] García Plaza E, Núñez López P, Caminero Torija M, Chacón Muñoz J. Analysis of PLA Geometric Properties Processed by FFF Additive Manufacturing: Effects of Process Parameters and Plate-Extruder Precision Motion. *Polymers* 2019;11(10):1581.
- [99] Zarringhalam H, Hopkinson N, Kamperman NF, Vlieger JJ de. Effects of processing on microstructure and properties of SLS Nylon 12. *Materials Science and Engineering: A* 2006;435-436:172–80.
- [100] Wegner A, Witt G. Correlation of Process Parameters and Part Properties in Laser Sintering using Response Surface Modeling. *Physics Procedia* 2012;39:480–90.
- [101] Jollivet, T., et al. Rapid Manufacturing of Polymer parts by SLS. *International Journal of Material Forming* 2009;2(1):697–700.
- [102] Ning Y, Wong YS, Fuh JYH. Effect and control of hatch length on material properties in the direct metal laser sintering process. *Proceedings of the Institution of Mechanical Engineers, Part B: Journal of Engineering Manufacture* 2005;219(1):15–25.
- [103] Jain PK, Pandey PM, Rao PVM. Effect of delay time on part strength in selective laser sintering. *Int J Adv Manuf Technol* 2009;43(1-2):117–26.
- [104] Amado-Becker A, Ramos-Grez J, José Yañez M, Vargas Y, Gaete L. Elastic tensor stiffness coefficients for SLS Nylon 12 under different degrees of densification as measured by ultrasonic technique. *Rapid Prototyp. J.* 2008;14(5):260–70.
- [105] Cooke W, Anne Tomlinson R, Burguete R, Johns D, Vanard G. Anisotropy, homogeneity and ageing in an SLS polymer. *Rapid Prototyp. J.* 2011;17(4):269–79.

- [106] Spoerk M, Savandaiah C, Arbeiter F, Traxler G, Cardon L, Holzer C et al. Anisotropic properties of oriented short carbon fibre filled polypropylene parts fabricated by extrusion-based additive manufacturing. *Compos Part A Appl Sci Manuf* 2018;113:95–104.
- [107] Ferreira RTL, Amatte IC, Dutra TA, Bürger D. Experimental characterization and micrography of 3D printed PLA and PLA reinforced with short carbon fibers. *Compos B Eng* 2017;124:88–100.
- [108] Tekinalp HL, Kunc V, Velez-Garcia GM, Duty CE, Love LJ, Naskar AK et al. Highly oriented carbon fiber–polymer composites via additive manufacturing. *Compos Sci Technol* 2014;105:144–50.
- [109] Lewicki JP, Rodriguez JN, Zhu C, Worsley MA, Wu AS, Kanarska Y et al. 3D-Printing of Meso-structurally Ordered Carbon Fiber/Polymer Composites with Unprecedented Orthotropic Physical Properties. *Sci Rep* 2017;7:43401.
- [110] Jing W, Hui C, Qiong W, Hongbo L, Zhanjun L. Surface modification of carbon fibers and the selective laser sintering of modified carbon fiber/nylon 12 composite powder. *Mater. Des.* 2017;116:253–60.
- [111] Jansson A, Pejryd L. Characterisation of carbon fibre-reinforced polyamide manufactured by selective laser sintering. *Additive Manufacturing* 2016;9:7–13.
- [112] Floersheim RB, Hou G, Firestone K. CFPC material characteristics and SLS prototyping process. *Rapid Prototyp. J.* 2009;15(5):339–45.
- [113] Barnes J. A., Byerly G. E. The formation of residual stresses in laminated thermoplastic composites. *Compos Sci Technol* 1994;51(4):479–94.
- [114] Parlevliet PP, Bersee HEN, Beukers A. Residual stresses in thermoplastic composites—A study of the literature—Part I: Formation of residual stresses. *Compos Part A Appl Sci Manuf* 2006;37(11):1847–57.
- [115] Mei Z., Chung D.D.L. Effect of heating time below the melting temperature on polyphenylene sulfide adhesive joint development. *International Journal of Adhesion and Adhesives* 2000;20(4).
- [116] Lebrun G, Denault J. Effect of annealing on the thermal expansion and residual stresses of bidirectional thermoplastic composite laminates. *Compos Part A Appl Sci Manuf* 2010;41(1):101–7.
- [117] Ray D, Comer AJ, Lyons J, Obande W, Jones D, Higgins RMO et al. Fracture toughness of carbon fiber/polyether ether ketone composites manufactured by autoclave and laser-assisted automated tape placement. *J. Appl. Polym. Sci.* 2014;132(11).
- [118] Sacchetti F, Groupe WJB, Warnet LL, Villegas IF. Effect of cooling rate on the interlaminar fracture toughness of unidirectional Carbon/PPS laminates. *Eng. Fract. Mech.* 2018;203:126–36.
- [119] Gao S-L, Kim J-K. Cooling rate influences in carbon fibre/PEEK composites. Part II: Interlaminar fracture toughness. *Compos Part A Appl Sci Manuf* 2001;32(6):763–74.
- [120] Beehag A YL. Influence of cooling rate on interlaminar fracture properties of unidirectional commingled CF/PEEK composites. *Applied Composite Materials* 1995;2(3):135–51.
- [121] Deporter J, Baird DG. The effects of thermal history on the structure/property relationship in polyphenylenesulfide/carbon fiber composites. *Polym. Compos.* 1993;14(3):201–13.
- [122] Sarrazin H SG. Thermochemical and mechanical aspects of composite tape laying. *Journal of Composite Materials* 1995;29(14):1908–43.
- [123] Gao S-L, Kim J-K. Cooling rate influences in carbon fibre/PEEK composites. Part 1. Crystallinity and interface adhesion. *Compos Part A Appl Sci Manuf* 2000;31(6):517–30.
- [124] Spruiell JE. A review of the measurement and development of crystallinity and its relation to properties in neat poly (phenylene sulfide) and its fiber reinforced composites: No. ORNL/TM-2004/304. Oak Ridge National Lab.(ORNL), Oak Ridge, TN (United States) 2005.
- [125] Khan MA, Mitschang P, Schledjewski R. Parametric study on processing parameters and resulting part quality through thermoplastic tape placement process. *J. Compos. Mater* 2013;47(4):485–99.

- [126] Gruber, M.B; Lockwood, I.Z; Dolan, T.L; Funck, S.B; Tierney, J.J; Simacek, P; Gillespie Jr, J.W; Advani, S.G; Jensen, B.J; Cano, R.J; Grimsley, B.W. Thermoplastic in situ placement requires better impregnated tapes and tows; 2012.
- [127] Tierney J, Gillespie JW. Modeling of Heat Transfer and Void Dynamics for the Thermoplastic Composite Tow-Placement Process. *J. Compos. Mater.* 2003;37(19):1745–68.
- [128] Pitchumani R, Ranganathan S, Don RC, Gillespie Jr JW, Lamontia MA. Analysis of transport phenomena governing interfacial bonding and void dynamics during thermoplastic tow-placement. *Int. J. Heat Mass Transf.* 1996;39(9):1883–97.
- [129] Anderson TL. *Fracture Mechanics: Fundamentals and Applications*: CRC press; 2017.
- [130] Watschke H, Waalkes L, Schumacher C, Vietor T. Development of Novel Test Specimens for Characterization of Multi-Material Parts Manufactured by Material Extrusion. *Applied Sciences* 2018;8(8):1220.
- [131] Forster AM. *Materials Testing Standards for Additive Manufacturing of Polymer Materials: State of the Art and Standards Applicability*: National Institute of Standards and Technology; 2015.
- [132] ISO15024: 2001. Fibre-reinforced Plastic Composites: Determination of Mode I Interlaminar Fracture Toughness, GIC, for Unidirectionally Reinforced Materials.: International Organization for Standardization; 2001.
- [133] ASTM D5528-13, Standard Test Method for Mode I Interlaminar Fracture Toughness of Unidirectional Fiber-Reinforced Polymer Matrix Composites.
- [134] Carlsson LA, Adams DF, Pipes RB. *Experimental characterization of advanced composite materials.*: CRC press; 2014.
- [135] Hart KR, Wetzel ED. Fracture behavior of additively manufactured acrylonitrile butadiene styrene (ABS) materials. *Eng. Fract. Mech.* 2017;177:1–13.
- [136] Song Y, Li Y, Song W, Yee K, Lee K-Y, Tagarielli VL. Measurements of the mechanical response of unidirectional 3D-printed PLA. *Mater. Des.* 2017;123:154–64.
- [137] Ahmed AA, Susmel L. A material length scale-based methodology to assess static strength of notched additively manufactured polylactide (PLA). *Fatigue Fract Eng Mater Struct* 2018.
- [138] Torres J, Cole M, Owji A, DeMastry Z, Gordon AP. An approach for mechanical property optimization of fused deposition modeling with polylactic acid via design of experiments. *Rapid Prototyp. J.* 2016;22(2):387–404.
- [139] McLouth TD, Severino JV, Adams PM, Patel DN, Zaldivar RJ. The impact of print orientation and raster pattern on fracture toughness in additively manufactured ABS. *Addit. Manuf.* 2017;18:103–9.
- [140] Arif MF, Kumar S, Varadarajan KM, Cantwell WJ. Performance of biocompatible PEEK processed by fused deposition additive manufacturing. *Mater. Des.* 2018;146:249–59.
- [141] Gardan J, Makke A, Recho N. Improving the fracture toughness of 3D printed thermoplastic polymers by fused deposition modeling. *Int J Fract* 2018;210(1-2):1–15.
- [142] Papon EA, Haque A. Fracture toughness of additively manufactured carbon fiber reinforced composites. *Additive Manufacturing* 2019;26:41–52.
- [143] Young D, Wetmore N, Czabaj M. Interlayer fracture toughness of additively manufactured unreinforced and carbon-fiber-reinforced acrylonitrile butadiene styrene. *Additive Manufacturing* 2018;22:508–15.
- [144] Barile C, Casavola C, Cazzato A. Acoustic Emissions in 3D Printed Parts under Mode I Delamination Test. *Materials* 2018;11(9).
- [145] Park S-i, Watanabe N, Rosen DW. Estimating failure of material extrusion truss structures based on deposition modeling and a cohesive zone model. *Mater. Des.* 2018;147:122–33.
- [146] Fonseca J, Ferreira IA, Moura MFSF de, Machado M, Alves JL. Study of the interlaminar fracture under mode I loading on FFF printed parts. *Compos Struct* 2019;214:316–24.

- [147] Linul E, Marsavina L, Stoia DI. Mode I and II fracture toughness investigation of Laser-Sintered Polyamide. *Theoretical and Applied Fracture Mechanics* 2020;106:102497.
- [148] Stoia DI, Marsavina L, Linul E. Mode I Fracture Toughness of Polyamide and Alumide Samples obtained by Selective Laser Sintering Additive Process. *Polymers* 2020;12(3).
- [149] Cano AJ, Salazar A, Rodríguez J. Effect of the orientation on the fatigue crack growth of polyamide 12 manufactured by selective laser sintering. *Rapid Prototyp. J.* 2019;25(5):820–9.
- [150] Brugo, T., Palazzetti, R., Ciric-Kostic, S., Yan, X.T., Minak, G. and Zucchelli, A. Fracture mechanics of laser sintered cracked polyamide for a new method to induce cracks by additive manufacturing. *Polym Test* 2016;50.
- [151] Salazar A, Rico A, Rodríguez J, Segurado Escudero J, Seltzer R, La Martin de Escalera Cutillas F. Monotonic loading and fatigue response of a bio-based polyamide PA11 and a petrol-based polyamide PA12 manufactured by selective laser sintering. *European Polymer Journal* 2014;59:36–45.
- [152] Salazar A, Rico A, Rodríguez J, Segurado Escudero J, Seltzer R, La Martin de Escalera Cutillas F. Fatigue crack growth of SLS polyamide 12: Effect of reinforcement and temperature. *Compos B Eng* 2014;59:285–92.
- [153] Blattmeier M, Witt G, Wortberg J, Eggert J, Toepker J. Influence of surface characteristics on fatigue behaviour of laser sintered plastics. *Rapid Prototyp. J.* 2012;18(2):161–71.
- [154] Modi, D; Comer, A; O'Higgins, R.M.O; McCarthy, M. A. Thermoplastic composites: in-situ consolidation or in-situ welding; 2013.
- [155] Bandaru, A.K; Clancy, G.J; Peeters, D; O'Higgins, R; Weaver, P.M. Interface characterization of thermoplastic skin-stiffener composite manufactured using laser-assisted tape placement; 2018.
- [156] Koissin V, Warnet LL, Akkerman R. Delamination in carbon-fibre composites improved with in situ grown nanofibres. *Eng Fract Mech* 2013;101:140–8.
- [157] Blackman BRK, Kinloch AJ, Rodriguez-Sanchez FS, Teo WS. The fracture behaviour of adhesively-bonded composite joints: Effects of rate of test and mode of loading. *Int J Solids Struct* 2012;49(13):1434–52.
- [158] Yao L, Alderliesten R, Zhao M, Benedictus R. Bridging effect on mode I fatigue delamination behavior in composite laminates. *Compos Part A Appl Sci Manuf* 2014;63:103–9.
- [159] Reiner J, Torres JP, Veidt M. A novel Top Surface Analysis method for Mode I interface characterisation using Digital Image Correlation. *Eng Fract Mech* 2017;173:107–17.
- [160] Mogadpalli GP, Parameswaran V. Determination of Stress Intensity Factor for Cracks in Orthotropic Composite Materials using Digital Image Correlation. *Strain* 2008;44(6):446–52.
- [161] Grabois TM, Negggers J, Ponson L, Hild F, Toledo Filho RD. On the validation of integrated DIC with tapered double cantilever beam tests. *Engineering Fracture Mechanics* 2018;191:311–23.
- [162] Merzkirch M, Ahure Powell L, Foecke T. Measurements of Mode I Interlaminar Properties of Carbon Fiber Reinforced Polymers Using Digital Image Correlation. *KEM* 2017;742:652–9.
- [163] Murray BR, Fonteyn S, Carrella-Payan D, Kalteremidou KA, Cernescu A, Van Hemelrijck D, Pyl L. Crack tip monitoring of mode I and mode II delamination in CF/Epoxyes under static and dynamic loading conditions using digital image correlation. *Multidisciplinary Digital Publishing Institute Proceedings* 2018;8(2):389.
- [164] Zhu M, Gorbatiikh L, Fonteyn S, Pyl L, van Hemelrijck D, Carrella-Payan D et al. Digital Image Correlation Measurements of Mode I Fatigue Delamination in Laminated Composites. *Proceedings* 2018;2(8):430.
- [165] Pan, B., Qian, K., Xie, H. and Asundi, A. Two-dimensional digital image correlation for in-plane displacement and strain measurement: a review. *Measurement science and technology* 2009;20(6).

- [166] Sutton MA. Three-dimensional digital image correlation to quantify deformation and crack-opening displacement in ductile aluminum under mixed-mode I/III loading. *Opt. Eng* 2007;46(5):51003.
- [167] Mehdikhani M, Aravand M, Sabuncuoglu B, Callens MG, Lomov SV, Gorbatikh L. Full-field strain measurements at the micro-scale in fiber-reinforced composites using digital image correlation. *Compos Struct* 2016;140:192–201.
- [168] Schreier, H., Orteu, J.J. and Sutton, M.A. *Image Correlation for Shape, Motion and Deformation Measurements: Basic Concepts, Theory and Applications*. Boston, MA: Springer-Verlag US; 2009.
- [169] Jones I, Iadicola ME (2018) *A good practices guide for digital image correlation*. International Digital Image Correlation Society.
- [170] ISO 15850:2014, *Plastics — Determination of tension-tension fatigue crack propagation — Linear elastic fracture mechanics (LEFM) approach*.
- [171] ASTM D 6115, *Standard Test Method for Mode I Fatigue Delamination Growth Onset of Unidirectional Fiber-Reinforced Polymer Matrix Composites*.
- [172] Blattmeier M, Witt G, Wortberg J, Eggert J, Toepker J. Influence of surface characteristics on fatigue behaviour of laser sintered plastics. *Rapid Prototyp. J.* 2012;18(2):161–71.
- [173] A. Brunner, S. Stelzer, G. Pinter. *Test protocol: Determination of mode I fatigue delamination propagation in unidirectionally reinforced materials* 2015.
- [174] Yao L, Alderliesten RC, Zhao M, Benedictus R. Discussion on the use of the strain energy release rate for fatigue delamination characterization. *Compos Part A Appl Sci Manuf* 2014;66:65–72.
- [175] Schön J, Nyman T, Blom A, Ansell H. A numerical and experimental investigation of delamination behaviour in the DCB specimen. *Compos Sci Technol* 2000;60(2):173–84.
- [176] Brunner AJ, Stelzer S, Pinter G, Terrasi GP. Cyclic fatigue delamination of carbon fiber-reinforced polymer-matrix composites: Data analysis and design considerations. *International Journal of Fatigue* 2016;83:293–9.
- [177] Brunner AJ, Murphy N, Pinter G. Development of a standardized procedure for the characterization of interlaminar delamination propagation in advanced composites under fatigue mode I loading conditions. *Eng. Fract. Mech.* 2009;76(18):2678–89.
- [178] Pascoe JA, Alderliesten RC, Benedictus R. Methods for the prediction of fatigue delamination growth in composites and adhesive bonds – A critical review. *Eng. Fract. Mech.* 2013;112-113:72–96.
- [179] Jones R, Stelzer S, Brunner AJ. Mode I, II and Mixed Mode I/II delamination growth in composites. *Compos Struct* 2014;110:317–24.
- [180] Jones R, Pitt S, Bunner AJ, Hui D. Application of the Hartman–Schijve equation to represent Mode I and Mode II fatigue delamination growth in composites. *Compos Struct* 2012;94(4):1343–51.
- [181] Jones R, Hu W, Kinloch AJ. A convenient way to represent fatigue crack growth in structural adhesives. *Fatigue Fract Eng Mater Struct* 2015;38(4):379–91.
- [182] Jones R, Kinloch AJ, Hu W. Cyclic-fatigue crack growth in composite and adhesively-bonded structures: The FAA slow crack growth approach to certification and the problem of similitude. *International Journal of Fatigue* 2016;88:10–8.
- [183] Jones R, Kinloch AJ, Michopoulos JG, Brunner AJ, Phan N. Delamination growth in polymer-matrix fibre composites and the use of fracture mechanics data for material characterisation and life prediction. *Compos Struct* 2017;180:316–33.
- [184] Vassilopoulos AP. The history of fiber-reinforced polymer composite laminate fatigue. *International Journal of Fatigue* 2020;134:105512.
- [185] Herráez M, Pichler N, Botsis J. Improving delamination resistance through tailored defects. *Compos Struct* 2020;247:112422.

- [186] Alderliesten R. Fatigue delamination of composite materials – approach to exclude large scale fibre bridging. *IOP Conf. Ser.: Mater. Sci. Eng.* 2018;388:12002.
- [187] Yao L, Sun Y, Guo L, Lyu X, Zhao M, Jia L et al. Mode I fatigue delamination growth with fibre bridging in multidirectional composite laminates. *Eng. Fract. Mech.* 2018;189:221–31.
- [188] Schneider, K., B. Lauke, and W. Beckert. Compression shear test (CST)—a convenient apparatus for the estimation of apparent shear strength of composite materials. *Applied Composite Materials* 2001;8(1):43–62.
- [189] ASTM D2344 / D2344M, Standard Test Method for Short-Beam Strength of Polymer Matrix Composite Materials and Their Laminates.
- [190] Lodeiro MJ, Broughton WR, Sims GD. Understanding limitations of through thickness test methods. *Plast Rubber Compos* 2013;28(9):416–24.
- [191] Rosselli F, Santare MH. Comparison of the short beam shear (SBS) and interlaminar shear device (ISD) tests. *Compos Part A Appl Sci Manuf* 1997;28(6):587–94.
- [192] Lauke, B., Beckert, W. and Schneider, K. Interlaminar shear strength evaluation of curved composite samples. *Applied Composite Materials* 1994;1(4):267–71.
- [193] Dutra T, Ferreira RTL, Resende H. Interlaminar shear strength of continuous carbon fiber reinforced thermoplastic composites manufactured by 3D printing. In: *Proceedings of the 24th ABCM International Congress of Mechanical Engineering: ABCM*; 2017.
- [194] Mazumdar, S.K. and Hoa, S.V. Application of Taguchi method for process enhancement of on-line consolidation technique. *Composites* 1995;26(9):669–73.

## Chapter 3. Characterisation of Mechanical Anisotropy in AM

### 3.1. Systematic analysis of the mechanical anisotropy of fibre-reinforced polymer specimens produced by laser sintering

#### 3.1.1. Bibliographic information

- Authors and their relevant contribution to the publication:
  - A. Khudiakova<sup>1</sup>: Writing – original draft, Writing - review and editing, Formal analysis, Investigation, Visualisation, Validation
  - M. Berer<sup>1</sup>: Conceptualisation, Methodology, Resources, Formal analysis, Validation, Writing - original draft, Writing – review and editing, Data curation, Supervision, Project administration
  - S. Niedermair<sup>2,3</sup>: Conceptualisation, Methodology, Resources, Investigation, Formal analysis, Validation
  - B. Plank<sup>4,5</sup>: Software, Resources, Methodology, Investigation, Formal analysis, Validation, Writing - original draft, Writing – review and editing, Visualisation
  - E. Truskiewicz<sup>1</sup>: Investigation, Formal analysis
  - G. Meier<sup>1</sup>: Investigation
  - H. Stepanovsky<sup>2,6</sup>: Investigation, Resources
  - M. Wolfahrt<sup>1</sup>: Project co-ordination, Supervision
  - G. Pinter<sup>7</sup>: Resources, Supervision
  - J. Lackner<sup>8</sup>: Conceptualisation, Project administration, Funding acquisition
  
- Affiliations:
  - <sup>1</sup>Polymer Competence Center Leoben GmbH, Roseggerstraße 12, 8700 Leoben, Austria
  - <sup>2</sup>Bernstein Innovation GmbH, Froschberg 3, 4020 Linz, Austria
  - <sup>3</sup>NBG Dimensions, Zweiländerstraße 1, 3950 Gmünd, Austria
  - <sup>4</sup>University of Applied Sciences Upper Austria, Stelzhamerstraße 23, 4600 Wels, Austria
  - <sup>5</sup>University of Augsburg, Universitätsstraße 2, 86159 Augsburg, Germany
  - <sup>6</sup>NEMETON Innovation GmbH, Jetzleser Straße 17, 3902 Vitis, Austria
  - <sup>7</sup>Institute of Materials Science and Testing of Polymers, Montanuniversitaet Leoben, Otto Gloeckel-Straße 2, 8700 Leoben, Austria
  - <sup>8</sup>JOANNEUM RESEARCH Forschungsgesellschaft mbH, Leobner Straße 94, 8712 Niklasdorf, Austria

Published in Additive manufacturing (2020)

*The manuscript is presented here in accordance with the publisher's copyright policy: 'Authors can include their articles in full or in part in a thesis or dissertation for non-commercial purposes.' Elsevier.com*

### 3.1.2. Abstract

Selective laser sintering (SLS) is an additive manufacturing process which nowadays receives abundant attention from industry sectors. However, the number of materials which can be processed by SLS is still very limited and requires further research. The present work aims to contribute to this topic by investigating the mechanical properties of neat and short carbon fibre reinforced polyamide 1212 processed by SLS. The specimens were built in different spatial alignments to obtain ample details on the tensile behaviour. The detailed examinations of the fractured specimens were performed by means of optical microscopy, scanning electron microscopy and X-ray computed tomography. The comprehensive analysis revealed that most of the fibres (85 – 95 %) were oriented in the plane of the powder layer and here, the majority along the direction of the moving roller coater, which distributes the powder on the powder bed of the SLS machine. It was shown that this effect has a direct impact on the strength and stiffness of the printed tensile bars and thus on the mechanical behaviour of SLS printed parts. Furthermore, the analysis results indicate the possibility to control this mechanical anisotropy through a systematic alignment of the components in the powder cake.

### 3.1.3. Introduction

Selective laser sintering (SLS) is one of the oldest techniques in the modern field of additive manufacturing. Its invention officially took place at the University of Texas and it dates back to the 1980s [1]. After its invention, it took many years until the first commercially available SLS machines were finally on the market. Subsequently, until 2014, this market was dominated by the companies 3D Systems (3D Systems Corporation, Rock Hill, South Carolina) and EOS (EOS GmbH – Electro Optical Systems, Krailling, Germany), which were holding the key patents for this technique at that time [2]. Since these patents expired, many new machine producers have appeared on the market, making it much more inhomogeneous now. The broader competition on the market has led to big progress steps in machine technology in recent years. As a result, SLS is not limited to the production of prototypes anymore, but is also accepted in the serial production of small and medium lots.

Compared to conventional polymer processing techniques, such as extrusion and injection moulding, SLS is still rather limited concerning the materials available for the process. However, since 2014, the boosted machine progress has caused a big number of newly developed polymer powders to be released. Aside from the extension of the SLS technique to new polymers [3–9], the compounding and reinforcement of the neat polymers, especially polyamide 12, are also in the focus for this. The modification of the powders aims at different material aspects, for instance improvement in the tribological behaviour with molybdenum disulphide ( $\text{MoS}_2$ ), modification of thermal and electrical conductivity and mechanical properties using carbon nanotubes, carbon black, etc. [10–16], and improvement in the mechanical behaviour using glass beads and carbon fibres [17–23].

The mechanical reinforcement of a polyamide powder using carbon fibres was also a topic in the present research. While other research in this field focused especially on the production of the composite [10,20,24,21,18], in this study, it was simply produced by directly



mixing polyamide powder with carbon fibres, both of which are commercial products. Adding the stiff fibres to the neat powder leads to the anisotropy of mechanical properties of the output part [25,19,26,23]. Few research works have found that the fibres tend to lie along the moving direction of a roller or a rake used to distribute the powder over the printing platform [19,26,23]. However, the fibre alignment and its influence on the mechanical performance were not characterised in details and require further analysis. Therefore, the clear focus in this research was to examine the influence of the SLS process on the resulting fibre orientation and, hence, the mechanical properties of the SLS printed components. For this, differently aligned dog-bone shaped tensile specimens were SLS printed using neat and reinforced powder. The mechanical performance of the specimens was characterised using tensile tests. Additionally, powder and part morphology were studied using microscopy and X-ray computed tomography.

#### 3.1.4. Experimental

##### Materials

Neat and reinforced specimens were produced out of the polyamide 1212 based nylon powder FS 3300PA provided by Farsoon (Farsoon Europe GmbH, Germany) [27]. For the reinforced specimens, the powder resin was directly mixed with 12 wt% of Sigrafil short carbon fibres (SGL Carbon, Germany) [28] in a barrel mixer. According to the supplier, the average fibre length and diameter was about 80  $\mu\text{m}$  and 7  $\mu\text{m}$ , respectively. The fibre content of 12 wt% was chosen on the grounds of preliminary tests with different fibre mass contents and literature research [22]. The basic material parameters of the components are presented in Table 1.

**Table 1**

Properties of components used for the powder mixture.

	FS 3300PA [27]	Carbon fibres [28]
<b>Melt temperature</b>	183 °C	
<b>Tensile strength</b>	46 MPa	4 GPa
<b>Tensile modulus</b>	1602 MPa	240 GPa
<b>Strain at break</b>	36 %	1.7 %

##### Specimen manufacturing

The powder mixture prepared was sintered in an sPro 60 SLS printer (3D System Corporation, SC, USA), which was modified by LSS Laser Sinter Service GmbH (Germany) in order to improve the uniformity and stability of the building process. Since adding of carbon fibres to the neat powder changes its absorption of the laser heat [11,23], the process parameters were optimised for neat and reinforced specimens separately. The layer thickness of 0.1 mm was used for both, neat and reinforced specimens. The specimens had a dog-bone shape with the type-A dimensions from ISO 527 [29]. Nylon powder, distributed with a roller moving in the  $x$ -direction, was sintered layer by layer till the specimens were completed (Fig. 1).

The specimens were printed in different directions to investigate the influence of the alignment in the powder cake on the mechanical properties. The specimens formed three fans in the  $xy$ -,  $xz$ - and  $yz$ -planes with printing orientations from 0° to 90° with steps of 22.5° (Fig.

1a). Three specimens were printed for every spatial position. For the sake of the test repeatability, an additional specimen set was printed in the other corner of the chamber with the same specimen alignment (Fig. 1b). Hereafter, the specimens are denominated according to their coordinate plane angle, where the coordinate plane is either  $xy$ ,  $xz$ , or  $yz$ , and the angle is either  $0^\circ$ ,  $22.5^\circ$ ,  $45^\circ$ ,  $67.5^\circ$  or  $90^\circ$ . For example,  $xz$ - $45^\circ$  refers to a specimen printed in the  $xz$ -plane at  $45^\circ$ , where  $x$  corresponds to the moving direction of the roller distributing the powder and  $z$  is the vertical axis normal to the printing platform. The same building configuration was used for neat polyamide specimens, which were printed for reference purposes. Prior to testing, all specimens were dried at  $80^\circ\text{C}$  for at least 12 days in a vacuum drying oven to eliminate the moisture content.

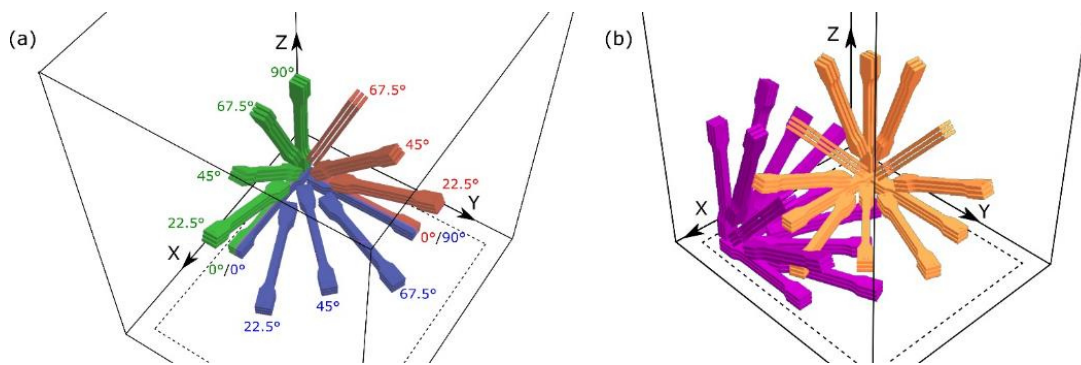


**Fig. 1.** Graphic representation of (a) the spatial alignment of the three fans of tensile bars in the build chamber (a) and the position of the additional specimen set (b). The roller spread the powder in the  $x$ -direction. For colour representation of the specimens, the reader is referred to the web version of this article.

### Tensile tests

Tensile tests were performed on the universal testing machine Zwick Z250 (Zwick GmbH & Co. KG, Germany), equipped with a load cell of 10 kN. The tests were carried out in accordance with ISO 527 [29]. The specimens were tested at room temperature with an initial pre-load of 0.1 MPa and a cross-head speed of 1 mm/min for the modulus determination regime (0.05 % to 0.25 %) and then at 50 mm/min till the final rupture. Specimens were compared in terms of maximum tensile strength  $\sigma$ , Young's modulus  $E$  and strain at break  $\varepsilon_b$ . Young's modulus was calculated according to Eq. 1 [29]. Three specimens were tested for every spatial position of both specimen fans.

$$E = \frac{\Delta\sigma}{\Delta\varepsilon} \quad (1)$$

where  $\Delta\varepsilon$  refers to the difference between two longitudinal strain points and  $\Delta\sigma$  to the difference in applied tensile stress between these two strain points. The values were evaluated with  $\Delta\varepsilon$  of 0.2% according to ISO 527 [29].

### X-ray computed tomography

The high-resolution X-ray computed tomography ( $\mu$ CT) was performed using the  $\mu$ CT device Nanotom 180 NF (GE Phoenix|X-ray, Wunstorf, Germany), equipped with a 180 kV nanofocus X-ray tube. The overall scans with an edge length of a volumetric pixel (voxel size) of  $(4.5 \mu\text{m})^3$  were carried out at the tube voltage, the integration time and the number of projections of 60 kV, 500 ms and 1700, respectively. For full fibre characterisation, detailed scans with the voxel size of  $(1.4 \mu\text{m})^3$  were performed. To achieve a small focal spot size, the maximum target power of the electron beam in the X-ray tube is limited, so the integration time was increased to 900 ms to achieve proper saturation of the detector image brightness. The parameters used yielded scan times of 177 and 233 minutes for the overall and detailed examinations, respectively. As a target material, molybdenum on a beryllium window was used for all scans.

To reach a resolution of  $(1.4 \mu\text{m})^3$  voxel size, small  $\mu$ CT samples of  $2 \times 2 \times 10 \text{ mm}^3$  were cut out near the specimen shoulders, as shown in Fig. 2. They were aligned inside the X-ray device in the same way for every specimen. The samples were taken from the fractured specimen parts after tensile testing. The  $\mu$ CT analysis was carried out for the reinforced specimens printed in the directions  $xy\text{-}0^\circ$ ,  $xy\text{-}45^\circ$ ,  $xy\text{-}90^\circ$ ,  $xz\text{-}45^\circ$ ,  $xz\text{-}90^\circ$  and  $yz\text{-}45^\circ$ . One sample cut out of one specimen was examined per printing direction. The  $\mu$ CT data analysis was performed using the commercially available software tool VG Studio MAX 3.3 (Volume Graphics, Germany) and the in-house developed software iAnalyse [30,31], for which most implementations are also available in the open-source software open\_iA [32]. Two software tools were used in order to compare and verify the results regarding the mean orientation of the fibres in the reinforced specimens. Using only iAnalysis would have led to a potential underestimation of the number of fibres in a certain direction, since the fibres shorter than  $50 \mu\text{m}$  were not examined. VG Studio MAX 3.3 uses a grey value based analysis method, delivering the orientation of all individual voxels within a certain grey value range, but has not the possibility to extract additional information such as the length of individual fibres.

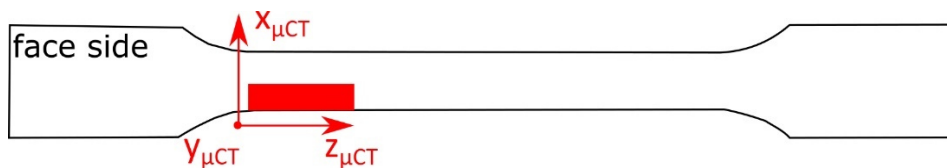


**Fig. 2.** Schematic illustration of a  $\mu$ CT sample cut out of the specimen produced by SLS. The coordinate system  $(x_{\mu\text{CT}}, y_{\mu\text{CT}}, z_{\mu\text{CT}})$  marked in red corresponds to the spatial alignments in the X-ray device, where the  $x_{\mu\text{CT}}y_{\mu\text{CT}}$  plane corresponds to the rotation stage and  $z_{\mu\text{CT}}$  to the rotation axis of the X-ray device.

### Optical analysis

Optical analyses were used to investigate the impact of the fibres on the mechanical behaviour of the material. After the tensile tests, the face (broad surface), side (thin surface) and fracture surfaces of the samples were examined by means of optical microscopy and scanning electron microscopy (SEM). The micrographs were made with the optical microscope Olympus SZX12 (Olympus Corporation, Japan). The SEM examination was performed with the

Tescan Vega II electron microscope (Tescan Orsay Holding, a.s., Brno, Czech Republic). Prior to the examination, the specimens were coated with gold to reduce the surface charging. The accelerating voltage for the electrons was set up to 5 kV; the working distance used was 8-16 mm. In addition, the morphology of the filled powder was characterised by SEM.

### 3.1.5. Results and discussion

The two specimen sets built in the different corners of the building chamber showed similar results within the corresponding angle alignments. This reveals that for the area examined, the mechanical properties were not significantly influenced by the position in the powder cake during production. Therefore, the results were combined and are presented for six specimens (instead of two times three) of every printing direction.

#### X-ray computed tomography of the reinforced specimens

The  $\mu$ CT analysis was performed to determine the void content as well as the length, number and orientation of the fibres in the  $xy$ - $0^\circ$ ,  $xy$ - $45^\circ$ ,  $xy$ - $90^\circ$ ,  $xz$ - $45^\circ$ ,  $xz$ - $90^\circ$  and  $yz$ - $45^\circ$  carbon fibre (CF) reinforced specimens. The alignment of the specimens inside the X-ray device during the overall scans and with respect to the coordinate axes is shown in Fig. 3. The detailed scans with the voxel size of  $(1.4 \mu\text{m})^3$  were performed in the mid-part of every sample.

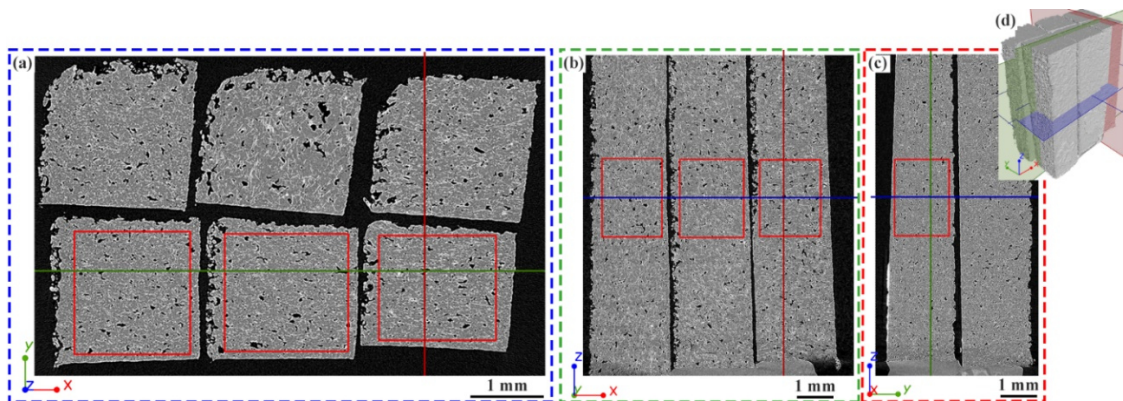


**Fig. 3.** Orthogonal  $\mu$ CT slice images through the individual samples scanned at  $(4.5 \mu\text{m})^3$  voxel size: top (a), front (b), right (c) and 3D rendering (d). Red areas identify the representative region of interest for porosity evaluation and detailed high resolution scans for full fibre characterisations. Samples  $xy$ - $0^\circ$ ,  $xy$ - $45^\circ$ ,  $xy$ - $90^\circ$  are represented in the bottom row and  $yz$ - $45^\circ$ ,  $xz$ - $45^\circ$ ,  $xz$ - $90^\circ$  are represented in the top row in (a). For colour representation of this figure, the reader is referred to the web version of this article.

For the porosity characterisation, voids in the  $xy$ - $0^\circ$  sample were evaluated semi-automatically using the voxel size of  $(1.4 \mu\text{m})^3$ . This scan yielded the reference value for the 'proper' porosity obtained at high resolution of 4.00 vol.-% (Fig. 4a,b), which was used to determine the threshold value from the grey-level intensity histogram. According to the positions of the air – and material peak, a ratio of 42% (ISO42) was determined as an optimum threshold value [33–35]. The threshold defined was used for the automated segmentation of voids in the  $xy$ - $0^\circ$  sample scanned at lower resolution using the voxel size of  $(4.5 \mu\text{m})^3$ . This led to the porosity content of 4.01 vol.-% (Fig. 4d,e). Application of the automated segmentation of

voids at lower resolution to the other five samples revealed porosity content of about 4.2 vol.% as an average of all six samples investigated by  $\mu$ CT (Table 2).

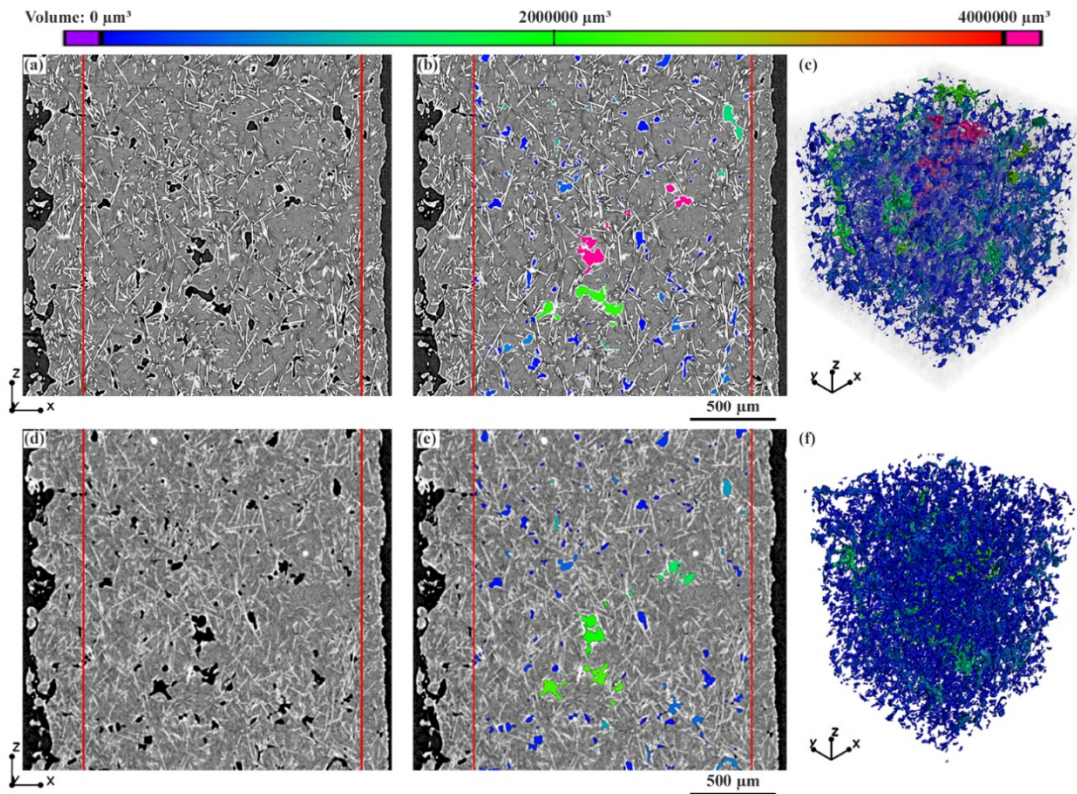


**Fig. 4.** A high resolution scan of the  $xy-0^\circ$  sample scanned at  $(1.4 \mu\text{m})^3$  voxel size (a), which was used for a semi-automated determination of the reference porosity of 4.00 vol.% (b). The same region of the sample scanned at  $(4.5 \mu\text{m})^3$  voxel size (d). An automated pore segmentation with the ISO42 threshold, which yielded a void content of 4.01 vol.% (e). 3D rendering of the segmented voids is demonstrated in (c) and (f). For colour representation of this figure, the reader is referred to the web version of this article.

The fibre characterisation was performed following the concept of medial axis extraction (MAE) implemented by using template matching (TM) [36,37]. According to the TM approach, the fibres evaluated are allowed to be curved and are considered to have circular cross sections of the same diameter. A voxel template generated had a spherical shape and the same diameter and grey value as the carbon fibres. The template was correlated with individual fibres in the scanned samples to define the fibre orientations. The ideal template to correlate with straight fibres would be a cylinder. However, the spherical shape was chosen over cylindrical based on the previous research [37] and in order to save calculation time. For the initial binarisation of every individual fibre, the ISO270 threshold was determined from the grey level histogram empirically and applied to every individual dataset. Fig. 5a,c shows the extracted medial axes of every individual carbon fibre in random colours depending on the individual fibre ID. For better visualisation of the individual fibres in 2D, which are usually not aligned completely within one slice plane, a thickness of  $25 \mu\text{m}$  was used for the maximum intensity image mode shown in Fig 5a. A length threshold of  $50 \mu\text{m}$  was chosen for the fibre evaluation to avoid miss-segmentations near voids. All fibres shorter than  $50 \mu\text{m}$  were not taken into consideration for

further quantitative evaluations. The start and end points obtained for every individual fibre were used for the calculations of the average fibre length and the weighted average fibre length according to ISO 22314 [38] as well as for the determination of the fibre orientation in the 3D volume (Table 2, Fig. 5). It was shown that most of the fibres had a weighted average length of about 101  $\mu\text{m}$  and an average fibre length of 86  $\mu\text{m}$  in all examined samples (Table 2). It is worthwhile noting that the fibre lengths obtained are rough guide values, because the fibres shorter than 50  $\mu\text{m}$  were not taken into account to avoid possible miss-segmentations of phase contrast edge effects along every void occurring in the high-resolution  $\mu\text{CT}$  [39]. For a small minority of fibre interacts, the algorithm was not able to track the entire fibre length, because of virtual fibre breakage. Therefore, the real average length is expected to be shorter. This finding is in good agreement with the data sheet from the supplier, where an average fibre length of 80  $\mu\text{m}$  is stated [28]. The maximum fibre length evaluated by means of  $\mu\text{CT}$  was 593  $\mu\text{m}$  (Table 2). The complete fibre length distribution of the relative number of fibres versus the length is illustrated in Fig. 6.

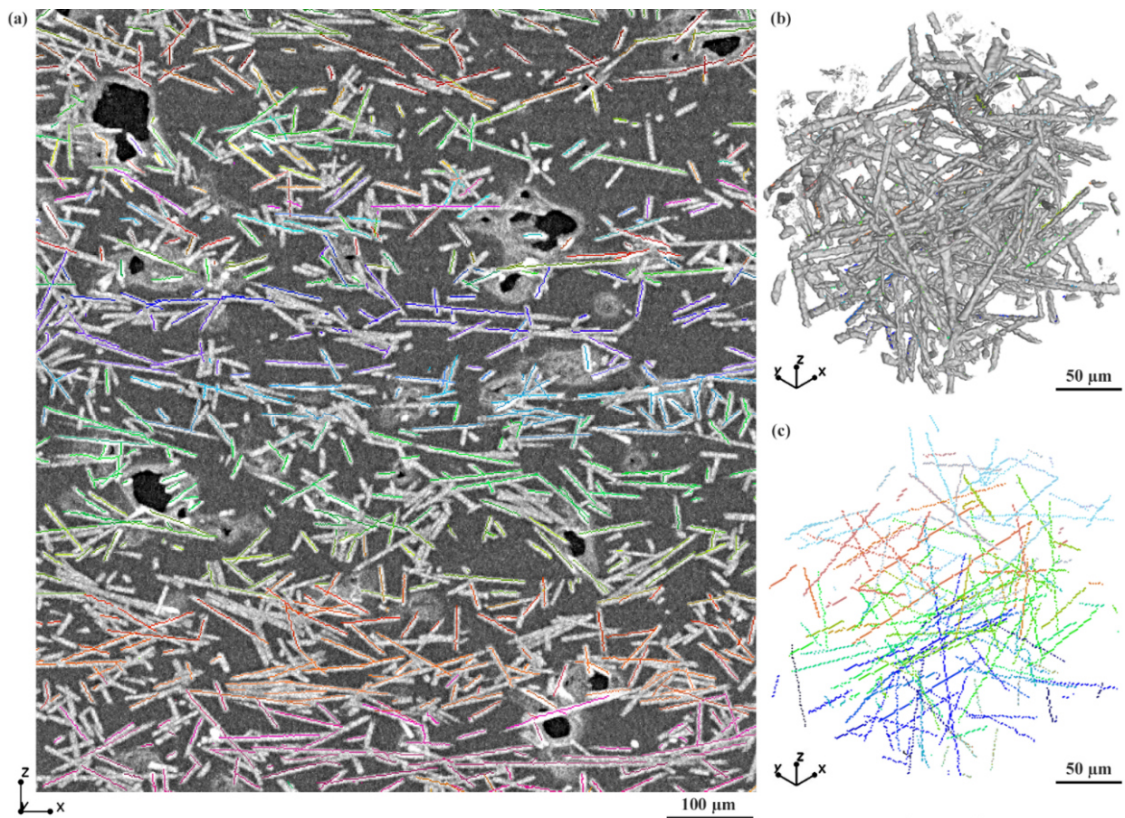


**Fig. 5.** Visualisation of the extracted medial axes of every individual fibre for the  $yz$ -45° sample scanned at  $(1.4 \mu\text{m})^3$  voxel size (a). 3D rendering of a small cut-out of the dataset of individual fibres (b) and their medial axes extractions (c). For colour representation of this figure, the reader is referred to the web version of this article.

**Table 2**

Void volume content and fibre lengths obtained using the X-ray computed tomography.

	$xy$ -0°	$xy$ -45°	$xy$ -90°	$xz$ -45°	$xz$ -90°	$yz$ -45°
--	----------	-----------	-----------	-----------	-----------	-----------

Void volume content, vol.%	4.01	4.05	4.15	4.37	4.53	4.09
Weighted average fibre length, $\mu\text{m}$	101.9	100.7	101.6	101.4	96.8	101.4
Average fibre length, $\mu\text{m}$	87.0	86.2	86.8	86.7	83.5	86.6
Total number of evaluated fibres	120200	120630	84080	90575	78410	102615
Maximum fibre length, $\mu\text{m}$	438.3	444.4	417.5	593.2	502.5	469.7

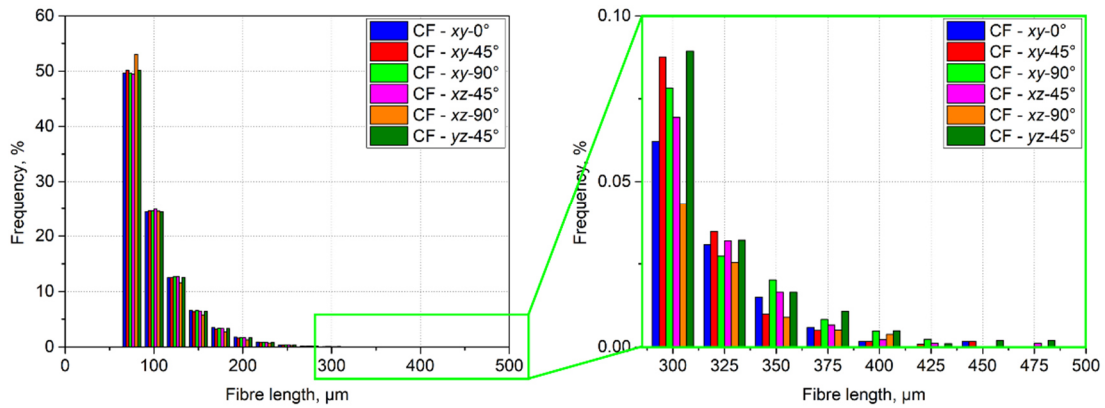


**Fig. 6.** Fibre length distribution in the CF reinforced specimens. For colour representation of this figure, the reader is referred to the web version of this article.

Further analysis revealed a significant difference in the fibre orientation, which supports the discussions below (Fig. 7). In the  $xy-0^\circ$  sample, more than 50% of the fibres were oriented along the  $z_{\mu CT}$ -axis. In the  $xy-90^\circ$  sample, most of the fibres were aligned along the  $x_{\mu CT}$ -axis and, in the  $xz-90^\circ$ , along the  $y_{\mu CT}$ -axis. In all cases, the preferable fibre orientation corresponded to the direction of the roller inside the SLS machine. These results were shown by both software tools, iAnalyse (Fig. 7a) and VG (Fig. 7b), for the extremely high numbers of fibres evaluated (Table 2). These findings offer overwhelming evidence for the existence of a preferable fibre orientation in the specimens produced in the SLS process. Moreover, there is a good correlation with the roller direction and the layer structure typical for SLS: 50 -60 % of the fibre orientation is in-plane of the powder layer along the roller direction ( $x$ -axis), 30 – 40 % perpendicular to it but also in-plane of the powder layer (along the  $y$ -axis) and another 5 – 15 % is oriented out-of-plane of the powder layer (along the  $z$ -axis).

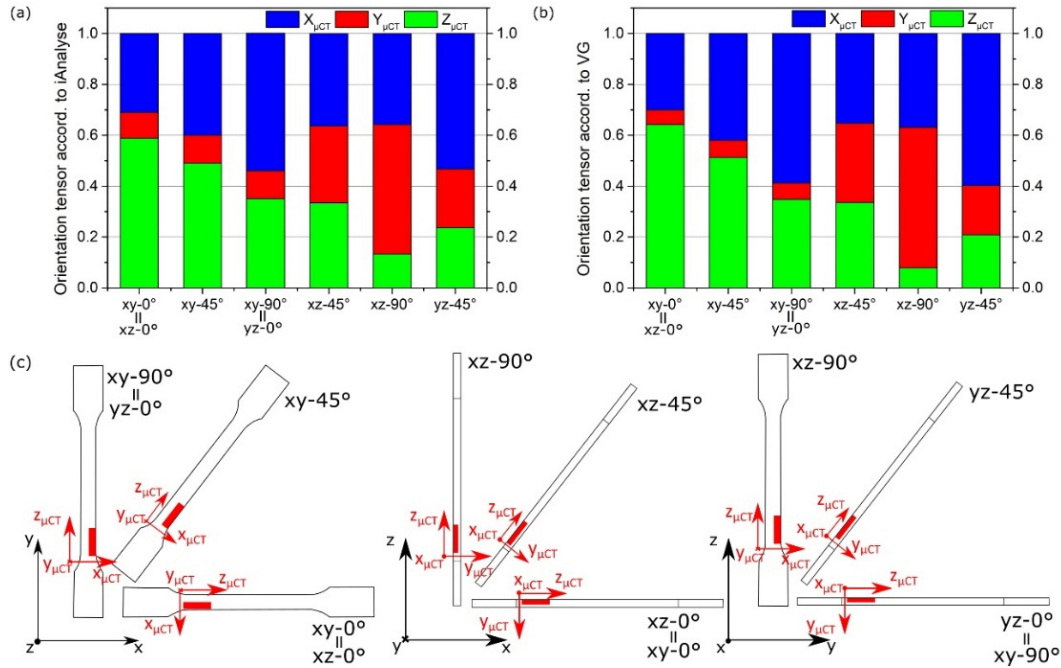


**Fig. 7.** Distributions of the fibre orientations in the  $\mu\text{CT}$  samples evaluated by the iAnalysis (a) and VG (b) software tools, and a schematic representation of the  $\mu\text{CT}$  samples (red rectangles) cut out of the SLS specimens (c).  $(x_{\mu\text{CT}}, y_{\mu\text{CT}}, z_{\mu\text{CT}})$  marked in red corresponds to the coordinate system of the X-ray device, where the  $x_{\mu\text{CT}}y_{\mu\text{CT}}$ -plane is a plane of the rotation stage and  $z_{\mu\text{CT}}$  is the rotation axis.  $(x, y, z)$  marked in black corresponds to the coordinate system of the SLS machine, where  $x$  is the direction of the powder distributing roller. For colour representation of this figure, the reader is referred to the web version of this article.

## Tensile test results

### Tensile tests of the neat specimens

The representative stress-strain curves of the neat specimens are illustrated in Fig. 8. The results of the tensile tests of the neat specimens are summarised in Table 3 and depicted in Fig. 9. The tensile strengths and Young's moduli obtained for the specimens from the  $xy$ ,  $xz$  and  $yz$ -planes showed nearly the same magnitudes for every printing direction - about  $43 \pm 4$  MPa and  $1803 \pm 47$  MPa, respectively. However, the more vertical printing directions like  $xz-67.5^\circ$ ,  $xz-90^\circ$ , etc. showed a bit lower values of tensile strength and Young's modulus in comparison with the other specimens. This can be explained by the fact that the loading force was applied (nearly) transverse to the layer interfaces created due to the layer-wise manufacturing process [40]. The results obtained are in good agreement with regard to the material data provided by the supplier [27] (Table 1). In addition, the present results obtained for PA1212 are consistent with other research works [40,41], which have investigated SLS specimens out of PA12, indicating the similarity of these two materials. Similar values for the neat specimens built in different directions, apart from the more vulnerable vertical directions, means low mechanical anisotropy [42] and further indicates well selected processing parameters. However, the strain at break, which is generally much more sensitive to the process parameters, in particular to the thermal history, than tensile strength or Young's modulus [40], did not show such a uniform behaviour. Instead, there was distinct scatter within the different specimen alignments and a strong



deviation between them. All together the values varied from a minimum value of 5% for  $xz$ -90° to a maximum value of 13.5% for  $xy$ -67.5°. The high scatter level within the same specimen alignments is attributed to variations of the porosity and the quality of the layer to layer fusion from specimen to specimen. Regarding the deviation between the different alignments, no unambiguous tendency can be deduced from the values in Table 3 and Fig. 9.

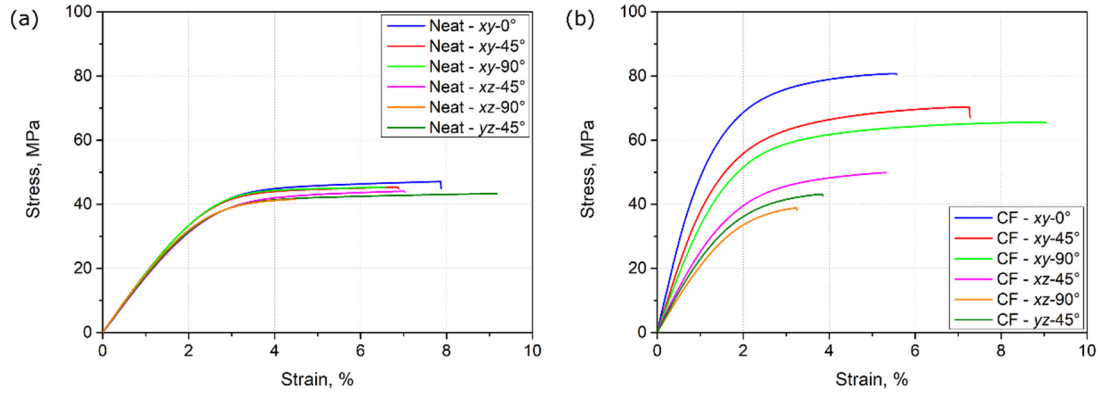


**Fig. 8.** Representative stress-strain curves of the neat (a) and CF reinforced (b) specimens. For colour representation of this figure, the reader is referred to the web version of this article.

#### **Tensile tests of the reinforced specimens**

The representative stress-strain curves of the carbon fibre reinforced polyamide specimens are shown in Fig. 8b. The corresponding tensile test results are presented in Table 3 and depicted in Fig. 9 and Fig. 10. As expected, the experiments demonstrated the strengthening and stiffening of the matrix reinforced with carbon fibres [23,21,18]. The tensile strength  $\sigma$  was increased by almost a factor of two for the  $xy$ -0° specimens and by a factor of 1.4 for the  $xy$ -90° specimens in comparison with the neat specimens. Regarding the  $xz$  and  $yz$  specimens, the carbon fibres made the specimen stronger for 0° and 22.5°, but starting from 45° the reinforcing effect started to disappear. This is well depicted as overlapping of the dashed green and red lines with the corresponding tendencies of the neat specimens in Fig. 10a. The biggest influence of the carbon fibres on Young's modulus  $E$  was achieved for the  $xy$  specimens. It was almost three times bigger for the  $xy$ -0° specimens reinforced with carbon fibres than for the neat specimens. This difference gradually decreased to a factor of two with the angle increase from 0° to 90°. The strain at break  $\varepsilon_b$  of the CF reinforced specimens showed less scattering in comparison with the results of the neat specimens. The  $xy$  specimens yielded the highest  $\varepsilon_b$  of 6-9%, followed by 3-6% for the  $xz$ - and 3-5% for the  $yz$  specimens.

For the CF reinforced specimens built in different directions, the highest  $\sigma$  of about 80 MPa and  $E$  of about 5600 MPa were achieved by the specimens printed along the  $x$ -axis. These results are consistent with [18], where  $\sigma$  of 72 MPa and  $E$  of 5500 MPa were reported for PA12 specimens reinforced with 30%wt carbon fibres. With the angle increase within the  $xy$ -plane from 0° to 90°, the tensile strength and the Young's modulus gradually decreased to 65 and 3500 MPa, respectively. The tensile strength and the Young's modulus of specimens in the  $xz$ - and  $yz$ -planes progressively reduced from the horizontally to the vertically oriented specimens. The

specimens printed vertically along the  $z$ -axis yielded the lowest  $\sigma$  and  $E$  among all specimens of 40 MPa and 2400 MPa, respectively.

**Table 3**

Results of the tensile tests: the strength, Young's modulus and strain at break of the neat and carbon fibre (CF) reinforced specimens built in different directions.

	$\sigma$ , MPa					
	XY		XZ		YZ	
	Neat	With CF	Neat	With CF	Neat	With CF
0°	47.2 ± 1.3*	80.8 ± 0.5*	47.2 ± 1.3*	80.8 ± 0.5*	45.2 ± 1.5**	64.9 ± 0.7**
22.5°	46.2 ± 2.0	76.1 ± 1.7	44.6 ± 1.2	62.2 ± 3.6	45.8 ± 0.2	53.9 ± 1.5
45°	45.4 ± 0.9	70.7 ± 0.3	44.1 ± 0.7	50.2 ± 1.5	43.8 ± 0.3	43.6 ± 2.0
67.5°	46.1 ± 1.6	66.0 ± 0.6	41.4 ± 1.2	43.0 ± 3.5	41.8 ± 0.3	38.8 ± 2.6
90°	45.2 ± 1.5**	64.9 ± 0.7**	41.7 ± 0.6	39.4 ± 2.1	-	-
	$E$ , MPa					
	XY		XZ		YZ	
	Neat	With CF	Neat	With CF	Neat	With CF
0°	1851 ± 14*	5644 ± 123*	1851 ± 14*	5644 ± 123*	1829 ± 36**	3616 ± 78**
22.5°	1863 ± 21	5104 ± 168	1806 ± 21	3871 ± 130	1809 ± 18	2917 ± 93
45°	1843 ± 19	4292 ± 185	1726 ± 28	2565 ± 96	1791 ± 25	2390 ± 66
67.5°	1854 ± 34	3731 ± 49	1741 ± 36	2301 ± 92	1756 ± 12	2213 ± 178
90°	1829 ± 36**	3616 ± 78**	1787 ± 45	2326 ± 77	-	-
	$\epsilon_b$ , %					
	XY		XZ		YZ	
	Neat	With CF	Neat	With CF	Neat	With CF
0°	10.1 ± 5.3*	6.3 ± 0.5*	10.1 ± 5.3*	6.3 ± 0.5*	8.1 ± 6.6**	8.5 ± 0.5**
22.5°	9.6 ± 6.1	6.0 ± 0.8	7.0 ± 3.7	4.6 ± 1.4	13.0 ± 1.8	5.3 ± 0.7
45°	8.8 ± 5.9	8.0 ± 0.6	10.1 ± 2.0	5.9 ± 1.2	10.0 ± 1.8	3.8 ± 0.6
67.5°	13.5 ± 9.3	8.9 ± 0.4	5.6 ± 1.9	3.6 ± 1.0	6.4 ± 0.9	2.8 ± 0.4
90°	8.1 ± 6.6**	8.5 ± 0.5**	5.0 ± 0.9	2.8 ± 0.5	-	-

\*XY-0° is identical to XZ-0°

\*\*XY-90° is identical to YZ-0°

These findings can be explained by the preferable fibre orientations in the specimens shown above, which influence the mechanical properties. As illustrated in Fig. 7, the roller orients the fibres along its moving direction ( $x$ -axis), when distributing a new layer of powder on the building platform. This effect was also reported in [19], where it was shown that most of the fibres were oriented in the  $x$ -direction of the build chamber. As a consequence, the specimens with the fibres oriented along the loading direction are able to bear higher stresses than those with the fibres oriented out of the loading plane [43]. That way, for example, the  $xy$ -90° specimens were stronger than the  $xz$ -90° specimens, although they have the same preferable fibre orientation along the  $x$ -direction. However, along the tensile loading direction, which is the  $y$ -direction for the  $xy$ -90° specimens and the  $z$ -direction for the  $xz$ -90° specimens, they have 30 % and 10 % of fibre orientation, respectively (Fig. 7). It is also interesting that specimens printed at 67.5° and 45° in the  $xz$ - and  $yz$ -planes have nearly the same Young's moduli, whereas Young's modulus of  $xz$ -22.5° are 25% higher than of corresponding  $yz$ -specimens (Fig. 10). These results indicate that the stiffening effect of the preferable fibre orientation along the  $x$ -axis is only efficient up to the 45° alignment of the specimens. For the

higher specimen alignment angles, however, there is still a small stiffening effect compared to the neat specimens, but to a much smaller extent.

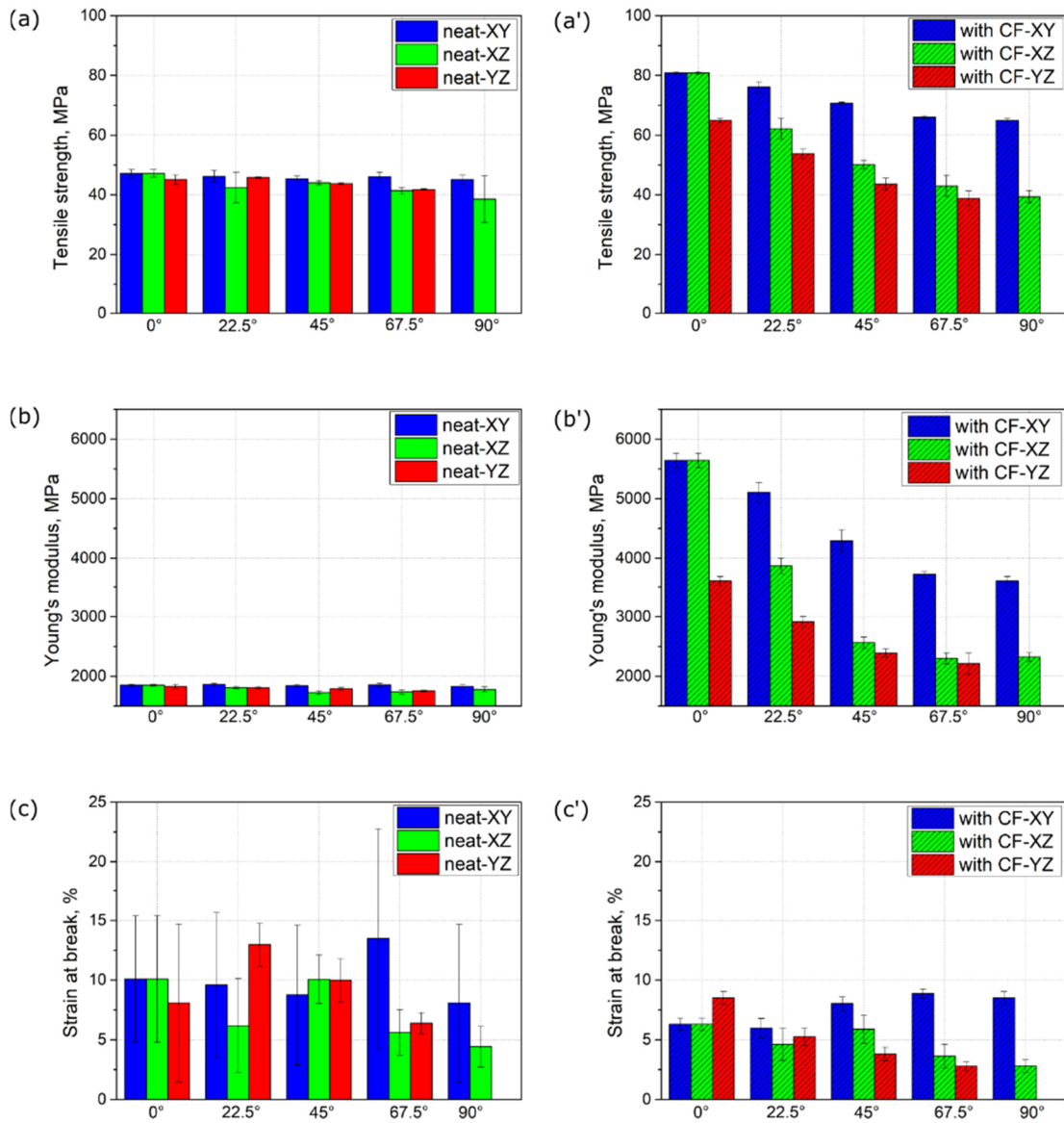


**Fig. 9.** Plots of the tensile strength, Young's modulus and strain at break obtained from the tensile tests of neat (a, b, c) and carbon fibre (CF) reinforced specimens (a',b',c') manufactured in different building directions. The error bars represent the standard deviation from the corresponding average value. For colour representation of this figure, the reader is referred to the web version of this article.

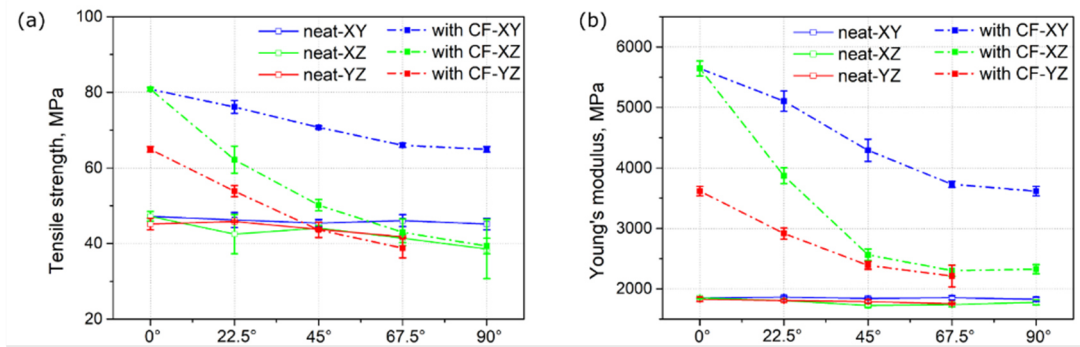


**Fig. 10.** Tendencies of the tensile strength (a) and Young's modulus (b) obtained for the neat and carbon fibre (CF) reinforced specimens. The error bars represent the standard deviation from the corresponding average value. For colour representation of this figure, the reader is referred to the web version of this article.

### Optical analysis

#### Powder

The morphology of the powder particles used to manufacture the specimens is presented in Fig. 11 (both, neat and carbon reinforced powder samples were taken from remaining powder after the processing of the tensile bars). The polyamide particles had a spherical and slightly elongated shape and a rough, porous surface. The typical particle size in Fig. 11 estimated by means of ImageJ is between 30 and 65  $\mu\text{m}$ . The size of porous voids did not exceed 5  $\mu\text{m}$  (Fig. 11b). The fibre lengths estimated in Fig. 11c vary between 50  $\mu\text{m}$  and 250  $\mu\text{m}$ .

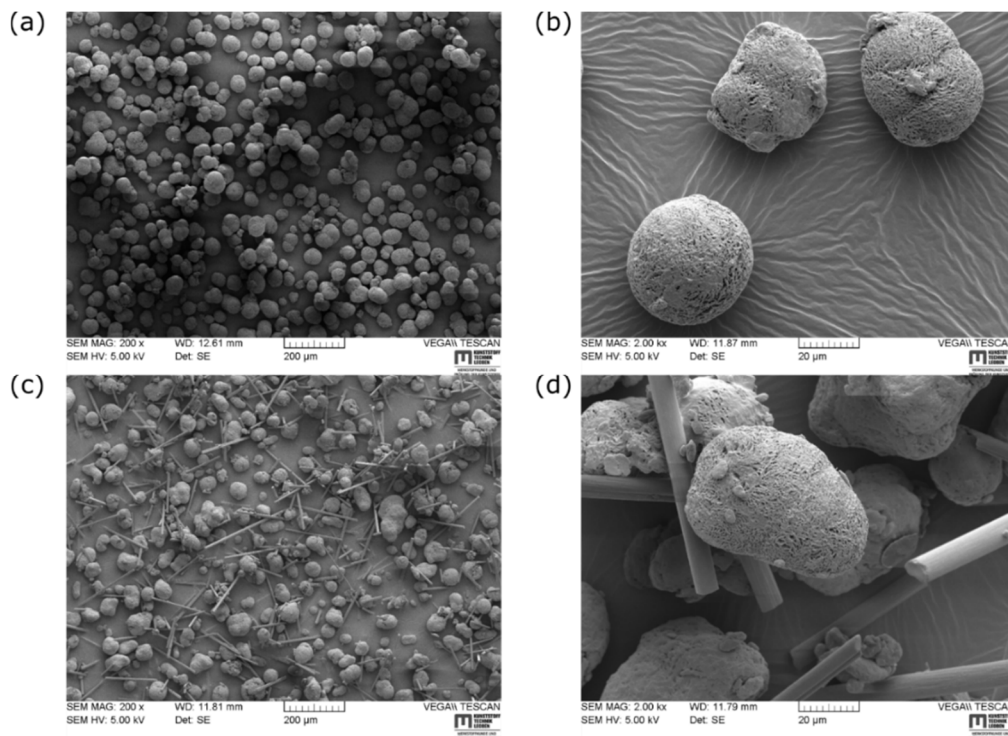


**Fig. 11.** SEM micrographs of the neat (a, b) and carbon fibre reinforced (c, d) powders used for sintering at low (a, c) and high (b, d) magnification.

### Neat specimens

The micrographs of neat specimens, namely  $xz-0^\circ$  (a, a') and  $xz-90^\circ$  (b, b') are demonstrated in Fig. 12. On the fracture surface of the  $xz-0^\circ$  specimens, which were printed horizontally along the  $x$ -axis, the typical SLS layer structure is visible (Fig. 12a). This is not the case for the  $xz-90^\circ$  specimens, which were printed vertically along the  $z$ -axis (Fig. 12b). This is because the tensile loads were applied parallel and transverse to the deposited powder layers, respectively. Due to the layer-by-layer manufacturing manner of the SLS process, both the face and side surfaces of  $xz-90^\circ$  had the layer structure, which is called the staircase effect [44], while  $xz-0^\circ$  only had it on the side surface. The measured thickness of one fused layer was about  $150\ \mu\text{m}$ , which corresponds to the recommendation of the layer thickness to be at least two times the average particle size [3]. The face surface of the horizontally oriented specimens had a plane and grainy texture, representing the typical surface structure along fused layers.

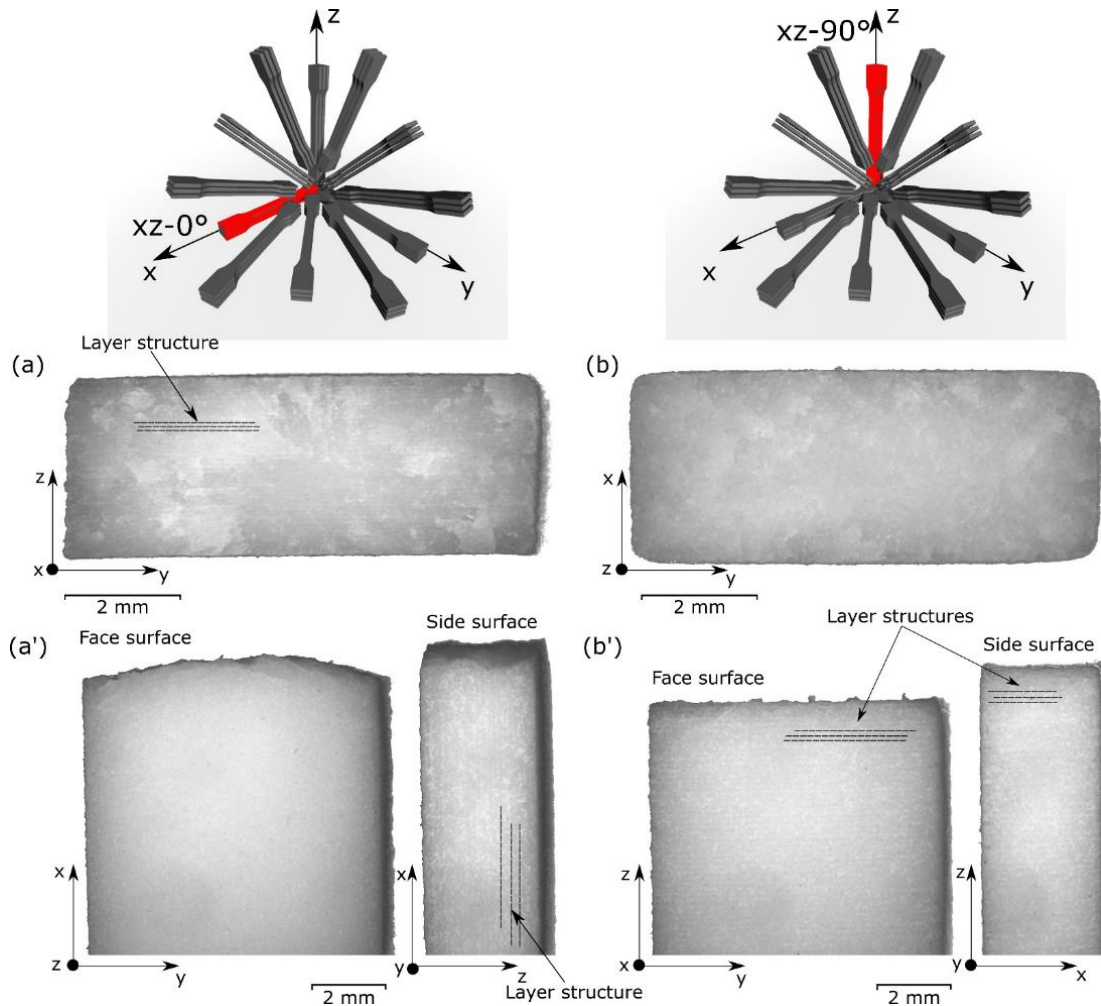


**Fig. 12.** Fracture surfaces of the  $xz-0^\circ$  (a) and  $xz-90^\circ$  (b) neat specimens and the face and side views of their fracture edges (a', b').

Correspondingly, the SEM micrographs of  $xz-0^\circ$  and  $xz-90^\circ$  are reported in Fig. 13. The images show that a lot of powder particles can be identified either in their full shape or at least their contour on the fracture surface of the  $xz-90^\circ$  specimen (Fig. 13b). In this regard, the

fracture surface of the  $xz$ -0° specimen has a more compact structure without the obvious presence of powder particles (Fig. 13a). This illustrates well the difference in the loading direction with respect to the printed layer structure: in case of the  $xz$ -0° alignment, the specimen was loaded parallel to the layer structure, while for the  $xz$ -90° specimen, the load was applied transverse to it. This means that there was the weaker interlayer adhesion and the higher void concentration in the interfaces between the layers in the latter case [40,45]. The interlayer voids are well illustrated in Fig. 13a. They had round and oblong shapes and sizes from 5 to 100  $\mu\text{m}$ . However, some voids are also visible in Fig. 13b. A further difference between  $xz$ -0° and  $xz$ -90° is that in Fig. 13a, a fracture initiation region with corresponding hackle lines [46] can be identified. Such a structure was not found on the  $xz$ -90° fracture surface (Fig. 13b). This further supports the impression of a more compact fracture surface in the case of the  $xz$ -0° specimen. In analogy to Fig. 12a' and Fig. 12b', the face and side surfaces of the specimens were also studied using SEM. Aside from the above-mentioned variation in the staircase structure, no differences were observed, neither between the front and side surfaces nor between the different printing directions. In all cases, the surfaces were rather homogenous on the macroscopic scale, but inhomogeneous on the microscopic scale. They showed sections with well combined material (molten), areas with clear powder particle contours (unmolten) as well as all intermediate steps in between.

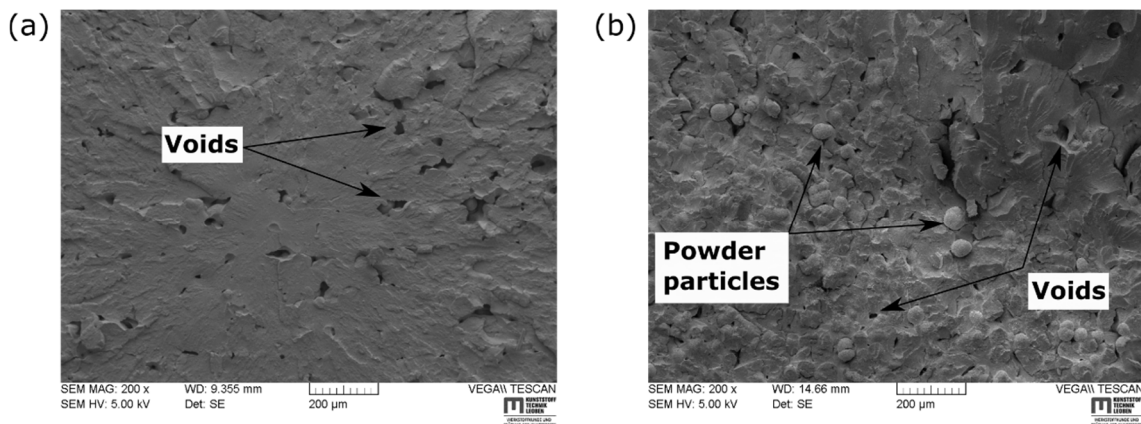


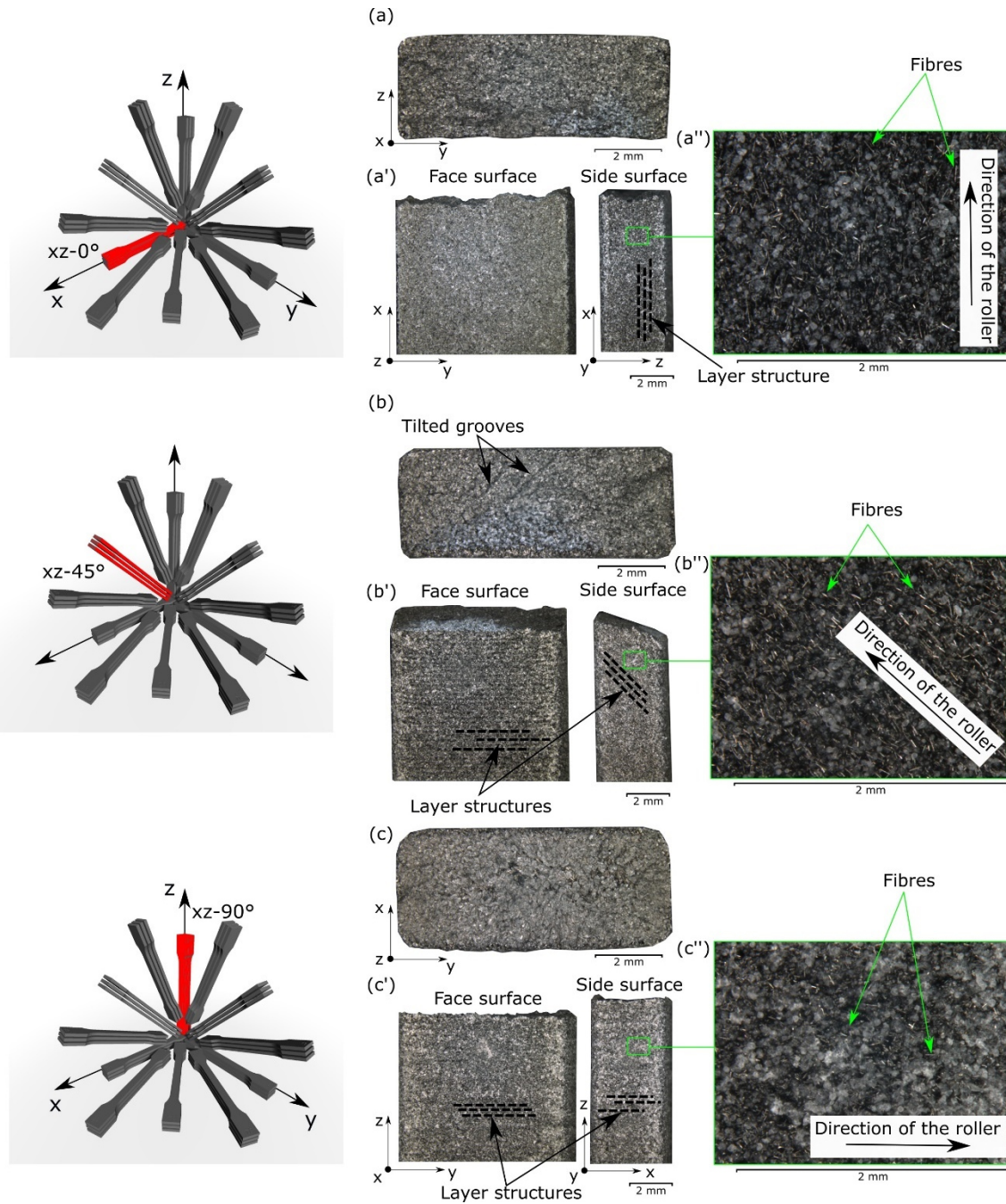
**Fig. 13.** SEM micrographs of the fracture surfaces of the  $xz$ -0° (a) and  $xz$ -90° (b) specimens.

### **Reinforced specimens**

The micrographs of the CF reinforced specimens made with the optical microscope are presented in Fig. 14 for  $xz$ -0° (a,a,a''),  $xz$ -45° (b,b',b'') and  $xz$ -90° (c,c',c''). The layer structure can be observed on the side surface of  $xz$ -0° (Fig. 14a') and the face and side surfaces of  $xz$ -45° (Fig. 14b') and  $xz$ -90° (Fig. 14c'). For  $xz$ -45° the layer lines were tilted at around 45° on the side surface, which corresponded to the building direction of the specimen (Fig. 14b'). The fracture in the  $xz$ -90° specimen occurred between the adjacent layers, which is identified by nearly straight fracture edges in Fig. 14c'. This is similar to the fracture surface characteristics of the neat  $xz$ -90° specimen in Fig. 12b' and can be explained by the weaker interlayer adhesion and the higher concentration of porosity between the layers [40,45], which indicates that there was no significant fibre reinforcing effect for  $xz$ -90°. Thus, the SLS layer structure of the matrix dominates the fracture behaviour in this case. The same was observed for the neat specimens.

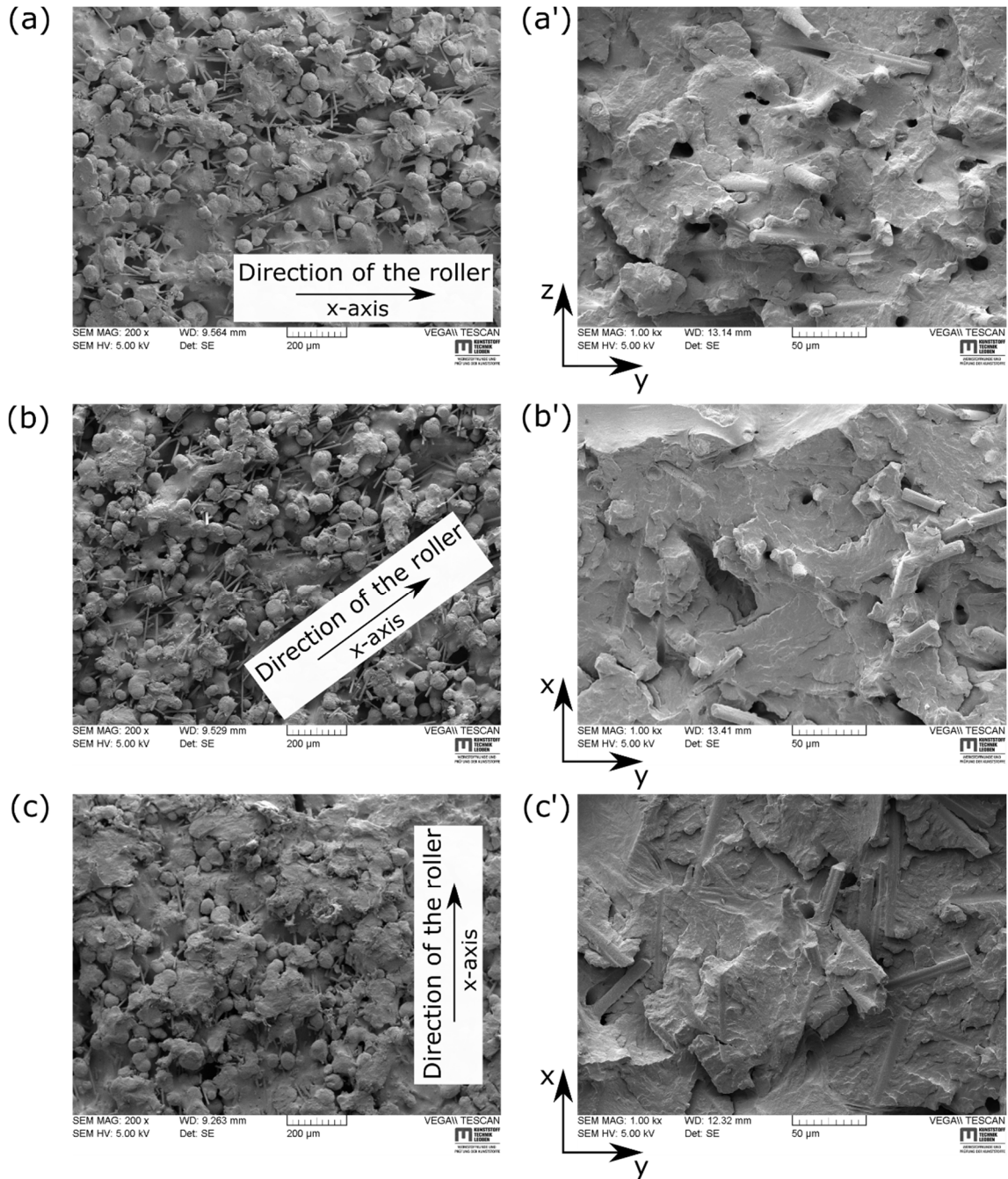
This agrees with the  $\mu$ CT results in Fig. 7 (only small fibre orientation along z-axis) and the tensile test results in Table 3. For the  $xz$ -45° specimens, the fracture surfaces are tilted with respect to the  $xz$ -0° and  $xz$ -90° fracture surface planes. The surfaces are tilted along the thickness with a rotation angle smaller than 45°, as shown in Fig. 14b'. Additionally, the fracture surface of the  $xz$ -45° specimens demonstrate grooves of the material, which are aligned at about 45° on the surface (Fig. 14b). Tilted fracture surfaces were also noticed for the  $yz$ -45° and  $xy$ -45° specimens. In the latter case, the difference was that the tilt was along the width instead of the thickness (rotation angle was also below 45°). Such tilted fracture surfaces are typical for fibre reinforced polymers with preferred fibre orientations not parallel or normal to the load direction [47–50]. Consequently, this effect was also found for the reinforced specimens printed in the 22.5° and 67.5° directions, but not for the corresponding neat specimens. It indicates that the fibre reinforcement dominates the fracture behaviour in these cases instead of the SLS layer structure of the matrix. For the  $xz$ -0° printing direction, the reinforced specimens show a rather unspecific fracture surface with wavy fracture edges, which was also observed for the neat specimens. Despite these unspecific fracture surfaces, it is clear from the  $\mu$ CT results (Fig. 7) and the tensile test results (Table 3) that the carbon fibre reinforcement dominated the fracture behaviour in the  $xz$ -0° direction. The higher magnified images of the side surface give a rough picture about the fibre orientations on the specimen surface (Fig. 14a'', b'', c''). A more detailed examination on this was performed using SEM.

Figure 15 shows SEM micrographs of the side surfaces of the  $xz$ -0° (a),  $xz$ -45° (b) and  $xz$ -90°(c) specimens, respectively. Only partly molten powder particles, which are typical for the surfaces of SLS printed parts and were also discussed for the neat specimens, with inclusions of the carbon fibres, can be easily distinguished on the side surfaces of the specimens (Fig. 15a,b,c). Contrary to that, the fracture surfaces have a rather homogeneous matrix appearance (Fig. 15a',b',c'). This phenomenon can be explained by the fact that the laser sintering causes elevated temperatures around the fused area, which yield melting of the loose powder in the immediate vicinity of it [2]. It can be seen that most of the fibres are oriented in the moving direction of the roller, as it is suggested by the  $\mu$ CT results. The presence of the preferable fibre orientation can be also seen in the micrographs of the specimens' fracture surfaces (Fig. 15a',b',c'). In  $xz$ -0°, the fibres stuck out of the matrix almost straight (Fig. 15a'), while in  $xz$ -45°, the fibres went out of the matrix more tilted (Fig. 15b'). In the case of  $xz$ -90° (built in z-direction), the fibres lay horizontally in the plane of the fracture surface (Fig. 15c'). The micrograph of the fracture surface of  $xz$ -0° made with the higher magnification demonstrated multiple dark holes in the matrix with a diameter of a fibre (Fig. 15a'). They appeared due to the pulling of fibres out of the matrix as a result of the failure process. The presence of this effect almost faded in  $xz$ -45° (Fig. 15b', less dark holes) and disappeared in  $xz$ -90° (Fig. 15c', almost no dark holes), which means the load applied was mostly borne by the matrix. These findings are in excellent agreement with the experimental tensile data, where  $xz$ -0° were the strongest specimens with the highest Young's modulus in comparison with the other building directions.



**Fig. 14.** Fracture surfaces of the  $xz-0^\circ$  (a),  $xz-45^\circ$  (b) and  $xz-90^\circ$  (c) carbon fibre reinforced specimens, their fracture edges (a', b', c') and micrographs of the corresponding side surfaces (a'', b'', c''). The corresponding specimen positions are marked in red on the left side of the figure.





**Fig. 15.** SEM images of the side (a,b,c) and fracture surfaces (a',b',c') of the  $xz$ -0°,  $xz$ -45° and  $xz$ -90° specimens, respectively.

In Fig. 16, less magnified images of the specimen fracture surfaces are presented to deepen the discussion of the fracture surface characteristics started above. The images belong to three specimens, each of them printed along another main coordinate axis in the building chamber ( $x$ -axis:  $xz$ -0°,  $y$ -axis:  $xy$ -90° and  $z$ -axis:  $xz$ -90°). Regarding the fibre characteristics on the fracture surfaces, the observations from Fig. 15 are also visible on these bigger length scales. For  $xz$ -0°, these are fibres coming out of the fracture surface perpendicularly and significant fibre pull-out indicated by numerous black holes on the fracture surfaces, which are in the dimension of the fibre diameter (Fig. 16a,a'). For  $xz$ -90° (Fig. 16c,c'), the absence of these holes

and the presence of in-plane fibres instead of out-of-plane fibres was also discussed above. Interestingly, in the  $xy$ -90° direction (Fig. 16b,b'), the fibre pull-out holes can be clearly identified and their number is not significantly smaller than for the  $xz$ -0° specimen (Fig. 16a,a'). However, a preferable orientation of the fibres along the roller direction ( $x$ -axis) can be clearly identified, while for the  $xz$ -0° specimen, the fibres were oriented mainly perpendicular to the fracture surface.

Looking at the global appearance of the fracture surfaces in Fig. 16, all samples show a brittle-like surface structure with a rocky texture. For  $xz$ -0° (Fig. 16a,a'), this texture is very rough with fine topographical details on the surface. This printing direction shows the roughest texture of all printing directions. The fracture surface texture observed for the  $xy$ -90° specimen (Fig. 16b,b') is also rough, but with fewer fine topographical surface details, and hence smoother than that of the  $xz$ -0° specimen. A global fracture surface texture similar to the latter was found for most of the printing directions. Finally, the fracture surface of the  $xz$ -90° specimen (Fig. 16c,c') is rather flat and significantly smoother than the surfaces of all other printing directions. However, it still shows a distinct rocky texture. Moreover, for the  $xz$ -90° fracture surface, small local areas with a very smooth surface can be identified. Since, in this printing direction, the specimens roughly broke along the SLS layer boundaries (Fig. 14c'), it is interpreted that these local areas represent the surface of interlayer voids. This also explains their smooth melt-like surface. The hypothesis is supported by some remaining voids visible in Fig. 16c,c', which partly have a connection to these smooth areas. These small void remains were also found on fracture surfaces of other printing directions but to a lesser extent than for  $xz$ -90°. Based on the images shown in this study and the fracture surface analysis of the further printing directions, it is concluded that the global fracture surfaces of the  $xz$ -0° and  $xz$ -90° specimens represent the two extremal values. For all other printing directions, the fracture surfaces can roughly be reduced to a mixture of these two with different mixing ratios.

Hence, recapitulating the discussion above, for the specimens examined in this study, the fibre reinforcement and the fibre orientation introduced by the SLS process were much more important for the mechanical and fracture behaviour than the typical SLS layer structure of the matrix. The only exception is the specimens printed in the  $xz$ -90° direction, which showed matrix-dominated fracture behaviour.

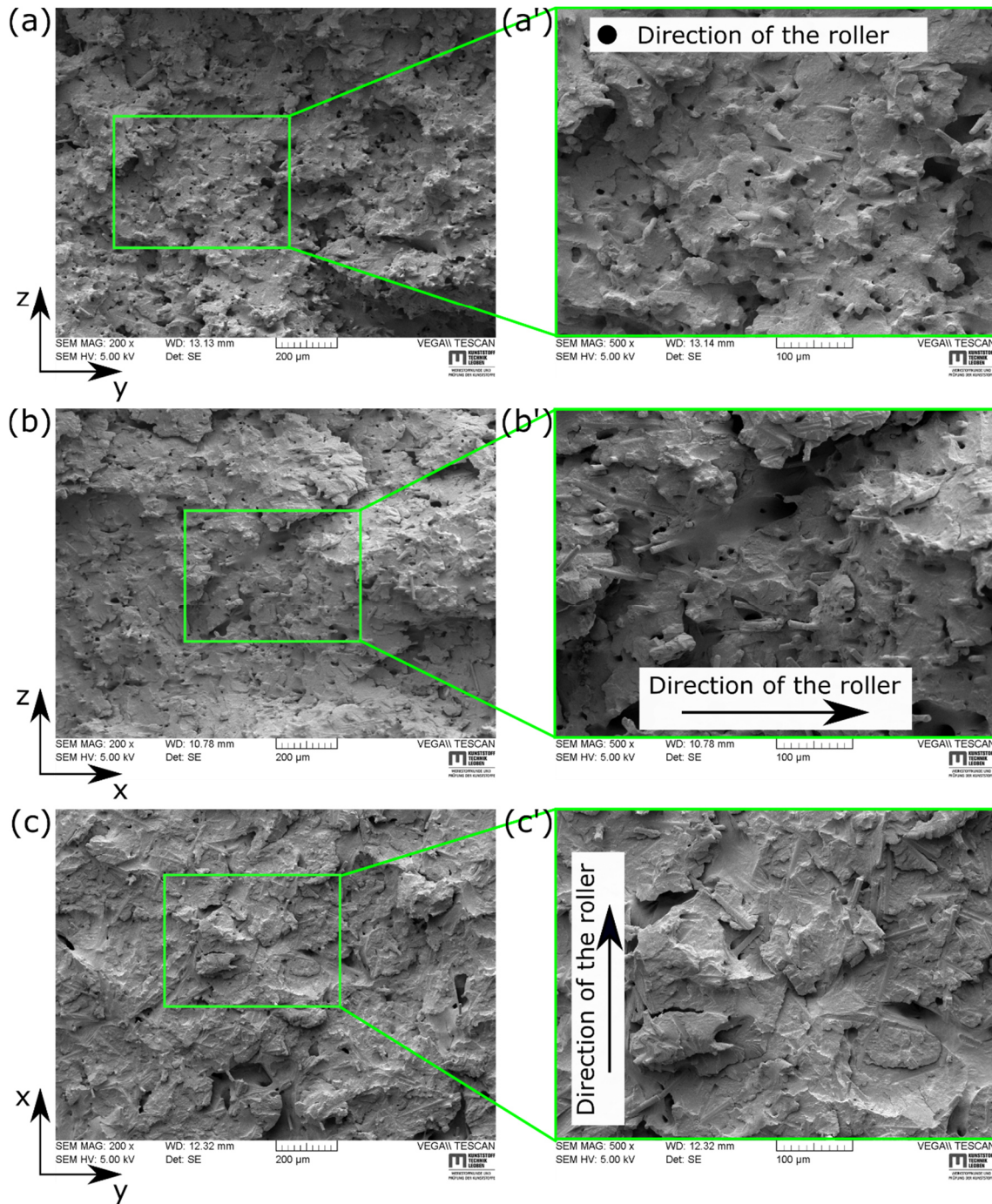


**Fig. 16.** SEM micrographs of the fracture surfaces of the  $xz-0^\circ$  (a),  $xy-90^\circ$  (b) and  $xz-90^\circ$  (c) specimens.

### 3.1.6. Conclusion

This paper presents the systematic and comprehensive analysis of the mechanical properties of neat and short carbon fibre reinforced polyamide specimens produced by selective laser sintering. The specimens were printed in different directions and different spatial positions in the build chamber. The mechanical parameters, namely tensile strength, Young's modulus

and strain at break, were characterised by tensile tests and analysed with respect to these specimen alignments.

The experiments showed a significant influence of the carbon fibres on the material behaviour in the different printing directions. The strength of the reinforced specimens built along the  $x$ -axis was increased by almost a factor of two, while the strength of the specimens built in the  $y$ -direction was increased by a factor of nearly 1.4 in comparison with the neat specimens. For the reinforced specimens, the tensile strength and Young's modulus decreased with increasing deviation from the  $x$ -axis (direction of the powder distribution roller) and with increasing  $z$ -axis components (manufacturing normal to the layer structure). These findings indicated the existence of a preferable fibre orientation created in the specimens. Detailed investigations with an optical microscope, scanning electron microscope and X-ray computed tomography showed that the fibres were mainly oriented in-plane of the powder layer in the SLS process and here, especially along the moving direction of the roller. The ratios of the fibre orientation tensor were found as:

- 50 – 60 % along the  $x$ -axis, which was the roller direction (in-plane of the SLS powder layer)
- 30 – 40 % along the  $y$ -axis, in-plane perpendicular to the roller direction
- 5 – 15 % along the  $z$ -axis, normal to the SLS layer structure (out-of-plane fibre orientation)

The  $\mu$ CT analysis showed that the different building alignments did not have an influence on the fibre length distribution. This further strengthened the finding that the change in the mechanical properties was dominated by the fibre orientations. It is worth noting that the  $\mu$ CT analysis was performed using two different software tools. The orientation tensor obtained by extracting individual fibres was in good agreement with the other software based on the grey value orientation analysis. To avoid miss-segmentations of the phase-contrast edge effects along voids, the evaluation of the fibre length was limited to fibres longer than 50  $\mu$ m for all specimens investigated. The analyses further revealed that the mechanism of the failure changed from 'fibre-matrix' failure for specimens with the fibres oriented along the loading direction to 'matrix-matrix' failure for specimens with the fibres oriented out of the loading direction due to the layer-wise building manner of SLS.

Taken together, the findings obtained highlight the importance of the printing alignment for short fibre reinforced polymer parts produced by SLS. It is clear that the exact values of the above-mentioned fibre orientation ratios in the different machine directions will be dependent on various parameters, such as:

- Type and version of SLS machine
- Powder distribution system: type (roller or blade), size and shape
- Powder characteristics: particle size and shape, packing density, powder ageing state, melt viscosity
- Fibre characteristics: type, size, shape and content
- SLS process parameters: roller speed, powder layer thickness, powder bed temperature, energy density, etc.

Thus, the fibre orientation ratios found in this study represent only a single-point result. Nevertheless, they are useful as guide values in component design for the SLS technique. Moreover, they show that through a smart alignment in the building chamber, the SLS process can be used for advanced processing of fibre reinforced components with optimised fibre orientation in essential and critical component parts. However, to fully understand the influence of the above listed parameters on the degree of anisotropy in carbon fibre reinforced specimens produced by SLS, further studies on this topic are required in the future.

### **Acknowledgments**

Special thanks go to Nicole Zarfl for the SEM examinations.

The research work of this paper was performed at the Polymer Competence Center Leoben GmbH (PCCL, Austria) within the framework of the funding programs ‘Production of the Future’, ‘Smart Mobility’, ‘TAKE OFF’ and ‘COMET-Module’ of the Federal Ministry for Transport, Innovation and Technology and the Federal Ministry of Digital and Economic Affairs with contributions by JOANNEUM RESEARCH Forschungsgesellschaft mbH, Institute for Materials Science and Testing of Polymers at the Montanuniversitaet Leoben and Material Center Leoben Forschungs GmbH as Scientific Partners and Rapid Product Development GmbH, LSS GmbH, Bernstein GmbH, Secar Technologie GmbH, F.LIST GmbH, AMES Aerospace and Mechanical Engineering Services, Ing. Walter Starzacher GesmbH, SinusPro GmbH, Inocon Technologie GmbH, Carbon Solutions Hintsteiner GmbH, XeNTiS Entwicklungs- und Produktions GmbH and RÜBIG GmbH & Co KG as company partners. The PCCL is funded by the Austrian Government and the State Governments of Styria, Lower Austria and Upper Austria.

$\mu$ CT scans and evaluations were performed within the projects ‘Interpretation and evaluation of defects in complex CFK structures based on 3D-XCT data and structural simulation - (DigiCT-Sim project number: 862015)’ and ‘Systematic analysis of three-dimensional pore structures in fibre-reinforced plastics using 3D X-ray methods - (pore3D project number: 868735).’ Both  $\mu$ CT projects were funded by the State Government of Upper Austria and Austrian Research Promotion Agency (FFG).

#### 3.1.7. References

- [1] University of Texas, Selective Laser Sintering, Birth of an Industry, 2012. <https://www.me.utexas.edu/news/news/selective-laser-sintering-birth-of-an-industry> (accessed 17 February 2020).
- [2] I. Gibson, D. Rosen, B. Stucker, Additive manufacturing technologies: 3D printing, rapid prototyping, and direct digital manufacturing, Second edition, Springer, New York, NY, 2015.
- [3] S. Berretta, O. Ghita, K.E. Evans, Morphology of polymeric powders in Laser Sintering (LS): From Polyamide to new PEEK powders, European Polymer Journal 59 (2014) 218–229.
- [4] D. Drummer, D. Rietzel, F. Kühnlein, Development of a characterization approach for the sintering behavior of new thermoplastics for selective laser sintering, Physics Procedia 5 (2010)
- [5] J. Bai, B. Zhang, J. Song, G. Bi, P. Wang, J. Wei, The effect of processing conditions on the mechanical properties of polyethylene produced by selective laser sintering, Polymer Testing 52 (2016) 89–93.

- [6] P. Chen, H. Wu, W. Zhu, L. Yang, Z. Li, C. Yan, S. Wen, Y. Shi, Investigation into the processability, recyclability and crystalline structure of selective laser sintered Polyamide 6 in comparison with Polyamide 12, *Polymer Testing* 69 (2018) 366–374.
- [7] D. Ritzel, F. Kühnlein, D. Drummer, Selektives Lasersintern von teilkristallinen Thermoplasten, *RTEjournal - Forum für Rapid Technologie* Vol. 6 (2011).
- [8] S. Berretta, K.E. Evans, O. Ghita, Processability of PEEK, a new polymer for High Temperature Laser Sintering (HT-LS), *European Polymer Journal* 68 (2015) 243–266.
- [9] W. Zhu, C. Yan, Y. Shi, S. Wen, J. Liu, Y. Shi, Investigation into mechanical and microstructural properties of polypropylene manufactured by selective laser sintering in comparison with injection molding counterparts, *Materials & Design* 82 (2015) 37–45.
- [10] R.D. Goodridge, M.L. Shofner, R.J.M. Hague, M. McClelland, M.R. Schlea, R.B. Johnson, C.J. Tuck, Processing of a Polyamide-12/carbon nanofibre composite by laser sintering, *Polymer Testing* 30 (2011) 94–100.
- [11] S.R. Athreya, K. Kalaitzidou, S. Das, Processing and characterization of a carbon black-filled electrically conductive Nylon-12 nanocomposite produced by selective laser sintering, *Materials Science and Engineering: A* 527 (2010) 2637–2642.
- [12] S.R. Athreya, K. Kalaitzidou, S. Das, Mechanical and microstructural properties of Nylon-12/carbon black composites: Selective laser sintering versus melt compounding and injection molding, *Compos. Sci. Technol.* 71 (2011) 506–510.
- [13] A.H. Espera, A. d. Valino, J.O. Palaganas, L. Souza, Q. Chen, R.C. Advincula, 3D Printing of a Robust Polyamide-12-Carbon Black Composite via Selective Laser Sintering: Thermal and Electrical Conductivity, *Macromol. Mater. Eng.* 304 (2019) 1800718.
- [14] J. Bai, R.D. Goodridge, R.J.M. Hague, M. Song, Carbon nanotube reinforced Polyamide 12 nanocomposites for laser sintering, in: D.L. Bourell, R.H. Crawford, C.C. Seepersad, J.J. Beaman, H.L. Marcus (Eds.), *23rd Annual International Solid Freeform Fabrication Symposium: An Additive Manufacturing Conference, Proceedings, August 6-8, 2012, University of Texas, 2012*, pp. 98–107.
- [15] J. Bai, R.D. Goodridge, R.J.M. Hague, M. Song, Improving the mechanical properties of laser-sintered polyamide 12 through incorporation of carbon nanotubes, *Polymer Engineering & Science* 53 (2013) 1937–1946.
- [16] B. Chen, S. Berretta, K. Evans, K. Smith, O. Ghita, A primary study into graphene/polyether ether ketone (PEEK) nanocomposite for laser sintering, *Applied Surface Science* 428 (2018) 1018–1028.
- [17] H. Chung, S. Das, Processing and properties of glass bead particulate-filled functionally graded Nylon-11 composites produced by selective laser sintering, *Materials Science and Engineering: A* 437 (2006) 226–234.
- [18] Jing, W., Hui, C., Qiong, W., Hongbo, L., Zhanjun, L., Surface modification of carbon fibers and the selective laser sintering of modified carbon fiber/nylon 12 composite powder, *Materials & Design* 116 (2017) 253–260.
- [19] A. Jansson, L. Pejryd, Characterisation of carbon fibre-reinforced polyamide manufactured by selective laser sintering, *Additive Manufacturing* 9 (2016) 7–13.
- [20] B. Chen, S. Berretta, R. Davies, O. Ghita, Characterisation of carbon fibre (Cf) - Poly Ether Ketone (PEK) composite powders for laser sintering, *Polymer Testing* 76 (2019) 65–72.
- [21] W. Jing, C. Hui, W. Qiong, L. Hongbo, L. Zhanjun, Surface modification of carbon fibers and the selective laser sintering of modified carbon fiber/nylon 12 composite powder, *Materials & Design* 116 (2017) 253–260.

- [22] M. Yan, X. Tian, G. Peng, D. Li, X. Zhang, High temperature rheological behavior and sintering kinetics of CF/PEEK composites during selective laser sintering, *Compos. Sci. Technol.* 165 (2018) 140–147.
- [23] G. Flodberg, H. Pettersson, L. Yang, Pore analysis and mechanical performance of selective laser sintered objects, *Additive Manufacturing* 24 (2018) 307–315.
- [24] B. Chen, Y. Wang, S. Berretta, O. Ghita, Poly Aryl Ether Ketones (PAEKs) and carbon-reinforced PAEK powders for laser sintering, *Journal of Materials Science* 52 (2017) 6004–6019.
- [25] W. Zhu, C. Yan, Y. Shi, S. Wen, J. Liu, Q. Wei, Y. Shi, A novel method based on selective laser sintering for preparing high-performance carbon fibres/polyamide12/epoxy ternary composites, *Sci. Rep.* 6 (2016) 33780
- [26] S. Arai, S. Tsunoda, A. Yamaguchi, T. Ougizawa, Effects of short-glass-fiber content on material and part properties of poly(butylene terephthalate) processed by selective laser sintering, *Addit. Manuf.* 21 (2018) 683–693.
- [27] [http://en.farsoon.com/products\\_detail/productId=41.html](http://en.farsoon.com/products_detail/productId=41.html) (accessed April 2020).
- [28] <https://www.sgicarbon.com/en/markets-solutions/material/sigrafil-short-carbon-fibers/> (accessed April 2020).
- [29] ISO 527, *Plastics - Determination of tensile properties.*
- [30] D. Salaberger, K.A. Kannappan, J. Kastner, J. Reussner, T. Auinger, Evaluation of computed tomography data from fibre reinforced polymers to determine fibre length distribution, *International Polymer Processing* 26 (2011) 283–291.
- [31] D. Salaberger, P.J. Hine, M. Jerabek, J. Kastner, Assessment of accuracy of fibre orientation measurement using X-ray computed tomography, in: *20th International Conference on Composite Materials*, 2015.
- [32] [github.com/3dct/open\\_iA](https://github.com/3dct/open_iA) (accessed April 2020).
- [33] Defect and Porosity Determination of Fibre Reinforced Polymers by X-ray Computed Tomography, in: *2nd International Symposium on NDT in Aerospace*, 2010.
- [34] S. Senck, M. Scheerer, V. Revol, K. Dobes, B. Plank, J. Kastner, Non-Destructive Evaluation of Defects in Polymer Matrix Composites for Aerospace Applications Using X-ray Talbot-Lau Interferometry and Micro CT., in: *AIAA SciTech Forum: 58th AIAA/ASCE/AHS/ASC Structures, Structural Dynamics, and Materials Conference*, 2017.
- [35] B. Plank, G. Rao, J. Kastner, Evaluation of CFRP-reference samples for porosity made by drilling and comparison with industrial porosity samples by means of quantitative XCT, in: *7th International Symposium on NDT in Aerospace*, 2015.
- [36] M. Reiter, M. Erler, C. Kuhn, C. Gusenbauer, J. Kastner, SimCT: a simulation tool for X-ray imaging, in: *6th Conference on Industrial Computed Tomography*, 2016.
- [37] D. Salaberger, Micro structure of discontinuous fibre polymer matrix composites determined by X-ray Computed Tomography. Doctoral dissertation, 2019.
- [38] ISO 22314:2006, *Plastics — Glass-fibre-reinforced products — Determination of fibre length.*
- [39] J. Kastner, B. Plank, G. Requena, Non-destructive characterisation of polymers and Al-alloys by polychromatic cone-beam phase contrast tomography, *Materials Characterization* 64 (2012) 79–87.
- [40] E.C. Hofland, I. Baran, D.A. Wismeijer, Correlation of Process Parameters with Mechanical Properties of Laser Sintered PA12 Parts, *Advances in Materials Science and Engineering* 2017 (2017) 1–11.

- [41] A. Wegner, G. Witt, Correlation of Process Parameters and Part Properties in Laser Sintering using Response Surface Modeling, *Physics Procedia* 39 (2012) 480–490.
- [42] J.R.C. Dizon, A.H. Espera, Q. Chen, R.C. Advincula, Mechanical characterization of 3D-printed polymers, *Additive Manufacturing* 20 (2018) 44–67.
- [43] C. Soutis, Carbon fiber reinforced plastics in aircraft construction, *Materials Science and Engineering: A* 412 (2005) 171–176.
- [44] M. Schmid, *Laser sintering with plastics: Technology, processes, and materials*, Carl Hanser Verlag, Munich, 2018.
- [45] B. Caulfield, P.E. McHugh, S. Lohfeld, Dependence of mechanical properties of polyamide components on build parameters in the SLS process, *Journal of Materials Processing Technology* 182 (2007) 477–488.
- [46] ASM International, *Characterization and failure analysis of plastics*, ASM International, Materials Park, OH, 2010.
- [47] A. Benaarbia, A. Chrysochoos, G. Robert, Fiber orientation effects on heat source distribution in reinforced polyamide 6.6 subjected to low cycle fatigue, *J Eng Math* 90 (2015) 13–36.
- [48] S. Mortazavian, A. Fatemi, Effects of fiber orientation and anisotropy on tensile strength and elastic modulus of short fiber reinforced polymer composites, *Composites Part B: Engineering* 72 (2015) 116–129.
- [49] S. Mortazavian, A. Fatemi, Fatigue behavior and modeling of short fiber reinforced polymer composites including anisotropy and temperature effects, *International Journal of Fatigue* 77 (2015) 12–27.
- [50] K. Tanaka, T. Kitano, N. Egami, Effect of fiber orientation on fatigue crack propagation in short-fiber reinforced plastics, *Engineering Fracture Mechanics* 123 (2014) 44–58.



### 3.2. Interlayer bonding characterisation between materials with different degrees of stiffness processed by fused filament fabrication

#### 3.2.1. Bibliographic information

- Authors and their relevant contribution to the publication:
  - A. Khudiakova<sup>1</sup>: Conceptualisation, Writing – original draft, Writing - review and editing, Investigation, Validation, Visualisation
  - F. Arbeiter<sup>2</sup>: Conceptualisation, Methodology, Writing - review and editing
  - M. Spoerk<sup>3</sup>: Conceptualisation, Writing - review and editing, resources
  - M. Wolfahrt<sup>1</sup>: Project administration, Funding acquisition
  - D. Godec<sup>4</sup>: Supervision, Writing - review and editing
  - G. Pinter<sup>2</sup>: Resources, Supervision
  
- Affiliations:
  - <sup>1</sup>Polymer Competence Center Leoben GmbH, Roseggerstraße 12, 8700 Leoben, Austria
  - <sup>2</sup>Institute of Materials Science and Testing of Polymers, Montanuniversitaet Leoben, Otto Gloeckel-Straße 2, 8700 Leoben, AT
  - <sup>3</sup>Institute of Polymer Processing, Montanuniversitaet Leoben, Otto Gloeckel-Straße 2, 8700 Leoben, AT
  - <sup>4</sup>Faculty of Mechanical Engineering and Naval Architecture, University of Zagreb, Ul. Ivana Lučića 5, 10000, Zagreb, HR

Published in Additive manufacturing 28 (2019)

*The manuscript is presented here in accordance with the publisher's copyright policy: 'Authors can include their articles in full or in part in a thesis or dissertation for non-commercial purposes.' Elsevier.com*

### 3.2.2. Abstract

One of the main benefits of material extrusion additive manufacturing, also known as fused filament fabrication (FFF) or 3D printing, is the flexibility in terms of printing materials. Locally reinforced components can be easily produced by selectively combining reinforced with unfilled tough thermoplastics. However, such multi-material composites usually lack sufficient weld strength in order to be able to withstand operation loads. The present study attempts to close this gap by characterising the cohesion between the strands of two materials with different stiffness, namely neat PLA and short carbon fibre reinforced PLA (CF-PLA), produced by FFF using advanced fracture mechanical techniques. The full set of engineering constants of both materials were obtained under the assumption of transverse isotropy from tensile tests in combination with digital image correlation. Double cantilever beam (DCB) and cracked round bar (CRB) tests were used to determine the critical energy release rate ( $G_{Ic}$ ). Both tests were in good correlation with each other and revealed that the interlayer PLA/CF-PLA bonding was at least as tough as the interlayer CF-PLA/CF-PLA bonding.

### 3.2.3. Introduction

On the contrary to formative and subtractive [1] manufacturing, additive manufacturing (AM) is a fabrication technique for three-dimensional (3D) objects that is based on the layer by layer material deposition. AM is considered as more economical in terms of material use and production speed, since material is placed only where it is required [2–4]. Fused filament fabrication (FFF) is a material extrusion AM technique, which is based on the fusion of thermoplastic filaments. Within this process, a spooled filament is heated up to a flowable state in a hot extruder and then deposited through a small nozzle according to a pre-defined geometry in a layer by layer manner onto a build platform [5]. Nowadays, FFF printers are moving towards a faster, more accurate and an operation-friendlier production. Concurrently, the range of printable materials broadens [6–11]. As a result, the FFF technology is becoming increasingly popular and attractive to use, not only for rapid prototyping, but also for end-user parts [12–15]. For successful use as end-user parts, reliable mechanical properties, especially of the welding zone between the filaments, are a must. There are numerous studies about tensile, compressive and bending properties of FFF printed parts [16,14]. However, engineering constants in the  $xz$ - and  $yz$ - directions are usually missing in the literature due to difficulties in obtaining strains from a relatively narrow side face of tensile specimens. For the design of load carrying parts, not only experimental, but also numerical analysis such as finite element modelling (FEM) is necessary. In FEM, engineering constants such as Young's and shear moduli, Poisson's ratios in different directions and tensile strength are needed as input parameters. Therefore, determination of the properties in the  $xz$ - and  $yz$ - directions is mandatory.

To get a full picture of the applicability of FFF parts in structurally loaded components, sophisticated knowledge regarding the fracture properties, e.g. toughness is required. Fracture mechanical (FM) tests are a common technique to characterise the toughness (e.g. between layers of materials) and to predict the fracture behaviour of materials [1,17]. There are three fundamental fracture modes: I - opening, II - in-plane shear, III – out-of-plane shear, and a

combination of those, referred to as mix-mode. The material toughness characterisation in mode I, when the delamination is caused by tension loads, is among the most common FM tests. Within the framework of linear elastic fracture mechanics (LEFM), fracture toughness can be characterised in terms of the energy release rate ( $G_I$ ) or the stress intensity factor ( $K_I$ ). Their critical values ( $G_{Ic}$  and  $K_{Ic}$ ), which are material constants, are usually obtained from monotonic tests, such as double cantilever beam (DCB) or compact tension (CT) tests [1]. Works, where the FM parameters were investigated on parts produced by FFF, are summarised in Table 1.

**Table 1.** Fracture mechanical tests and materials used by researchers for the characterisation of specimens fabricated by FFF. PLA refers to poly(lactic acid), ABS to acrylonitrile butadiene styrene, CF-ABS to carbon fibre reinforced acrylonitrile butadiene styrene, and PEEK to polyether ether ketone.

Test	Author	Material
<b>Peel test</b>	Levenhagen et al. [18]	PLA
	Davis et al. [19]	ABS
<b>Single edge notched tensile (SENT)</b>	Griffiths et al. [20]	PLA
<b>Single edge notched bend (SENB)</b>	Torres et al. [21]	PLA
	Hart et al. [22]	ABS
	Song et al. [23]	PLA
	Arbeiter et al. [24]	PLA
<b>Compact tension (CT) fracture test</b>	McLouth et al. [25]	ABS
	Arif et al. [26]	PEEK
	Gardan et al. [27]	ABS
	Arbeiter et al. [24]	PLA
	Papon et al. [28]	PLA, CF-PLA
<b>Double cantilever beam (DCB) mode I test</b>	Aliheidari et al. [29,30]	ABS
	Spoerk et al. [31]	PLA
	Young et al. [32]	ABS, CF-ABS
	Barile et al. [33]	ABS

Apart from studies on simple peel tests, or more complex SENB, SENT, and CT tests (Table 1), which go beyond the scope of the present manuscript, the DCB test in mode I is a common FM test for the toughness characterisation of laminated structures, which is standardised by the American Society for Testing and Materials (ASTM, USA) [34]. For example, Spoerk et al. [31] showed the applicability of the DCB test on 3D-printed PLA specimens. The authors demonstrated the importance of the right choice of printing parameters, such as printing temperature and layer thickness, for achieving optimal inter-layer strengths. Their specimens were approximately four times thicker than it is recommended in the standard for classical unidirectional carbon fibre reinforced composites to avoid plastic deformations in the beams under load. For the crack initiation in the mid-plane, the samples were grooved on the side and a wedge-shaped blade was used to create a pre-crack.  $G_{Ic}$  was calculated by the area method [35]. Similarly thick DCB specimens were also used by Aliheidari et al. [29,30], who characterised the inter-layer adhesion between ABS layers by means of the J-integral, which was obtained from finite element modelling (FEM) by using experimental results as input parameters. It was shown that higher printing temperatures provided better inter-layer bonding, similarly to the results of PLA [31]. The DCB test was also used by Young et al. [32] to

obtain the fracture toughness of ABS and carbon fibre reinforced ABS specimens, respectively. The authors used a Kapton insert to create a pre-crack and also composite doublers to prevent high bending of the specimen beams during the test. The  $G_{IC}$  value was calculated according to the unmodified beam theory (BT) [36]. Barile et al. [33] performed DCB tests on ABS specimens printed with different temperatures. It was again shown that higher extrusion temperatures lead to higher values of  $G_{IC}$ . Values of  $G_{IC}$  were calculated according to the unmodified BT and the modified BT (MBT) [37].

Besides printing with a single material, two or more materials can be used in FFF [38]. For example, locally reinforced parts can be produced by direct printing of fibre reinforced thermoplastics onto previously deposited neat thermoplastics. Dickson et al. [39], for example, investigated the tensile and flexural behaviour of 3D-printed parts consisting of materials with different degrees of stiffness, namely neat PA6 and continuous fibre reinforced PA6. The same material combination was additionally used by Caminero et al. [40,41] to characterise impact behaviour. Watschke et al. [42] printed specimens out of PLA and ABS for tensile, lap-shear and compression-shear tests. However, none of the presented studies investigated the cohesion between the two different 3D-printed materials in detail by FM analyses. In this regard, a particular focus should be on the cohesion between adjacent layers (inter-layer cohesion) of different materials, as for most part geometries and failure modes, the inter-layer strands exhibit a weaker cohesion than the intra-layer strands. This is due to the fact that the time between the deposition of two adjacent strands within the same layer is considerably lower than that of two strands from two contiguous layers.

Therefore, the present work aims at closing this gap by characterising the inter-layer cohesion between 3D-printed neat PLA and short carbon fibre reinforced PLA (CF-PLA) in detail, which are both easily available on the market and widely used in FFF [43]. The multi-material DCB tests are for the first time complemented in a systematic manner by cracked round bar (CRB) tests on specimens produced by FFF. The obtained results are an important step towards a better understanding of the interfacial strength of multi-materials and of novel characterisation techniques connected to additively manufactured specimens.

#### 3.2.4. Experimental

As stated above, determining properties in the  $xz$ - and  $yz$ - directions demands sophisticated experimental procedures. Therefore, digital image correlation (DIC) was used to measure strains during tensile tests and determine Young's moduli  $E_x$ ,  $E_y$ , Poisson's ratios  $\nu_{xy}$ ,  $\nu_{yx}$ ,  $\nu_{xz}$ ,  $\nu_{yz}$ , and shear moduli  $G_{xy}$ ,  $G_{yz}$ . DIC is a non-contact technique, which enables obtaining of displacement and strain fields on the sample surface from images made during the test. The work of DIC is based on the tracking of initially introduced stochastic dot pattern on the sample surface which is changing during the sample loading [44].

For DCB testing, it has to be considered that the different stiffness of beams leads to uneven bending moments during loading. This results in mix-mode I/II fracture, not desired pure mode I values [45]. The difference in stiffness could be compensated by different beam thicknesses, where the stiffer beam would be thinner than the other. However, preliminary tests

on stiffness-balanced beams (based on Euler beam theory [1]) with different bending arm thicknesses always led to almost instantaneous crack propagation within the CF-PLA bending arm. For unbalanced DCB specimens, the crack propagation remained within its initial plane longer. Therefore, further specimens were tested with DCB specimens of equally thick beams. Hereafter, DCB samples with different beam materials are named as “unbalanced” in the sense of different degrees of stiffness of the bending arms due to different material properties of PLA and CF-PLA. To fully avoid the mix-mode situation and to confirm results of the DCB tests, CRB tests were performed. The CRB test is a fracture mechanics test, where the material crack resistance could be measured over applied load and characterised by  $K_{Ic}$  [46]. Sample geometry used in Watschke et al. [42] is similar with a sample geometry required for the CRB test [47], but they did not characterise the interface adhesion in terms of FM.

A scheme of the present work is presented in Fig. 1. It also gives an overview of the results that can be expected for every test.

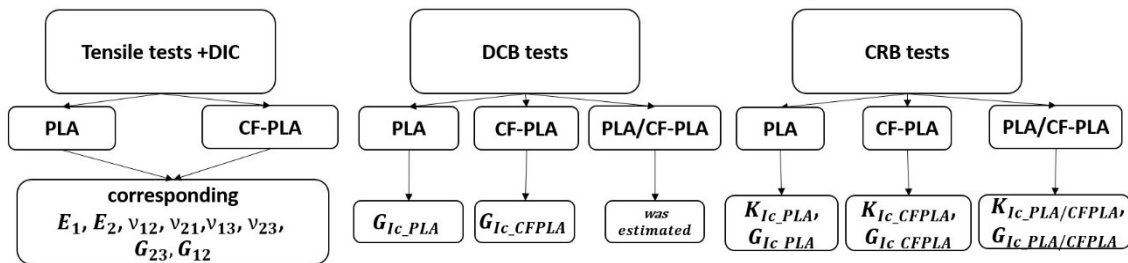


**Fig. 1.** Scheme of the present work to characterise the bonding between materials with different mechanical characteristics.

## Materials

For all tests in this manuscript, a commercially available PLA filament (Pirevo e.U., Austria) and a short carbon fibre reinforced PLA filament (CF-PLA, FFF world S.L., Spain) were used as received (not pre-dried).

## Specimen preparation

All specimens were sliced in the software Slic3r 1.2.8 by Alessandro Ranellucci and shaped on a Hage 3DpA2 (Hage Sondermaschinenbau GmbH & Co. KG, Austria) FFF printer with a dual printing head. The settings summarised in Table 2 were used for all prints, independent of the specimen type. As recommended by Ref. [48], the build platform temperature was set slightly higher than the glass transition temperatures of the filament materials (60.6 °C for PLA and 65.5 °C for CF-PLA) in order to guarantee sufficient adhesion of the first layer during printing and a defect-free removal after the finalisation of the print. The finalised specimens were removed from the build platform with a spatula and stored under standardised conditions (23 °C air temperature, 50% relative humidity) for at least 48 h until subsequent tests were performed.

**Table 2.** Printing parameters used for all specimens and both material types.

Printing parameters	
Nozzle diameter, mm	0.5
Nozzle material	Brass
Nozzle temperature, °C	230
Filament diameter, mm	1.75
Build platform temperature, °C	70
Build platform material	Glass mirror
Printing speed, mm/s	80
Layer thickness, mm	0.2

### Tensile test specimens

Dog-bone shaped specimens (Fig. 2a) of each material (PLA, CF-PLA) were printed in a horizontal position with  $0^\circ$ ,  $90^\circ$  and  $\pm 45^\circ$  raster orientations, respectively. Prior to testing, a contrast speckle pattern was applied on the specimen surface, both on the  $xy$ - (Fig. 2b) and the  $xz$ -plane (Fig. 2c) in order to conduct DIC.

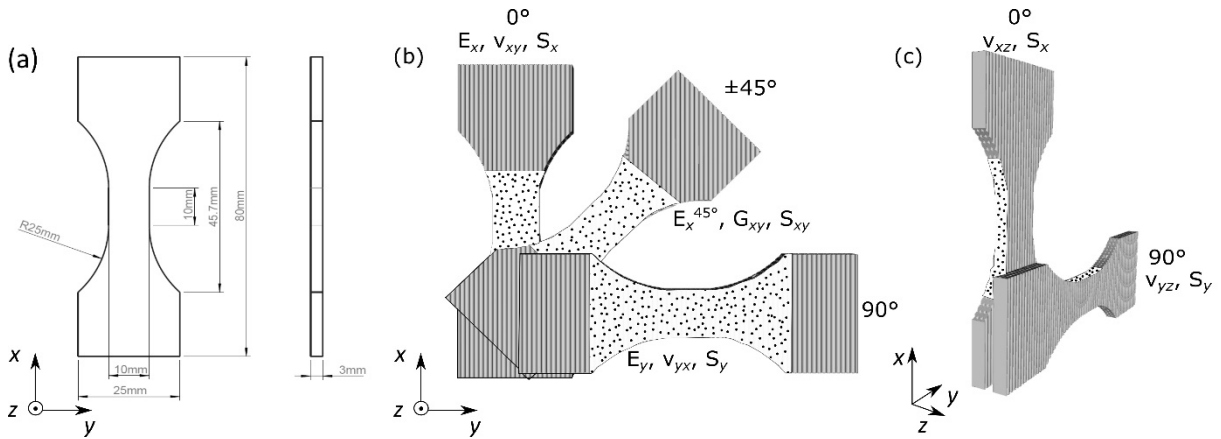


**Fig. 2.** Tensile test specimen dimensions (a) and a representation of 3D-printed specimens with an applied stochastic dot pattern to obtain strains from covered surfaces with digital image correlation in the  $xy$ - (b) and  $xz$ -plane (c). The  $\pm 45^\circ$ ,  $0^\circ$ , and  $90^\circ$  strand orientations are indicated in (b) and (c). The obtained engineering constants from each orientation are highlighted below each sample in (b) and (c). ( $S_{xy}$ ,  $S_x$ ,  $S_y$ ) refer to tensile strength of  $\pm 45^\circ$ ,  $0^\circ$ , and  $90^\circ$  specimens, respectively. The coordinate system is used throughout the present work. The  $z$ -coordinate is the direction, in which the layers are deposited upon each other.

### DCB test specimens

The specimen dimensions and the  $0^\circ$  raster orientation (along the long side of the specimen) for the DCB tests (Fig. 3a) were chosen based on Ref. [31], in which PLA specimens were successfully tested without plastic deformations in the beams. In order to initiate a crack, a Kapton separation film was inserted in the interface in a printing pause after the finalisation of the first half of the beam, as reported in on Ref. [32]. The other half of the material was printed directly after inserting 25 mm of the tape directly onto the tape. DCB specimens were produced either solely containing PLA, solely containing CF-PLA, or consisting of half CF-PLA and half PLA with the Kapton tape in between the two materials (Fig. 3b). Similarly to Ref. [31], after

printing, a hole with a diameter of 6 mm was drilled into the specimens at a distance of 20 mm from the edge to fix the specimens in the clamping system. The samples were coated on the sides with a white typewriter correction fluid for better visualisation of the crack onset. Additionally, a scale of 5 mm marks was drawn along the crack plain for measurements of the delamination length.

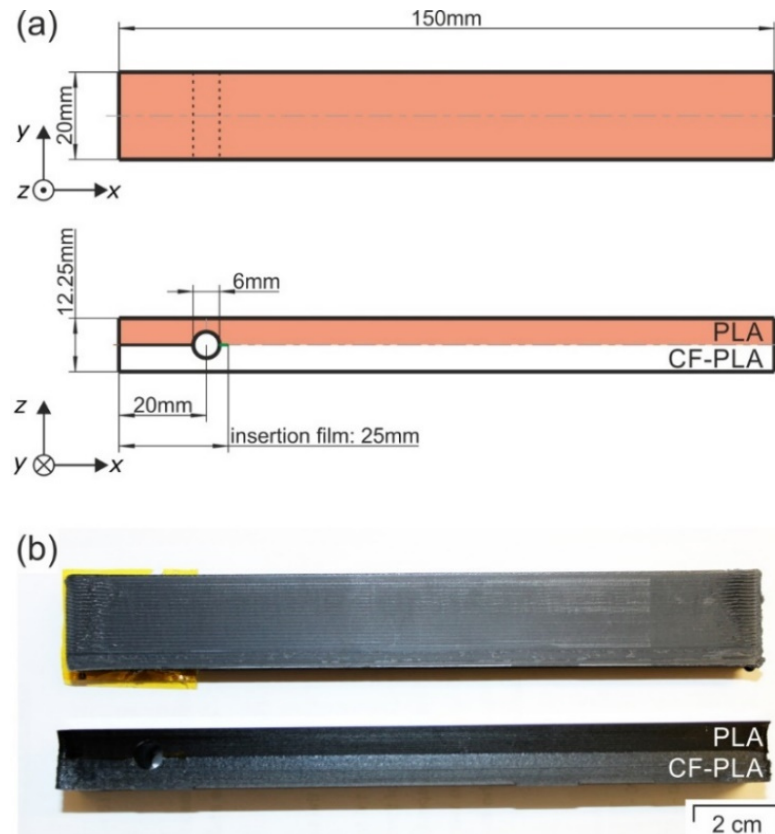


**Fig. 3.** Double cantilever beam test specimen dimensions (a) and two 3D-printed specimens (b). The  $z$ -coordinate of the coordinate system presented in (a) is the direction, in which the layers are deposited upon each other.

### CRB test specimens

CRB specimens were printed with a  $0^\circ$  raster orientation (Fig. 4a) of PLA, CF-PLA, and a combination of the two materials (Fig. 4b). For cost reasons, CF-PLA was placed onto neat PLA only in the central part of the specimens. A pre-notch was introduced along a circular cross-section in the middle of the specimens to initiate a crack exactly there. Thus, the PLA part printed on the top of the specimen does not affect the measurements. Unless stated otherwise, the pre-notch had a length of 1 mm and was introduced by a razor blade on a lathe machine as described in ISO 18489 [47].

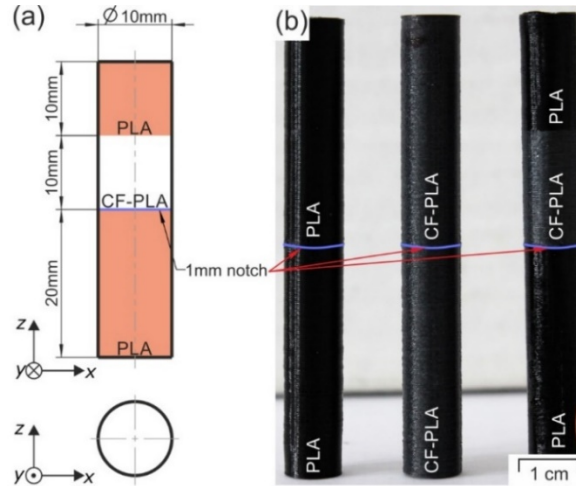


**Fig. 4.** Cracked round bar specimen dimensions of one representative set-up (a) and a representation of the three 3D-printed set-ups (b). The  $z$ -coordinate of the coordinate system presented in (a) is the direction, in which the layers are deposited upon each other.

### Testing parameters

#### Tensile tests

Tensile tests were performed on the universal testing machine Zwick Z250 (Zwick GmbH & Co. KG, Germany) equipped with a load cell of 10 kN in accordance with ASTM D 638 [49]. Five specimens for every configuration were tested under standardised laboratory conditions with an initial pre-load of 0.1 MPa and a constant head-speed of 2 mm/min till rupture. To prevent slippage in the clamping jaws, the ends of the samples were ground with sandpaper. The tensile tests were recorded and analysed at a sampling rate of 1 Hz with two 16 megapixel video cameras of the Mercury RT<sup>®</sup> system (Sobriety s.r.o., Czech Republic) for DIC. The cameras were focused on the front sample surface ( $xy$ -plain, Fig. 2b) to obtain strains  $\varepsilon_{xx}$ ,  $\varepsilon_{yy}$  for calculating  $E_x$ ,  $E_y$ ,  $\nu_{xy}$ ,  $\nu_{yx}$ ,  $G_{xy}$  and on the side surface ( $xz$ -plain, Fig. 2c) to obtain strains  $\varepsilon_{xz}$ ,  $\varepsilon_{yz}$  for calculating  $\nu_{xz}$ ,  $\nu_{yz}$ ,  $G_{yz}$ . The specimens were additionally illuminated with a monolight for better contrast.

The engineering constants of the tensile test specimens with raster angles of  $0^\circ$  and  $90^\circ$  were defined by an assumption of a transversely isotropic material behaviour due to a cylindrical shape of the strands. The obtained strains from DIC of these specimens were used for calculating Poisson's ratios  $\nu_{xy}$ ,  $\nu_{yx}$ ,  $\nu_{xz}$ ,  $\nu_{yz}$ , Young's moduli  $E_x$ ,  $E_y$ , and the shear modulus  $G_{yz}$  (Fig. 2b and Fig. 2c) according to Eq. 1-3, respectively [50].

$$\nu_{ij} = -\frac{\Delta\varepsilon_j}{\Delta\varepsilon_i} \quad (1)$$

$$E_i = \frac{\Delta\sigma_i}{\Delta\varepsilon_i} \quad (2)$$

$$G_{yz} = \frac{E_2}{2 * (1 + \nu_{23})} \quad (3)$$



in which  $\nu_{ij}$  refers to the Poisson's ratio,  $\Delta\varepsilon_j$  to a difference in lateral strain between the two longitudinal strain points,  $\Delta\varepsilon_i$  to a difference between the two longitudinal strain points,  $\Delta\sigma_i$  to a difference in applied tensile stress between the two strain points, and  $E_i$  to the Young's modulus. The values were evaluated from the linear elastic section of the stress-strain curves according to ATSM D 638 and with  $\Delta\varepsilon_i$  of 0.2%.

Based on the strains obtained from testing the samples with a raster angle of  $\pm 45^\circ$ , the Young's modulus  $E_x^{45^\circ}$  was calculated according to Eq. 2 and was additionally used for defining the shear modulus  $G_{xy}$  according to Eq. 4 [51].

$$G_{xy} = \frac{E_x^{45^\circ} * E_x * E_y}{4 * E_x * E_y - E_x^{45^\circ} * (E_y - 2 * \nu_{xy} * E_y + E_x)} \quad (4)$$

### DCB tests

The DCB tests were performed on the servo-hydraulic test machine MTS 810 (MTS Systems Corporation, Germany) with a 25 kN load cell according to ASTM D 5528. Four PLA, four CF-PLA and five unbalanced specimens were tested. The tests were done under standardised laboratory conditions. After applying an initial load, which is required to create a pre-crack within the material and exclude the influence of the separation film, the specimens were tested at 10 mm/min under displacement control until a delamination of about 100 mm. The delamination was observed with a magnifying glass and recorded along with the applied forces for every crack increment of 5 mm.

The  $G_{Ic}$  values were calculated based on the modified beam theory (MBT) [37] according to Eq. 5. On the contrary to the recommendation of the standard ASTM D 5528, the factors accounting for large displacements and influences of the loading blocks were neglected, as the used gripping system was different from the standard blocks and piano hinges.

$$G_{Ic} = \frac{3P\delta}{2B(a + |\Delta|)} \quad (5)$$

in which  $P$  refers to the applied load,  $\delta$  to the displacement,  $B$  to the specimen width,  $a$  to the delamination length, and  $|\Delta|$  to the  $x$ -intercept of the cube root of compliance,  $C^{1/3}$ , plotted over the delamination length,  $a$ .

### CRB tests

The CRB tests were performed on the servo-hydraulic testing machine MTS 858 (MTS Systems Corporation, Germany) with a 15 kN load cell under standardised laboratory conditions. After clamping the specimens in the bottom grip under displacement control and the upper part under load control, five specimens for every configuration were tested in displacement control with a testing speed of 10 mm/min.

The resulting  $K_{Ic}$  values were calculated according to Eq. 6 (Benthem and Koiter [52]), which has been successfully applied in other research works [53,54]. However, in the stated literature the formula has been used in cyclic tests, but in the present work it is applied for a

monotonic test. This means that the  $a$  value, as the current crack length, is equal to the initial length of the pre-notch.

$$K_{Ic} = \frac{P}{\pi * b^2} * \sqrt{\frac{\pi * a * b}{R}} * f(b/R) \quad (6)$$

$$f(b/R) = \frac{1}{2} \left[ 1 + \frac{1}{2} * \frac{b}{R} + \frac{3}{8} * \left(\frac{b}{R}\right)^2 - 0.363 * \left(\frac{b}{R}\right)^3 + 0.731 * \left(\frac{b}{R}\right)^4 \right]$$

$b = R - a$

in which  $R$  refers to the specimen radius, and  $b$  to the ligament radius.

Based on the assumption that the CRB specimens nearly have plain strain conditions [55],  $G_{Ic}$  can be calculated as the following [1]:

$$G_{Ic} = \frac{(1 - \nu^2) * K_{Ic}^2}{E} \quad (7)$$

### Optical analyses

After the DCB tests, the specimens were cryo-fractured to evaluate the fractured area by means of optical microscopy. The CRB specimens did not require any specific fracture surface preparations and were examined directly after testing. Micrographs of fractured surfaces of the DCB and CRB specimens were made with the optical microscope Olympus SZX12 (Olympus Corporation, Japan).

#### 3.2.5. Results and discussion

### Engineering constants from the tensile tests

The engineering constants obtained from the tensile tests are summarised in Table 3. As expected from the high degree of fibre orientation during extrusion and 3D-printing [7], CF-PLA specimens printed with the  $0^\circ$  raster angle are found to be stiffer than the neat PLA specimens. The presence of carbon fibres makes the matrix stiffer and more brittle by locally constraining the matrix. The Young's moduli of all raster orientations of PLA have nearly the same values. This means that the raster orientation did not influence PLA stiffness that much as in case of CF-PLA, where  $0^\circ$  specimens of CF-PLA have the highest Young's modulus. The higher  $E_x$  value of CF-PLA and nearly the same  $\nu_{xz}$  values of PLA and CF-PLA led to a higher value of  $G_{xz}$  for CF-PLA. In  $0^\circ$  orientation, CF-PLA specimens were up to 35% stiffer than PLA specimens. Obtained results are in good agreement with Ref. [56], where tensile properties of PLA and short carbon fibre reinforced PLA were investigated.

In DIC, the strains were obtained from the middle area of the specimen planes, where filaments are more constrained by each other in specimen width ( $xy$ -plane) than in specimen thickness ( $xz$ -plane). Therefore, for PLA and CF-PLA specimens,  $\nu_{xz}$  is higher than  $\nu_{xy}$  due to the less pronounced constriction in the  $y$ -direction of the  $xy$ -plane than in the  $z$ -direction of the  $xz$ -plane. The same implies to  $\nu_{yz}$  and  $\nu_{yx}$ . The different values of Poisson's ratios in

different planes prove the non-isotropic behaviour of printed parts as it was also discussed in Ref. [5,57].

In contrast to Ref. [56], the present specimens showed nearly the same strength values for PLA and CF-PLA independent of the raster angle. The similarities in strength may indicate that optimal printing parameters were used in the present work that provide a better bonding between the strands [31]. Short carbon fibres did not improve the strength significantly, as it was expected from Ref. [58], but rather slightly deteriorated it, similarly to Ref. [56]. This implies that loads were carried mostly by the matrix without means of load transfer to the fibre-matrix. However, PLA and CF-PLA filaments used in the present study were provided by different suppliers, so the PLA matrices themselves could have slightly different mechanical properties.

**Table 3.** Engineering constants of the PLA and CF-PLA tensile test samples calculated from strains obtained by DIC.

Property	PLA	CF-PLA
$E_x$ (MPa)	3280±80	4426±70
$E_y$ (MPa)	3443±50	3579±126
$E_x^{45^\circ}$ (MPa)	3464±65	3467±210
$\nu_{xy}$	0.3±0.01	0.33±0.01
$\nu_{xz}$	0.37±0.01	0.35±0.02
$\nu_{yx}$	0.32±0.01	0.28±0.2
$\nu_{yz}$	0.35±0.01	0.33±0.01
$G_{xy}$ (MPa)	1337±40	1249±110
$G_{yz}$ (MPa)	1273±18	1349±48
$S_x$ (MPa)	56±1	52±3
$S_y$ (MPa)	53±2	51±1
$S_{xy}$ (MPa)	59±2	56±2

Obtained engineering parameters (Table 3) can be directly used as input parameters in FEM of mechanical behaviour of PLA and CF-PLA printed parts with an assumption of transversely isotropic material behaviour.

### Results of the experimental DCB tests

The obtained crack resistance curves are presented in Fig. 5a, where the mean-lines represent a trend of the fracture behaviour of the specimens. The crack propagation in the PLA specimens can be divided in three distinctive zones, and for CF-PLA in two zones, as highlighted in Fig. 5a. The corresponding zones are also marked in Fig. 5b of the fracture surfaces. For both materials, the first zone corresponds to a decrease of  $G_{Ic}$  due to a high plasticity at the beginning of the pre-cracks created at the initial loading (Fig. 5b). Especially for PLA, the strong decrease of  $G_{Ic}$  is in accordance with the whitish pre-crack areas in the fracture surfaces (Fig. 5b and Fig. 5c). High plasticity at the pre-crack tip leads to a higher amount of energy released at the beginning of the tests to further extent delamination over the pre-crack area. Zone II of PLA, which lies in between 40 mm and 75 mm of the delamination, exhibits a more stable behaviour, which corresponds to steady crack propagation. In this area,  $G_{Ic}$  of PLA and CF-PLA can be estimated to 2400±280 J/m<sup>2</sup> and 1160±210 J/m<sup>2</sup>, respectively. After roughly 75 mm of the crack

length (zone III),  $G_{Ic}$  of PLA increases due to the same reason of plasticity in the crack front. On the other hand,  $G_{Ic}$  of CF-PLA specimens reveals a more stable behaviour during the tests due to a higher embrittlement, because of the presence of carbon fibres. Thus, less energy dissipates through plastic deformations at the crack tip. As a result, the CF-PLA fracture surfaces do not exhibit visible crack fronts after the pre-crack (Fig. 5d and Fig. 5e) in contrast to PLA. The overall higher scatter of PLA compared to CF-PLA can be explained by the fact that cracks in PLA are more prone to deviate into different layers (Fig. 5b and Fig. 5d).

$G_{Ic}$  for PLA was obtained in Ref. [31], but only by the area method without reporting crack resistance curves. The reported value of  $2800 \text{ J/m}^2$  is in good correlation with the present result. However, similar crack resistance curves were reported in Ref. [32] for 3D-printed ABS and CF-ABS DCB specimens. In this study, there was no significant decrease of  $G_{Ic}$  for neat ABS at the beginning of the crack, which can be explained by different material properties and printing parameters.

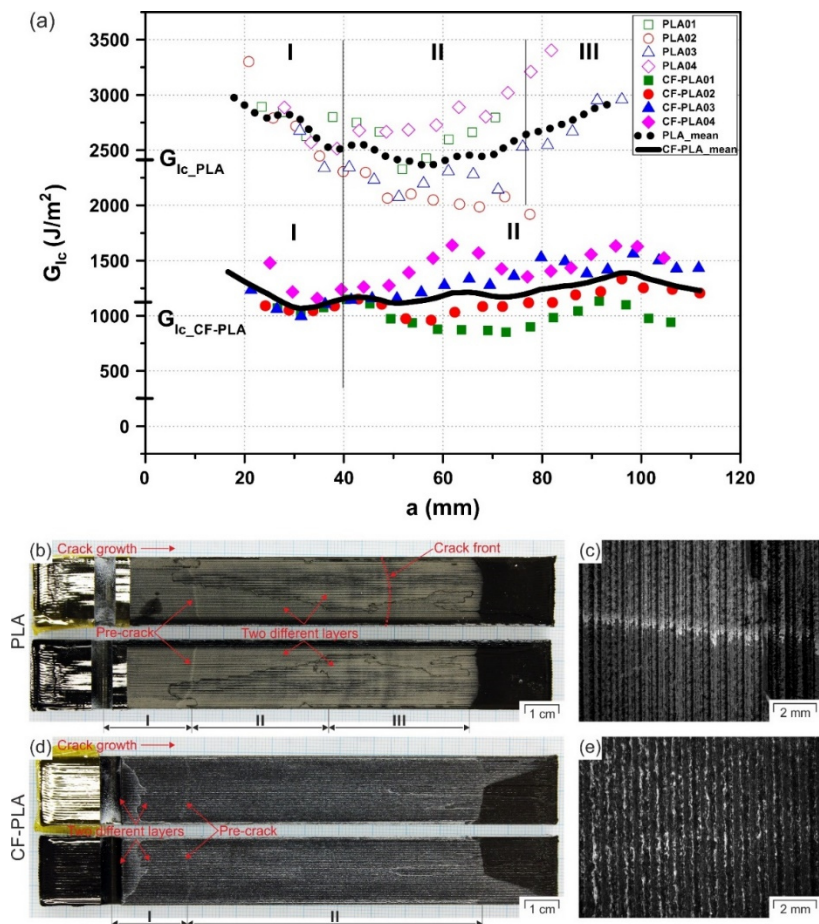


**Fig. 5.** Crack resistance curves of tested DCB specimens of PLA and CF-PLA according to the modified beam theory (a) and fracture surfaces of the tested DCB specimens of PLA (b, c) and CF-PLA (d, e). To visualise the pre-crack, a representation of higher magnification is given in (c) for PLA and (e) for CF-PLA. In (b), the dashed line serves as a facilitation of the visibility of the crack front. In (b) and (d), the right dark spots represent the cryo-fracture for the separation of the two beams.

Although the area method does not give full understanding of the material crack resistance, it was used to confirm and complement the MBT results. The  $G_{Ic}$  values were calculated method according to Eq.8

$$G_{Ic} = \frac{A}{a * B} * 10^3 \left[ \frac{J}{m^2} \right] \quad (8)$$

in which  $A$  refers to the energy required to reach the total propagated crack length, which is equal to the area under the load-displacement curve (Fig. 6),  $a$  to the delamination length, and  $B$  to the specimen width [35]. The areas of the fractured surfaces were measured in ImageJ software as the area between the initial pre-crack and the final crack fronts (Fig. 5b). The results are in good agreement ( $2308 \pm 235 \text{ J/m}^2$  for PLA and  $1093 \pm 171 \text{ J/m}^2$  for CF-PLA) with those obtained by the MBT ( $2400 \pm 280 \text{ J/m}^2$  for PLA and  $1160 \pm 210 \text{ J/m}^2$  for CF-PLA).

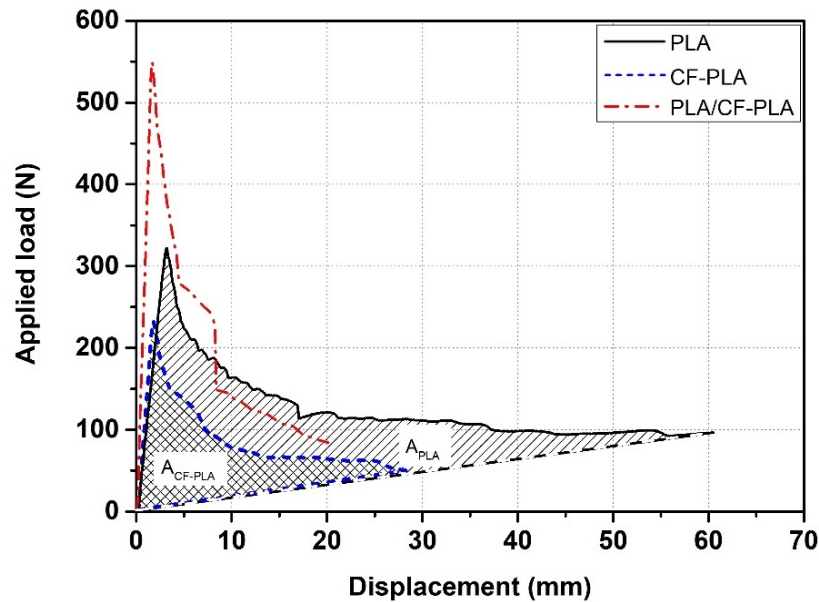


**Fig. 6.** Force-displacement curves from the DCB tests of PLA, CF-PLA and PLA/CF-PLA specimens.  $A_{PLA}$  and  $A_{CF-PLA}$  refer to the area under the corresponding force-displacement curves.

In PLA and CF-PLA specimens, the delamination always deviated out of the crack plane into adjacent layers (Fig. 5b and Fig. 5d). This effect was also observed for the same type of PLA for DCB specimens in Ref. [31] and for CT specimens in Ref. [24]. This indicates the use of optimal printing parameters for the specimens. Otherwise, the crack would have propagated within the interface between two layers.

Unbalanced DCB specimens with one beam of CF-PLA and the other of neat PLA always revealed crack propagation into the CF-PLA beam (Fig. 7a). After passing the separation film, the crack deflected immediately through several CF-PLA layers and propagated in the CF-PLA part (Fig. 7b), instead of a continuous propagation in the PLA/CF-PLA interface. This trend can also be confirmed by fracture micrographs (Fig. 7c), in which both fracture surfaces reveal carbon fibres. The force required to open the beams was more than twice as high as in the CF-PLA specimens (Fig. 6). This can be explained by the larger amount of fracture surface, created by

the crack growing in different layers (Fig. 7b), as well as the fact that the crack was not able to grow within its favoured trajectory (pure mode I). Instead it had to deviate towards the CF-PLA beam due to its lower  $G_{Ic}$ . This deviation from pure mode I into mix-mode I/II needs a higher force and energy at the beginning of the tests. A similar deflection of the delamination from the initial trajectory was observed in Ref. [18]. The crack in the specimens printed out of a PLA blend grew in one of the specimen's beams. This was explained by the enhanced cohesion between beams by means of the ameliorated material. The model of the crack behaviour between two dissimilar materials was presented in Ref. [59], where two possible delamination scenarios are postulated. The first is the crack propagation within the interface, and the second is the crack penetration to the other layer. The comparison of energy release ratios of those cases with the fracture energy of the interface defined the crack behaviour. Therefore, the exhibited behaviour implies that the bonding between PLA and CF-PLA layers is stronger than between CF-PLA layers. This leads to the conclusion that the PLA/CF-PLA interface fracture toughness is equal or higher than the CF-PLA toughness. To verify the DCB results and fully exclude a possibility of the mix-mode fracture, CRB tests were performed.

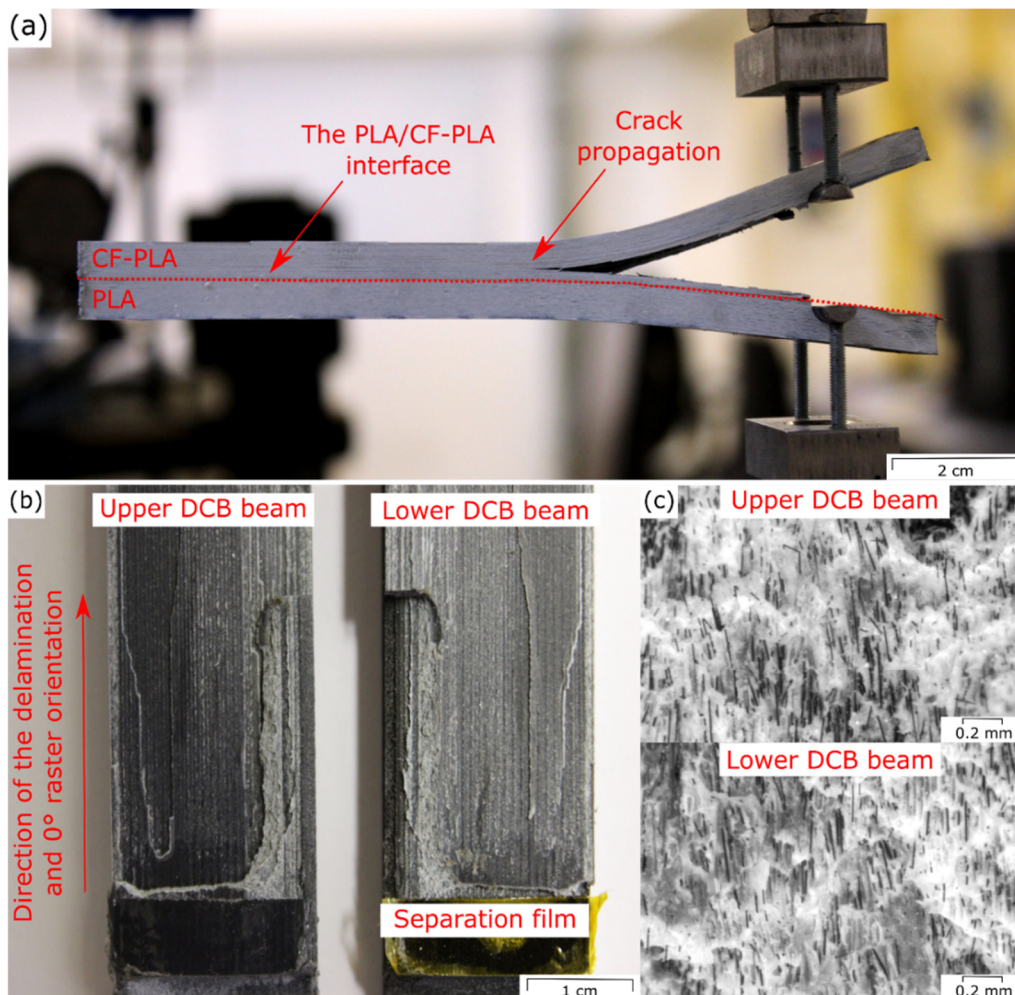


**Fig. 7.** Delamination in the CF-PLA part of an unbalanced DCB sample (a), the fracture between the beams (b), and corresponding micrographs (c).

**$K_{Ic}$  and  $G_{Ic}$  obtained from the CRB specimens**

Results of the CRB tests are presented in Table 4. The  $G_{Ic}$  results obtained for CF-PLA from the CRB tests are in good correlation with the results of the DCB tests, because the CRB specimens fractured, similarly to the DCB specimens in the pre-notched planes (Fig. 8c and Fig. 8d). Moreover, the fracture of all CRB specimens starts with a localised area of plastically deformed material in the direct vicinity of the crack tip similarly to the DCB tests (Fig. 5b), as can be seen by the white fracture surfaces (Fig. 8a, Fig. 8c, Fig. 8e, and Fig. 8g). For PLA, however, the CRB tests resulted in insignificantly lower values of  $G_{Ic}$  than the DCB tests,  $2002 \pm 145 \text{ J/m}^2$  and  $2400 \pm 280 \text{ J/m}^2$ , respectively. This deviation of about 20% can be explained by a higher amount of energy released in the DCB test, since the crack propagated within different layers, whereas the crack in the CRB specimen propagated between two layers in the pre-notched plane without any trajectory change (Fig. 8a and Fig. 8b). Additionally, the CRB specimen has the benefit of a circumferential notch hindering the formation of a plane stress state at the side surface of the specimen, as is the case for the DCB samples. While for a rather brittle material (CF-PLA), this difference in stress states might not significantly influence the results, it could be a reason for the difference for neat PLA. A strong indication for this are the semi-elliptical, stress whitened striations, which appeared on the DCB samples of neat PLA, but not for CF-PLA (Fig. 5b). The differences in  $K_{Ic}$  between the present work ( $2.69 \pm 0.10 \text{ MPa}\cdot\text{m}^{1/2}$ ) and Ref. [24] (roughly  $5 \text{ MPa}\cdot\text{m}^{1/2}$ ) of the same neat PLA can be related to the difference of 20 °C of the used nozzle temperature. This is one more confirmation that higher temperatures lead to better fusion and improve the inter-layer cohesion.

**Table 4.** The parameters for calculating  $K_{Ic}$  and  $G_{Ic}$  from the CRB test specimens of the four investigated material combinations. Different pre-notch lengths are designated by  $\_X\text{mm}$ , in which X refers to the pre-notch length. For PLA/CF-PLA specimens, the Young's modulus was assumed to be equal to the Young's modulus of CF-PLA, because the specimens were fractured in the CF-PLA part.

Material	$a_0$ , mm	$b$ , mm	$f(b/R)$	$F_{max}$ , N	$K_{Ic}$ , $\text{MPa}\cdot\text{m}^{1/2}$	$G_{Ic}$ , $\text{J/m}^2$
PLA_1mm	$1.0 \pm 0.1$	$4.1 \pm 0.1$	$0.87 \pm 0.02$	$3201 \pm 94$	$2.69 \pm 0.10$	$2002 \pm 145$
CF-PLA_1mm	$1.3 \pm 0.0$	$4.0 \pm 0.0$	$0.84 \pm 0.01$	$2552 \pm 44$	$2.34 \pm 0.05$	$1104 \pm 48$
PLA/CF-PLA_1mm	$0.9 \pm 0.1$	$4.3 \pm 0.1$	$0.91 \pm 0.01$	$3424 \pm 102$	$2.54 \pm 0.09$	$1304 \pm 94$
PLA/CF-PLA_1.5mm	$1.6 \pm 0.1$	$3.7 \pm 0.1$	$0.80 \pm 0.01$	$2393 \pm 125$	$2.54 \pm 0.11$	$1301 \pm 116$

The multi-material CRB test specimens with a pre-notch of 1 mm (PLA/CF-PLA\_1mm) did not fail in the pre-notched plane, but immediately deflected towards an adjacent CF-PLA layer (Fig. 8e), as the notch of 1 mm was not enough to initiate the failure in the pre-notched plane. Therefore, the fracture surface of both halves of the CRB specimen contain CF (Fig. 8f and Fig. 8f') that are oriented along the printing orientation, similarly to the DCB tests (Fig. 7c). The fibre orientation along the filament placement was also reported in Refs. [7,56]. This finding additionally confirms the better adhesive strength between PLA and CF-PLA layers compared to between CF-PLA and CF-PLA layers. To overcome this failure behaviour, additional specimens with a deeper notch of 1.5 mm were produced (Fig. 8g). The resulting specimens reveal a fracture surface, in which the crack stayed for most of the testing time as intended between the two different materials (Fig. 8g). However, towards the end of testing, the crack deflected again

towards the weaker CF-PLA interface (Fig. 8h). Due to this fracture deflections, both multi-material CRB specimens (PLA/CF-PLA\_1mm and PLA/CF-PLA\_1.5mm) led to about 20% higher  $G_{IC}$  values than the pure CF-PLA specimens (Table 4).

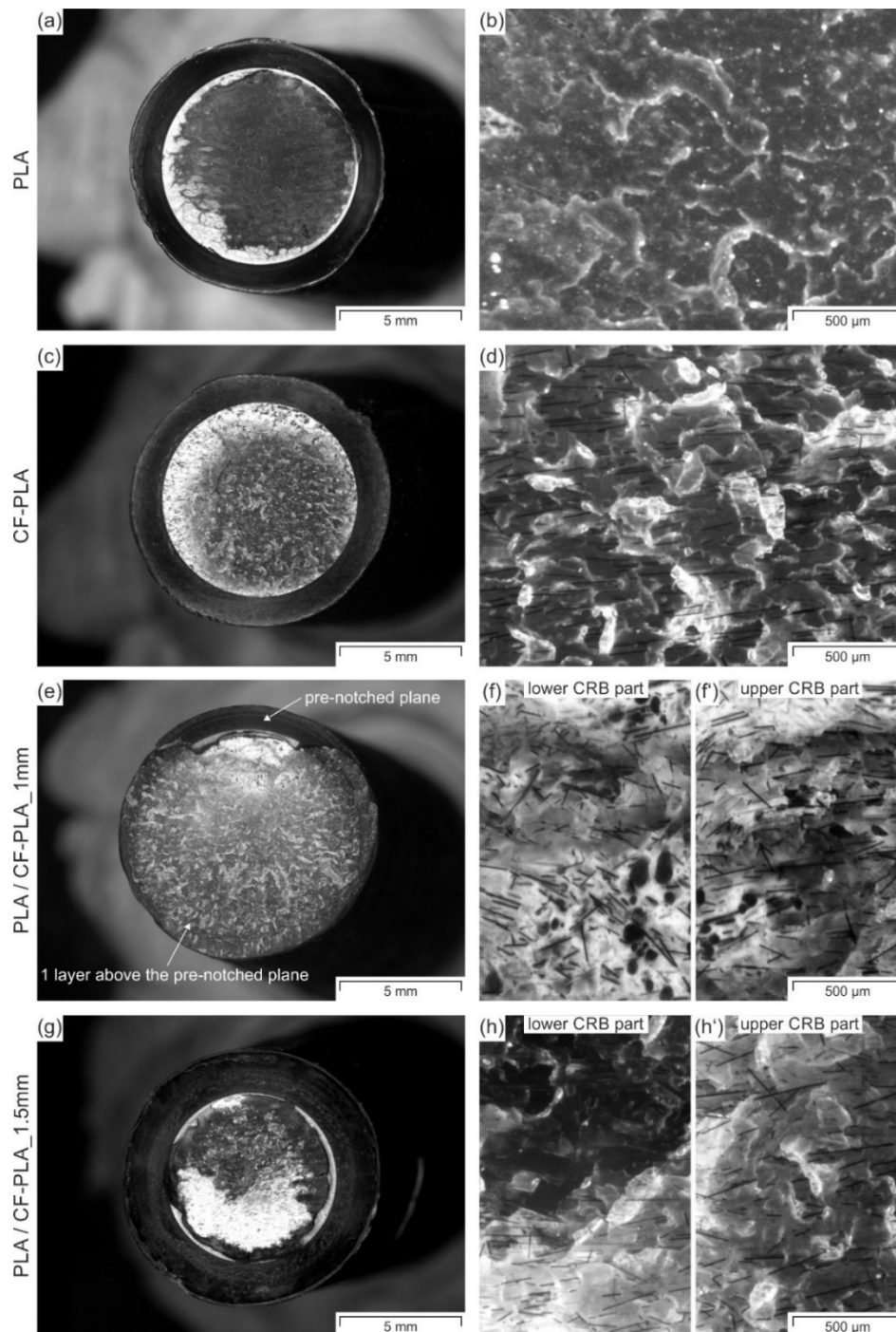


**Fig. 8.** Fracture surfaces of the tested CRB specimens PLA/PLA (a, b), CF-PLA/CF-PLA (c, d), PLA/CF-PLA\_1mm (e, f), and PLA/CF-PLA\_1.5mm (g, h). The suffix \_Xmm refers to the pre-notch length. For the multi-material parts, the magnified images represent the fracture surfaces of the lower (f, h) and the upper CRB part halves (f', h'), respectively.



### 3.2.6. Conclusion

The present work focused on the bonding characterisation between parts produced by FFF. For the first time, fracture mechanical techniques were used to characterise the inter-layer bonding between two materials of different degrees of stiffness. Tensile, double cantilever beam (DCB), and crack round bar (CRB) tests were performed on specimens made of PLA and short carbon fibre reinforced PLA (CF-PLA), and a combination of both materials. Besides obtaining engineering parameters in the  $xy$ - and  $yx$ - planes, the tensile tests were performed with the help of DIC to obtain strains from the side of the samples ( $xz$ - and  $yz$ -planes). These values were required for calculations of Poisson's ratios and shear moduli in the corresponding directions, which are usually missing in literature, but are necessary for accurate finite element modelling of parts printed with reinforced materials.

Independent of the calculation method employed (modified beam theory or area method),  $G_{Ic}$  obtained by the DCB tests of PLA were approximately twice as high as that of CF-PLA, with 2400 J/m<sup>2</sup> against 1160 J/m<sup>2</sup>, respectively. This is due to the local matrix constraint in the vicinity of the CF. The multi-material DCB samples did not break in the interface, but the crack always deflected towards and propagated in the stiffer and more brittle CF-PLA layers, as the interface PLA/CF-PLA was stronger than CF-PLA/CF-PLA. To fully exclude the mix-mode fracture, CRB tests on PLA, CF-PLA and their combinations were performed and were found to be in agreement with the DCB results for the more brittle CF-PLA. For neat PLA,  $G_{Ic}$  values obtained by the CRB tests were 20% lower than for the DCB test, which might be due to the circumferential notch, which prohibits plane stress conditions. The CRB test revealed to be a promising technique to characterise the fracture toughness of 3D-printed specimens. It can be recommended as a less time and effort consuming testing technique than the DCB test, in terms of both specimen manufacturing and testing. Especially for the multi-material parts, the CRB tests seemed promising, since a change in the pre-notch length could regulate the crack propagation to mainly remain in the interface. Therefore, this technique can be successfully used to determine  $G_{Ic}$  of the multi-material specimens.

Future studies could focus on further inter-layer characterisations of specimens produced by FFF in terms of fracture mechanics, for instance, by mode II, or mode I/II testing. In addition, mechanical parameters defined in the present work could be used as input parameters in finite element modelling of structurally loaded parts, made from these materials by means of FFF.

### Acknowledgements

The research work was performed within the COMET-project VI-2.06 "New strategies towards laser assisted manufacturing of fibre reinforced thermoplastic composites" at the Polymer Competence Center Leoben GmbH (PCCL, Austria) within the framework of the COMET-program of the Federal Ministry for Transport, Innovation and Technology and the Federal Ministry of Science, Research and Economy with contributions by Technical University of Munich (Lehrstuhl für Carbon Composites), Montanuniversitaet Leoben (Institute of Material Science and Testing of Polymers), Boeing and AFPT. The PCCL is funded by the Austrian Government and the State

Governments of Styria, Lower Austria and Upper Austria. Martin Spoerk was funded by the Austrian Research Promotion Agency as part of the AddManu project (“Staerkung der oesterreichischen Wertschoepfungsketten für generative Fertigung in der industriellen Produktion”, grant agreement 849297) and by the European Union’s Horizon 2020 research and innovation programme as part of the INEX-ADAM project (grant agreement 810708). Special thanks go to Christof Lichal, Ivan Raguž and Franz Grassegger for the assistance in printing of samples and their preparation for testing, Isabelle Berger for the CRB testing, and Astrid Elisabeth Macher for the DSC measurements.

### 3.2.7. References

- [1] Anderson TL (2017) Fracture mechanics: fundamentals and applications. CRC press.
- [2] Attaran M. The rise of 3-D printing: The advantages of additive manufacturing over traditional manufacturing. *Bus Horiz* 2017;60(5):677–88.
- [3] Ford S, Despeisse M. Additive manufacturing and sustainability: An exploratory study of the advantages and challenges. *J Clean Prod* 2016;137:1573–87.
- [4] Weller C, Kleer R, Piller FT, Hinke C. Economic Implications of 3D Printing: Market Structure Models Revisited. *AMPROC* 2014;2014(1):10947.
- [5] Ahn S-H, Montero M, Odell D, Roundy S, Wright PK. Anisotropic material properties of fused deposition modeling ABS. *Rapid Prototyp J* 2002;8(4):248–57.
- [6] Kalsoom U, Nesterenko PN, Paull B. Recent developments in 3D printable composite materials. *RSC Adv.* 2016;6(65):60355–71.
- [7] Spoerk M, Savandaiah C, Arbeiter F, Traxler G, Cardon L, Holzer C et al. Anisotropic properties of oriented short carbon fibre filled polypropylene parts fabricated by extrusion-based additive manufacturing. *Compos Part A Appl Sci Manuf* 2018;113:95–104.
- [8] Spoerk M, Savandaiah C, Arbeiter F, Sapkota J, Holzer C. Optimization of mechanical properties of glass-spheres-filled polypropylene composites for extrusion-based additive manufacturing. *Polym. Compos.* 2017;83:768.
- [9] Kaynak B, Spoerk M, Shirole A, Ziegler W, Sapkota J. Polypropylene/Cellulose Composites for Material Extrusion Additive Manufacturing. *Macromol. Mater. Eng.* 2018;303(5):1800037.
- [10] Spoerk M, Arbeiter F, Raguž I, Weingrill G, Fischinger T, Traxler G et al. Polypropylene Filled With Glass Spheres in Extrusion-Based Additive Manufacturing: Effect of Filler Size and Printing Chamber Temperature. *Macromol. Mater. Eng.* 2018;303(7):1800179.
- [11] Spoerk M, Gonzalez-Gutierrez J, Lichal C, Cajner H, Berger G, Schuschnigg S et al. Optimisation of the Adhesion of Polypropylene-Based Materials during Extrusion-Based Additive Manufacturing. *Polymers* 2018;10(5):490.
- [12] Bogue R. 3D printing: The dawn of a new era in manufacturing? *Assembly Autom* 2013;33(4):307–11.
- [13] Petrovic V, Vicente Haro Gonzalez J, Jordá Ferrando O, Delgado Gordillo J, Ramón Blasco Puchades J, Portolés Griñan L. Additive layered manufacturing: Sectors of industrial application shown through case studies. *Int J Prod Res* 2010;49(4):1061–79.
- [14] Guo N, Leu MC. Additive manufacturing: Technology, applications and research needs. *Front. Mech. Eng.* 2013;8(3):215–43.
- [15] Berman B. 3-D printing: The new industrial revolution. *Bus Horiz* 2012;55(2):155–62.

- [16] Brenken B, Barocio E, Favaloro A, Kunc V, Pipes RB. Fused filament fabrication of fiber-reinforced polymers: A review. *Additive Manufacturing* 2018;21:1–16.
- [17] J.M. Whitney, C.E. Browning, and W. Hoogsteden. A Double Cantilever Beam Test for Characterizing Mode I Delamination of Composite Materials. *JRPC* 1982;1(4):297–313.
- [18] Levenhagen NP, Dadmun MD. Bimodal molecular weight samples improve the isotropy of 3D printed polymeric samples. *Polymer* 2017;122:232–41.
- [19] Davis CS, Hillgartner KE, Han SH, Seppala JE. Mechanical strength of welding zones produced by material extrusion additive manufacturing. *Addit. Manuf.* 2017;16:162–6.
- [20] Griffiths CA, Howarth J, Almeida-Rowbotham G, Rees A. A design of experiments approach to optimise tensile and notched bending properties of fused deposition modelling parts. *Proc. Inst. Mech. Eng., Part B* 2016;230(8):1502–12.
- [21] Torres J, Cole M, Owji A, DeMastry Z, Gordon AP. An approach for mechanical property optimization of fused deposition modeling with polylactic acid via design of experiments. *Rapid Prototyp. J.* 2016;22(2):387–404.
- [22] Hart KR, Wetzel ED. Fracture behavior of additively manufactured acrylonitrile butadiene styrene (ABS) materials. *Eng. Fract. Mech.* 2017;177:1–13.
- [23] Song Y, Li Y, Song W, Yee K, Lee K-Y, Tagarielli VL. Measurements of the mechanical response of unidirectional 3D-printed PLA. *Mater. Des.* 2017;123:154–64.
- [24] Arbeiter F, Spoerk M, Wiener J, Gosch A, Pinter G. Fracture mechanical characterization and lifetime estimation of near-homogeneous components produced by fused filament fabrication. *Polym Test* 2018;66:105–13.
- [25] McLouth TD, Severino JV, Adams PM, Patel DN, Zaldivar RJ. The impact of print orientation and raster pattern on fracture toughness in additively manufactured ABS. *Addit. Manuf.* 2017;18:103–9.
- [26] Arif MF, Kumar S, Varadarajan KM, Cantwell WJ. Performance of biocompatible PEEK processed by fused deposition additive manufacturing. *Mater. Des.* 2018;146:249–59.
- [27] Gardan J, Makke A, Recho N. Improving the fracture toughness of 3D printed thermoplastic polymers by fused deposition modeling. *Int J Fract* 2018;210(1-2):1–15.
- [28] Papon EA, Haque A. Fracture toughness of additively manufactured carbon fiber reinforced composites. *Additive Manufacturing* 2019;26:41–52.
- [29] Koissin V, Warnet LL, Akkerman R. Delamination in carbon-fibre composites improved with in situ grown nanofibres. *Eng Fract Mech* 2013;101:140–8.
- [30] Aliheidari N, Christ J, Tripuraneni R, Nadimpalli S, Ameli A. Interlayer adhesion and fracture resistance of polymers printed through melt extrusion additive manufacturing process. *Mater. Des.* 2018;156:351–61.
- [31] Spoerk M, Arbeiter F, Cajner H, Sapkota J, Holzer C. Parametric optimization of intra- and inter-layer strengths in parts produced by extrusion-based additive manufacturing of poly(lactic acid). *J. Appl. Polym. Sci.* 2017;134(41):45401.
- [32] Young D, Wetmore N, Czabaj M. Interlayer fracture toughness of additively manufactured unreinforced and carbon-fiber-reinforced acrylonitrile butadiene styrene. *Addit. Manuf.* 2018;22:508–15.
- [33] Barile C, Casavola C, Cazzato A. Acoustic Emissions in 3D Printed Parts under Mode I Delamination Test. *Materials* 2018;11(9).
- [34] ASTM D5528-13, Standard Test Method for Mode I Interlaminar Fracture Toughness of Unidirectional Fiber-Reinforced Polymer Matrix Composites.
- [35] DIN, EN. "6033.", 1996. Bestimmung der interlaminaren Energiefreisetzungsrates Mode I.

- [36] Hashemi S, Kinloch AJ, Williams JG. The Analysis of Interlaminar Fracture in Uniaxial Fibre-Polymer Composites. *Proc R Soc Lond* 1990;427(1872):173–99.
- [37] Williams JG. On the calculation of energy release rates for cracked laminates. *Int J Fract* 1988;36(2):101–19.
- [38] Bandyopadhyay A, Heer B. Additive manufacturing of multi-material structures. *Materials Science and Engineering: R: Reports* 2018;129:1–16.
- [39] Dickson AN, Barry JN, McDonnell KA, Dowling DP. Fabrication of continuous carbon, glass and Kevlar fibre reinforced polymer composites using additive manufacturing. *Addit. Manuf.* 2017;16:146–52.
- [40] Caminero MA, Chacón JM, García-Moreno I, Rodríguez GP. Impact damage resistance of 3D printed continuous fibre reinforced thermoplastic composites using fused deposition modelling. *Compos B Eng* 2018;148:93–103.
- [41] Caminero MA, Chacón JM, García-Moreno I, Reverte JM. Interlaminar bonding performance of 3D printed continuous fibre reinforced thermoplastic composites using fused deposition modelling. *Polym Test* 2018;68:415–23.
- [42] Watschke H, Waalkes L, Schumacher C, Vietor T. Development of Novel Test Specimens for Characterization of Multi-Material Parts Manufactured by Material Extrusion. *Applied Sciences* 2018;8(8):1220.
- [43] Farah S, Anderson DG, Langer R. Physical and mechanical properties of PLA, and their functions in widespread applications - A comprehensive review. *Adv Drug Deliv Rev* 2016;107:367–92.
- [44] Mehdikhani M, Aravand M, Sabuncuoglu B, Callens MG, Lomov SV, Gorbatikh L. Full-field strain measurements at the micro-scale in fiber-reinforced composites using digital image correlation. *Compos Struct* 2016;140:192–201.
- [45] Sørensen BF, Jørgensen K, Jacobsen TK, Østergaard RC. DCB-specimen loaded with uneven bending moments. *Int J Fract* 2006;141(1-2):163–76.
- [46] Frank A, Arbeiter FJ, Berger IJ, Hutař P, Náhlík L, Pinter G. Fracture Mechanics Lifetime Prediction of Polyethylene Pipes. *J. Pipeline Syst. Eng. Pract.* 2019;10(1):4018030.
- [47] ISO 18489:2015. Polyethylene (PE) materials for piping systems — Determination of resistance to slow crack growth under cyclic loading — Cracked Round Bar test method.
- [48] Spoerk M, Gonzalez-Gutierrez J, Sapkota J, Schuschnigg S, Holzer C. Effect of the printing bed temperature on the adhesion of parts produced by fused filament fabrication. *Plast Rubber Compos* 2017;47(1):17–24.
- [49] ASTM D 638-14, 2014, Standard Test Method for Tensile Properties of Plastics, ASTM International, West Conshohocken, PA, 2014, [www.astm.org](http://www.astm.org).
- [50] Brinson, Hal F., and L. Catherine Brinson. *Polymer engineering science and viscoelasticity: An Introduction*. New York: Springer 2008;66:79.
- [51] Tsai SW. A Test Method for the Determination of Shear Modulus and Shear Strength. Air Force Materials Laboratory Technical Report, AFML-TR-66-372 1967.
- [52] Benthem, J. P., and W. T. Koiter. *Asymptotic approximations to crack problems: Methods of analysis and solutions of crack problems*. Springer, Dordrecht 1973:131–8.
- [53] Arbeiter, Frank, Mohammed, Pinter. Influence of Long-Term Annealing on Residual Stress Distribution and Quasi-Brittle Failure Properties of Talcum Reinforced Pipe Grade Polypropylene. ANTEC, 2017, Anaheim.
- [54] Moore DR, Williams JG, Pavan A. *Fracture mechanics testing methods for polymers, adhesives and composites: Vol 28*. Elsevier; 2001.

- [55] Andreas Frank. Fracture Mechanics Based Lifetime Assessment and Long-term Failure Behavior of Polyethylene Pressure Pipes. PhD dissertation, Montanuniversität Leoben; 2010.
- [56] Ferreira RTL, Amatte IC, Dutra TA, Bürger D. Experimental characterization and micrography of 3D printed PLA and PLA reinforced with short carbon fibers. *Compos B Eng* 2017;124:88–100.
- [57] Bellini A, Güçeri S. Mechanical characterization of parts fabricated using fused deposition modeling. *Rapid Prototyp J* 2003;9(4):252–64.
- [58] Ning F, Cong W, Qiu J, Wei J, Wang S. Additive manufacturing of carbon fiber reinforced thermoplastic composites using fused deposition modeling. *Compos B Eng* 2015;80:369–78.
- [59] Ming-Yuan, He, and John W. Hutchinson. Crack deflection at an interface between dissimilar elastic materials. *Int J Solids Struct* 1989;25(9):1053–67.

## Chapter 4. Characterisation of Interlayer Bonding in AM

### 4.1. On the investigation of quasi-static and fatigue crack resistance of thermoplastic tape layered composites with multiple delaminations: Approaches for quantification

#### 4.1.1. Bibliographic information

- Authors and their relevant contribution to the publication:
  - A. Khudiakova<sup>1</sup>: Conceptualisation, Methodology, Software, Validation, Investigation, Data curation, Writing—original draft preparation, Visualisation, Writing—review and editing
  - A. Brunner<sup>2</sup>: Conceptualisation, Methodology, Software, Data curation, Writing—review and editing
  - M. Wolfahrt<sup>1</sup>: Conceptualisation, Methodology, Data curation, Writing—review and editing, Supervision, Funding acquisition
  - T. Wettemann<sup>3</sup>: Methodology, Project administration, Funding acquisition
  - D. Godec<sup>4</sup>: Writing—review and editing, Supervision
  - G. Pinter<sup>5</sup>: Conceptualisation, Methodology, Software, Resources, Data curation, Writing—review and editing, Supervision
  
- Affiliations:
  - <sup>1</sup>Polymer Competence Center Leoben GmbH, Roseggerstraße 12, 8700 Leoben, Austria
  - <sup>2</sup>Empa, Swiss Federal Laboratories for Materials Science and Technology, Laboratory for Mechanical Systems Engineering, Überlands Strassße 129, 8600 Dübendorf, Switzerland
  - <sup>3</sup>Chair of Carbon Composites, Technical University of Munich, Boltzmannstraße 15, 85748 Garching, German
  - <sup>4</sup>Faculty of Mechanical Engineering and Naval Architecture, University of Zagreb, Ul. Ivana Lučića 5, 10000, Zagreb, Croatia
  - <sup>5</sup>Institute of Materials Science and Testing of Polymers, Montanuniversitaet Leoben, Otto Gloeckel-Straße 2, 8700 Leoben, AT

In preparation for publication in a peer-reviewed scientific journal

#### 4.1.2. Abstract

Automated tape placement with in-situ consolidation (ATPisc) is a layer-wise manufacturing process in which the achievement of proper interlayer bonding constitutes one of the most challenging aspects. In the present study, unidirectional carbon fibre reinforced thermoplastic laminates were produced following different manufacturing protocols using ATPisc. The interlayer bonding of the laminates produced was characterized using quasi-static and fatigue mode I fracture test with double cantilever beam (DCB) specimen. Independent of the manufacturing approach, the laminates exhibited multiple cracking during DCB testing, which could not be evaluated simply following standard methods. Thus, various data analysis methodologies from literature were applied for the quantitative assessment of the laminate quality. The examination of the evolution of the damage parameter  $\varphi$  and the effective flexural modulus throughout testing enabled a better understanding of the damage accumulation. The Hartman-Schijve based approach revealed to be a convenient method to present fatigue crack growth curves of laminates with multiple delaminations. Moreover, a preliminary attempt was made to employ the 'zero fibre bridging' methodology to eliminate the effect of additional damage processes on the fatigue crack growth.

**Keywords:** automated tape placement, interlayer bonding, mode I fracture, double cantilever beam, multiple delaminations, crack branching, damage index

#### 4.1.3. Introduction

The interlayer bonding is one of the most critical issues of thermoplastic carbon fibre laminates produced using an additive manufacturing method such as automated tape placement with in-situ consolidation (ATPisc). In this process, an incoming prepreg tape is heated with, e.g., a diode laser up to the melting temperature of the thermoplastic matrix and placed on a mould using a compaction roller. The intimate contact created between the tape and the roller ideally leads to inter-diffusion of the polymer chains across the bond interface followed by material solidification with subsequent cooling [51]. Fast placement speeds (up to 12 m/min [52]) and rapid cooling rates (up to 500 °C/s [53]) applied in ATPisc lead to very short time of the intimate contact as well as to the limited dwell time of the material above the thermoplastic's glass transition temperature  $T_g$ , when the polymer chains are mobile and the inter-diffusion occurs across the interfaces. This results in a short healing time that hinders the development of the bonding between the incoming tape and the substrate [54]. In addition, laminates produced by ATPisc suffer from thermal residual stresses, which are caused by a non-uniform shrinkage of the matrix and the fibres upon cooling and also by temperature gradients throughout the laminate thickness as a result of layer-wise manufacturing. Excessive residual stresses lead to laminate curvature, which may cause delamination between the layers [55–58]. Moreover, the interlayer bonding is a potential site for the accumulation of defects such as voids, which deteriorate the interlayer bonding [59,60]. Thus, all these issues mentioned above make the production of a flat laminate with a proper interlayer bonding using ATPisc challenging.

The present work investigates the delamination resistance of unidirectional (UD) carbon fibre (CF) reinforced polyphenylene sulphide (PPS) laminates produced by ATPisc. The laminates were manufactured following two different design approaches with an additional application of different tape placement speeds and process temperatures. The delamination resistance was characterized using both the quasi-static [61] and the fatigue [62,63] mode I double cantilever beam (DCB) tests. Regardless of the manufacturing approach, the mid-plane delamination propagation was found to be not the only damage process occurring in the laminates during both quasi-static and fatigue tests. Instead, it was accompanied by the formation of multiple interlayer delaminations in addition to fibre bridging. The effect of fibre bridging in UD fibre reinforced composites is well-known in the literature

[64–68], including studies on UD CF/PPS laminates [69,70], while multiple delaminations have been addressed only in few research works [71–73]. These additional damage processes affect the main mid-plane crack propagation and lead to data that could not be reasonably quantified according to the standard data analysis. Hence, an important goal of this study was to find ways to quantitatively characterize the laminate quality. For this purpose, the evolution of the crack length correction factor  $\Delta$  and the effective flexural modulus was examined throughout the tests. In addition, the damage parameter  $\varphi$  [74] was calculated to characterize the degree of damage at the beginning and at the end of testing. The quasi-static delamination resistance was presented using R-curves (resistance curves), while the fatigue delamination resistance was characterized using both, the classic Paris relation and the modified Hartman-Schijve equation [75]. In addition, three-point bending tests were performed on specimens prior to and after DCB testing to determine a possible change in the flexural modulus. Moreover, the ‘zero fibre bridging’ methodology for the determination of ‘conservative’ mode I delamination resistance data [76] was applied as a preliminary attempt to exclude the effect of multiple cracking and fibre bridging on the fatigue crack propagation. To the best of the authors' knowledge, such a complex crack propagation behaviour with multi-cracking has not been reported in former studies of ATPisc laminates [56,77–80] nor the approach for their characterization aiming at quantification, making the present work valuable in this field.

#### 4.1.4. Materials and methods

##### **Materials and specimen manufacturing**

The material used in the present study is a continuous carbon fibre reinforced polyphenylene sulphide (CF-PPS) tape with a width of 264 mm and a thickness of 0.14 mm. The unidirectional laminates were manufactured using ATPisc by following two different approaches as illustrated in Fig. 1. According to the first approach, which is called clamping, a picture frame made out of aluminium profiles was installed above the first four layers that were placed on a flat tool (Fig. 1a). The remaining 20 layers were then laid up on each other within the frame. A polyimide insert film (from Ube Industries, Japan) with a thickness of 12.5  $\mu\text{m}$  was used for every laminate manufactured. This film was placed between the upper surface of the 12<sup>th</sup> layer and the bottom surface of the 13<sup>th</sup> layer to create a pre-crack for delamination testing. The clamping approach provided a manufacturing process without interruptions, except one for placing the insert film. According to the second approach, which is called flipping, the manufacturing process was stopped to flip the laminate and to place the insert film after the deposition of the first 4 layers (Fig. 1b). After that, the deposition process was continued for the next 4 layers. Thus, the interface with a pre-crack was created between the bottom surface of the 1<sup>th</sup> layer and the bottom surface of the 5<sup>th</sup> layer. The flipping of the laminate after placing of every 4 layers was repeated until 24 layers were placed in total.

To investigate the influence of the placement speed and the process temperature on the fracture toughness, two different sets with extreme manufacturing parameters were chosen. The laminates produced with 5 m/min and 330 °C present the ‘slow and cold’ case, while the laminates manufactured with 10 m/min and 350 °C present the ‘fast and hot’ case. The process parameters are listed in Table 1. With respect to the nomenclature of the tests, the letters ‘c’ and ‘f’ refer to the manufacturing methods, clamping and flipping. The first number after the letter refers to the placement speed and the second number to the process temperature used. For example, a panel produced at 5 m/min and at 330 °C following the flipping approach is called f-5-330.



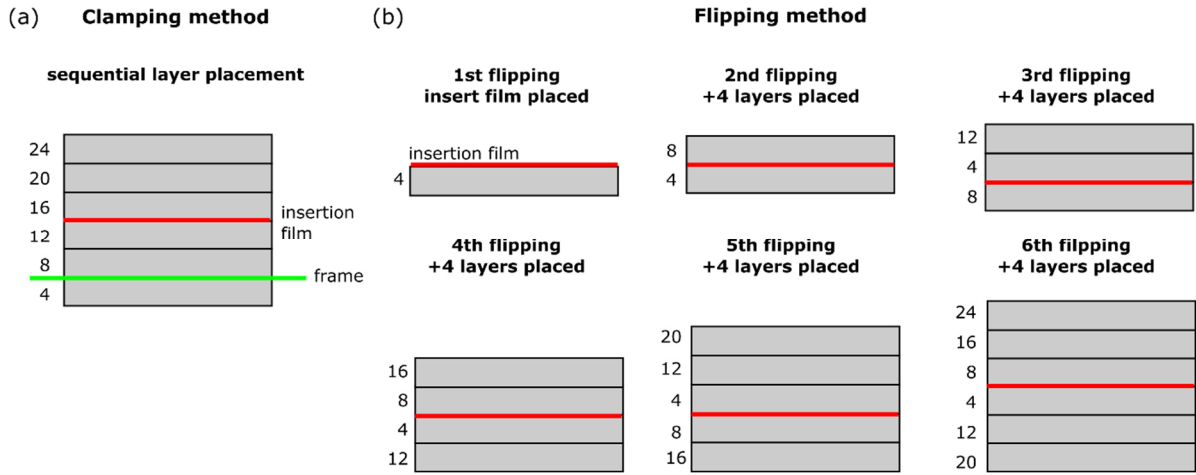


**Fig. 1.** Schematic drawing of the clamping (a) and the flipping (b) method. The insert film is marked in red, the frame is marked in green. The fibre direction is into the page.

**Table 1.** Manufacturing parameters of UD CF/PPS panels produced by ATPisc.

Specimen ID	Manufacturing method	Number of plies	Placement speed, m/min	Process temperature, °C
c-5-330	clamping	24	5	330
c-10-350	clamping	24	10	350
f-5-330	flipping	24	5	330
f-10-350	flipping	24	10	350

### DCB mode I testing

Rectangular DCB specimens with dimensions of  $150 \times 20 \times 3.2 \text{ mm}^3$  and  $200 \times 20 \times 3.2 \text{ mm}^3$  were cut out of the laminates using a waterjet cutting machine for the quasi-static and fatigue tests, respectively. Prior to testing, steel load-blocks were glued to all specimens using a two-component adhesive (Scotch-weld DP 490, 3M, USA). After that, the specimens were placed in an oven for 2 h at  $65 \text{ }^\circ\text{C}$  to cure the adhesive. The side surface of the specimens was covered with a thin layer of a white correction fluid to facilitate the visual detection of delamination onset. The tests were performed on an electro-dynamic test machine (type Instron E3000, from Instron USA) equipped with a 250 N load cell. The mode I quasi-static tests were performed according to ISO 15024, while a test protocol developed by the European Structural Integrity Society (ESIS) [81,82,63] was used for fatigue loading. All specimens were tested ‘as received’ under standard laboratory conditions ( $23 \text{ }^\circ\text{C}$  air temperature, 50% relative humidity).

To exclude the influence of the insert film, the specimens were firstly pre-cracked with a loading speed of 2 mm/min. After that, the quasi-static tests were carried out at the same loading speed of 2 mm/min, again under displacement control. During testing, the crack length  $a$  in the mid-plane of the specimen was visually measured using a travelling microscope, while the load and the displacement were recorded by the test machine. Five specimens per laminate were tested under monotonic loading.

Prior to fatigue testing, the specimens were loaded at 1 mm/min until the pre-crack propagated 1-5 mm beyond the tip of the insert film. The displacement value at which pre-cracking was stopped was taken as the  $\delta_{max}$  value for fatigue loading. The cyclic tests were performed at a frequency of 5 Hz and an  $R_\delta$ -ratio ( $\delta_{min}/\delta_{max}$ ) of 0.1 under displacement control until either a number of  $10^6$  cycles or a crack growth rate of about  $10^{-6} \text{ mm/cycle}$  was reached. The mid-plane delamination was read during the short stop at the mean displacement ( $\frac{\delta_{min} + \delta_{max}}{2}$ ) using a travelling microscope. During fatigue testing maximum and minimum values of load and displacement ( $P_{max}$ ,  $\delta_{max}$  and

$P_{min}, \delta_{min}$ ) were recorded by the test machine. The values were recorded every 10 cycles up to 1000, every 100 cycles up to 10000, every 500 cycles up to 50000, and every 1000 cycles until the end of the test. Three specimens per laminate were tested under cyclic loading.

Additionally, a series of fatigue tests were performed on one DCB specimen as a preliminary attempt to check the applicability of the ‘zero fiber bridging’ methodology [83,67] to laminates with multiple cracking. According to the methodology, a DCB specimen was first pre-cracked under quasi-static loading at a rate of 1 mm/min, yielding  $\delta_{max}$  for following fatigue test with  $R_\delta$ -ratio of 0.1. Upon reaching a crack growth rate of about  $10^{-6}$  mm/cycle, fatigue loading was terminated. After that, the specimen was quasi-statically loaded again to further propagate the crack, giving a new value of  $\delta_{max}$  for the next series of fatigue cycles. In total, this procedure was repeated four times. It should be clearly stated that in all quasi-static and fatigue tests, the reading of the crack length was done for the mid-plane delamination, which started to grow from the insert film.

### Three-point bending

Pristine specimens and specimens after quasi-static or fatigue loadings were tested using three-point bending to examine the change in flexural modulus  $E_1$  before and after testing. The tests were performed on an universal testing machine (type Zwick Z010 from Zwick GmbH & Co. KG, Germany) equipped with a load cell of 10 kN in accordance with ASTM D 790 [84]. The loading and support noses had radii of 5 mm. The span to thickness ratio of 50:1 used for all specimens was chosen as large as possible for the available lengths (150 mm and 200 mm, respectively). The formulas for the loading rates and flexural modulus can be found in the standard [84]. The flexural tests were performed under standard laboratory conditions on specimens without any conditioning. The pristine specimens refer to additional DCB specimens of the same dimensions that were not tested neither under quasi-static nor fatigue loading. The specimens that were tested under quasi-static and fatigue loadings were cryo-fractured along the mid-plane, resulting in two individual beams of the same thickness. After that, these individual beams were tested under three-point bending.

### Optical analysis

In order to investigate the effect of both loading conditions on the delamination propagation between the laminate layers, polished cross sections of the specimens were observed using the optical 3D measurement system (type Alicona InfiniteFocus from Alicona Imaging GmbH, Austria) prior to and after testing. The cutting schematic of the samples are illustrated in Fig. 2.

### Thermogravimetric analysis (TGA)

The TGA analysis was performed to determine the fiber volume fraction using the thermogravimetric analyzer TGA/DSC1 Star System (Mettler Toledo, USA). The CF-PPS samples were cut out of the laminates at three equally spaced positions (start, middle and end of lamination) and had a mass of about 20 mg. Firstly, the specimens were heated from 30 °C to 600 °C at 5 K/min under nitrogen atmosphere in order to perform pyrolysis of the PPS matrix. After that the samples were cooled down to 200 °C at -20 K/min under the nitrogen atmosphere and then heated up to 800 °C at 5 K/min under oxygen atmosphere to fully combust the carbon fibers. The fiber volume fraction  $f_v$  was found according to Eq. 1 [85].

$$f_v = \frac{\frac{w_f}{\rho_f}}{\frac{w_f}{\rho_f} + \frac{1 - w_f}{\rho_m}} \quad (1)$$

where  $\rho_f, \rho_m$  are the densities of the fibre and matrix, respectively.

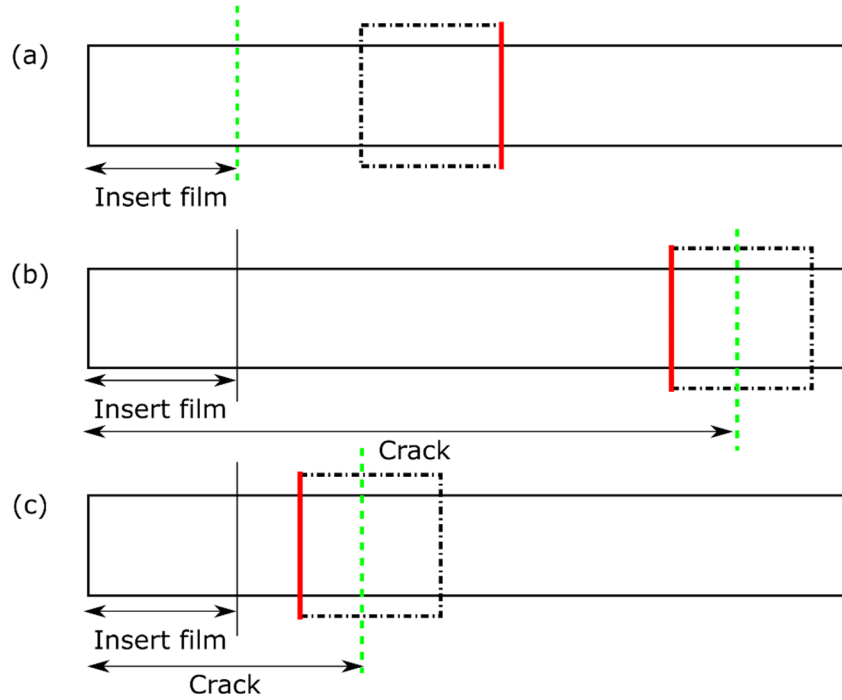


**Fig. 2.** Schematic illustrations of the samples extracted out of the DCB specimens for the microscopic examinations: pristine specimens (a), specimens after quasi-static testing (b), and specimens after fatigue testing (c). The view is on the top specimen surfaces. The green dashed lines refer either to the end of the insert film starter crack (a) or to the final crack tip after testing (b, c). The black dot-dashed lines refer to the samples cut out of the DCB specimens, with the surfaces examined using the optical microscope marked in red. The figure is not scaled.

#### 4.1.5. Data analysis techniques

##### Crack length correction factor $\Delta$ and effective flexural modulus $E_1$

During both quasi-static and fatigue loadings, the mid-plane crack propagation was accompanied by additional multiple interlayer delaminations observed visually on the side specimen surfaces. In order to examine their effect on the main mid-plane crack growth, the cubic root of the compliance  $(C/N_{block})^{1/3}$  was plotted versus crack length  $a$  defined in three different ways. The crack length  $a$  was taken to be equivalent to (i)  $a_m$  visually observed with a travelling microscope during testing, (ii)  $a_{calc}$  back-calculated from the machine compliance using Eq. 3, and (iii)  $a_{eff}$  calculated using the effective crack length method (ECLM, Eq. 4). The compliance calibration enables calculation of the crack length taking into account changing of the specimen compliance  $C$  that was automatically measured by the test machine [86]. Whereas ECLM enables calculations of the effective crack length  $a_{eff}$  using  $C$  and an independently measured flexural modulus  $E_1$ , and accounts for the fracture process zone and associated crack tip effects [87]. These plots were further used to obtain the crack length correction factor  $\Delta$  from Eq. 2 which is defined as the absolute value of the intersection of the linear fit with the negative X-axis (Eq. 2).  $\Delta$  is set to zero in case of a positive intercept [61].

$$(C/N_{block})^{1/3} = A_0 + A_1 a \quad (2)$$

$$\Delta = -\frac{A_0}{A_1}$$

where  $C$  is the compliance,  $N_{block}$  is the load block correction,  $A_0$  and  $A_1$  are parameters of the linear fit.

$$C = D * a^m \quad (3)$$

where  $D$  is a constant and  $m$  is the exponent of the power law.

$$a_{eff} = \frac{h}{2} \left( \frac{E_1 b C}{N_{block}} \right)^{1/3} \quad (4)$$

where  $h$  is the thickness of one beam,  $b$  is the specimen width,  $E_1$  is the flexural modulus. For analysis of every fractured specimen, a value of  $E_1$  was taken to be equivalent to that obtained from a three-point bending test performed on these specimen beams after either quasi-static or fatigue testing. In addition, the effective flexural modulus  $E_1$  was calculated at each data point for every specimen using Eq. 5.

$$E_1 = \frac{8N_{block}(a + |\Delta|)^3}{Cbh^3} \quad (5)$$

#### Elastic $\Delta$ and damage parameter $\varphi$

In order to estimate the degree of damage, elastic values of  $\Delta$  and values of the damage factor  $\varphi$  were deduced via Eq. 6, 7 and 7' [74,88]. The damage parameter  $\varphi$  characterizes the damage at the crack tip caused by micro-cracking. It has a value in a range between 0 and 1 meaning the total loss of shear transverse stiffness for  $\varphi = 0$  and the absence of damage for  $\varphi = 1$  taking on a value of  $\Delta_{elastic}$ .

$$\left( \frac{\Delta_{elastic}}{h} \right)^2 = \frac{1}{10} \left( \frac{E_1}{G_{12}} - 2\vartheta \right) + 0.24 \sqrt{\frac{E_1}{E_2}} \quad (6)$$

$$\chi^2 = \left( \frac{\Delta}{h} \right)^2 = \frac{1}{10} \left( \frac{E_1}{\varphi G_{12}} - 2\vartheta \right) + 0.24 \sqrt{\frac{E_1}{\varphi E_2}} \quad (7)$$

$$\varphi = \left( \frac{0.12}{\chi^2 + 0.06} \sqrt{\frac{E_1}{E_2}} \left( 1 + \sqrt{1 + 7(\chi^2 + 0.06) \frac{E_2}{G_{12}}} \right) \right)^2 \text{ for } \vartheta = 0.3 \quad (7')$$

where  $E_2$  is the transverse modulus,  $G_{12}$  is the shear modulus and  $\vartheta$  is the Poisson's ratio. The calculations of  $\varphi$  were performed using the flexural modulus  $E_{1,3pb}$  obtained from three point bending tests.  $E_2$  and  $G_{12}$  were determined using the Reuss model for each laminate type (Appendix A) [89].

#### Calculations of $G_I$

The mode I energy release rate (ERR),  $G_I$ , was calculated according to either corrected beam theory (CBT) (Eq. 8) or ECLM (Eq. 9) for both quasi-static and fatigue tests.

$$G_I = \frac{3P\delta}{2b(a + |\Delta|)} \frac{F_{displ}}{N_{block}} \quad (8)$$

$$F_{displ} = 1 - \frac{3}{10} \left( \frac{\delta}{a} \right)^2 - \frac{3}{2} \left( \frac{\delta l_1}{a^2} \right)$$

$$N_{block} = 1 - \left( \frac{l_2}{a} \right)^3 - \frac{9}{8} \left[ 1 - \left( \frac{l_2}{a} \right)^2 \right] \frac{\delta l_1}{a^2} - \frac{9}{35} \left( \frac{\delta}{a} \right)^2$$

$$G_I = \frac{3P\delta}{2ba_{eff}} \frac{F_{displ}}{N_{block}} \quad (9)$$

where  $P$  is the applied load,  $\delta$  is the displacement,  $F_{displ}$  is the large-displacement correction,  $l_1$  is the distance between the center of loading pin to the mid-plane of the half-beam of the DCB specimen,  $l_2$

is the distance between the centre of the loading pin to the edge of load block. In quasi-static tests,  $G_I$  was calculated for every value of the crack length  $a$  and corresponding  $P$  and  $\delta$ . The data obtained was presented using R-curves. In fatigue tests,  $P_{max}$ ,  $\delta_{max}$  and  $P_{min}$ ,  $\delta_{min}$  recorded were used to deduce corresponding  $G_{I_{max}}$  and  $G_{I_{min}}$ .

### The Paris relation and the modified Hartman-Schijve equation

The fatigue crack growth curves were firstly presented using the classic Paris relation of the crack growth rate  $\frac{da}{dN}$  as a function of  $\sqrt{G_{I_{max}}}$  described by Eq. 10.

$$\frac{da}{dN} = M * \sqrt{G_{I_{max}}}^s \quad (10)$$

where  $M$  and  $s$  are material parameters,  $N$  is the number of cycles.  $M$  corresponds to the intersection of the linear region of the Paris-plot with Y-axis and  $s$  describes its slope. Crack growth rate  $\frac{da}{dN}$  was calculated using the nine-point incremental polynomial technique as described in ASTM E 647 [90].

Further, the fatigue crack growth curves were presented using the modified Hartman-Schijve equation [91] (Eq. 11), which was applied to try to collapse the curves into the single 'master' curve [92].

$$\frac{da}{dN} = D \left[ \frac{\sqrt{G_{I_{max}}} - \sqrt{G_{I_{max},thr}}}{\sqrt{1 - \frac{\sqrt{G_{I_{max}}}}{\sqrt{A}}}} \right]^n \quad (11)$$

where  $D$ ,  $n$  are the constants of the power law,  $D$  corresponds to the intersection of the linear fit of the data with Y-axis and  $n$  describes its slope. The terms  $\sqrt{G_{I_{max},thr}}$  and  $A$  are chosen so that the plot of Eq. 11 becomes virtually linear with the highest  $R^2$ -ratio of the linear fit [92].

It should be noted that some studies have used  $(\Delta\sqrt{G_I} = \sqrt{G_{I_{max}}} - \sqrt{G_{I_{min}}})$  instead of  $\sqrt{G_{I_{max}}}$  in Eq. 10 and in the numerator of Eq. 11 [93–96,75,62]. However, in the present work, several specimens have exhibited extremely low  $P_{min}$  around 0.35 N, which could not be properly measured by the load cell of 250 N used. In order to be consistent with data reduction for all laminates, only maximum values were used for all calculations in order to avoid a usage of questionable minimum loads measured. Therefore,  $\sqrt{G_{I_{max}}}$  was used in both Eq. 10 and Eq.11. Such a form of equations has also been used in [97–99].

#### 4.1.6. Results and discussion

##### Laminate quality after manufacturing

The laminates produced by the clamping method were flat as long as they stayed fixed with the frame on the manufacturing table (Fig. 3a). After removing the frame, as expected, the laminate edges bent upwards (Fig. 3a',a''). Such a distortion can be attributed to temperature gradients throughout the laminate thickness caused by the layer-wise manufacturing [100,101]. The farther from the uppermost layer, which is subjected to the laser heat, the temperature of the layers is lower [102,103]. This means that bottom layers, which have already solidified, constrain the shrinkage of the upper layers during their cooling down. As a consequence, residual stresses gradually accumulate throughout the laminate thickness, which lead to parabolic buckling of the laminate [100]. In c-5-330 laminates, residual stresses have reached such a high level, that transverse cracking of the laminate has occurred (Fig. 3a'''). This was not observed for the c-10-350 laminate. It is expected that the

laminates will affect the beam stiffness and therefore the fracture toughness obtained using DCB testing [104]. In addition, thermal residual stresses have an influence on the effective fracture toughness [105,106]. Yokozeki et al. [105] have applied models to estimate the effect of thermal residual stresses on the interfacial fracture toughness in carbon fiber reinforced polymer composites. Finite element modelling (FEM) performed by the authors has revealed that the energy release rate is lower when thermal residual stresses are considered. In their study, Yokozeki et al. [105] have not mentioned the type of polymer matrix investigated. However, the material values used for FEM were reported and can be related to carbon fiber reinforced thermoplastics. This means that the effect of residual stresses likely applies to CF-PPS of the present study.

Such a strong curvature of the laminate plates was not observed for laminates manufactured by the flipping method (Fig. 3b,b'). This can possibly be explained by two reasons. On the one hand, the flipping process leads to a faster laminate cooling with a reduced heat build-up within the laminate, so accumulation of residual stresses did not take place or to a much lesser extent. On the other hand, the residual stresses accumulating during manufacturing within every four layers could be compensated by the following laminate flipping and heat and pressure application. There was no observable impact of the printing speed and the control temperature on the laminate curvature for the flipping method.

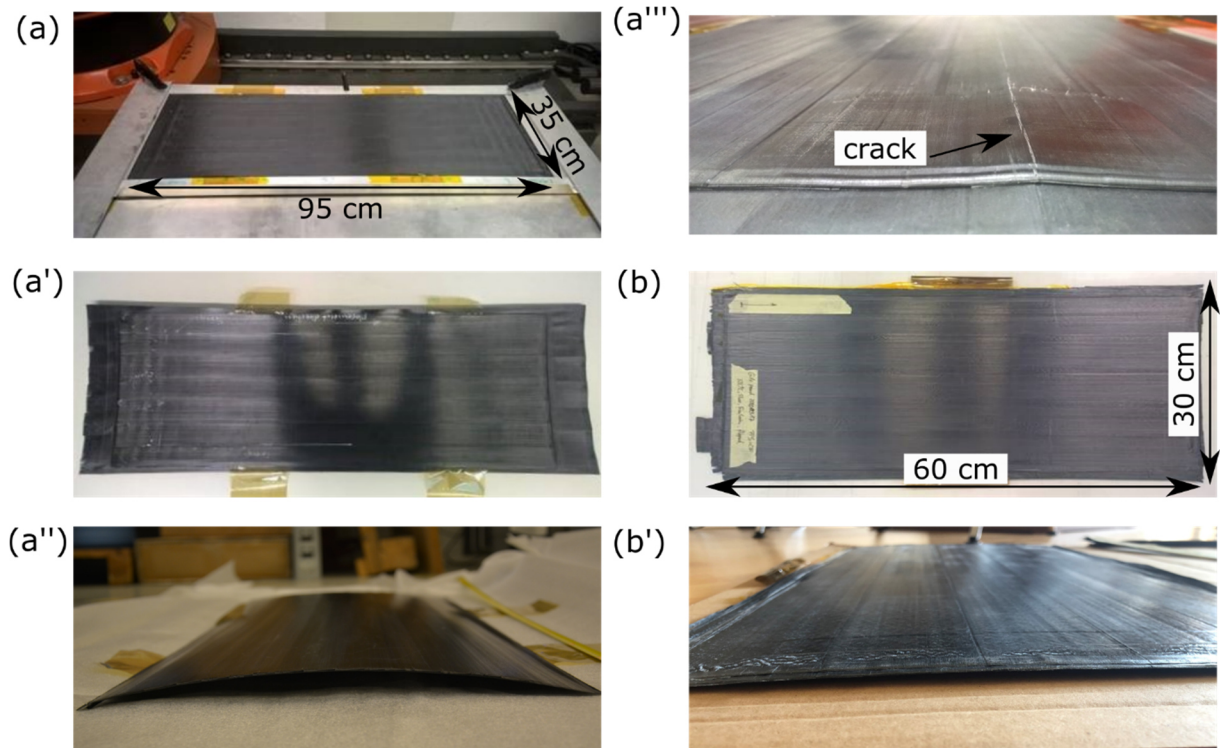


**Fig. 3.** The laminates produced by the clamping method fixed on the table (a), top (a') and side (a'') views after removing the frame, closer view on the crack due to residual stresses in c-5-330 (a''') and the flipping method (top (b) and side (b') views).

The micrographs of the laminate cross sections made prior to testing are shown in Fig. 4. The regions with high porosity concentration formed delamination as within individual layers (Fig. 4a) and also between the layers (Fig. 4b). Both resin rich and resin poor regions were observed in the specimens (Fig. 4b,b'). Areas with non-uniform fiber distribution and misalignment of the layers were also detected (Fig. 4b'). The optical analysis revealed the presence of multiple interlayer delamination in f-5-330 marked in red in Fig. 4b. On the one hand, these delaminations could indicate a poor level of interlayer bonding formed during laminate manufacturing. On the other hand, they could be an artefact from cutting and preparing of the laminate cross-sections, but still reflecting weak interlayer bonding. This could be explained by the process interruptions to flip the laminate, which conducted to

faster temperature dissipation and faster cooling of the laminate, which in turn led to insufficient inter-diffusion of the polymer chains. Such delaminations were not observed in f-10-350, meaning that process parameters of 5 m/min and 330 °C did not provide the heat to sufficiently melt the substrate and to develop the proper intimate contact with the incoming tape.

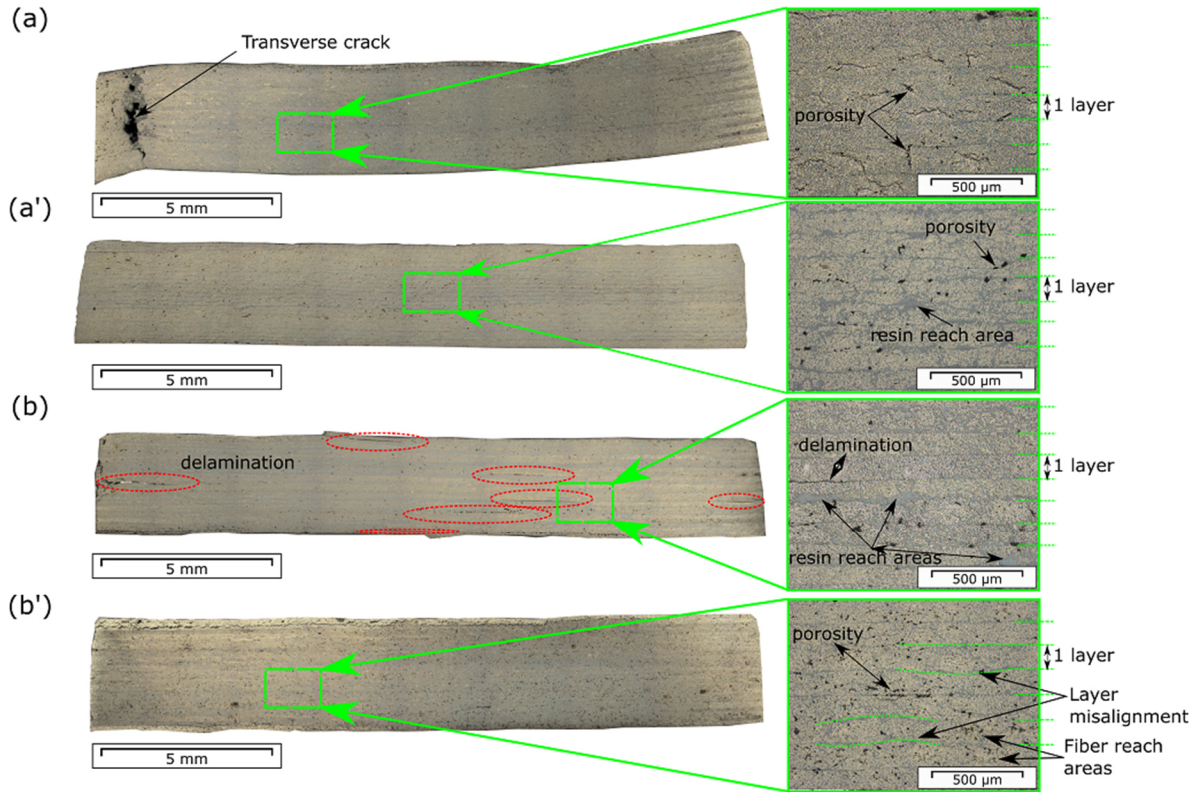


**Fig. 4.** Micrographs of the laminate cross sections made prior to testing for c-5-330-01 (a), c-10-350-02 (a'), f-5-330-04 (b) and f-10-350-05 (b').

### TGA analysis

The results of specific fibre weight fraction  $w_f$  values are summarized in Table 2. The corresponding fibre volume fractions  $f_v$  were calculated using Eq. 1 with fibre density  $\rho_f$  of 1.8 g/cm<sup>3</sup> and PPS density  $\rho_m$  of 1.35 g/cm<sup>3</sup> [107]. It should be noted that  $f_v$  obtained was further used for the calculations of both the transverse and shear moduli (Appendix A).

**Table 2.** Fibre weight and volume fractions of the laminates obtained using TGA analysis.

Laminate	$m$ , mg	$w_f$ , %	$f_v$ , %
c-5-330	20.8±0.1	64.7±2.0	57.9±0.2
c-10-350	20.0±0.6	60.6±1.7	53.6±1.7
f-5-330	20.3±0.6	58.7±0.9	51.6±1.0
f-10-350	20.0±0.4	67.1±0.8	60.4±0.9

### Three-point bending tests

Table 3 shows the results of three-point bending tests performed on the pristine specimens, the specimens after quasi-static testing and the specimens after fatigue testing. The pristine specimens have exhibited fairly low deviations in the results obtained for every laminate type, which indicates the consistency of the specimens with each other. Their average  $E_{1\_3pb}$  obtained was of about 106±8 GPa. Although the specimens exhibited a varying extent of multiple cracking during both quasi-static

and fatigue tests, there was no significant difference in their flexural moduli obtained using three-point bending. The specimens after the quasi-static tests exhibited nearly the same  $E_{1_{3pb}}$  as the pristine specimens. The flexural moduli of the specimens after fatigue testing were also very close to the values of the pristine specimens. All flexural moduli of pristine specimens exhibited the standard deviation within 5% of the respective average. This can be interpreted as reasonable, but not excellent, quality (high-quality CFRP can get down to about 1% scatter/standard deviation in modulus). The scatter after quasi-static fracture testing is the same, except for f-5-330 type specimens. After fatigue testing, the highest scatter is found for the 350-type specimens (both f and c) rather than the c-5-330 type, whereas f-5-330 tends to be higher (around 9%), but not as much as the 350-type specimens. This can possibly imply different damage types between quasi-static and fatigue loadings. The absence of a pronounced change in the modulus values determined before and after testing indicates that most of damage that affects the flexural modulus was already induced in the laminates during their manufacturing (Fig. 4). On the other hand, these findings can indicate that the three-point bending modulus is not sensitive to delaminations in the beam. Compression and shear may 'close' some of the delaminations present and hence the modulus may not be as sensitive to existing damage.

**Table 3.** The flexural moduli obtained from three-point bending tests performed on pristine specimens and on specimens after quasi-static and fatigue testing. The values presented were calculated as the arithmetic mean of four pristine specimens for c-5-330; of five pristine specimens for c-10-350, f-5-330 and f-10-350; of four specimens tested under quasi-static loading for every laminate type; of two specimens tested under fatigue for every laminate type.

Laminate	$E_{1_{3pb}}$ , GPa		
	Pristine specimens	After quasi-static	After fatigue
c-5-330	111±6 (6%)	111±5 (5%)	109±4 (3%)
c-10-350	96±4 (4%)	95±5 (5%)	109±20 (18%)
f-5-330	104±3 (3%)	100±15 (15%)	90±8 (9%)
f-10-350	112±8 (7%)	112±6 (5%)	100±18 (18%)

### Quasi-static loading

#### *Damage processes in the specimens*

Besides the main mid-plane crack propagation, the specimens exhibited additional damage processes during quasi-static testing. Table 4 presents the information about whether a single or multiple crack propagation was observed during quasi-static testing. Fig. 5 demonstrates selected examples of fracture behaviour visually observed during the tests, while Fig. 6 illustrates micrographs of the cross-sections of selected specimens made after the tests. Most of the specimens yielded pronounced fibre bridging appeared as a net of fibres pull out of the opened beams (Fig. 5c,d, c',d'). In addition, several specimens showed multiple delamination growth above and/or below the mid-plane (Table 4, Fig. 5a,b,a',b').

Although, visually, a single mid-plane delamination was observed during testing in c-5-330-01 and c-10-330-01, the micrographs of their cross sections made after testing revealed the presence of additional delaminations in them (Fig. 6a,a'). The transverse intralaminar cracking observed in c-5-330-01 provoked extra delamination growth above and below the mid-plane (Fig. 6a). Similarly, for c-10-350-01 the main crack did not propagate only in the mid-plane, but it deviated from it to the adjacent layers (Fig. 6b). The micrograph of f-10-350-05 with a single delamination observed during testing also revealed the presence of crack branching out of the mid-plane to adjacent layers. These findings indicate that although only one mid-plane delamination was visually observed on the side specimen



surface during testing, other damage processes have also occurred in the specimen body (Fig. 6d). This raises the question, how this additional damage could possibly be accounted for in the data analysis. It is further interesting to note that both f-5-330-04 and -05 exhibited critical layer delamination due to layer 'buckling' close to the upper surface (Fig. 5c'). It is important to note that this type of damage did not have a significant effect on the flexural modulus measured by three-point bending test. Such a type of delamination was not observed for any other specimens in this study.

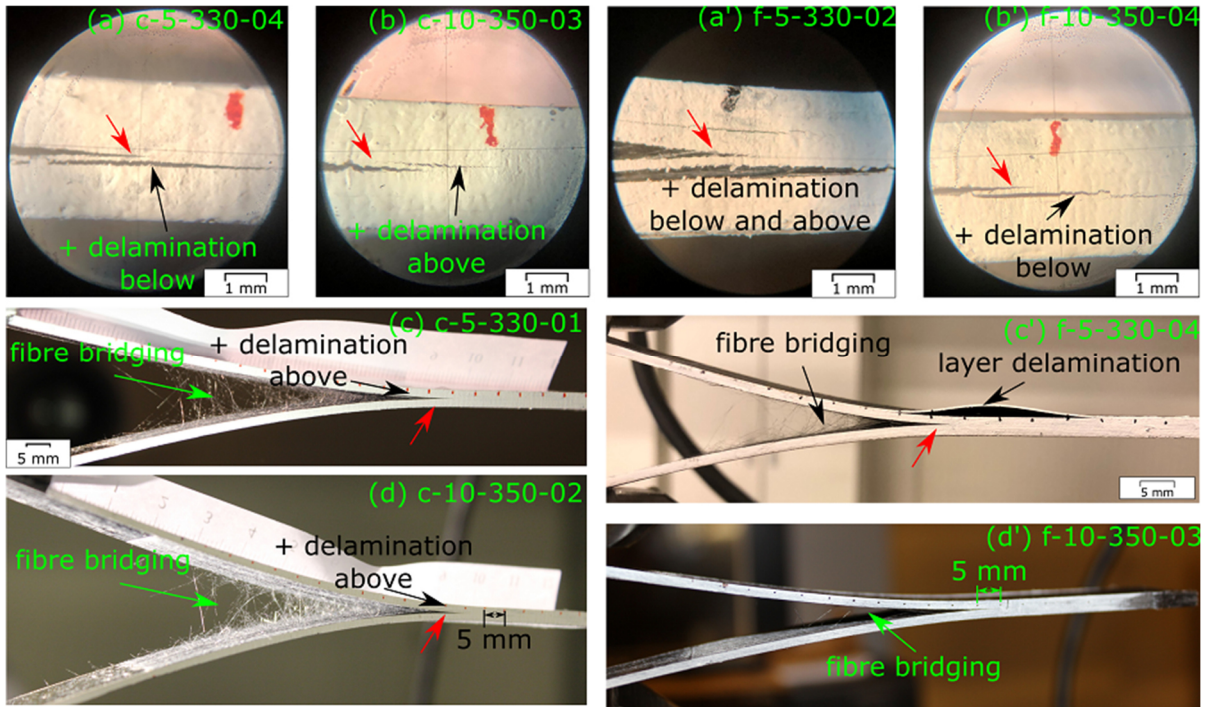
**Table 4.** Damage processes visually observed on the side specimen surfaces during the quasi-static tests.

Specimen	Visually observed damage process	Specimen	Visually observed damage process
c-5-330-01	Single delamination	f-5-330-01	Single delamination
c-5-330-02	Single delamination	f-5-330-02	Multiple cracking
c-5-330-03	Multiple cracking	f-5-330-03	Multiple cracking
c-5-330-04	Multiple cracking	f-5-330-04	Multiple cracking
c-5-330-05	Single delamination	f-5-330-05	Multiple cracking
c-10-350-01	Single delamination	f-10-350-01	Multiple cracking
c-10-350-02	Multiple cracking	f-10-350-02	Multiple cracking
c-10-350-03	Multiple cracking	f-10-350-03	Single delamination
c-10-350-04	Multiple cracking	f-10-350-04	Multiple cracking
c-10-350-05	Single delamination	f-10-350-05	Single delamination

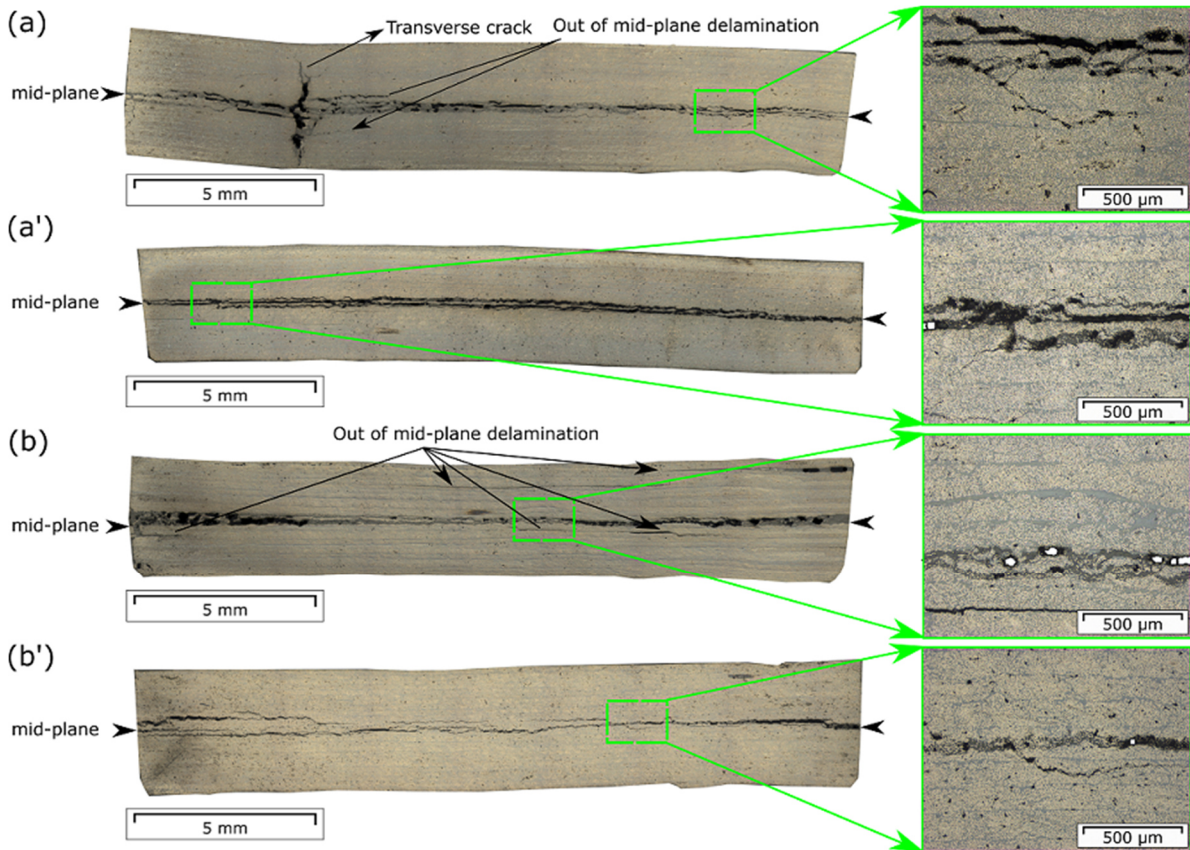
#### **Crack length correction factor $\Delta$ and effective flexural modulus $E_1$**

Figure 7 illustrates the comparison of  $(C/N_{block})^{1/3}$  plotted versus  $a_m$  visually measured during testing,  $a_{calc}$  calculated from the machine compliance (Eq. 3), and  $a_{eff}$  calculated using Eq. 4, where the curves were shifted along the Y-axis for ease of comparison. In order to check the linearity of the data obtained, linear regressions were fitted to every dataset out of five consecutive points (Fig. 7a). These slope values are shown in Fig. 8, where the curves were again shifted along the X-axis.

The slopes of the visual data exhibited a pronounced scatter for every laminate (Fig. 8), indicating the deviation of  $(C/N_{block})^{1/3}$  plotted versus  $a_m$  from linearity (Fig. 7). This implies that the crack length correction  $\Delta$  and the flexural modulus  $E_1 \sim (a + |\Delta|)^3$  are highly dependent on the number of points fitted to the linear regression. Unlike these visual data, the slopes of the machine data either continuously increased, decreased or stayed stable with the crack growth. The continuous change resulting in increasing slopes can be explained by the development of additional damage processes occurring during testing, which effectively reduces the specimen stiffness and hence increases the slope of the fit. The lower slopes correspond to higher  $\Delta$  and  $E_1$ , while the higher slopes correspond to lower  $\Delta$  and  $E_1$  [74]. The trend in the slopes of the visual data often contradicted that of the machine data, when comparing their first and last data points in Fig. 8. For example, for c-5-330-01, a slope of the visual data was smaller at the beginning than at the end of testing, while the opposite was true for the machine data.



**Fig. 5.** Selected examples of crack growth and fibre bridging in laminates produced by clamping (a-d) and flipping (a'-d') methods. The total crack length was about 60 mm in (a), 85 mm in (b), 60 mm in (a') and 55 mm in (b').



**Fig. 6.** Micrographs of the polished cross sections of selected laminates made after quasi-static testing for c-5-330-01 (a), c-10-350-01 (a'), f-5-330-04 (b) and f-10-350-05 (b').

On the one hand, this discrepancy suggests that the visual measurements were affected by additional damage processes that could not be observed on the edge of the specimens. On the other hand, it is possible that the crack length was erroneously measured by the machine operator. The crack tip was defined by cracking of a white coating on the side specimen surface which was visually monitored using a travelling microscope. Micro-cracking and fiber bridging at the crack tip made the measurements of the crack length particularly difficult. In addition, there could be inaccuracies of the visual crack length measurement caused by the crack front curvature [74]. The slopes of the effective crack length data stayed at the same value with the crack growth indicating the linear relationship between  $(C/N_{block})^{1/3}$  and  $a_{eff}$  as follows from Eq. 4.

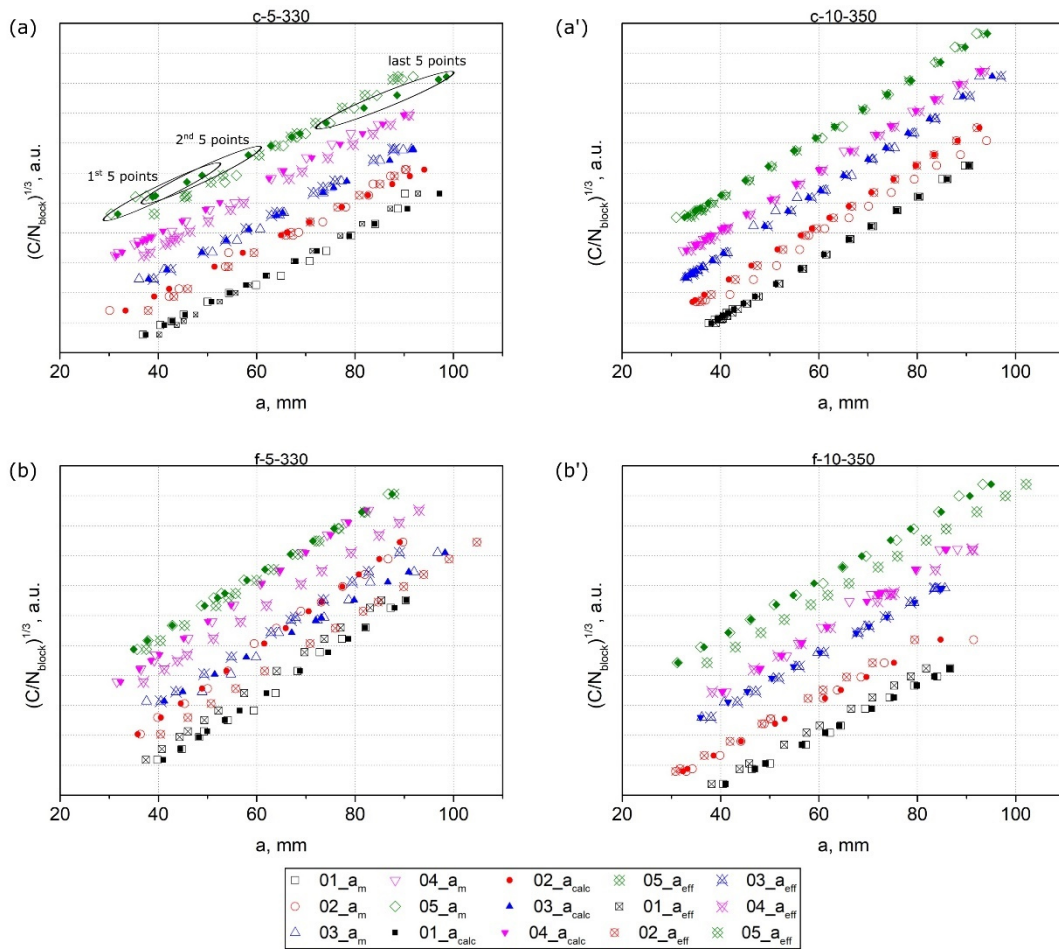


**Fig. 7.** Plots of  $(C/N_{block})^{1/3}$  versus  $a$ , where  $a$  is either  $a_m$ ,  $a_{calc}$ , or  $a_{eff}$  for c-5-330 (a), c-10-350 (a'), f-5-330 (b) and f-10-350 (b'). The legend below refers to every plot. An example of datasets out of five consecutive points used for linear regressions is demonstrated in (a).

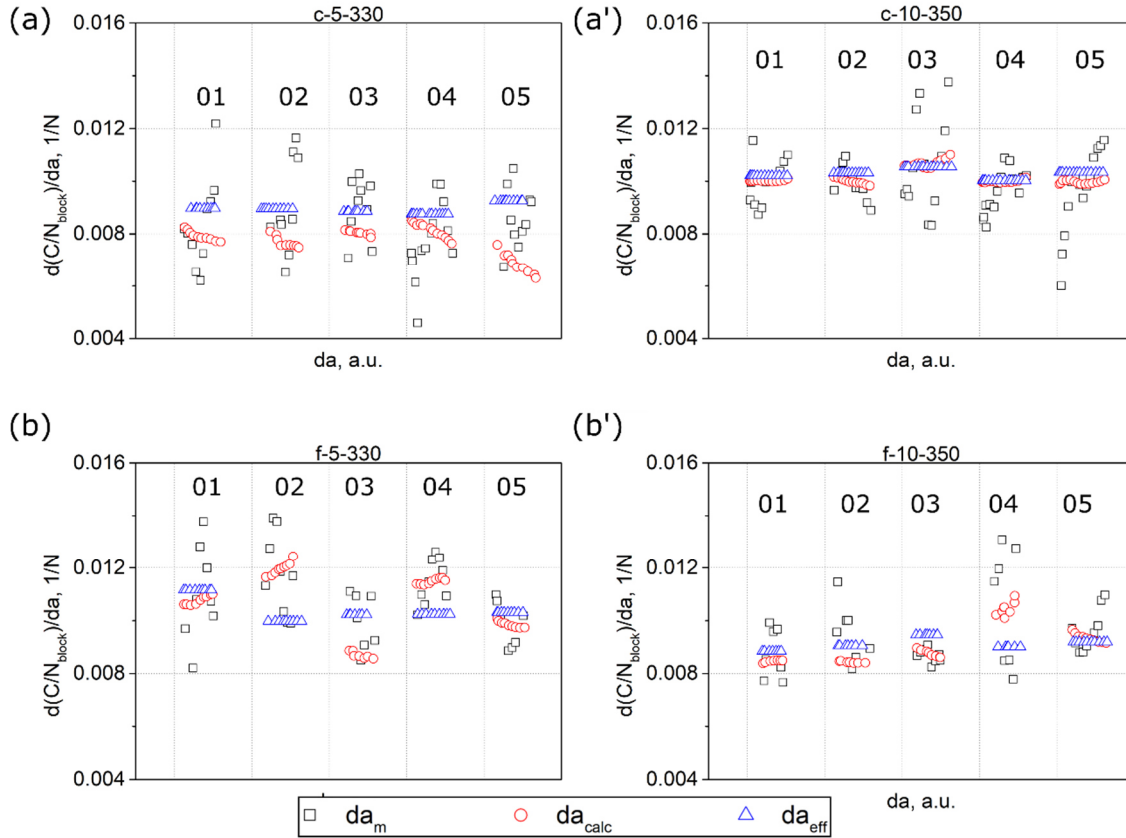


**Fig. 8.** The values of the slopes of linear regressions, which were fitted to datasets of five consecutive points from the start to the end of the test, for c-5-330 (a), c-10-350 (a'), f-5-330 (b) and f-10-350 (b') tested under quasi-static loading. 01-05 numbers refer to serial numbers of the specimens. The legend refers to every plot.

The machine data was further used to examine the evolution of the crack length correction factor  $\Delta$  and the back calculated flexural modulus  $E_1$  throughout the tests. For this purpose, linear regressions were fitted to the data range of the first and last 25 mm of the crack increment. Thus,  $\Delta$  and  $E_1$  were calculated at the beginning and at the end of crack growth, yielding corresponding  $\Delta_{\text{start}}$ ,  $E_{1\text{ start}}$  and  $\Delta_{\text{end}}$ ,  $E_{1\text{ end}}$ . For comparison, a linear regression was also fitted to all data points. The results obtained are summarized in Table 5 and Table 6 for clamping- and flipping-laminates, respectively. All specimens of c-5-330 and f-10-350 with  $\Delta < 0$ , showed  $|\Delta|_{\text{start}}$  smaller than  $|\Delta|_{\text{end}}$ , yielding  $E_{1\text{ start}}$  smaller than  $E_{1\text{ end}}$ . This effect can be explained by fiber bridging developed at the crack tip, which increases the effective stiffness of the DCB specimen [108]. For almost all specimens of c-10-350 and f-5-330 with  $\Delta < 0$ , the  $\Delta$ -values were nearly the same at the start, end and throughout the entire data range, resulting in nearly constant  $E_1$ . Clearly, the specimens, for which a zero value of  $\Delta$  was used, yielded the constant  $E_1$ . The absolute values of  $\Delta$  and  $E_1$  obtained on the entire data range were in a range between  $|\Delta|_{\text{start}}$  and  $|\Delta|_{\text{end}}$  and  $E_{1\text{ start}}$  and  $E_{1\text{ end}}$  for every specimen with  $\Delta < 0$ . Interestingly, the average effective flexural modulus  $E_{1\text{ all points}}$  for c-5-330 and f-10-350 were 1.6 and 1.1 times higher than the corresponding  $E_{1\text{ 3pb}}$  obtained using three-point bending tests (Table 3). While the average  $E_{1\text{ all points}}$  for c-10-350 and f-5-330 correlated fairly well with the corresponding  $E_{1\text{ 3pb}}$ . The higher  $E_1$  obtained from DCB tests has been also reported in [74], where it was attributed to the fiber bridging effect. It has also been noted there that  $E_1$  obtained in DCB tests should not be quoted as the flexural modulus of the laminates due to this discrepancy.

**Table 5.**  $\Delta$  and  $E_1$  calculated at the first and the last 25 mm of the crack increment ( $\Delta_{start}$ ,  $E_{1\ start}$  and  $\Delta_{end}$ ,  $E_{1\ end}$ ), and at the entire range of the crack length  $a_{calc}$  ( $\Delta_{all\ points}$ ,  $E_{1\ all\ points}$ ) for c-5-330 and c-10-350 tested under quasi-static loading.

Specimen	$\Delta_{start}$ , mm	$\Delta_{end}$ , mm	$\Delta_{all\ points}$ , mm	$E_{1\ start}$ , GPa	$E_{1\ end}$ , GPa	$E_{1\ all\ points}$ , GPa
c-5-330-01	-7.29	-9.98	-8.73	153±12	173±14	163±13
c-5-330-02	-8.74	-14.11	-11.23	154±18	193±25	171±20
c-5-330-03	-4.52	-6.44	-5.20	149±11	163±12	154±11
c-5-330-04	-7.38	-10.97	-9.38	133±8	160±10	148±8
c-5-330-05	-17.92	-30.38	-23.04	222±34	348±61	269±42
Average ± st.dev.   (%)	<b>9.17±5.13 (56%)</b>	<b>14.38±9.36 (65%)</b>	<b>11.52±6.80 (59%)</b>	<b>162±34 (21%)</b>	<b>207±80 (38%)</b>	<b>181±50 (28%)</b>
c-10-350-01	-1.68	-1.58	-1.62	101±3	101±3	101±3
c-10-350-02	-2.30	-3.61	-2.81	101±3	108±4	104±3
c-10-350-03	0.02 *	0.87 *	0.18 *	87±6	87±6	87±6
c-10-350-04	-1.22	-0.96	-1.06	103±3	101±3	102±3
c-10-350-05	-2.58	-2.62	-2.61	106±6	106±6	106±6
Average ± st.dev.   (%)	<b>1.56±1.02 (65%)</b>	<b>1.75±1.41 (80%)</b>	<b>1.62±1.15 (71%)</b>	<b>100±7 (7%)</b>	<b>101±8 (8%)</b>	<b>100±8 (8%)</b>

\*  $\Delta > 0$  were excluded from the calculations of the average values, further  $\Delta=0$  was used for the calculations of  $E_1$

**Table 6.**  $\Delta$  and  $E_1$  calculated at the first and the last 25 mm of the crack increment ( $\Delta_{start}$ ,  $E_{1\ start}$  and  $\Delta_{end}$ ,  $E_{1\ end}$ ), and at the entire range of the crack length  $a_{calc}$  ( $\Delta_{all\ points}$ ,  $E_{1\ all\ points}$ ) for f-5-330 and f-10-350 tested under quasi-static loading.

Specimen	$\Delta_{start}$ , mm	$\Delta_{end}$ , mm	$\Delta_{all\ points}$ , mm	$E_{1\ start}$ , GPa	$E_{1\ end}$ , GPa	$E_{1\ all\ points}$ , GPa
f-5-330-01	1.89 *	3.35 *	2.57 *	99±8	99±8	99±8
f-5-330-02	1.48 *	4.91 *	2.35 *	74±5	74±5	74±5
f-5-330-03	-5.35	-7.89	-6.41	165±22	184±25	173±23
f-5-330-04	-0.93	-0.02	-0.53	75±3	72±3	74±3
f-5-330-05	-3.86	-5.34	-4.60	114±4	123±5	118±4
Average ± st.dev.   (%)	<b>3.38±2.25 (67%)</b>	<b>4.42±4.02 (91%)</b>	<b>3.85±3.01 (78%)</b>	<b>105±37 (35%)</b>	<b>110±46 (42%)</b>	<b>108±41 (38%)</b>
f-10-350-01	0.84 *	1.47 *	1.16 *	136±6	136±6	136±6
f-10-350-02	-0.76	-1.32	-0.95	139±17	138±16	142±17
f-10-350-03	-4.51	-6.96	-5.42	128±3	143±5	133±3
f-10-350-04	6.49 *	10.65 *	8.01 *	110±12	110±12	110±12
f-10-350-05	-4.44	-7.54	-5.87	100±4	116±6	107±4
Average ± st.dev.   (%)	<b>3.24±2.15 (66%)</b>	<b>5.27±3.44 (65%)</b>	<b>4.08±2.72 (67%)</b>	<b>123±17 (14%)</b>	<b>129±15 (11%)</b>	<b>126±16 (13%)</b>

\*  $\Delta > 0$  were excluded from the calculations of the average values, further  $\Delta=0$  was used for the calculations of  $E_1$

### The damage parameter $\varphi$

The  $\Delta$ -values acquired in the previous paragraph were further used for calculations of  $\chi_{start}$ ,  $\chi_{end}$  and  $\chi_{all\ points}$  (Eq. 7) and damage parameters  $\varphi$  (Eq. 7'). The results obtained are presented in Table 7 and Table 8 for clamping- and flipping-specimens, respectively. All c-5-330 specimens exhibited  $\varphi$  in a range between 0 and 1, while none of c-10-350 specimens showed  $\varphi$  in this range, except c-10-350-02 with  $\varphi_{end}$  of 0.908. For both f-5-330 and f-10-350, two out of five specimens yielded physically acceptable values of  $\varphi$ . In order for  $\varphi$  to be in a range between 0 and 1,  $|\Delta|$  should be greater than  $|\Delta|_{elastic}$ , which was estimated to be of about 3.7 mm (Eq. 6). Additionally, it can be derived from

Eq. 7 that  $\chi^2$  smaller than 5.23 yields values of  $\varphi$  higher than 1. This corresponds to too steep slopes of  $(C/N_{block})^{1/3}$  plotted versus crack length  $a$ , where the intercept is at a positive crack length value.

According to Eq. 7, higher  $|\Delta|$  yield higher  $\chi^2$  which in turn leads to smaller  $\varphi$ . Hence, for  $\varphi$  in a range between 0 and 1,  $\varphi_{end}$  was smaller than  $\varphi_{start}$ , indicating a larger extent of damage at the end of testing. The damage parameter decreased by a factor of two during testing for specimens -01, -03 and -04 of c-5-330, and f-5-330-05, by a factor of three for specimens -03 and -05 of f-10-350, and by a factor of four for f-5-330-03. It is also important to note that  $\varphi$ -values of specimens with a single mid-plane delamination visually observed on the side specimen surface during testing were smaller than those of specimens with observed multiple cracking (Table 4). For example,  $\varphi_{all\ points}$  of c-5-330-01 that showed a single mid-plane delamination on the side surface is smaller than  $\varphi_{all\ points}$  of c-5-330-03 exhibited multi-cracking; 0.182 against 0.565. This can be explained by a pronounced transverse cracking observed in the cross-sections of c-5-330-01 (Fig. 6a). This finding has further strengthened the statement that a single mid-plane crack visually observed during testing was not the sole damage process occurring in the specimen body. In general, the damage parameter factors obtained seem to correlate well with the extent of damage observed in the micrographs of the specimen cross-sections. For example, more damage can be observed in the cross-section of c-5-330-01 (Fig. 6a) in comparison with the cross-section of f-10-350-05 (Fig. 6b'). This is in agreement with their damage parameters, which are smaller for c-5-330-01 than for f-10-350-05 (Table 7).

**Table 7.**  $\chi^2$  and  $\varphi$  calculated using  $\Delta_{start}$ ,  $\Delta_{end}$  and  $\Delta_{all\ points}$  for clamping-specimens tested under quasi-static loading.

Specimen	$\chi^2_{start}$	$\chi^2_{end}$	$\chi^2_{all\ points}$	$\varphi_{start}$	$\varphi_{end}$	$\varphi_{all\ points}$
c-5-330-01	18.2	34.1	26.0	0.266	0.138	0.182
c-5-330-02	26.0	67.6	42.8	0.180	0.067	0.107
c-5-330-03	7.0	14.3	9.3	0.765	0.358	0.565
c-5-330-04	18.3	40.5	29.6	0.274	0.120	0.166
c-5-330-05	116.5	334.9	192.6	0.037	0.013	0.022
c-10-350-01	1.1	1.0	1.1	5.225	6.083	5.688
c-10-350-02	2.2	5.3	3.2	2.470	0.908	1.582
c-10-350-03	0	0	0	368.749	368.749	368.749
c-10-350-04	0.6	0.4	0.5	11.786	20.580	16.313
c-10-350-05	2.8	2.8	2.8	1.902	1.836	1.860

**Table 8.**  $\chi^2$  and  $\varphi$  calculated using  $\Delta_{start}$ ,  $\Delta_{end}$  and  $\Delta_{all\ points}$  for flipping-specimens tested under quasi-static loading.

Specimen	$\chi^2_{start}$	$\chi^2_{end}$	$\chi^2_{all\ points}$	$\varphi_{start}$	$\varphi_{end}$	$\varphi_{all\ points}$
f-5-330-01	0	0	0	332.410	332.410	332.410
f-5-330-02	0	0	0	471.264	471.264	471.264
f-5-330-03	8.7	34.6	27.6	0.624	0.145	0.183
f-5-330-04	0.8	0.0003	0.1	21.595	11.846	74.291
f-5-330-05	6.4	12.3	9.1	0.839	0.419	0.576
f-10-350-01	0	0	0	416.757	416.757	416.757
f-10-350-02	0.2	0.6	0.3	39.986	11.271	24.090
f-10-350-03	7.5	18.0	10.9	0.623	0.246	0.418
f-10-350-04	0	0	0	442.804	442.804	442.804
f-10-350-05	7.2	20.7	12.6	0.698	0.225	0.383

**R-curves**

For characterization of the delamination resistance under quasi-static loading,  $G_{Ic}$  was calculated using both CBT with  $a_{calc}$  (Eq. 8) and ECM with  $a_{eff}$  (Eq. 9). In CBT, the crack length correction factor  $\Delta_{all\ points}$  was used as a value in a range between  $\Delta_{start}$  and  $\Delta_{end}$  (Table 7, Table 8). The comparison of the R-curves obtained for different laminates are presented in Fig. 9. The R-curves of clamping-laminates exhibited a better correlation with each other within one parameter set than those of flipping-laminates. The higher repeatability of the results shown by clamping-laminates indicates that this method yields specimens with more consistent properties than the flipping method. The R-curves of both clamping and flipping-laminates obtained using ECLM showed less scatter than those obtained using CBT. Thus, the comparison of fracture behaviors was based on the effective data. The  $G_{Ic\_initiation}$  values were determined from the initial load-displacement curves using the '5%/MAX point' method described in ISO 15024 [61].  $G_{Ic\_propagation}$  was defined as the arithmetic mean of the points on the plateau regions between 50 mm and 80 mm (Fig. 9). The results of  $G_{Ic\_initiation}$  and  $G_{Ic\_propagation}$  are summarized in Table 9.

Both  $G_{Ic\_initiation}$  and  $G_{Ic\_propagation}$  obtained for c-10-350 were higher than for c-5-330; averaging 1042 against 701 J/m<sup>2</sup> and 1635 against 1134 J/m<sup>2</sup>, respectively. The observed increase in fracture toughness might be explained by being a result of both higher temperature and faster placement speed applied. The higher temperature yielded longer dwell time of the laminate above  $T_g$  of the matrix, which favoured the better inter-diffusion of the polymer chains [51]. The faster placement speed led to the faster building process and less temperature fluctuations within the laminate, so laminates c-10-350 had a more stable thermal history. For the flipping-method, higher  $G_{Ic}$  was demonstrated by the laminates produced with slower speed and lower temperatures; 1250 J/m<sup>2</sup> against 1096 J/m<sup>2</sup> for  $G_{Ic\_propagation}$ . This could probably imply that the heat accumulation did not take place in the flipping method due to multiple process interruptions made to flip the laminate. Thus, the use of higher temperatures did not result in better adhesion between the layers. For most of the c-10-350 and f-5-330 specimens, R-curves rise with increasing crack growth. Usually such a behaviour is explained by fibre bridging and multi-cracking occurring in specimens, which lead to increasing  $G_{Ic}$  [109]. In general, the laminates exhibiting a multiple cracking are expecting to show higher  $G_{Ic}$  than if they would not have this effect. This is due to the fact that multiple cracking causes additional energy released per newly fractured surfaces. In addition, the multiple cracking can cause secondary fracture modes, which also increase  $G_{Ic}$  [72]. The second factor contributing to the overestimation of  $G_{Ic}$  is the fiber bridging that significantly slows down the main crack propagation [66]. This would mean that the results obtained here overestimate the real  $G_{Ic}$  value of CF/PPS material without fibre bridging and multiple cracking.

**Table 9.**  $G_{Ic\_initiation}$  and  $G_{Ic\_propagation}$  of the DCB specimens.

Laminate	$G_{Ic\_initiation}, J/m^2$	$G_{Ic\_propagation}, J/m^2$
c-5-330	128±16 (12%)	1234±101 (8%)
c-10-350	245±25 (10%)	1635±85 (5%)
f-5-330	173±44 (26%)	1250±220 (18%)
f-10-350	112±41 (36%)	1096±228 (21%)

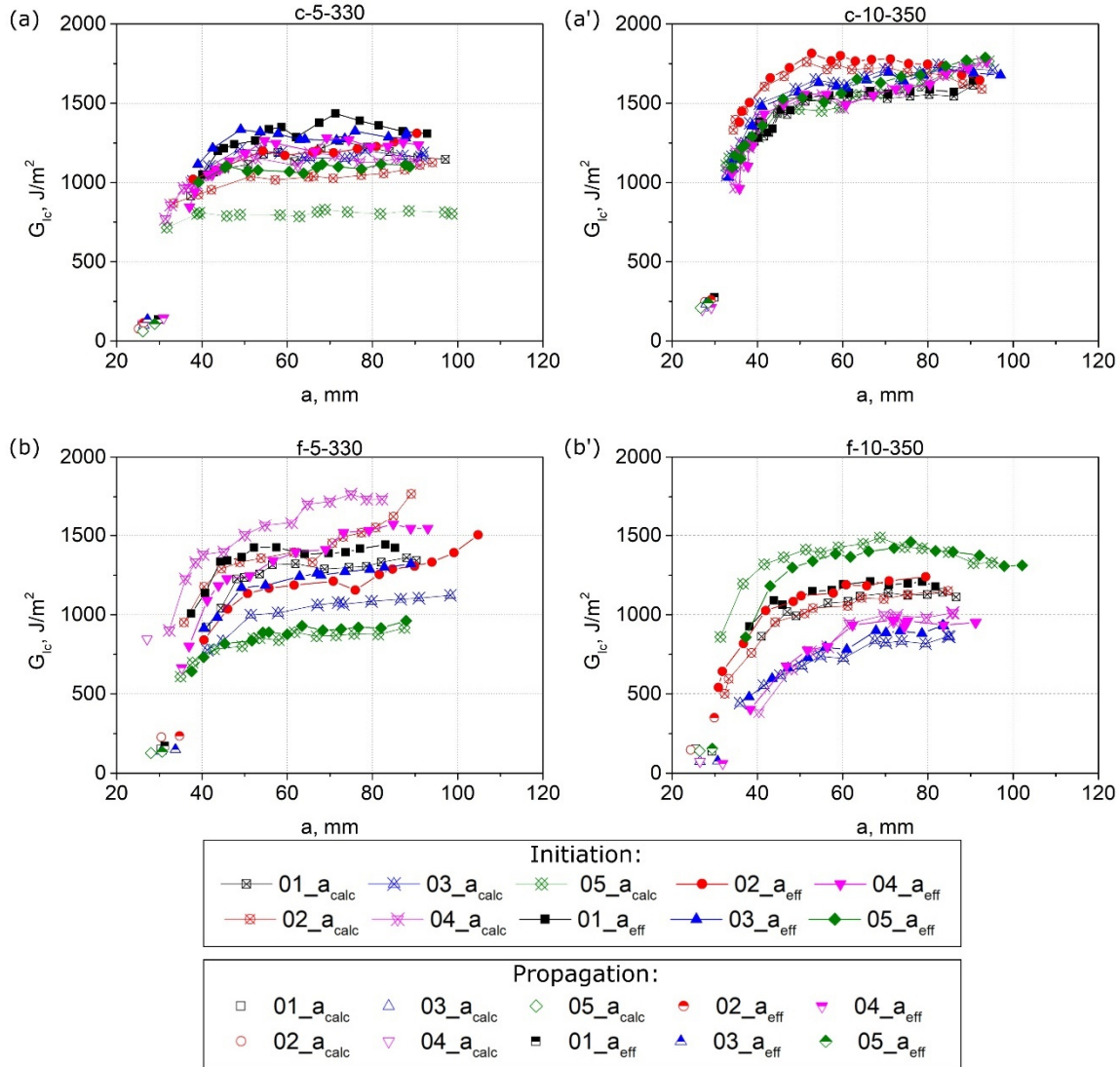


**Fig. 9.** R-curves for c-5-330 (a), c-10-350 (a'), f-5-330 (b) and f-10-350 (b'), where  $G_{Ic}$  was calculated using either CBT with  $a_{calc}$  or ECM with  $a_{eff}$ . The legends refer to every plot.

### Fatigue loading

#### Damage processes in the specimens

The delamination behaviour visually observed in the specimens during fatigue testing is summarized in Table 10 and Fig. 10. The micrographs of the cross sections of selected specimens are shown in Fig. 11. Similar to quasi-static loading, some of the specimens tested under fatigue loading exhibited additional interlayer delamination growth parallel to the mid-plane. Among the specimens displaying a visually observable single mid-plane crack growth were c-5-330-02, c-10-350-02, f-5-330-02 and f-10-350-01. It should be noted that the visually observed extent of fibre bridging was smaller in the specimens tested under fatigue loading compared to the specimens tested under quasi-static loading. The microscopic analysis, performed on selected specimens, revealed the deviation of the crack from the mid-plane to the adjacent layers (Fig. 11). A transverse cracking was found in c-5-330-01, which was a source for additional interlayer cracks, as it was also the case in quasi-static testing (Fig. 11a, Fig. 6a). The multiple interlayer delamination was observed in f-5-330-01, which was already seen in not-tested and quasi-static tested specimens (Fig. 11b, Fig. 4b, Fig. 6b).



**Table 10.** Number of delaminations visually observed on the side specimen surfaces during fatigue tests.

Specimen	Damage process observed	Specimen	Damage process observed
c-5-330-01	+1 delamination below	f-5-330-01	+1 delamination below
c-5-330-02	single delamination	f-5-330-02	single delamination
c-5-330-03	+1 delamination below	f-5-330-03	+1 delamination below
c-10-350-01	+1 tiny delamination below	f-10-350-01	single delamination
c-10-350-02	single delamination	f-10-350-02	+1 delamination below
c-10-350-03	+1 tiny delamination below	f-10-350-03	+1 delamination below

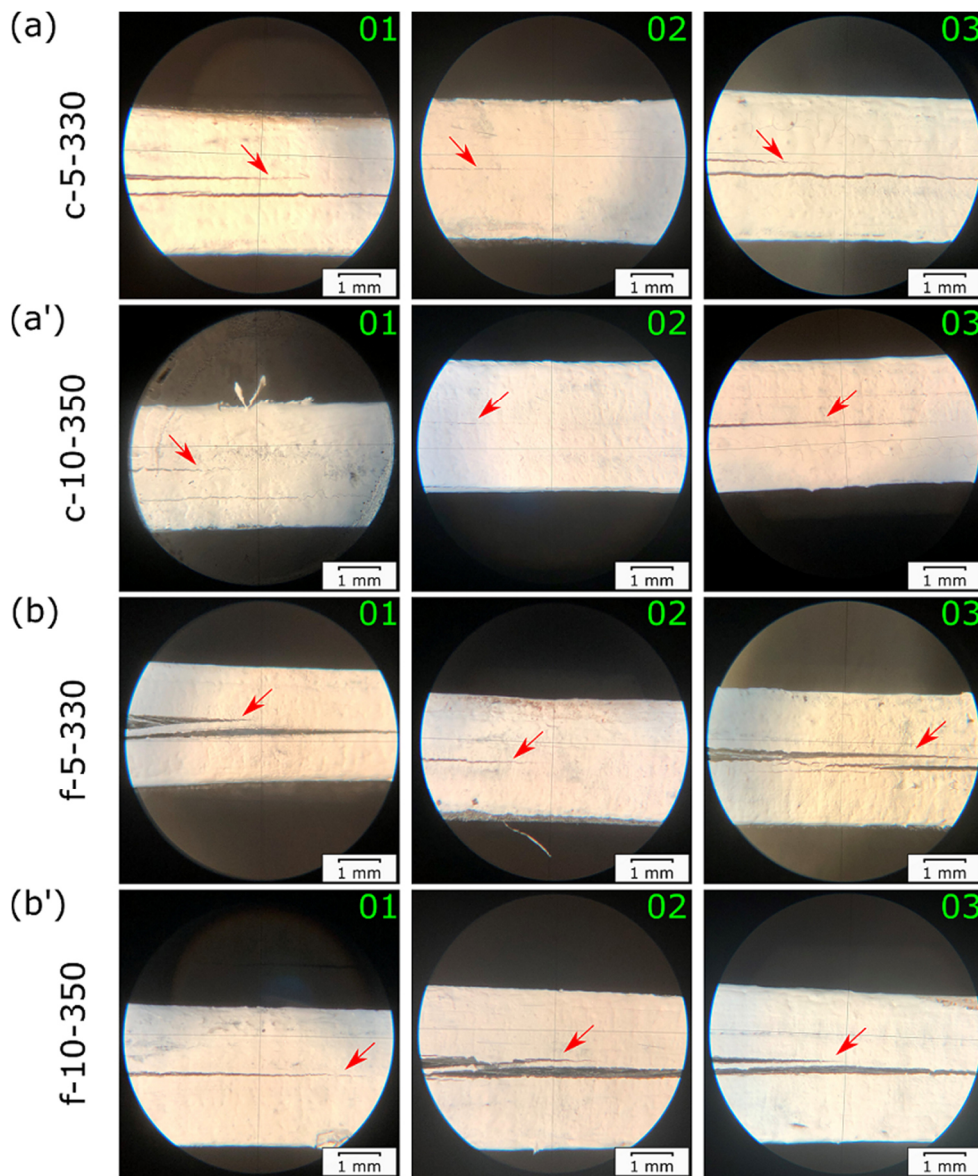


**Fig. 10.** Illustrative images of delamination growth in c-5-330 (a), c-10-350 (a'), f-5-330 (b) and f-10-350 (b') tested under fatigue. Three specimens for every laminate are presented and sequentially numbered with 01, 02 and 03. The pictures were taken when the crack length reached about 40 mm. The red arrows point at the mid-plane delamination.

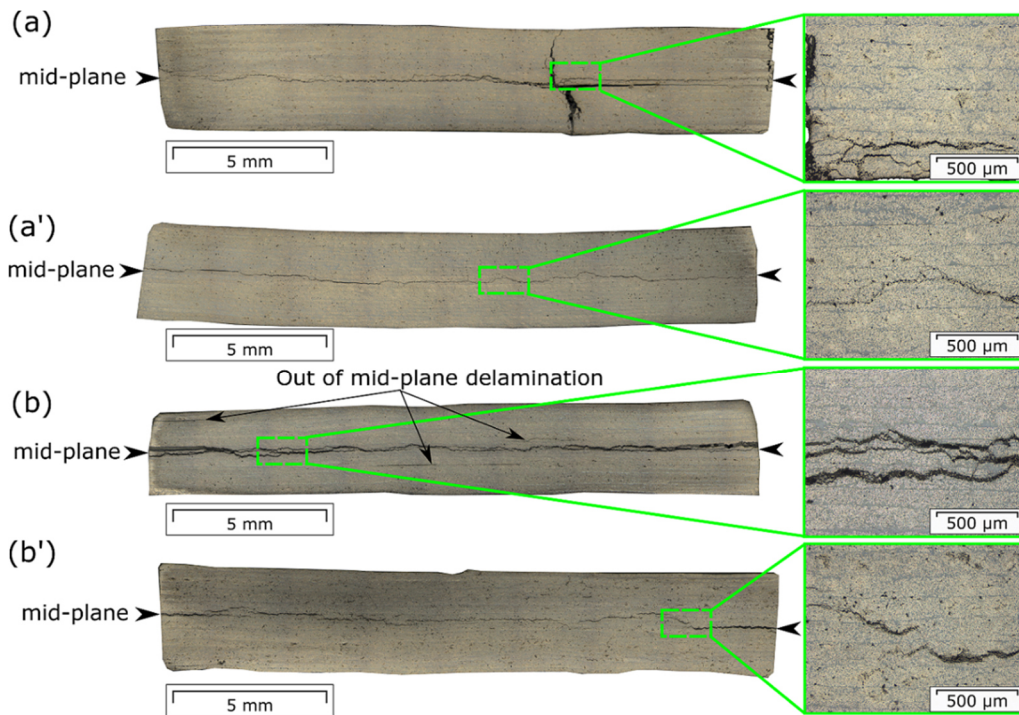


**Fig. 11.** Micrographs of the polished cross sections of selected specimens after fatigue testing: c-5-330-01 (a), c-10-350-03 (a'), f-5-330-01 (b) and f-10-350-02 (b'). The black arrows point at the mid-plane delamination.

#### **Crack length correction factor $\Delta$ and effective flexural modulus $E_1$**

Figure 12 shows the comparison of the cubic root of the compliance, measured during fatigue tests, plotted versus (i)  $a_m$  visually measured during testing, (ii)  $a_{calc}$  calculated from the machine compliance using Eq. 3, and (iii)  $a_{eff}$  calculated using Eq. 4. In order to check the linearity of the data obtained, linear regressions were fitted to every dataset out of five consecutive points. The results obtained are presented in Fig. 13.

The slope-values of the linear regressions fitted to the visual data exhibited a pronounced scatter, indicating deviation of  $(C/N_{block})^{1/3}$  plotted  $a_m$  from linearity. This implies that the length correction factor  $\Delta$  found using the visual data highly depends on the number of points fitted to the linear regression. It should be noted that the deviation from linearity could be also caused by erroneous crack length measurements made using a travelling microscope, as already discussed for the measurements under quasi-static loading. Interestingly, when the crack length reached about 39 and 48 mm in c-5-330-01 and f-5-330-03, respectively, the compliance continued to increase with following cyclic loading without the crack increment (Fig. 12). This likely implies that although there was no visual crack increment, the specimen compliance increased due to other damage processes occurring in the specimens. In contrast to the visual data, the linear regression slopes of the machine data, obtained for  $a_{calc}$ , gradually decreased with the crack growth, or stayed nearly constant (Fig. 13). Whereas the effective data, obtained for  $a_{eff}$ , had a constant slope over the entire range of the crack length for every specimen, implying the linear relationship between  $(C/N_{block})^{1/3}$  and  $a_{eff}$  as follows from Eq. 4.

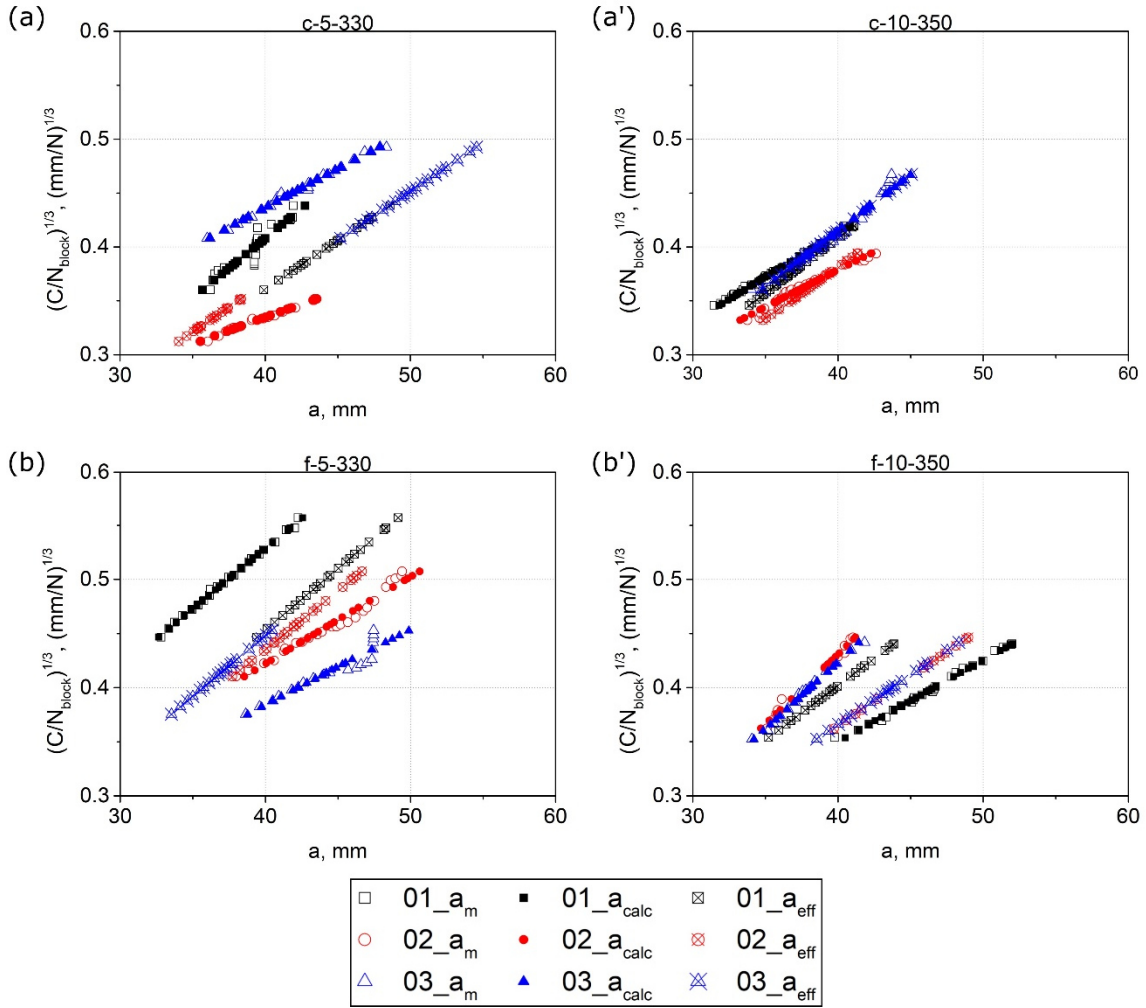


**Fig. 12.** Plots of  $(C/N_{block})^{1/3}$  versus  $a$ , where  $a$  is either  $a_m$ ,  $a_{calc}$  or  $a_{eff}$  for c-5-330 (a), c-10-350 (a'), f-5-330 (b) and f-10-350 (b') tested in fatigue. The legend refers to every plot.

The change in the crack length correction factor  $\Delta$  and the effective flexural modulus  $E_1$  throughout the tests was investigated using the machine data. To this end, linear regressions were fitted to the data range of the first and last 2.5 mm of the crack increment, also to the entire data range. The results obtained are summarized in Table 11 and Table 12 for clamping- and flipping-laminates, respectively. For all specimens with  $\Delta < 0$ , the absolute value of  $\Delta$  was higher at the end than at the beginning of testing, indicating that the effective flexural modulus was increasing with the crack growth. Their values of  $\Delta_{all\ points}$  obtained from the entire data range were in a range between corresponding  $\Delta_{start}$  and  $\Delta_{end}$ . For the specimens with positive  $\Delta$ , the effective flexural modulus had a constant value throughout testing since for its calculation a zero value of  $\Delta$  was used (Eq. 5). The effective flexural moduli of specimens with  $\Delta < 0$  significantly exceeded their  $E_{1,3pb}$  obtained using the three-point bending test (Table 3). High absolute values of the crack length correction factor  $\Delta$  lead to a rapid increase in values of the effective flexural modulus  $E_1$  because the latter is a cubic function of the crack length (Eq. 5).

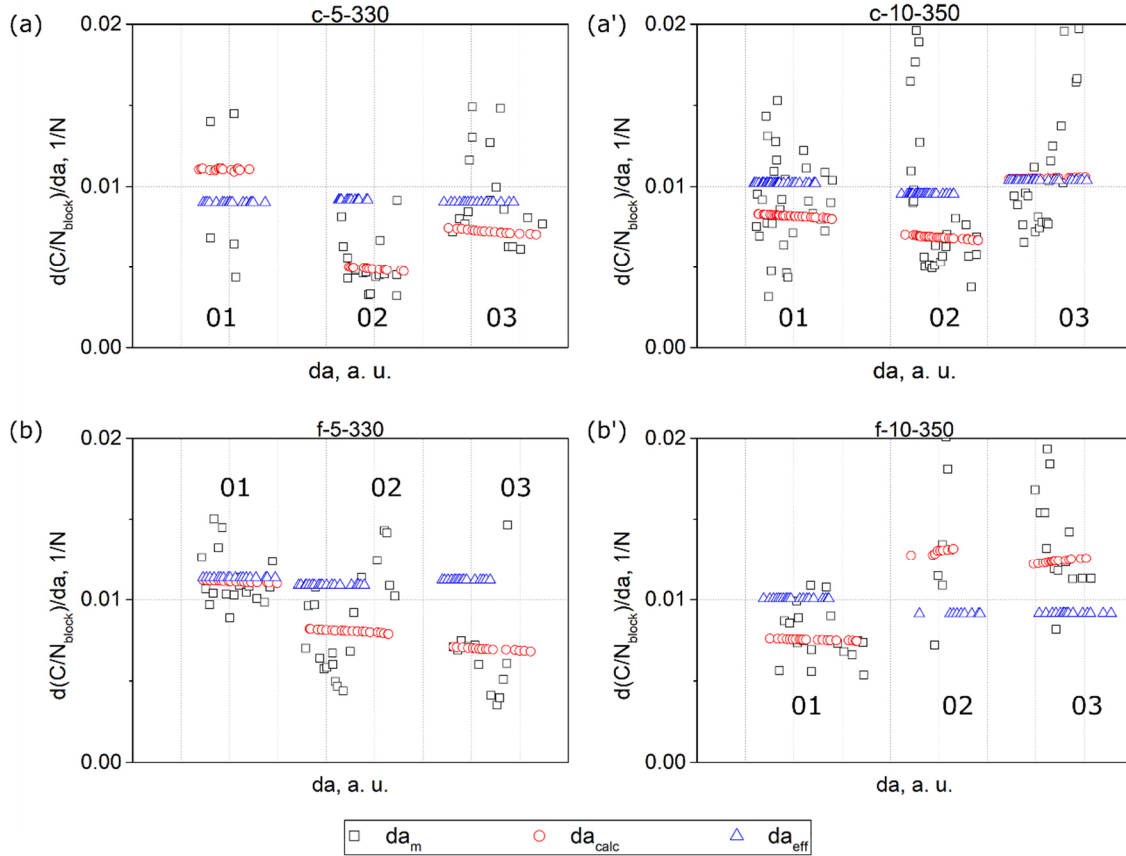


**Fig. 13.** The values of the slopes of linear regressions, which were fitted to datasets of five consecutive points, for c-5-330 (a), c-10-350 (a'), f-5-330 (b) and f-10-350 (b') tested under fatigue loading. 01-03 numbers refer to serial numbers of the specimens. The legend refers to every plot.

**Table 11.**  $\Delta$  and  $E_1$  calculated at the first and the last 2.5 mm of the crack increment ( $\Delta_{\text{start}}, E_{1\text{ start}}$  and  $\Delta_{\text{end}}, E_{1\text{ end}}$ ), and at the entire range of the crack length  $a_{\text{calc}}$  ( $\Delta_{\text{all points}}, E_{1\text{ all points}}$ ) for c-5-330 and c-10-350 tested under fatigue loading.

Specimen	$\Delta_{\text{start}}, \text{mm}$	$\Delta_{\text{end}}, \text{mm}$	$\Delta_{\text{all points}}, \text{mm}$	$E_{1\text{ start}}, \text{GPa}$	$E_{1\text{ end}}, \text{GPa}$	$E_{1\text{ all points}}, \text{GPa}$
c-5-330-01	2.95 *	3.47 *	3.19 *	77±1	77±1	77±1
c-5-330-02	-26.48	-30.24	-28.41	639±2	754±2	697±1
c-5-330-03	-18.47	-22.22	-20.32	197±1	236±1	215±1
<b> Average ± st.dev.   (%)</b>	<b>22.48±5.66 (25%)</b>	<b>26.23±5.67 (22%)</b>	<b>24.37±5.7 (23%)</b>	<b>304±296 (97%)</b>	<b>356±354 (100%)</b>	<b>330±326 (99%)</b>
c-10-350-01	-9.95	-11.17	-10.66	179±1	192±1	186±1
c-10-350-02	-14.16	-16.39	-15.26	311±1	353±1	331±1
c-10-350-03	0.34 *	0.87 *	0.57 *	96±1	96±1	95±1
<b> Average ± st.dev.   (%)</b>	<b>12.06±2.98 (25%)</b>	<b>13.78±3.69 (27%)</b>	<b>12.96±3.26 (25%)</b>	<b>195±109 (56%)</b>	<b>214±130 (61%)</b>	<b>204±119 (58%)</b>

\*  $\Delta > 0$  were excluded from the calculations of the average value, further  $\Delta=0$  was used for the calculations of  $E_1$

**Table 12.**  $\Delta$  and  $E_1$  calculated at the first and the last 2.5 mm of the crack increment ( $\Delta_{start}$ ,  $E_{1\ start}$  and  $\Delta_{end}$ ,  $E_{1\ end}$ ), and at the entire range of the crack length  $a_{calc}$  ( $\Delta_{all\ points}$ ,  $E_{1\ all\ points}$ ) for f-5-330 and f-10-350 tested under fatigue loading.

Specimen	$\Delta_{start}$ , mm	$\Delta_{end}$ , mm	$\Delta_{all\ points}$ , mm	$E_{1\ start}$ , GPa	$E_{1\ end}$ , GPa	$E_{1\ all\ points}$ , GPa
f-5-330-01	-7.26	-8.00	-7.62	99±1	104±1	101±1
f-5-330-02	-11.47	-13.74	-12.56	222±1	250±1	235±1
f-5-330-03	-14.01	-16.67	-15.28	330±1	377±2	352±1
Average ± st.dev.   (%)	10.91±3.41 (31%)	12.80±4.41 (34%)	11.82±3.88 (33%)	217±116 (53%)	244±137 (56%)	229±126 (55%)
f-10-350-01	-6.02	-7.05	-6.55	202±1	214±1	208±1
f-10-350-02	6.27 *	7.27 *	6.72 *	70±3	70±3	70±3
f-10-350-03	5.37 *	6.25 *	5.82 *	75±2	75±2	75±2
Average ± st.dev.   (%)	-	-	-	116±75 (65%)	120±82 (68%)	118±78 (67%)

\*  $\Delta > 0$  were excluded from the calculations of the average value, further  $\Delta=0$  was used for the calculations of  $E_1$

### Damage parameter $\varphi$

The degree of damage in the specimens tested under fatigue loading was estimated using the damage parameter  $\varphi$  that was calculated using  $\Delta_{start}$ ,  $\Delta_{end}$  and  $\Delta_{all\ points}$  obtained in the previous paragraph (Eq. 7'). The results obtained are summarized in Table 13 and Table 14 for clamping- and flipping-laminates, respectively. Since a zero value was used instead of positive  $\Delta$ ,  $\chi^2$  that is  $(\Delta/h)^2$  was equivalent to zero, yielding unphysical values of  $\varphi$  greater than 1. For specimens with  $\varphi$  in a range between 0 and 1,  $\varphi_{start}$  was slightly greater than  $\varphi_{end}$ , indicating the absence of a progressive damage accumulation in them, while in case of quasi-static static testing, the difference between  $\varphi_{start}$  and  $\varphi_{end}$  was more pronounced, reaching a factor of three for some specimens (Table 7, Table 8) However, damage parameters of the specimens tested under fatigue loading were closer to zero than those from quasi-static testing. This could probably indicate that fatigue loading causes a higher degree of damage in specimens than quasi-static loading. Probably this could be explained by a combination of short stress cycles, creep and slight hysteretic heating over a sufficiently long duration of fatigue tests that could yield small distributed damage rather than larger multiple delaminations running parallel to the main delamination in the quasi-static tests. It is also interesting to note that the specimens that exhibited a single mid-plane delamination visually observed on the side specimen surface, namely c-5-330-02, c-10-350-02, f-5-330-02 and f-10-350-01, had damage parameters  $\varphi$  smaller than those obtained for the specimens with multi-cracking (Table 10, Fig. 10). This finding highlights that the mid-plane delamination was not a sole damage process occurring in specimens also during fatigue loading. With regard to the results of the microscopic analysis of the selected specimens cross-sections after fatigue testing, only one of them showed  $\varphi$  in a range between 0 and 1, namely f-5-330-01 (Fig. 11b', Table 14). However, comparing the micrograph of f-5-330-01 after fatigue (Fig. 11b') with that of f-10-350-05 after quasi-static loading (Fig. 6b'), a higher degree of damage can be observed in the former. This is also in agreement with their damage parameters obtained, e.g.  $\varphi_{all\ points}$  of f-5-330-01 (fatigue) is 0.158 and  $\varphi_{all\ points}$  of f-10-350-05 (quasi-static) is 0.383.

**Table 13.**  $\chi^2$  and  $\varphi$  calculated using  $\Delta_{start}$ ,  $\Delta_{end}$  and  $\Delta_{all\ points}$  for the clamping-specimens tested under fatigue loading.

Specimen	$\chi^2_{start}$	$\chi^2_{end}$	$\chi^2_{all\ points}$	$\varphi_{start}$	$\varphi_{end}$	$\varphi_{all\ points}$
c-5-330-01	0	0	0	426.171	426.171	426.171
c-5-330-02	244.1	318.291	280.9	0.018	0.014	0.016
c-5-330-03	118.4	171.344	143.3	0.038	0.026	0.031
c-10-350-01	39.5	49.8	45.4	0.112	0.088	0.097
c-10-350-02	83.2	111.5	96.6	0.066	0.049	0.056
c-10-350-03	0	0	0	391.190	391.190	391.190

**Table 14.**  $\chi^2$  and  $\varphi$  calculated using  $\Delta_{start}$ ,  $\Delta_{end}$  and  $\Delta_{all\ points}$  for the flipping-specimens tested under fatigue loading.

Specimen	$\chi^2_{start}$	$\chi^2_{end}$	$\chi^2_{all\ points}$	$\varphi_{start}$	$\varphi_{end}$	$\varphi_{all\ points}$
f-5-330-01	26.0	31.5	28.6	0.175	0.143	0.158
f-5-330-02	59.7	85.6	71.5	0.074	0.051	0.061
f-5-330-03	87.2	123.5	103.8	0.044	0.031	0.037
f-10-350-01	13.3	18.3	15.8	0.279	0.200	0.233
f-10-350-02	0	0	0	417.974	417.974	417.974
f-10-350-03	0	0	0	432.337	432.337	432.337

#### **Fatigue crack resistance curves: the Paris relation based approach**

In the first step of the fatigue data evaluation, the Paris relation (Eq. 10) was used to present the fatigue delamination resistance using the classic Paris-type plots, where  $da/dN$  was plotted versus  $\sqrt{G_{I_{max}}}$ .  $G_{I_{max}}$  was calculated using either CBT with  $a_{calc}$  or ECM with  $a_{eff}$ . The Paris-like plots obtained are shown in Fig. 14. It can be seen that the position of the plots along the X-axis varied from specimen to specimen within every laminate set, leading to variations of threshold values  $\sqrt{G_{I_{max},th}}$  (Table 15). The smallest standard deviation among the machine data was shown by c-10-350 specimens, in which the lowest extent of damage was visually observed on their side surfaces during testing compared to the other specimens (Fig. 11a'). Importantly, the machine data calculated with  $a_{calc}$  exhibited a larger scatter than the effective data calculated with  $a_{eff}$ . More precisely, the highest standard deviation among the machine data reached 30% for c-5-330, while the highest standard deviation among the effective data was 16% for f-5-330. Thus, the effective data was used for further analysis. The values of standard deviations are given for  $\sqrt{G_{I_{max},th}}$ , which means that the standard deviation for  $G_{I_{max},th}$  is twice as large. The scatter in the fatigue data of UD carbon fibre reinforced composites is well-known in the literature and was discussed in detail in [110]. The authors have differentiated between intrinsic and extrinsic scatter. With regard to the present work, the former comes from the process induced material morphology of the laminates including, e.g., voids, interlayer delaminations, fibre misalignment and other defects observed in the laminate micrographs (Fig. 4). The extrinsic scatter could be caused by possible deficiencies in the test set-up, erroneous crack length measurements by the machine operator and variations in the specimen geometries. In numerous works, e.g. Mujtaba et al. [93], Jones et al. [97], Yao et al. [92], the authors have shown that a fatigue data with a large scatter can be collapsed into a single linear 'master' curve, using the modified Hartman-Schijve equation [75] to present the fatigue data. Therefore, it was decided to apply the Hartman-Schijve based approach in the present research, too.

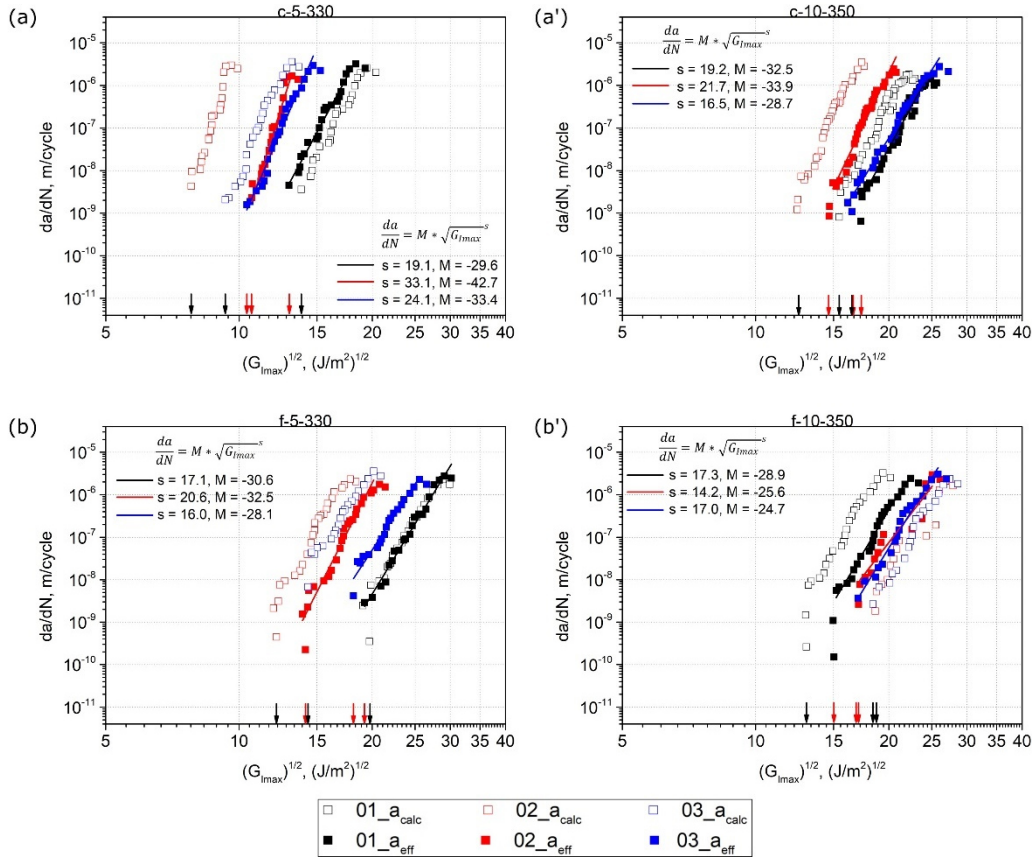


**Fig. 14.** Paris-type plots of  $da/dN$  plotted versus  $\sqrt{G_{I_{max}}}$  calculated using CBT with  $a_{calc}$  and ECLM with  $a_{eff}$  (Eq. 4) for c-5-330 (a), c-10-350 (a'), f-5-330 (b) and f-10-350 (b'). The black and red arrows along the X-axis refer to  $\sqrt{G_{I_{max,th}}}$  of the data calculated using  $a_{calc}$  and  $a_{eff}$ , respectively. Black, red and blue lines refer to linear regressions fitted to the effective data.

**Table 15.** Quasi-static initiation value of the crack growth  $G_{c0}$  and  $\sqrt{G_{I_{max,th}}}$  of the Paris-type plots showed in Fig. 14.

Laminate	$G_{c0}, J/m^2$	$\sqrt{G_{I_{max,th}}}, J/m^2$ using $a_{calc}$	$\sqrt{G_{I_{max,th}}}, J/m^2$ using $a_{eff}$
c-5-330	80.4±64.8 (81%)	10.3±3.1 (30%)	11.4±1.4 (12%)
c-10-350	205.4±40.7 (20%)	14.8±2.1 (14%)	16.1±1.4 (8%)
f-5-330	366.9±401.1 (109%)	15.4±3.9 (25%)	17.2±2.7 (16%)
f-10-350	195.4±58.6 (30%)	16.7±3.2 (19%)	16.4±1.2 (7%)

### Fatigue crack resistance curves: the Hartman-Schijve based approach

The modified H-S equation includes two parameters  $A$  and  $\sqrt{G_{I_{max,thr}}}$  that should be defined for every fatigue data set. According to Jones et al. [75], these parameters are (cite) 'perhaps best viewed as parameters that are used to ensure that the entire range of data fits the equation'. Further, Jones et al. [91] write that  $da/dN$  should be plotted versus  $(\sqrt{G_{I_{max}}} - \sqrt{G_{I_{max,thr}}}) / \sqrt{1 - \frac{\sqrt{G_{I_{max}}}}{\sqrt{A}}}$  on a logarithmic scale, taking parameter  $A$  (cite) 'to be the quasi-static value of the fracture energy,  $G_c$ , or any reasonable first estimate'. Jones et al. [97] noted that  $A$  corresponds to the quasi-static initiation value of the crack growth,  $G_{c0}$ . Thereby,  $A$  equivalent to  $G_{c0}$  was used in the H-S based approach, for example, in [92,62,96]. However, Yao et al. [92] have reported  $A$ -values that significantly exceeded

corresponding  $G_{c0}$ . In the present study, hence two different approaches were applied to use the modified H-S equation to present the fatigue crack growth curves.

According to the first approach, both parameters  $A$  and  $\sqrt{G_{I_{max},thr}}$  were varied for every individual test data set in a way that a linear regression fitted to this data reaches the highest  $R^2$ -ratio. In the second approach,  $A$  was kept constant and  $\sqrt{G_{I_{max},thr}}$  was varied to achieve the highest  $R^2$ -ratio of the linear fit. The appropriate parameters were configured automatically by means of a script written in Python. From the formula (Eq. 11),  $\sqrt{G_{I_{max},thr}}$  must be smaller than the smallest value of  $\sqrt{G_{I_{max}}}$  from a dataset, so that the right-hand member of the equation is positive, while  $\sqrt{A}$  must be greater than this value, so that the radicand of the square root is positive. Thus, in the first approach,  $A$  was continuously increased from a value a bit higher than  $G_{I_{max}}$  with an increment step of  $50 \text{ J/m}^2$ . In the second approach, a value of  $950 \text{ J/m}^2$  was used for  $A$ , which was reported in [80] as a reference value for UD CF/PPS laminates produced by ATPisc.  $A$  could not be taken to be equivalent to actual  $G_{c0}$  values obtained from the quasi-static pre-cracking, because they were smaller than the smallest value of  $\sqrt{G_{I_{max}}}$  for nearly all specimens (Table 15). For every  $A$ ,  $\sqrt{G_{I_{max},thr}}$  was continuously increased from a value of  $1 \text{ VJ/m}$  with an increment step of  $0.05 \text{ VJ/m}$  till the highest value of  $\sqrt{G_{I_{max}}}$ . Following this procedure, the highest  $R^2$ -ratios of the linear fits were determined. The results obtained are summarized in Table 16. Figure 15 illustrates the crack growth rate  $da/dN$  plotted versus the right-hand component of the modified H-S equation with  $A$  and  $\sqrt{G_{I_{max},thr}}$  from Table 16.

Following the first approach, the highest  $R^2$ -ratios of linear regressions were achieved with  $A$ -values significantly higher than  $G_{c0}$  (Table 15), which can no longer have a physical meaning. Only  $A$  of about  $690 \text{ J/m}^2$  obtained for specimens f-10-350-01 and -02 were in a comparable range with  $G_{c0}$ . Remarkably, the second approach where  $A$  was kept constant of  $950 \text{ J/m}^2$ , which seems to be a reasonable value for the initiation value of the crack growth in UD CF/PPS laminates, yielded the results of  $\sqrt{G_{I_{max},thr}}$  close to those from the first approach. At the same time, the difference in their  $R^2$ -ratios was observed only in the third digit after the decimal point. In addition, the second approach yielded a better agreement of the fatigue crack growth curves of the flipping laminates compared to the first approach (Fig. 15). There was no such significant difference observed between the curves of the clamping laminates. These findings highlight the second approach using a constant value of  $A$  of  $950 \text{ J/m}^2$  to make overall sense in the application to the laminates investigated.

**Table 16.**  $A$  and  $\sqrt{G_{I_{max},thr}}$  which yield the highest  $R^2$ -ratios of the linear fits of the fatigue data using the modified Hartman-Schijve equation where ( $A$  was varied//  $A$  kept constant) (Eq. 11).

Specimen	$A, \text{J/m}^2$	$\sqrt{G_{I_{max},thr}}, \sqrt{\text{J/m}}$	$R^2$ -ratio
c-5-330-01	5322 // 950	9.8 // 10.5	0.9852 // 0.9845
c-5-330-02	5135 // 950	4.1 // 5.1	0.9700 // 0.9698
c-5-330-03	5183 // 950	7.7 // 8.0	0.9854 // 0.9849
<b>Average ± st.dev.</b>		<b>7.2±2.9 (40%) // 7.9±2.7 (34%)</b>	
c-10-350-01	5606 // 950	12.5 // 14.8	0.9815 // 0.9792
c-10-350-02	5381 // 950	11.9 // 12.4	0.9894 // 0.9888
c-10-350-03	5694 // 950	11.6 // 14.3	0.9904 // 0.9863
<b>Average ± st.dev.</b>		<b>12.0±0.5 (4%) // 13.8±1.3 (9%)</b>	
f-5-330-01	5861 // 950	10.8 // 17.9	0.9907 // 0.9707
f-5-330-02	5408 // 950	10.9 // 11.8	0.9728 // 0.9719
f-5-330-03	5655 // 950	13.6 // 16.2	0.9791 // 0.9779
<b>Average ± st.dev.</b>		<b>11.8±1.6 (14%) // 15.3±3.1 (21%)</b>	
f-10-350-01	652 // 950	13.8 // 13.2	0.9713 // 0.9709
f-10-350-02	731 // 950	16.4 // 15.9	0.9683 // 0.9663
f-10-350-03	5677 // 950	11.9 // 14.8	0.9825 // 0.9766
<b>Average ± st.dev.</b>		<b>14.1±2.2 (16%) // 14.6±1.4 (9%)</b>	



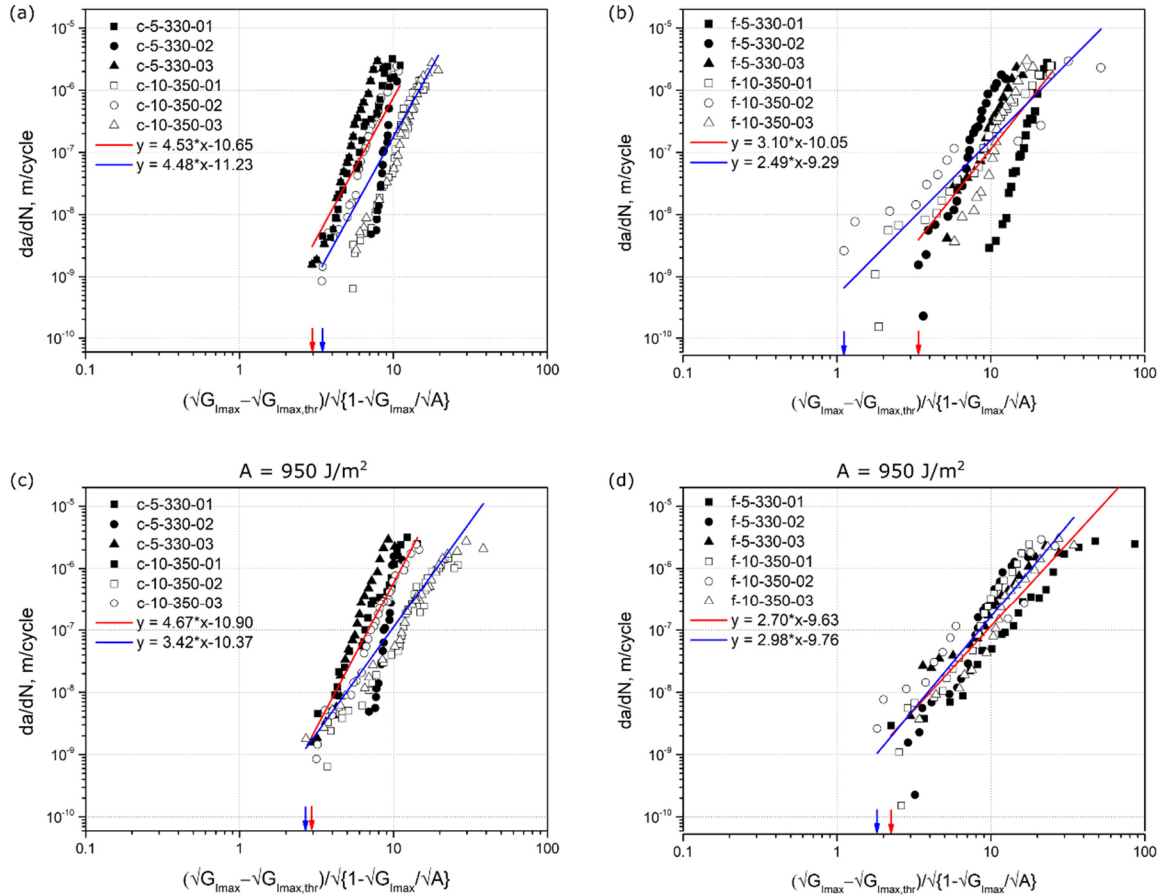


**Fig. 15.** Fatigue crack growth resistance curves obtained using the modified Hartman-Schijve equation, where the parameter  $A$  was either varied (a, b) or kept constant (c, d) for every specimen of clamping- (a,c) and flipping- (b,d) laminates. Red and blue lines refer to linear regressions fitted to the data of laminates produced with 5 m/min and 330 °C and to those produced with 10 m/min and 350 °C, respectively.

### Zero fibre bridging approach

The fatigue crack growth curves of fatigue loadings sequentially performed on a single DCB specimen of the c-10-350 laminate type are shown in Fig. 16. In this figure,  $da/dN$  is plotted versus  $\sqrt{G_{I_{max}}}$ , where  $a$  refers to either  $a_m$  measured visually with the microscope during testing (Fig. 16a),  $a_{calc}$  calculated using Eq. 3 (Fig. 16b), or  $a_{eff}$  calculated using Eq. 4 (Fig. 16c).

According to the ‘zero fibre bridging’ methodology [76], the fatigue delamination curves shift to the right along the X-axis when sequential, quasi-static pre-cracking is performed after a given number of fatigue cycles yielding one mode I H-S-curve length and developing fibre bridging between the specimen beams. The moment when these curves no longer shift to the right, but overlap, corresponds to the fully developed fibre bridging state, i.e., - fibre bridging saturation. In the visually measured data, the shift to the right was observed for the second fatigue loading with respect to the first fatigue loading (Fig. 16a). This is in agreement with the ‘zero fibre bridging’ methodology. However, the curve of the third fatigue loading appeared to the left of the second curve. The fourth curve of the last fatigue loading performed nearly overlapped with the third curve, indicating an apparent saturation state. Whether this is really the case requires further quasi-static pre-cracking followed by cyclic fatigue fracture steps. The unexpected shift to the left of the 3rd curve could possibly be caused by a failure of a larger fibre or fibre bundle bridge connecting two specimen beams. After

such a breakage, the crack would propagate faster due to a lesser retarding effect of fibre bridging, which would lead to a reduction of  $G_{I_{max}}$ . Thereby, two competing mechanisms can be distinguished, i.e., a consistent increase of fibre bridging until a saturation state is reached versus the discrete formation and stochastic failure of ‘large’ fibre bridges. In addition, interlayer delaminations developing during testing influence the bending moments of the specimen beams, which in turn effects the specimen stiffness and the strain energy release rate. Therefore, the ‘zero fibre bridging’ methodology may not work in case of a discontinuous development of fibre bridging (or of more massive bridging of the main delamination, e.g. caused by multiple cracks) that results in stochastic bridge-breaks and hence does not continuously evolve into a steady-state.

Interestingly, the shift to the left of the 3<sup>rd</sup> and 4<sup>th</sup> curves was not so pronounced for the data of  $a_{calc}$  (Fig. 16b). Whereas for the effective data of  $a_{eff}$ , the 2<sup>nd</sup>, 3<sup>rd</sup> and 4<sup>th</sup> curves overlapped at their upper parts and even exhibited a shift to the right comparing their middle parts (Fig. 16c). These findings indicate that the mid-plane crack propagation was significantly influenced by multiple cracking. On the other hand, they could also suggest that the crack length was incorrectly measured during testing. The crack length measurements were very challenging to perform visually using a travelling microscope in the case of such a complex crack propagation behaviour combined with the sequential series of quasi-static and fatigue loadings.

Next steps of the ‘zero fibre bridging’ methodology were performed on the fatigue crack growth curves with  $a_{eff}$  (Fig. 16c), since they showed the most similar behaviour to that described in this methodology [76]. Firstly, the data points of every curve were translated to an arbitrary value of  $da_{eff}/dN$  of  $10^{-7}$  m/cycle using Eq. 12 (Fig. 17). After that, average values  $(\sqrt{G_{I_{max}}})_{avr,T}$  of the data translated were calculated for every curve.

$$\log_{10}\sqrt{G_{I_{max},T}} = \frac{1}{m} \left( \log_{10} \frac{da}{dN_T} - \log_{10} \frac{da}{dN} \right) + \log_{10}\sqrt{G_{I_{max}}} \quad (12)$$

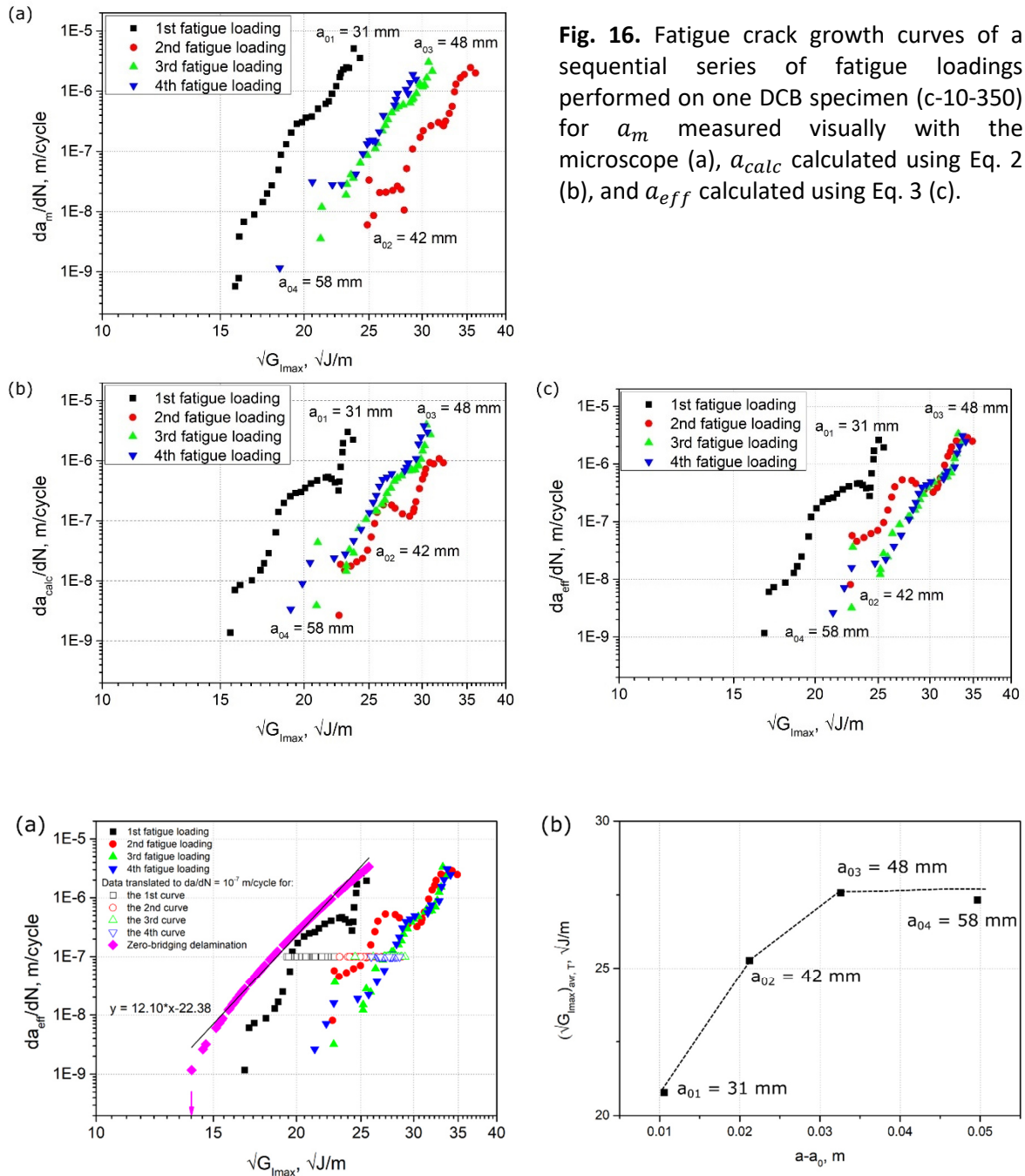
where  $da/dN_T = 10^{-7}$  m/cycle,  $m$  is the power index in the Paris equation (Eq. 3).

Figure 17b shows a plot of  $(\sqrt{G_{I_{max}}})_{avr,T}$  versus the corresponding crack length, which is described with a non-linear relationship. Alderliesten et al. [76] write that this relationship can be described with a second order polynomial function of  $a - a_0$ , which reaches a horizontal asymptote at the moment of full development of fiber bridging. Further, the regression analysis was performed using Eq. 13 as described in the methodology. Finally, the zero fiber bridging curve ( $a - a_0 = 0$ ) was obtained then using Eq. 14 and presented in Fig. 17a.  $\sqrt{G_{I_{max},thr}}$  deduced from this curve is about  $13.9 \sqrt{J}/m$ , which is in good agreement with the Hartman-Schijve results for c-10-350 (Table 16).

$$\log_{10}\sqrt{G_{I_{max}}} = C_0 + C_1(a - a_0) + C_2 \log_{10} \frac{da}{dN} + C_3(a - a_0)^2 + C_4 \left( \log_{10} \frac{da}{dN} \right)^2 \quad (13)$$

where  $C_i$  are constants obtained through regression,  $i = [0, 4]$ .

$$\log_{10}(\sqrt{G_{I_{max}}})_{a-a_0} = C_0 + C_2 \log_{10} \frac{da}{dN} + C_4 \left( \log_{10} \frac{da}{dN} \right)^2 \quad (14)$$



**Fig. 16.** Fatigue crack growth curves of a sequential series of fatigue loadings performed on one DCB specimen (c-10-350) for  $a_m$  measured visually with the microscope (a),  $a_{calc}$  calculated using Eq. 2 (b), and  $a_{eff}$  calculated using Eq. 3 (c).

**Fig. 17.** The ‘zero fibre bridging’ analysis: the data translated to an arbitrary value of  $da/dN = 10^{-7}$  m/cycle for every curve (unfilled symbols) and the final zero-bridging curve (pink rhombuses) (a), the average values of the translated data versus the crack length (b).

#### 4.1.7. Conclusion

The present study deals with the problem of multiple cracking in unidirectional CF/PPS laminates produced by automated tape placement with in-situ consolidation (ATPisc). The laminates, produced by following different manufacturing protocols, exhibited multiple interlayer cracking during mode I DCB testing under both quasi-static and fatigue loading. Therefore, various analysis techniques were applied and compared in an attempt at quantifying the damage effects in the laminates.

Three different definitions of the crack length  $a$  were applied: (i)  $a_m$  measured visually with a travelling microscope, (ii)  $a_{calc}$  back-calculated using the machine compliance and (iii)  $a_{eff}$  calculated using the flexural modulus and the compliance. The cubic root of the compliance plotted versus the crack length visually measured was found to have different slopes at the beginning and at the end of both quasi-static and fatigue tests. These results may indicate the presence of additional damage processes occurred in the specimens during main mid-plane crack growth. In order to quantify the degree of damage in the specimens, the damage parameter  $\varphi$  [74] was used. The comparison of  $\varphi$  at the beginning and at the end of testing enabled a better understanding of the damage development in every specimen tested. The quasi-static crack growth was presented using R-curves. The fatigue crack growth was presented using both the classic Paris relation based approach [63,82] and a modified Hartman-Schijve equation based approach [91]. In addition, the methodology eliminating fibre bridging in fatigue testing [76] was applied for the first time to the laminates with multiple cracking. Three-point bending tests were employed to identify if whether the damage effects led to a change in flexural modulus, but these turned out to be not sensitive enough. Moreover, a microscopic analysis of the laminate cross-sections was performed to examine damage in the specimens prior to and after DCB testing.

Thereby, the present study provides a sort of report on the quantitative characterization of UD carbon fibre reinforced thermoplastic laminates exhibiting multiple cracking during mode I DCB testing. Future research can focus on a finite element modelling of crack propagation in such laminates in order to estimate the effect of multiple cracking on the bending moments of specimen beams and to calculate the real change of energy release rate. In addition, further tests and analysis are required to validate the applicability of the 'zero fibre bridging' approach to the laminates with multiple cracking.

## Appendix A

The transverse and shear moduli were estimated according to Reuss model using Eq. 1a and Eq. 2a.

$$E_2 = \frac{E_{2f}E_m}{E_m f_v + E_{2f}(1 - f_v)} \quad (1a)$$

$$G_{12} = \frac{G_{12f}G_m}{G_m f_v + G_{12f}(1 - f_v)} \quad (2a)$$

$$G_m = \frac{E_m}{2(1 + \nu_m)}$$

The following values were used for Young's modulus and Poisson's ratio of PPS, transverse and shear moduli of the carbon fibre:  $E_m = 3.45$  GPa [111],  $\nu_m = 0.38$  [112],  $E_{2f} = 13$  GPa [113],  $G_{12f} = 11.3$  GPa [113].

**Table 1a.** The transverse and shear moduli calculated for every laminate.

Laminate	$E_2$ , GPa	$G_{12}$ , GPa
c-5-330	6.01	2.58
c-10-350	5.69	2.39
f-5-330	5.56	2.31
f-10-350	6.20	2.70

## Funding

The research work was performed within the COMET project VI-2.06, 'New strategies towards laser assisted manufacturing of fibre reinforced thermoplastic composites,' at the Polymer Competence Center Leoben GmbH (PCCL, Austria) within the framework of the COMET program of the Federal Ministry for Transport, Innovation and Technology and the Federal Ministry of Science, Research and Economy with contributions by Technical University of Munich (Institute for Carbon Composites), Montanuniversitaet Leoben (Institute of Material Science and Testing of Polymers), AFPT and Cevotec. The PCCL is funded by the Austrian Government and the State Governments of Styria, Lower Austria and Upper Austria.

## Acknowledgments

Special thanks go to Sebastian Maar and Franz Grassegger for their assistance with the specimen preparations.

### 4.1.8. References

- [1] Grouve WJB, Warnet LL, Rietman B, Visser HA, Akkerman R. Optimization of the tape placement process parameters for carbon-PPS composites. *Compos. Part A Appl. Sci. Manuf.* 2013;50:44–53.
- [2] Comer AJ, Ray D, Obande WO, Jones D, Lyons J, Rosca I et al. Mechanical characterisation of carbon fibre-PEEK manufactured by laser-assisted automated-tape-placement and autoclave. *Compos Part A Appl Sci Manuf* 2015;69:10–20.
- [3] Stokes-Griffin CM, Compston P. Investigation of sub-melt temperature bonding of carbon-fibre/PEEK in an automated laser tape placement process. *Compos Part A Appl Sci Manuf* 2016;84:17–25.
- [4] Stokes-Griffin CM, Compston P. The effect of processing temperature and placement rate on the short beam strength of carbon fibre-PEEK manufactured using a laser tape placement process. *Compos Part A Appl Sci Manuf* 2015;78:274–83.
- [5] Adams ME, Campbell GA, Cohen A. Thermal stress induced damage in a thermoplastic matrix material for advanced composites. *Polym. Eng. Sci.* 1991;31(18):1337–43.
- [6] Ray D, Comer AJ, Lyons J, Obande W, Jones D, Higgins RMO et al. Fracture toughness of carbon fiber/polyether ether ketone composites manufactured by autoclave and laser-assisted automated tape placement. *J. Appl. Polym. Sci.* 2014;132(11).
- [7] Zhang Y, Xia Z, Ellyin F. Evolution and influence of residual stresses/strains of fiber reinforced laminates. *Compos Sci Technol* 2004;64(10-11):1613–21.
- [8] Gillespie JW, Chapman TJ. The Influence of Residual Stresses on Mode I Interlaminar Fracture of Thermoplastic Composites. *J. Thermoplast. Compos. Mater.* 1993;6(2):160–74.
- [9] Khan MA, Mitschang P, Schledjewski R. Parametric study on processing parameters and resulting part quality through thermoplastic tape placement process. *J. Compos. Mater* 2013;47(4):485–99.
- [10] Pitchumani R, Ranganathan S, Don RC, Gillespie Jr JW, Lamontia MA. Analysis of transport phenomena governing interfacial bonding and void dynamics during thermoplastic tow-placement. *Int. J. Heat Mass Transf.* 1996;39(9):1883–97.
- [11] ISO15024: 2001. Fibre-reinforced Plastic Composites: Determination of Mode I Interlaminar Fracture Toughness, GIC, for Unidirectionally Reinforced Materials.: International Organization for Standardization; 2001.
- [12] Brunner AJ, Stelzer S, Pinter G, Terrasi GP. Cyclic fatigue delamination of carbon fiber-reinforced polymer-matrix composites: Data analysis and design considerations. *International Journal of Fatigue* 2016;83:293–9.

- [13] Stelzer S, Pinter G, Brunner AJ. Comparison of Quasi-static and Cyclic Fatigue Delamination Resistance of Carbon Fiber Reinforced Polymer-matrix Laminates under Different Mode Loading. *Procedia Materials Science* 2014;3:1087–92.
- [14] Sørensen BF, Gamstedt EK, Østergaard RC, Goutianos S. Micromechanical model of cross-over fibre bridging – Prediction of mixed mode bridging laws. *Mechanics of Materials* 2008;40(4-5):220–34.
- [15] Hashemi S, Kinloch AJ, Williams JG. The Analysis of Interlaminar Fracture in Uniaxial Fibre-Polymer Composites. *Proc R Soc Lond* 1990;427(1872):173–99.
- [16] Yao L, Alderliesten R, Zhao M, Benedictus R. Bridging effect on mode I fatigue delamination behavior in composite laminates. *Compos Part A Appl Sci Manuf* 2014;63:103–9.
- [17] Yao L, Alderliesten RC, Benedictus R. The effect of fibre bridging on the Paris relation for mode I fatigue delamination growth in composites. *Compos Struct* 2016;140:125–35.
- [18] Albersen H, Ivens J, Peters P, Wevers M, Verpoest I. Interlaminar fracture toughness of CFRP influenced by fibre surface treatment: Part 1. Experimental results. *Compos Sci Technol* 1995;54(2):133–45.
- [19] Sorensen L, Botsis J, Gmür Th, Humbert L. Bridging tractions in mode I delamination: Measurements and simulations. *Compos Sci Technol* 2008;68(12):2350–8.
- [20] Sorensen L, Botsis J, Gmür T, Cugnoni J. Delamination detection and characterisation of bridging tractions using long FBG optical sensors. *Compos Part A Appl Sci Manuf* 2007;38(10):2087–96.
- [21] Herráez M, Pichler N, Botsis J. Improving delamination resistance through tailored defects. *Compos Struct* 2020;247:112422.
- [22] Kachanov, M., Montagut, E.L.E. and Laures, J.P. Mechanics of crack—microcrack interactions. *Mechanics of Material* 1990;10(1-2):59–71.
- [23] Chudnovsky A WS. Effect of crack-microcracks interaction on energy release rates. *Int J Fract* 1990;44(1):43–56.
- [24] Brunner AJ, Blackman BRK, Williams JG. Calculating a damage parameter and bridging stress from GIC delamination tests on fibre composites. *Compos Sci Technol* 2006;66(6):785–95.
- [25] Jones R, Pitt S, Bunner AJ, Hui D. Application of the Hartman–Schijve equation to represent Mode I and Mode II fatigue delamination growth in composites. *Compos Struct* 2012;94(4):1343–51.
- [26] Alderliesten R (ed.). *Fatigue delamination of composite materials—approach to exclude large scale fibre bridging*. 1st ed; 2018.
- [27] Modi, D; Comer, A; O'Higgins, R.M.O; McCarthy, M. A. *Thermoplastic composites: in-situ consolidation or in-situ welding*; 2013.
- [28] Qureshi Z, Swait T, Scaife R, El-Dessouky HM. In situ consolidation of thermoplastic prepreg tape using automated tape placement technology: Potential and possibilities. *Compos B Eng* 2014;66:255–67.
- [29] Bandaru, A.K; Clancy, G.J; Peeters, D; O'Higgins, R; Weaver, P.M. *Interface characterization of thermoplastic skin-stiffener composite manufactured using laser-assisted tape placement*; 2018.
- [30] Sacchetti F, Groupe WJB, Warnet LL, Villegas IF. Effect of cooling rate on the interlaminar fracture toughness of unidirectional Carbon/PPS laminates. *Eng. Fract. Mech.* 2018;203:126–36.
- [31] Brunner AJ, Stelzer S, Pinter G. *Determination of Mode I Fatigue Delamination Propagation in Unidirectionally Reinforced Materials: Test Protocol*.
- [32] Stelzer, S and Pinter, G and Wolfahrt, M and Brunner, AJ and Noisternig, J. *Cyclic Interlaminar Crack Growth in Unidirectional and Braided Composites. Fatigue Behaviour of Fiber Reinforced Polymers: Experiments and Simulations*, Weixing 2012.
- [33] Alderliesten R. *Fatigue delamination of composite materials – approach to exclude large scale fibre bridging*. *IOP Conf. Ser.: Mater. Sci. Eng.* 2018;388:12002.

- [34] Standard test methods for flexural properties of unreinforced and reinforced plastics and electrical insulating materials (ASTM D790).
- [35] Brunner AJ, Murphy N, Pinter G. Development of a standardized procedure for the characterization of interlaminar delamination propagation in advanced composites under fatigue mode I loading conditions. *Eng. Fract. Mech.* 2009;76(18):2678–89.
- [36] Morais AB de, Pereira AB. Application of the effective crack method to mode I and mode II interlaminar fracture of carbon/epoxy unidirectional laminates. *Compos Part A Appl Sci Manuf* 2007;38(3):785–94.
- [37] Brunner AJ, Blackman BRK, Williams JG. Deducing Bridging Stresses and Damage from GIC Tests on Fibre Composites. In: Blackman BRK, Pavan A, Williams JG, editors. *Fracture of polymers, composites, and adhesives II*. Amsterdam, Boston: Elsevier; 2003, p. 479–490.
- [38] Younes R, Hallal A, Fardoun F, Hajj F. Comparative Review Study on Elastic Properties Modeling for Unidirectional Composite Materials. In: Hu N, editor. *Composites and Their Properties: InTech; uuuu-uuuu*.
- [39] ASTM E 647. Standard test method for measurement of fatigue crack growth rates: Annual book of ASTM standards; 2011.
- [40] Jones R, Hu W, Kinloch AJ. A convenient way to represent fatigue crack growth in structural adhesives. *Fatigue Fract Eng Mater Struct* 2015;38(4):379–91.
- [41] Yao L, Alderliesten RC, Jones R, Kinloch AJ. Delamination fatigue growth in polymer-matrix fibre composites: A methodology for determining the design and lifing allowables. *Compos Struct* 2018;196:8–20.
- [42] Mujtaba A, Stelzer S, Brunner AJ, Jones R. Influence of cyclic stress intensity threshold on the scatter seen in cyclic Mode I fatigue delamination growth in DCB tests. *Compos Struct* 2017;169:138–43.
- [43] Jones R, Kinloch AJ, Hu W. Cyclic-fatigue crack growth in composite and adhesively-bonded structures: The FAA slow crack growth approach to certification and the problem of similitude. *International Journal of Fatigue* 2016;88:10–8.
- [44] Yao L, Sun Y, Guo L, Lyu X, Zhao M, Jia L et al. Mode I fatigue delamination growth with fibre bridging in multidirectional composite laminates. *Eng. Fract. Mech.* 2018;189:221–31.
- [45] Jones R, Hu W, Kinloch AJ. A convenient way to represent fatigue crack growth in structural adhesives. *Fatigue Fract Eng Mater Struct* 2015;38(4):379–91.
- [46] Jones R, Kinloch AJ, Michopoulos JG, Brunner AJ, Phan N. Delamination growth in polymer-matrix fibre composites and the use of fracture mechanics data for material characterisation and life prediction. *Compos Struct* 2017;180:316–33.
- [47] Brunner AJ, Stelzer S, Mujtaba A, Jones R. Examining the application of the Hartman-Schijve equation to the analysis of cyclic fatigue fracture of polymer-matrix composites. *Theoretical and Applied Fracture Mechanics* 2017;92:420–5.
- [48] Brunner AJ, Mujtaba A, Stelzer S, Jones R. Modified Hartman-Schijve fitting of mode I delamination fatigue data and the resulting variation in threshold values  $G_{thr}$ . *Procedia Structural Integrity* 2016;2:88–95.
- [49] Yee RY, Stephens TS. A TGA technique for determining graphite fiber content in epoxy composites. *Thermochimica Acta* 1996;272:191–9.
- [50] Barnes J. A., Byerly G. E. The formation of residual stresses in laminated thermoplastic composites. *Compos Sci Technol* 1994;51(4):479–94.
- [51] Sonmez FO, Hahn HT, Akbulut M. Analysis of Process-Induced Residual Stresses in Tape Placement. *J. Thermoplast. Compos. Mater.* 2002;15(6):525–44.

- [52] Tafreshi OA, van Hoa S, Shadmehri F, Hoang DM, Rosca D. Heat transfer analysis of automated fiber placement of thermoplastic composites using a hot gas torch. *Advanced Manufacturing: Polymer & Composites Science* 2019;5(4):206–23.
- [53] Kollmannsberger A, Lichtinger R, Hohenester F, Ebel C, Drechsler K. Numerical analysis of the temperature profile during the laser-assisted automated fiber placement of CFRP tapes with thermoplastic matrix. *J. Thermoplast. Compos. Mater.* 2018;31(12):1563–86.
- [54] Ghadirdokht A, Heidari-Rarani M. Delamination R-curve behavior of curved composite laminates. *Compos B Eng* 2019;175:107139.
- [55] Yokozeki T, Ogasawara T, Aoki T. Correction method for evaluation of interfacial fracture toughness of DCB, ENF and MMB specimens with residual thermal stresses. *Compos Sci Technol* 2008;68(3-4):760–7.
- [56] Nairn JA. Energy release rate analysis for adhesive and laminate double cantilever beam specimens emphasizing the effect of residual stresses. *International Journal of Adhesion and Adhesives* 2000;20(1):59–70.
- [57] Liu D, Zhu Y, Ding J, Lin X, Fan X. Experimental investigation of carbon fiber reinforced poly(phenylene sulfide) composites prepared using a double-belt press. *Compos B Eng* 2015;77:363–70.
- [58] Choi NS, Kinloch AJ, Williams JG. Delamination Fracture of Multidirectional Carbon-Fiber/Epoxy Composites under Mode I, Mode II and Mixed-Mode I/II Loading. *Journal of Composite Materials* 1999;33(1):73–100.
- [59] Davies P, Cantwell W, Moulin C, Kausch HH. A study of the delamination resistance of IM6/PEEK composites. *Compos Sci Technol* 1989;36(2):153–66.
- [60] Alderliesten RC, Brunner AJ, Pascoe JA. Cyclic fatigue fracture of composites: What has testing revealed about the physics of the processes so far? *Eng. Fract. Mech.* 2018;203:186–96.
- [61] <https://www.bearingworks.com/uploaded-assets/pdfs/retainers/pps-datasheet.pdf>.
- [62] [https://www.celanese.com/-/media/Engineered%20Materials/Files/Product%20Technical%20Guides/PPS-050\\_Fortron\\_DesignManualTG\\_AM\\_0913.pdf](https://www.celanese.com/-/media/Engineered%20Materials/Files/Product%20Technical%20Guides/PPS-050_Fortron_DesignManualTG_AM_0913.pdf).
- [63] Herráez M, Mora D, Naya F, Lopes CS, González C, LLorca J. Transverse cracking of cross-ply laminates: A computational micromechanics perspective. *Compos Sci Technol* 2015;110:196–204.



## 4.2. Automated monitoring of the crack propagation in mode I testing of thermoplastic composites by means of digital image correlation

### 4.2.1. Bibliographic information

- Authors and their relevant contribution to the publication:
  - A. Khudiakova<sup>1</sup>: Conceptualisation, Methodology, Software, Validation, Investigation, Writing-original draft, Writing – review and editing
  - V. Grasser<sup>1</sup>: Investigation, Validation
  - C. Blumenthal<sup>2</sup>: Software, Methodology
  - M. Wolfahrt<sup>1</sup>: Project administration, Funding acquisition, Writing – review and editing, Supervision
  - G. Pinter<sup>3</sup>: Resources, Supervision, Writing – review and editing, Conceptualisation
  
- Affiliations:
  - <sup>1</sup>Polymer Competence Center Leoben GmbH, Roseggerstraße 12, 8700 Leoben, Austria
  - <sup>2</sup>GOM GmbH, Schmitzstraße 2, 38122 Braunschweig, Germany
  - <sup>3</sup>Institute of Materials Science and Testing of Polymers, Montanuniversität Leoben, Otto Gloeckel-Straße 2, 8700 Leoben, AT

Published in Polymer Testing 82 (2020)

*The manuscript is presented here in accordance with the publisher's copyright policy: 'Authors can include their articles in full or in part in a thesis or dissertation for non-commercial purposes.' Elsevier.com*

#### 4.2.2. Abstract

One of the main challenges of the mode I double cantilever beam (DCB) test is the simultaneous determination of the applied load and displacement with the developing delamination length. The present work addresses this issue by side-view tracking the crack propagation by means of digital image correlation (DIC). Two different reduction methods were developed to determine the crack length from the DIC data. On the one hand, the crack tip position was defined by the high strain concentration in the immediate vicinity of the crack tip, and on the other hand, by crack tip opening displacement (CTOD). The data obtained enabled the calculation of the energy release rate of carbon fibre reinforced thermoplastic specimens with either run-arrest or stable crack extension. For reasons of comparability, top surface analysis (TSA), as recently reported, was also carried out. Following this approach, the crack propagation was tracked applying DIC to the top specimen surface. The methods developed showed a good correlation with both the standardised procedure and TSA. It was shown that DIC can be used as an alternative to the conventional optical measuring tools to follow the crack propagation in the mode I DCB test.

#### 4.2.3. Introduction

The mode I double cantilever beam (DCB) test is a fracture mechanics (FM) test commonly applied to investigate the material resistance to crack propagation in unidirectional (UD) composites [114,115]. The procedure of the mode I DCB test is standardised and presented in ASTM D 5528 [116] and ISO 15024 [61], where the interlaminar fracture toughness is characterised in terms of strain energy release rate (ERR),  $G_I$ . According to the standards, every crack increment of 5 mm has to be recorded together with the corresponding force and displacement signals. These values are required for calculations of  $G_{Ic}$ , the critical value of ERR, which corresponds to the released energy per crack area sufficient for the crack growth [117]. Force and displacement values are usually acquired by means of an action button in the machine software, which should be pressed at the moment of the crack increment. At the same time, a travelling microscope or any equivalent magnifying device is used to follow the delamination on the specimen edge with the hand-marked scale. Therefore, the DCB testing can be a time and effort consuming process, the results of which rely on a well-practiced machine operator ensuring the accuracy of the experimental data.

To make the testing procedure less labour-intensive, methods other than the conventional optical approach were applied, for instance acoustic emission [68], Moiré interferometry [118,119], fibre Bragg grating sensing techniques [69] and digital image correlation (DIC) [120–126]. In contrast to the first three methods, DIC does not require complex sample preparations and is faster in post-processing the data [127]. DIC allows the detection of the full-field displacement on the sample surface by correlating images taken during the test. Displacement is computed by tracking the initially introduced stochastic dot pattern (speckle) on the sample surface, which changes during load application [128–130]. Although there is an increasing amount of literature on the application DIC in fracture mechanical testing, there are only few studies which have used DIC to follow mode I crack propagation in fibre reinforced plastic (FRP) laminates [121–125].

Merzkirch et al. [121] tested UD carbon fibre reinforced epoxy laminates under mode I quasi-static loading along with DIC. In their work, the absolute coordinate of the crack tip position was defined by a parameter ‘sigma,’ which describes the quality of the pixel correlation to the reference image. It was shown that the crack length can be obtained by monitoring the loss of the image

correlation in the vicinity of a crack tip, where 'sigma' is zero due to the absence of the speckle between open beams. The same methodology was used by Murray et al. [122], where the application of DIC was extended to static and dynamic loading conditions, including mode II testing. Zhu et al. [125] applied DIC to monitor the crack propagation in the mode I fatigue test of carbon fibre reinforced epoxy laminates. The crack tip position was determined by a coordinate where the variation of vertical displacement became zero. In the authors' previous work [123], DIC was applied to monitor crack propagation in UD CF/ PPS laminates by means of strains. The crack tip position was defined by a coordinate of a certain strain value obtained along a line drawn parallel to the crack propagation plane. The certain strain value, which yielded better agreement with the conventional measurements, was defined by a visual comparison of the DIC strain field with the actual crack tip on the images. In the aforementioned studies, the DIC cameras monitored the crack propagation on the side specimen surface in common with the conventional approach described in the standards. Reiner et al. [124] proposed a new methodology to apply DIC to the top surface of the specimen in order to obtain crack length, called top surface analysis (TSA). According to TSA, the crack tip position is defined by crack tip opening displacement (CTOD) computed along lines drawn parallel to the long specimen edge. Such an approach enables additional determination of the crack tip position along the width of a DCB sample. TSA showed good agreement with the conventional measurements of the mode I fracture performed on carbon and glass fibre reinforced epoxy (CFRP, GFRP) laminates.

The present paper aims to contribute to the development of the automated measurement of the crack propagation in mode I DCB testing by means of DIC. The tests were performed on carbon fibre reinforced polyether ether ketone (CF/PEEK) laminates with two already known behaviours of crack propagation, stable and abrupt [131]. Two different reduction methods were introduced to define crack length from the DIC data obtained from the side-view measurements. In the first method, the crack tip position is localised by means of the high strain concentration in the immediate vicinity of the crack tip. It was proposed that the absolute maximum strain be used instead of a certain strain value used in the previous study [123] to define a crack tip position. This method is called the strain method. In the second method, the crack tip position is defined by means of CTOD measured between opened beams. This method is called the CTOD method. For reasons of comparability, TSA was performed additionally according to Reiner et al. [124]. The application of TSA was extended to a material system different from that used by Reiner et al. [124]. Crack length measured according to the proposed methods was used for calculations of  $G_{Ic}$ . The results obtained regarding crack length and  $G_{Ic}$  were compared with the conventional measurements performed with a magnifying glass. The results were in good agreement with the standardised procedure proving that DIC can be used as a promising technique to follow the crack propagation in the mode I DCB test, instead of conventional optical tools, such as a microscope or a magnifying glass. The application of DIC is especially recommended in case of a high number of tests. The essential advancement of the present manuscript over the state of the art is the detailed description of the newly developed methods, which are meant to serve as a guideline for the interested reader.

#### 4.2.4. Experimental

##### **DCB specimens and testing**

Unidirectional CF/PEEK specimens with two ways of crack growth, a slow stable extension and a run-arrest extension, were used in the present work. The different crack growth behaviours were known beforehand from the previous study [131], where different types of carbon fibres were used in

the production of the laminates. Hereafter, specimens with the stable crack propagation are called 'CF/PEEK\_stable,' and those with abrupt jumps 'CF/PEEK\_unstable.' Measurements performed with a magnifying glass are named 'conventional.'

Double cantilever beam specimens had a rectangular shape and geometrical dimensions of 145 x 20 x 3 mm<sup>3</sup>. The specimens had a separation Teflon<sup>®</sup> film with a thickness of 20 µm and a length of 35 mm for the crack initiation. Steel blocks were glued to the specimens with DP 490 Scotch Weld adhesive (3M, United Kingdom) and cured at 65 °C for 2 hours. Prior to testing, the specimens were pre-notched with a sharp blade to avoid tab separation while loading. A millimetre scale was hand-marked on the side specimen surface to follow the delamination length with a magnifying glass.

The mode I interlaminar fracture toughness tests were performed on a servo-hydraulic test machine, MTS 810 (MTS Systems Corporation, Germany), with a 25 kN load cell according to ASTM D 5528 [116]. Four specimens of each crack propagation type were tested under standardised laboratory conditions (23 °C air temperature, 50% relative humidity). After creating a pre-crack to exclude the influence of the separation film, the specimens were tested at 2.5 mm/min under displacement control. For CF/PEEK\_stable, the crack increment was recorded every 5 mm together with corresponding force and displacement using an action button in the MTS software. For CF/PEEK\_unstable, the length of every crack increment was recorded, and force and displacement were taken from the force-displacement curves at the run and arrest points. The tests were interrupted as the delamination was about 100 mm and the specimens were unloaded.

### **DIC preparations and setup**

Prior to testing, a fine black and white stochastic dot pattern was introduced on the side and top surfaces for the side (the strain and CTOD methods) and top (TSA) measurements, respectively. As the pattern quality plays a decisive role in the DIC results, it is important that the speckle stays on the specimen surface during testing and does not vanish due to crack propagation [122]. This often occurs in cases of abrupt delamination, when the speckle disappears in front of the crack tip, causing a failure in the DIC analysis. Therefore, the coating should adhere well to the surface to ensure data processing in DIC. This was achieved with the white correction fluid Tipp-Ex (Société Bic, France). The black spray paint Graphit33 (CRC Industries Europe, Belgium) was used to apply the speckle pattern following the procedure established thorough the measuring routine.

The Aramis optical system (GOM GmbH, Germany), with two 4 megapixel cameras, was used to perform the DIC. Force and displacement signals from the testing machine were recorded in the DIC software, which was started simultaneously with the tests. For the strain and CTOD methods, the cameras directly faced the side specimen surface. For the TSA method, the cameras were tilted 60° from the vertical (Fig. 1). The cameras were calibrated using a calibrating panel with reference points to define the respective measuring volumes. The calibration deviation was less than 0.03 pixels in all tests and the cameras took two pictures per second.

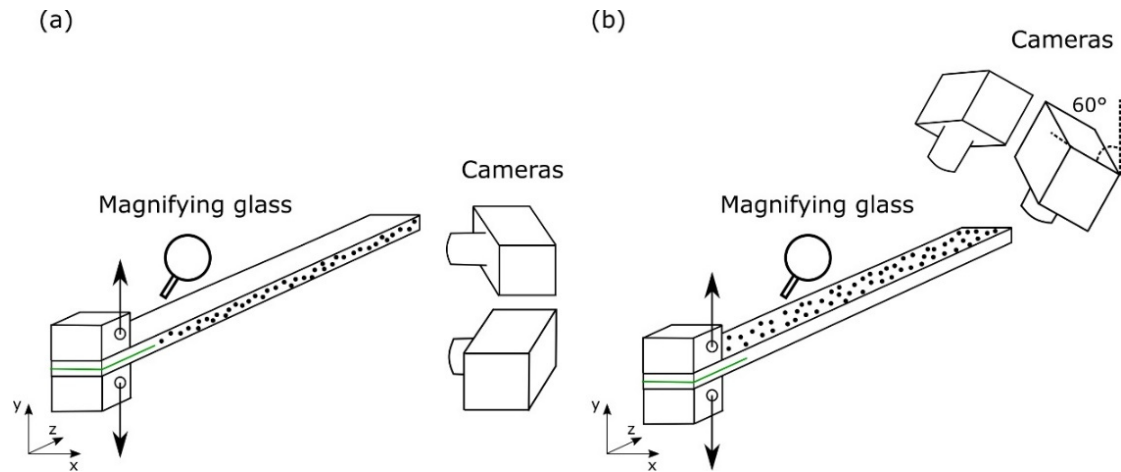


**Fig. 1.** Arrangement of the cameras relative to the specimen for measurements using (a) the strain and CTOD methods and (b) the TSA method. The green colouring identifies the separation film.

### DIC parameters

The DIC analysis was performed using GOM Correlate Professional software (GOM GmbH, Germany). The region of interest (ROI) was a side surface in the strain and CTOD methods, and a top surface in TSA. The optimal subset and step sizes were chosen after preliminary examinations of the applied stochastic dot patterns. According to recommendations from the international DIC society [132], a subset should have a size containing sufficient information such that one subset can be distinguished from all other subsets in the ROI. One subset should include nearly the same number of light and dark pattern. A subset should not be so large that the data is excessively smoothed and specific features, such as the crack tip, cannot be differentiated. At the same time, too small subset size leads to higher displacement noise. Step size defines the distance between subsets and the number of points with computed data. It is recommended that a step size of one-third to one-half of the subset size be used [132]. The crack tip is a relatively tiny feature, so big subsets led to the excessive spatial smoothing of the data near it. Figure 2 demonstrates a difference between two ROIs computed with different subset and step sizes in the side DIC measurements performed. The bigger subsets of  $21 \times 21 \text{ pixel}^2$  and a step of 7 pixels included a large portion of the crack tip area, which led to the excessive data smoothing. The bigger subset size also resulted in a processing area far behind the crack tip, where no more pattern was between open beams. A smaller subset size in conjunction with a smaller step size allowed data processing close to the crack edges. Subsets of  $6 \times 6 \text{ pixel}^2$  and a step of 3 pixels were used as the smallest parameters, which yielded a well-processed area. The subset size smaller than 6 pixels led to an area maculated with non-computed domains such that the investigated data reduction methods could not be applied. Regarding the top surface measurements, the ROI did not contain small features, such as the crack tip. It was also bigger than the ROI in the side surface measurements, which caused a longer computing time. For that reason, bigger subset and step sizes were chosen for the top surface analysis;  $21 \times 21 \text{ pixel}^2$  and 7 pixels, respectively [132].

Another parameter which can be varied in the data processing is the strain filter. The filter can be applied to reduce possible data noise or to emphasise local effects (e.g. local strain concentrations) [133]. The DIC software used offers options for a temporal and a spatial strain filter. The temporal filter considers a point over a certain period of time, whereas the spatial filter takes into account the neighbourhood of a computing point. Each of the filters can be selected as average, binomial or polynomial. The influence of the filtering on the DIC results was investigated for instance in [134,135].

It was shown that filtering can lead to the loss of the information due to smoothing of the strain gradients and that it is a time-consuming process in case of the processing of big data files [135]. Since the primary goal of the present work was to verify the applicability of the developed data reduction methods in general, the effect of the strain filter was beyond the scope of this study. Thus, the strain filter was set to zero in all DIC analyses.

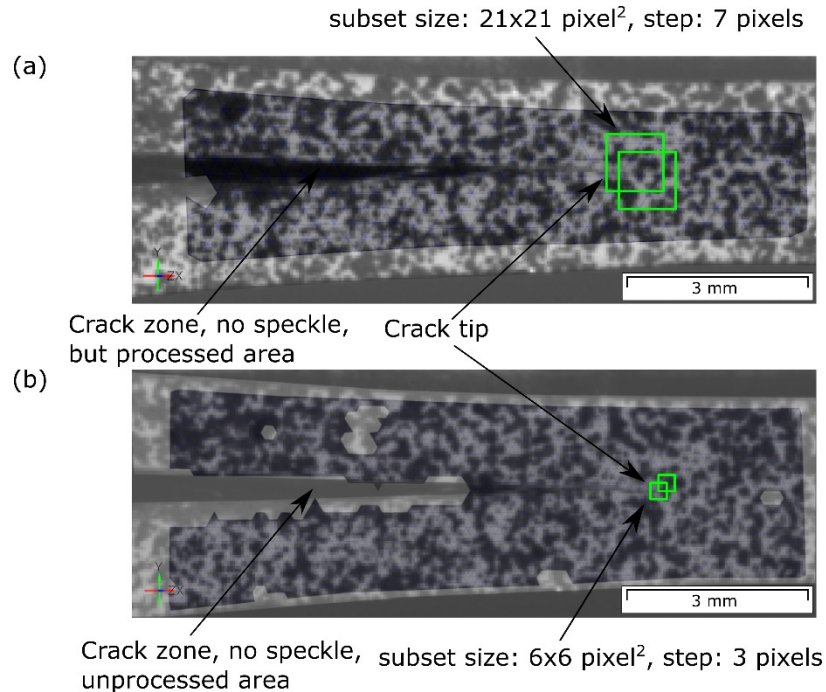


**Fig. 2.** Computed regions of interest in the vicinity of the crack tip with the subset and step sizes of (a) 21x21 pixel<sup>2</sup>, 7 pixels and (b) 6x6 pixel<sup>2</sup>, 3 pixels, respectively. 1 pixel was about 0.05 mm. The green squares identify subsets that were used to compute the regions of interest.

#### 4.2.5. Data reduction methods

##### The strain method

According to the elastic stress field solutions, stress tends to infinity at the tip of an elastic crack [115,117]. The stress singularity leads to the high strain concentration in the near-tip region. Therefore, the developed strain method proposes defining the crack tip position by the maximum strain value in the immediate vicinity of the crack tip. In this method, strains in transverse direction  $\varepsilon_y$  are obtained along a section (line) drawn in the crack propagation plane (Fig. 3a). Thus, every image has a distribution of strains with corresponding coordinates along the crack plane. From nearly zero in a part of the specimen not yet damaged, strains increase close to the crack tip and reach the maximum value. The length coordinate of the line which corresponds to the maximum strain is used to calculate crack length.

In terms of using the maximum strain to determine the crack propagation, this method is similar to the approach followed by Mallon et al. [126]. The authors determined the temporal onset of the crack propagation in the mode I test of single-edge notched specimens by means of DIC. They monitored the history of the strain magnitude  $\varepsilon_y$  during loading at a point placed slightly below or above the crack propagation path. The dramatic drop in the strain magnitude corresponded to the

exact moment of the crack growth initiation. The present study proposes to obtain strains along the line in order to assure a continuous monitoring of the crack propagation throughout the test (Fig. 3a).

### The CTOD method

In the CTOD method developed, measurements are also performed on the side specimen surface, but a quantity of interest obtained here is displacement. According to this approach, crack opening displacement (COD)  $d$ , which corresponds to the distance between opened beams, is continuously measured between two sections (lines) drawn parallel above and below the crack propagation plane (Fig. 3b). There are two possibilities to define a criterion to localise the crack tip by COD. The first and most obvious is that a coordinate of the crack tip is defined as a coordinate where the absolute difference between  $d$ , calculated along the lines in the opposite direction to the crack propagation, exceeds zero. However, this can be applied only in a case of the linear elastic crack propagation with a sharp tip. In case of the plastic deformation in front of the crack tip, the change in the COD corresponds to the plastic deformation of the matrix, and not to the crack tip. Moreover, there is always a greater or smaller presence of noise in the DIC data. This means that the absolute difference between  $d$  is never equal to zero and a small tolerance value should be used. The second possibly is to use a threshold value of COD  $d_{th}$ , which can be estimated by crack tip opening displacement (CTOD). CTOD is a crack tip characterising parameter which can be found, according to Eq. 1, within the framework of linear elastic fracture mechanics (LEFM) [115].

$$CTOD = \frac{4 G_{Ic}}{\pi \sigma_{ys}} \quad (1)$$

in which  $\sigma_{ys}$  refers to the yield strength and  $G_{Ic}$  to the mode I strain energy release rate obtained from the preliminary tests. As  $d$  exceeds a value of CTOD  $d_{CTOD}$ , the corresponding coordinate is used to calculate the crack length. As per Eq. 1, the CTOD calculated using  $\sigma_{ys}$  of 1.5 GPa taken from [136] and the obtained  $G_{Ic}$  of 1880 J/m<sup>2</sup> for CF/PEEK\_stable was about 0.002 mm assuming the linear elastic behaviour [137]. This value was used for  $d_{CTOD}$  to define the crack length. However, Eq. 1 cannot be applied to laminates with the run-arrest behaviour due to uncertainty regarding which  $G_{Ic}$  value to use,  $G_{Ic\_start}$  or  $G_{Ic\_arrest}$ . For this reason, crack length was additionally defined with  $d_{th}$  of 0.005 mm and 0.015 mm for CF/PEEK\_unstable. These thresholds were chosen from the preliminary DIC analysis, where higher values led to the underestimated crack length.

### The TSA method

In the TSA method, the crack tip position is also defined by a coordinate of CTOD, but obtained from the top surface. Following the approach developed by Reiner et al. [124], the displacement  $d_y$  of the top surface is computed along sections (lines) drawn parallel to the long specimen edge (Fig. 3c). In the present paper,  $d_y$  was obtained along 13 lines. The central axis of the specimen, which corresponds to the crack path, is found as a linear regression of  $d_y$  along every line length. Considering the noise effect in the DIC data measurements, a small tolerance value  $d_{th}$  of 0.02 mm was used to localise the crack tip [124]. The crack tip position is defined as a deviation point of  $d_y$  from the linearity  $d_{linear}$ , when  $(d_y - d_{linear})$  exceeds  $d_{th}$  for every line. More details on TSA can be found in [124].

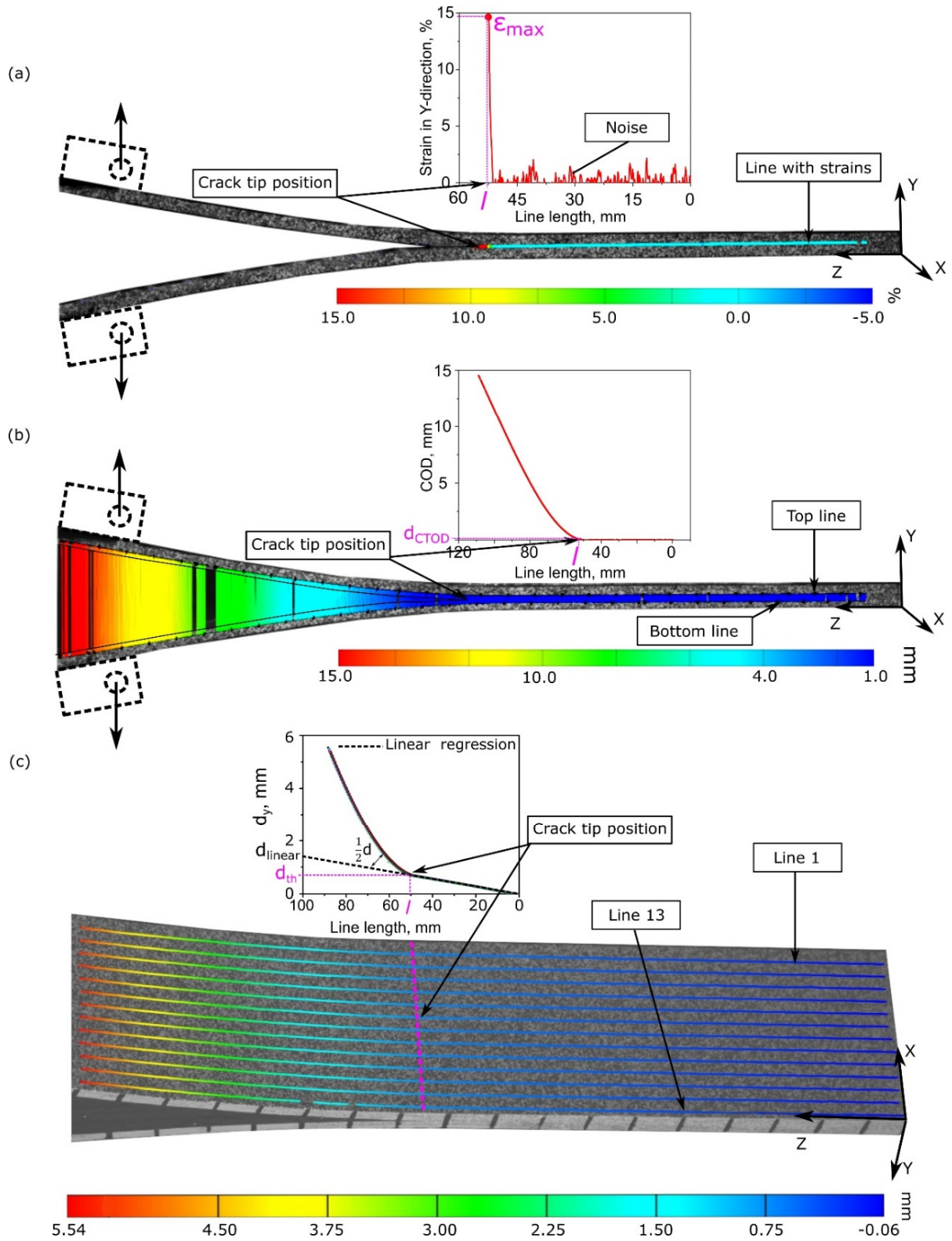


**Fig. 3.** Schemes of the data reduction methods: (a) the strain method, (b) the CTOD method and (c) the TSA method. The pink dashed line on the specimen surface presents the crack front.

### $G_{IC}$ calculations

Crack lengths obtained by the aforementioned methods were used for calculations of  $G_{IC}$ , which was determined according to the simple beam theory (BT) (Eq. 2).



$$G_{Ic} = \frac{3P\delta}{2Ba} \quad (2)$$

in which  $P$  refers to the load,  $\delta$  to the displacement,  $B$  to the specimen width and  $a$  to the delamination length [116]. The results achieved were compared with  $G_{Ic}$  calculated with  $a$  measured with a magnifying glass. Figure 4 presents flowcharts which were used for the data processing according to the strain, CTOD and TSA methods.

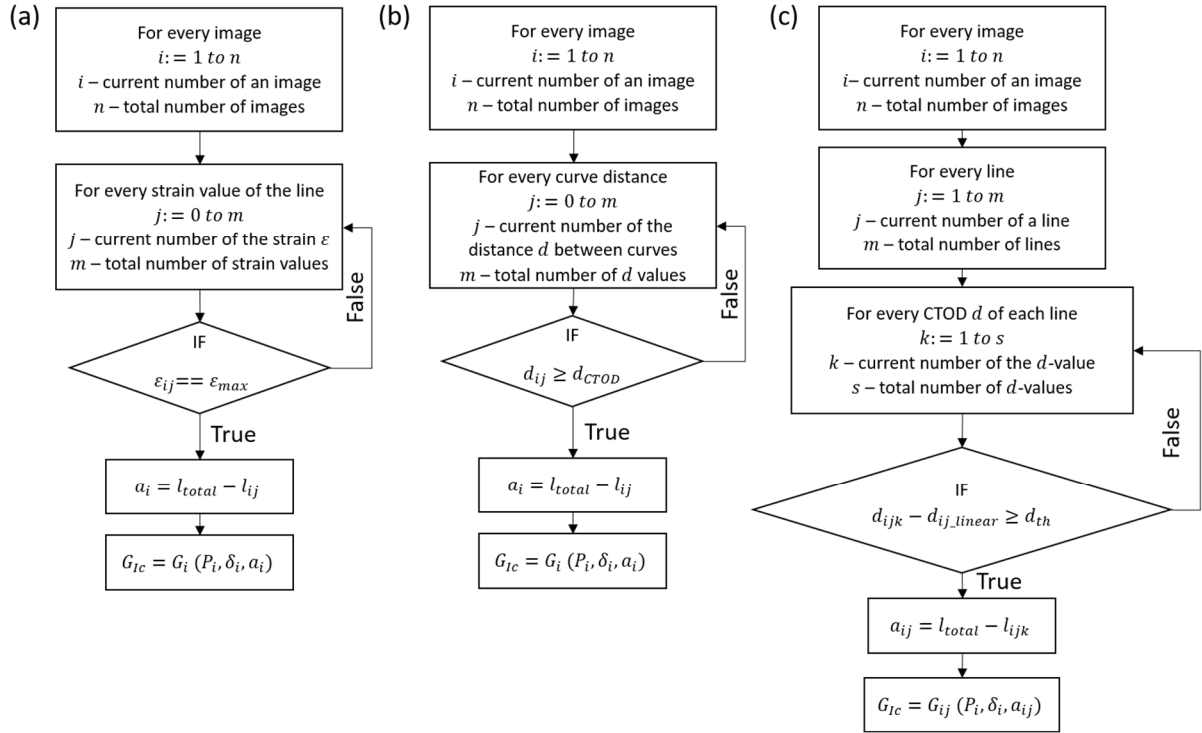


**Fig. 4.** Flowcharts of  $G_{Ic}$  calculations with data obtained by means of DIC according to (a) the strain method, (b) the CTOD method and (c) the TSA method.

#### 4.2.6. Results and discussions

The first paragraph of this section presents  $G_{Ic}$  results yielded in the conventional way according to ASTM D 5528 [116]. The results of CF/PEEK\_stable and CF/PEEK\_unstable are presented separately in the following paragraphs for the strain and CTOD methods. The last paragraph of this section contains TSA results for both laminate types.

#### Fracture toughness $G_{Ic}$ by the conventional measurements

For specimens with stable crack growth,  $G_{Ic\_propagation}$  was calculated for every crack increment of 5 mm with the corresponding force and displacement. The results showed about  $1880 \pm 50$  J/m<sup>2</sup> (Fig. 6a', b', Fig. 8a'). Figure 5a demonstrates the fracture surface of CF/PEEK\_stable with a smooth structure and good fibre alignment. The presence of plastically deformed ridges of PEEK matrix, appeared as white lines oriented parallel to the direction of crack growth, indicates sufficient fibre/matrix adhesion (Fig. 5a'). The  $G_{Ic\_propagation}$  correlates favourably with other works about fracture toughness characterisations of CF/PEEK DCB specimens [131,65,138,139].

In the case of the run-arrest delamination, the force-displacement curve has a saw-toothed shape, where force drops after every crack extension and increases again [140,141]. Therefore, two

data sets  $G_{Ic\_start}$  and  $G_{Ic\_arrest}$  were calculated using the maximums and minimums of the force-displacement curve, respectively [142]. For CF/PEEK\_unstable,  $G_{Ic\_start}$  and  $G_{Ic\_arrest}$  were about  $2030 \pm 110 \text{ J/m}^2$  and  $950 \pm 100 \text{ J/m}^2$ , respectively (Fig. 7a',b', Fig. 8b').  $G_{Ic\_start}$ , which is considered as a static property characterising the amount of energy required for the crack extension, was found to be close to  $G_{Ic\_propagation}$  of CF/PEEK\_stable [142]. The fracture surface of the tested CF/PEEK\_unstable specimen is depicted in Fig. 5b. The surface contains white striations perpendicular to the crack growth direction, corresponding to plastic deformations of the matrix in front of the crack tip. The plastic deformations cause the crack blunting, which is one of the reasons for the run-arrest propagation [143]. A micrograph of CF/PEEK\_unstable demonstrates a pronounced waviness of the fibres (Fig. 5b'), which is not the case for CF/PEEK\_stable (Fig. 5a). This also explains the difference in the crack propagation behaviours. Micrographs were made with the optical microscope Olympus SZX12 (Olympus Corporation, Japan).

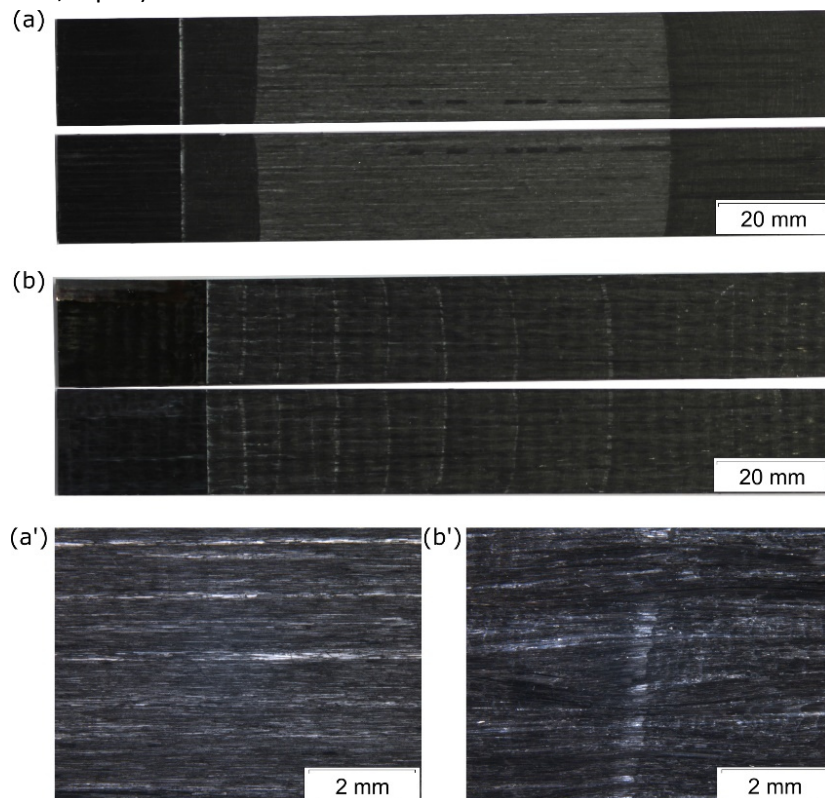


**Fig. 5.** Pictures of fracture surfaces of the (a) CF/PEEK\_stable and (b) CF/PEEK\_unstable specimens after testing and their corresponding micrographs (a', b').

#### DIC results of specimens with the stable crack propagation

The results of the crack length achieved with the strain and CTOD methods for specimens with the stable delamination are presented in Fig. 6a and b, respectively. The methods were applied to the same specimens due to the equivalent side-view testing procedure. Both the strain and CTOD methods resulted in good agreement with the conventional measurements. The crack growth characterised using DIC completely repeats the tendency of the conventional results.

Plots of  $G_{Ic}$  calculated with the obtained crack length are depicted in Fig. 6a' and b' for the strain and CTOD methods, respectively. The DIC data contains a large number of dots, because every image is processed with corresponding values of force, displacement and crack length. When the crack remains stationary, but force and displacement increase, the  $G_{Ic}$  data assumes the shape of bars for

every crack length. For CF/PEEK\_stable, the bars are short and situated close to each other. This conveys that the crack propagated in a not perfectly stable way, but with micro jumps, whose start and arrest points were not possible to record due to the short time between them. A scatter between minimum and maximum values of bars increased from about 200 J/m<sup>2</sup> to 360 J/m<sup>2</sup> during the test. This corresponds to a slight change in the crack propagation manner, when there were little jumps closer to the end of the test. The average lines of the DIC data for the strain and CTOD methods have the same tendency as the R-curves of the conventional measurements and nearly the same values of  $G_{IC\_propagation}$ ; 1860±45 J/m<sup>2</sup>.

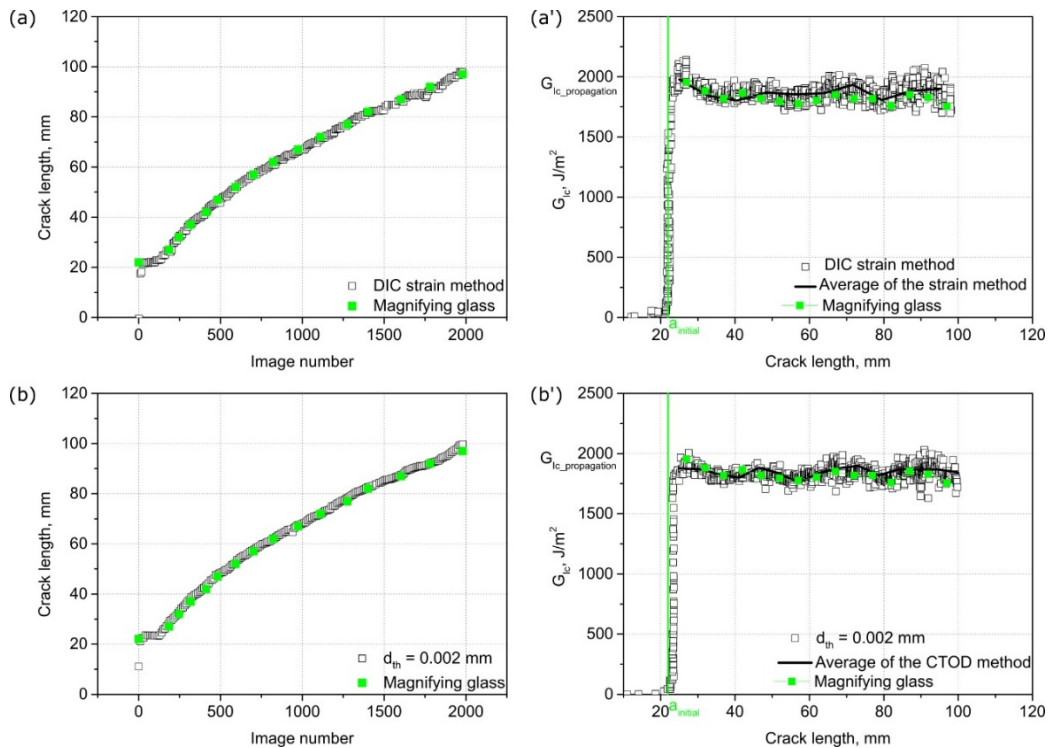


**Fig. 6.** Crack length growth (a, b) and R-curves (a', b') of CF/PEEK\_stable defined using the strain and CTOD methods, respectively. The green colour corresponds to the conventional measurements performed with a magnifying glass.

#### DIC results of specimens with the unstable crack propagation

Figures 7a and b present the results of crack length growth produced using the strain and CTOD methods for CF/PEEK\_unstable. The crack length over the number of images (testing time) has a stair-shape due to the stationary behaviour of the crack between the crack increments. The horizontal bars became longer during the test, which means that the time between crack jumps became longer as a result of the compliance increase. For both methods, the crack length deviates slightly from the conventional results. This insignificant variation of about 2% might have been caused by noise in the displacement data measured by DIC. The other possible reason can be a slightly asymmetrical crack front, which was measured using DIC and a magnifying glass on opposite sides of the specimen (Fig. 5b). In the CTOD method, the smallest  $d_{th}$  of 0.002 mm used for calculation of the crack length appeared in better agreement with the conventional measurements than  $d_{th}$  of 0.005 and 0.015 mm (Fig. 7b). The bigger thresholds yielded shorter crack length, because COD increased behind the crack tip.

Figures 7a' and b' show  $G_{IC}$  results obtained with the strain and CTOD methods. The  $G_{IC}$  data has the shape of bars, which are much longer than in the case of CF/PEEK\_stable. This corresponds to the unstable crack propagation with pronounced crack jumps in CF/PEEK\_unstable. There were eight crack increments of different lengths with increasing time between them. The latter parameter is defined by the number of points in the bars. The first three bars contain fewer data points than the following bars, which means that the time between the first three increments was shorter. Lines drawn through the maximum and minimum values of every bar have the same tendency as  $G_{IC\_start}$  and  $G_{IC\_arrest}$  of the conventional measurements with a small deviation of magnitudes (Fig. 7a',b'). The mean values of  $G_{IC\_start}$  and  $G_{IC\_arrest}$  are about 5% and 1.5% higher than the conventional results. This disturbance can be explained by the difference between the crack lengths being measured using DIC and the magnifying glass.

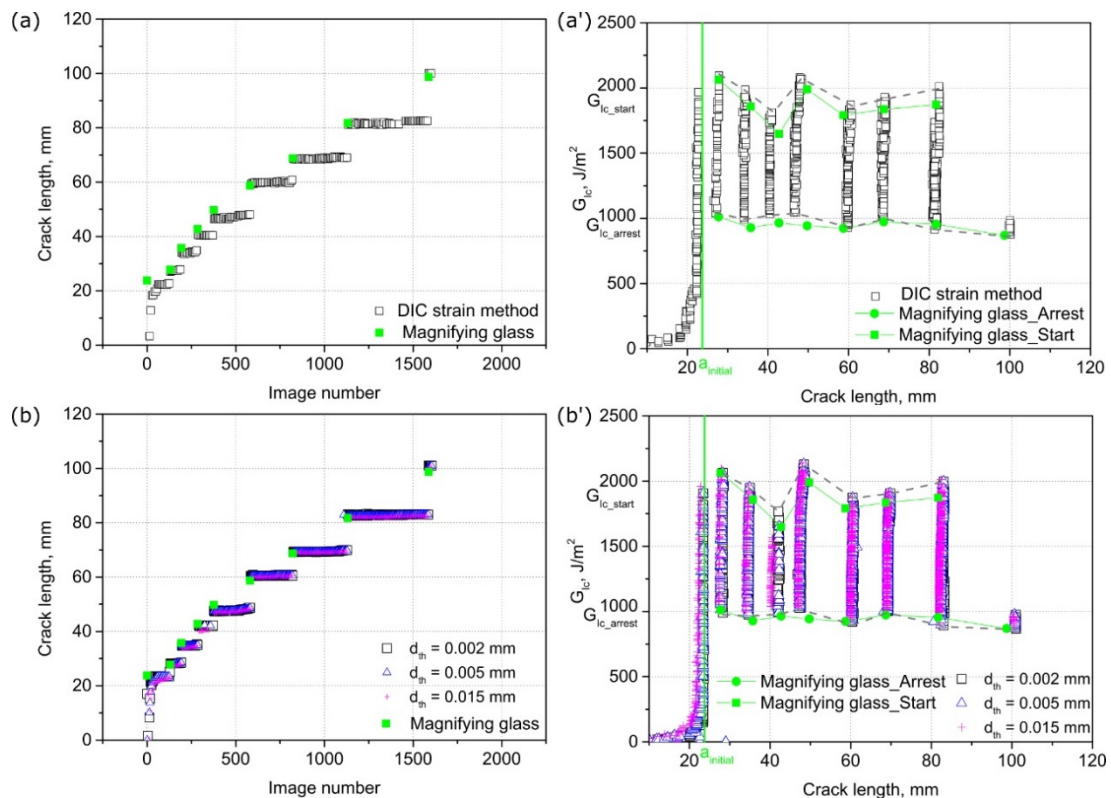


**Fig. 7.** Crack length growth (a, b) and R-curves (a', b') of CF/PEEK\_unstable defined using the strain and CTOD methods respectively. The green colour corresponds to the conventional measurements performed with a magnifying glass. The grey dashed lines identify the tendencies of  $G_{IC\_start}$  and  $G_{IC\_arrest}$  obtained using the strain and CTOD methods (b, b').

### Top surface analysis

The results of the crack length growth, according to TSA and their comparison with the conventional measurements, are shown in Fig. 8a and b for CF/PEEK\_stable and CF/PEEK\_unstable, respectively. There is no data at the beginning of the plots because the start of crack propagation was not visible to the cameras due to the machine gripping system. For CF/PEEK\_stable, the TSA results were found to be in good agreement with the conventional measurements (Fig. 8a). For CF/PEEK\_unstable, the crack length over the number of images has a stair-shape due to the alternation of stationary crack states and its abrupt propagation (Fig. 8b). The time between the crack increments increased during the test, which is explained by a decrease in specimen stiffness leading to the

compliance rise. The values of the crack length at the arrest moments from TSA are consistent with the conventional measurements.

The  $G_{IC}$  results of CF/PEEK\_stable and CF/PEEK\_unstable are shown in Fig. 8a' and b'. For the specimen with the stable delamination,  $G_{IC}$  over the crack length is presented in shapes of short, densely-spaced bars (Fig.8a'). This indicates that the crack propagation consisted of tiny crack increments invisible to the eye. The same behaviour was also detected for the specimens, where the strain and CTOD methods were applied. A curve plotted through the average values of  $G_{IC}$  obtained with TSA is in good agreement with the R-curve of the conventional measurements and yielded  $G_{IC\_propagation}$  of  $1900 \pm 55 \text{ J/m}^2$ . For CF/PEEK\_unstable, TSA results correlate fairly well with the conventional results (Fig. 8b'). However, a slight deviation of about 5-8% from the conventional results can be explained by noise in the DIC data. In the DCB mode I test, the specimen moves in the yz-plane when the bottom clamp is fixed and the load is applied to the top clamp (Fig. 1). Hence, the distance between the specimen and the cameras changes in TSA, which leads to defocusing and partial blooming of the images (Fig. 1b). The image blooming causes a loss of the speckle tracking, which leads to the data noise and loss. This is not the case in the strain and CTOD methods, where the distance between the specimen surface and the cameras does not change during the test (Fig. 1a).

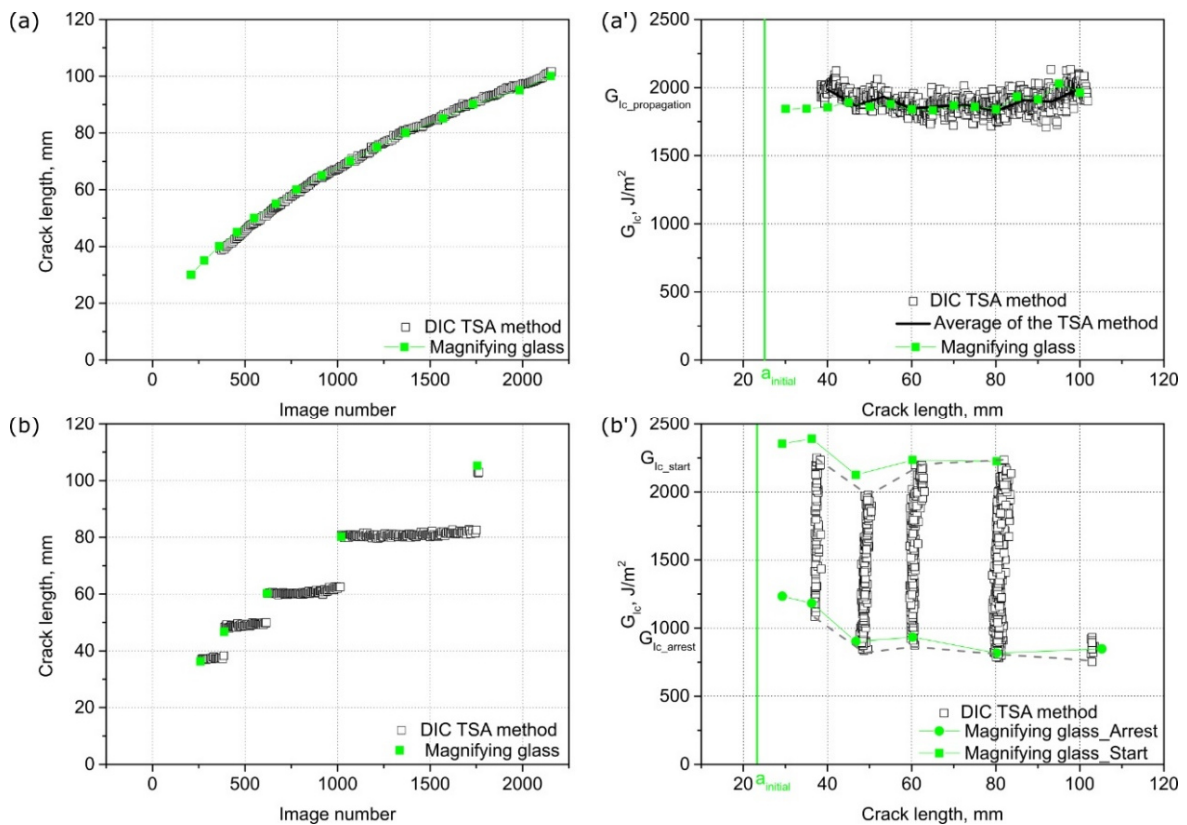


**Fig. 8.** Crack length growth (a, b) and R-curves (a', b') defined using the TSA methods for CF/PEEK\_stable and CF/PEEK\_unstable, respectively. The green colour corresponds to the conventional measurements performed with a magnifying glass. The grey dashed lines identify the tendencies of  $G_{IC\_start}$  and  $G_{IC\_arrest}$  obtained using TSA (b, b').

One practical advantage of the TSA method is the determination of the crack length and the crack front from one measurement [124]. The advantage becomes all the more significant when the formation of the plane stress on the side surface of the specimen is most pronounced or when the contour of the crack front is not symmetrical, for instance in the case of non-UD laminates [115,144].

However, this was not the case in the present work. Figure 9 presents the crack length and the  $G_{Ic}$  distributions over the specimen width. The crack front had a nearly straight shape throughout the test, which corresponds to the shape of the final crack front visible on the fracture surface (Fig. 5b). A nearly straight crack front was also reported by Reiner et al. [124] for CFRP and GFRP.

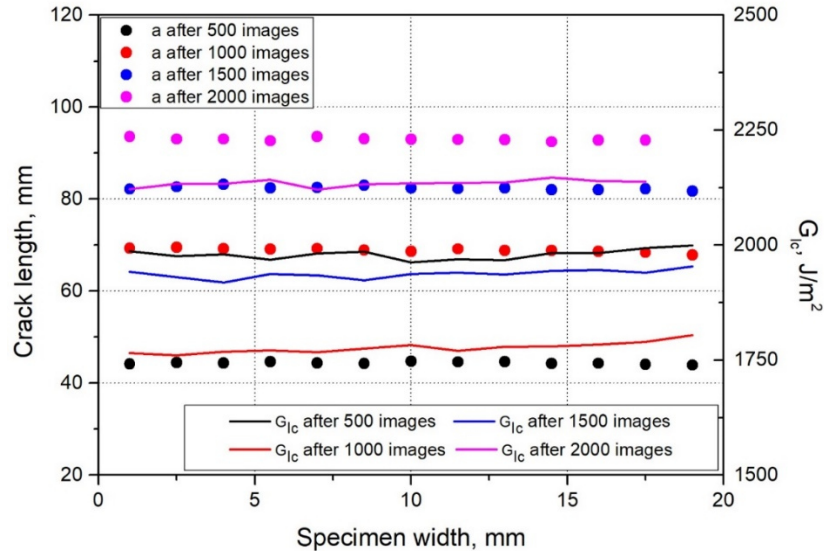


**Fig. 9.** Crack length  $a$  and  $G_{Ic}$  over the specimen width in CF/PEEK\_stable defined by the TSA method.

#### 4.2.7. Conclusion

The present work addresses the application of DIC in the mode I DCB test of carbon fibre reinforced PEEK laminates. DIC was used in order to rectify the problem of the simultaneous determination of force and displacement with the delamination length during the test. Automated tracking of the crack tip position enabled the determination of the crack length, which is required for  $G_{Ic}$  calculations. Two different reduction methods of the DIC data were developed in order to define the crack tip position. The methods were verified for specimens with abrupt and stable behaviours of the delamination.

According to the first method, the crack tip position is defined by the high strain concentration in the vicinity of a crack tip. In comparison with the previous work [123], the strain method was improved in terms of it not depending on a certain strain value, but rather its maximum. This means that the strain method developed can be applied to detect crack length by means of DIC irrespective of the material. According to the second method, the crack tip position is localised by the coordinate of crack tip opening displacement along the crack plane. The crack lengths obtained using both methods were in good agreement with measurements performed with a magnifying glass according to the standardised testing procedure [116]. Despite the complexities inherent in unstable crack propagation, the moments of the abrupt crack increments were successfully detected by means of DIC. Both the strain and CTOD methods showed nearly the same results of  $G_{Ic}$  with a minor difference from the conventional results. However, the CTOD method proposes the implicit definition of the crack length in terms that it requires the beforehand determination of CTOD, which is defined by  $G_{Ic}$  depending on the crack length. In this sense, the strain method with the crack localisation by the absolute strain maximum is more versatile and can be applied to materials which properties are not known in advance.

For reasons of comparability, top surface analysis (TSA) was performed additionally, according to Reiner et al. [124]. Following this approach, measurements were made on the top specimen surface, in contrast to the strain and CTOD methods, where the region of interest is a side surface. The TSA method showed a positive correlation with the conventional measurements for specimens with stable and unstable crack propagations. The advantage of TSA is that the crack length can be defined together with the contour of the crack front from one measurement. The crack front was nearly straight in CF/PEEK specimens with stable crack propagation.

It can be concluded that DIC is a powerful non-contact optical technique, which can be applied to follow crack growth in the mode I DCB test. DIC enables an automated crack length detection, which makes the test less time and effort consuming, especially in the case of testing a large number of specimens. Moreover, it is always an advantage to have access to the images of the entire test to solve questions, which can possibly arise during the investigation process of the crack propagation. Future studies could focus on the application of the proposed data reduction methods to FM tests under mode II or mix-mode loadings. The methods could be extended to specimens with compact-tension geometry and also to specimens with a bigger plastic zone at the crack tip.

### **Acknowledgments**

The research work was performed within the COMET project VI-2.06, 'New strategies towards laser assisted manufacturing of fibre reinforced thermoplastic composites,' at the Polymer Competence Center Leoben GmbH (PCCL, Austria) within the framework of the COMET program of the Federal Ministry for Transport, Innovation and Technology and the Federal Ministry of Science, Research and Economy with contributions by Technical University of Munich (Institute for Carbon Composites), Montanuniversitaet Leoben (Institute of Material Science and Testing of Polymers), AFPT and Cevotec. The PCCL is funded by the Austrian Government and the State Governments of Styria, Lower Austria and Upper Austria. Special thanks go to Franz Grassegger, Gerald Meier and Jürgen Grosser for their assistance with the specimen preparations and the DIC measurements.

### 4.2.8. References

- [1] M. S. Sham Prasad, C. S. Venkatesha, T. Jayaraju, Experimental methods of determining fracture toughness of fiber reinforced polymer composites under various loading conditions, *JMMCE*, 10 (13) (2011), p. 1263.
- [2] T. L. Anderson, *Fracture mechanics: fundamentals and applications*, CRC press, (2005),
- [3] ASTM D5528-13, Standard test method for mode I interlaminar fracture toughness of unidirectional fiber-reinforced polymer matrix composites, ASTM International, West Conshohocken, PA, (2013).
- [4] ISO15024: 2001, Fibre-reinforced plastic composites determination of mode I interlaminar fracture toughness, GIC, for unidirectional reinforced materials. International Organization for Standardization, Ginebra
- [5] D. Broek, *Elementary engineering fracture mechanics*, Springer Science & Business Media, (2012)
- [6] H. Albertsen, J. Ivens, P. Peters, M. Wevers, I. Verpoest, Interlaminar fracture toughness of CFRP influenced by fibre surface treatment: Part 1. Experimental results, *Compos. Sci. Technol.*, 54 (2) (1995), pp. 133–145.
- [7] K. E. Perry, J. McKelvie, Measurement of energy release rates for delaminations in composite materials, *Exp. Mech.*, 36 (1) (1996), pp. 55–63.

- [8] K. Arakawa, M. Ishiguma, K. Takahashi, Study of mode I interlaminar fracture in CFRP laminates by moiré interferometry, *Int. J. Fract.*, 66 (3) (1994), pp. 205–212.
- [9] L. Sorensen, J. Botsis, T. Gmür, L. Humbert, Bridging tractions in mode I delamination: Measurements and simulations, *Compos. Sci. Technol.*, 68 (12) (2008), pp. 2350–2358.
- [10] K. Colavito, E. Madenci, Adhesive failure in hybrid double cantilever beams by digital image correlation, *Proceedings of 51st AIAA/ASME/ASCE/AHS/ASC Structures, Structural Dynamics, and Materials Conference 18th AIAA/ASME/AHS Adaptive Structures Conference*, (2010), p. 2603.
- [11] M. Merzkirch, L. Ahure Powell, T. Foecke, Measurements of mode I interlaminar properties of carbon fiber reinforced polymers using digital image correlation, *KEM*, 742 (2017), Trans. Tech. Publications Ltd, pp. 652–659.
- [12] B. R. Murray, S. Fonteyn, D. Carrella-Payan, K. A. Kalteremidou, A. Cernescu, D. Van Hemelrijck, L. Pyl, Crack tip monitoring of mode I and mode II delamination in CF/Epoxy under static and dynamic loading conditions using digital image correlation, *Multidisciplinary Digital Publishing Institute Proceedings*, 8 (2) (2018), p. 389.
- [13] A. Khudiakova, M. Wolfahrt, D. Godec, G. Pinter, Determination of the mode I strain energy release rate in carbon fibre reinforced composites by means of digital image correlation technique, *Proceedings of ECCM-18 Conference*, Athens, (2018)
- [14] J. Reiner, J. P. Torres, M. Veidt, A novel top surface analysis method for mode I interface characterisation using digital image correlation, *Eng. Fract. Mech.*, 173 (2017), pp. 107–117.
- [15] M. Zhu, L. Gorbatiikh, S. Fonteyn, L. Pyl, D.V. Hemelrijck, D. Carrella-Payan, S.V. Lomov, Digital Image Correlation Measurements of Mode I Fatigue Delamination in Laminated Composites, *Multidisciplinary Digital Publishing Institute Proceedings*, 2 (8) (2018), p. 430. doi: 10.3390/ICEM18-05289
- [16] S. Mallon, B. Koohbor, A. Kidane, M.A. Sutton, Fracture Behavior of Prestressed Composites Subjected to Shock Loading: A DIC-Based Study. *Exp Mech.*, 55 (1) (2015), pp. 211–225.
- [17] J. Rethore, A. Gravouil, F. Morestin, A. Combescure, Estimation of mixed-mode stress intensity factors using digital image correlation and an interaction integral, *Int. J. Fract.*, 132 (1) (2005), pp. 65–79.
- [18] M. A. Sutton, J. J. Orteu, H. Schreier, *Image correlation for shape, motion and deformation measurements: basic concepts, theory and applications*, Springer Science & Business Media, (2009)
- [19] B. Pan, K. Qian, H. Xie, A. Asundi, Two-dimensional digital image correlation for in-plane displacement and strain measurement: a review, *Meas. Sci. Technol.*, 20 (6) (2009), p. 062001.
- [20] A. Forsström, S. Bossuyt, G. Scotti, H. Hänninen, Quantifying the effectiveness of patterning, test conditions, and DIC parameters for characterization of plastic strain localization, *Exp. Mech.*, (2019), pp. 1-10.
- [21] M. K. Cvitkovich, Polymer matrix effects on interlaminar crack growth in advanced composites under monotonic and fatigue mixed-mode I/II loading conditions, PhD thesis, Montanuniversität Leoben, (1995)
- [22] E. Jones, M. Iadicola, *A good practices guide for digital image correlation*. International Digital Image Correlation Society, (2018).
- [23] Aramis v6.1 and higher, User manual – software, GOM mbH (2009).
- [24] M. Palanca, G. Tozzi, L. Cristofolini, The use of digital image correlation in the biomechanical area: a review, *International Biomechanics* 3 (1) (2016), pp. 1–21.



- [25] J. Baldoni, G. Lionello, F. Zama, L. Cristofolini, Comparison of different filtering strategies to reduce noise in strain measurement with digital image correlation, *J. Strain. Anal. Eng.*, 51 (6) (2016), pp. 416–430.
- [26] M. Kawai, Y. Masuko, Y. Kawase, R. Negishi, Micromechanical analysis of the off-axis rate-dependent inelastic behavior of unidirectional AS4/PEEK at high temperature, *Int. J. Mech. Sci.*, 43 (9) (2001), pp. 2069–2090.
- [27] A. J. Brunner, Fracture mechanics characterization of polymer composites for aerospace applications, *Polymer composites in the aerospace industry*, Woodhead Publishing, (2015), pp. 191-230.
- [28] S. Hashemi, A. J. Kinloch, J. M. Williams, The analysis of interlaminar fracture in uniaxial fibre-polymer composites, *Proc. R. Soc. Lond.*, 427 (1872) (1990), pp. 173–199.
- [29] Jr. J. W. Gillespie, L. A. Carlsson, A. J. Smiley, Rate-dependent mode I interlaminar crack growth mechanisms in graphite/epoxy and graphite/PEEK, *Compos. Sci. Technol.*, 28 (1) (1987), pp. 1-15.
- [30] H. Yoon, K. Takahashi, Mode I interlaminar fracture toughness of commingled carbon fibre/PEEK composites, *J. Mater. Sci.*, 28 (7) (1993), pp. 1849–1855.
- [31] D. R. Moore, J. G. Williams, A. Pavan, Fracture mechanics testing methods for polymers, adhesives and composites, Elsevier, 28 (2001).
- [32] I. De Baere, S. Jacques, W. Van Paepegem, J. Degrieck, Study of the Mode I and Mode II interlaminar behaviour of a carbon fabric reinforced thermoplastic, *Polym. Test.*, 31 (2) (2012), pp. 322–332.
- [33] V. Koissin, L. L. Warnet, R. Akkerman, Delamination in carbon-fibre composites improved with in situ grown nanofibers, *Eng. Fract. Mech.*, 101 (2013), pp. 140–148.
- [34] K. Tohgo, Y. Hirako, H. Ishii, K. Sano, Mode I interlaminar fracture toughness and failure mechanism of angle-ply carbon/Nylon laminates, *J. Compos. Mater.*, 30 (6) (1996), pp. 650–661.
- [35] S. Samborski, Effect of boundary conditions on the distribution of mode I fracture toughness along delamination front in CFRP laminates with general fiber orientation, *Mech. Mech. Eng.*, 20 (2) (2016), pp. 121–127.

### 4.3. A comparative study for shear testing of thermoplastic-based composites and metal-composite hybrids

#### 4.3.1. Bibliographic information

- Authors and their relevant contribution to the publication:
  - V. Zinnecker<sup>1</sup>: Writing - original draft, Visualization, Investigation, Conceptualisation
  - C. M. Stokes-Griffin<sup>1</sup>: Writing - review and editing, Visualisation, Supervision, Investigation, Conceptualisation
  - A. Khudiakova<sup>2</sup>: Investigation, Writing - review and editing
  - M. Wolfahrt<sup>2</sup>: Writing - review and editing, Funding acquisition
  - P. Compston<sup>1</sup>: Writing- review and editing, Supervision, Project administration, Conceptualisation, Funding acquisition
  
- Affiliations:
  - <sup>1</sup>ARC Training Centre for Automated Manufacture of Advanced Composites, Research School of Electrical, Energy and Materials Engineering, Australian National University, Canberra, ACT 2600, Australia
  - <sup>2</sup>Polymer Competence Center Leoben GmbH, Roseggerstraße 12, 8700 Leoben, Austria

Published in Composites Part A: Applied Science and Manufacturing (2020)

*The manuscript is presented here in accordance with the publisher's copyright policy: 'Authors can include their articles in full or in part in a thesis or dissertation for non-commercial purposes.' Elsevier.com*

#### 4.3.2. Abstract

This study presents the novel application of the compression shear test (CST) for characterising bonding strength of metal-composite hybrids made of steel and carbon fibre/polyamide 6 (CF/PA6). An automated laser-assisted tape placement (ATP) process was used to lay-up the CF/PA6 tapes on laser textured steel substrates. CST is of interest due to the ease of sample manufacturing as a relatively small test specimen is required. The results were compared with standardised single lap shear tests (ASTM D3165), which requires manufacturing of a double notched test specimen. For benchmarking purposes, the compression shear test was also used to characterise the interlaminar shear strength of a plain CF/PA6 composite. The results showed equivalent shear strength and similar failure modes for both tests of the metal-composite hybrid specimens. Grooved texturing of the steel substrate in the hybrid specimens promoted a mixed-mode (cohesive and adhesive) failure and a higher shear strength than for the composite-only specimens. Overall, the results showed that the compression shear test is a valid and efficient method to characterise the bonding strength of metal-composite hybrids and composites.

#### 4.3.3. Introduction

Composites with thermoplastic matrices are increasingly popular due to their capacity for high-rate in-situ consolidation and their potential for end-of-life recyclability. With thermoplastic composites (TPC), automated manufacturing processes such as laser-assisted automated tape placement (ATP) with in-situ consolidation are possible. Here, thermoplastic prepreg tapes are placed in an additive way by a tape placement head equipped with a heat source mounted, for instance, on a robot. The main process steps for the ATP process are heating of the incoming tape and the substrate with the heat source above the polymer's melting temperature ( $T_m$ ), bonding of the joining partners by autohesion followed by cooling under the consolidation roller below the  $T_m$ . This process shows high potential for fast production cycle times and high output, which makes it interesting for industry application; especially as the in-situ consolidation for thermoplastics is happening in a fraction of a second depending on the placement rate [1]. For a rapid manufacturing process such as ATP with a multitude of quality-influencing process parameters, a relatively quick assessment of the bonding strength would be desirable. Furthermore, specimen preparation time is always a limiting factor. Square or rectangular test specimens, which correspond in width to the width of the tape placed during ATP, can be easily produced with this manufacturing process. The thickness of the specimens can be adjusted with the number of plies placed. As a result, the cutting time can be reduced significantly with a single cut necessary for trimming to the required specimen length.

High-toughness material combinations, such as thermoplastic composites or metal-TPC hybrids, lead to challenges to test the apparent shear strength in the laminate, which is one of the reasons for their limited adoption for large-scale manufacturing [2]. Conventional interlaminar bonding strength test methods have different limitations when it comes to testing of TPCs. Single lap shear testing (SLST), for example, is known for a high specimen preparation time and a complex, mixed stress state including out-of-plane bending moments and, consequently, high peel stresses [3]. The stress distribution is depicted in Fig. 1a. The high specimen preparation time is mainly dominated by the required double notches on opposing sides of the specimen, cut down precisely to the bond-line. Additionally, such mechanical properties as stiffness of the adhesive and adherends need to be taken into account, especially for adhesively bonded material combinations, such as metal composite hybrids [3].

Another commonly used test method is the short beam strength (SBS) test (ASTM D3165 [4] and DIN EN 2563 [5]). Here, the apparent interlaminar strength is tested in an indirect method that uses bending load applied to carefully selected span-to-length ratios that induces shear in the mid-plane of the sample. Generally, short beam strength determined by this test method can be used for process specification purposes, quality control or comparative testing of composite materials, provided that failures occur consistently in the same mode [6]. The SBS testing requires the specimen planes to be parallel to the span direction. There are also limitations of the composite lay-up for valid test specimens corresponding to the stiffness requirements [6]. The geometry of the specimen is highly dependent on the thickness of the laminate and the ratio of the span distance to the thickness. Several studies have reported successful short beam strength testing for TPC using polyether ether ketone (PEEK) matrix [1,7,8]. However, for carbon fibre/polyamide6 (CF/PA6), a lower cost thermoplastic system, no mid-plane interlaminar shear failure could be observed for tested SBS specimens [9,10]. Instead, the specimens showed an invalid failure mode in form of inelastic deformation, due to the lower stiffness and high toughness of the matrix. To date this methodology has been applied to plain composites or fiber metal laminates with metal films thinner than 0.5 mm [11–14]. No testing on metal-composite hybrid structures, with metals thicker than 2 mm, such as introduced in this paper, has been reported. For testing metal-composite hybrids with SBS, the stiffness of both adherends would have to be equivalent for a valid failure mode to occur. Achieving this is very challenging and might not result in the laminate lay-up that is of interest for investigation. Additionally, CF/PA6 yields invalid failure using SBS [10], therefore, achieving a valid failure mode with metal-CF/PA6 hybrids is questionable.

Schneider et al. [15] proposed a novel test method, the compression shear test (CST), to determine the interlaminar shear strength of flat as well as curved composite materials and adhesive joints. The recommended dimensions for the samples are width  $b \leq 20$  mm, maximum parallel length of the specimen  $l \leq 20$  mm and the total thickness  $d \leq 1.5 * l$ . The internal radius for curved specimens is recommended to be  $R_i \geq 50$  mm. This testing method has such advantages as reduced sample preparation effort and time, as the specimen geometry is a rectangular cut from the material of interest. The precise application of the load to the bonding area will lead to a shear failure in the specimen (Fig. 1). The stress distribution for a loaded test specimen is presented in Fig. 1b. Thus, it makes CST one of the few methods reported to measure the interlaminar shear strength of tough thermoplastic composites. It was shown that with this test method it is possible to overcome invalid fracture behaviour for tough materials such as thermoplastic polymers [9,15,16]. First studies showed a good quantitative correlation between SBS and CST for curved CF/PEEK samples stating that both methods would be suitable for a screening and quality assessment [16]. Using the finite element analysis, CST was found to give a simpler and better-defined shear stress distribution compared to SBS [16]. Bothelo et al. [9] showed that SBS tests resulted in invalid failure modes for carbon fibre/PA6 composites, but valid test results can be achieved with the CST method.

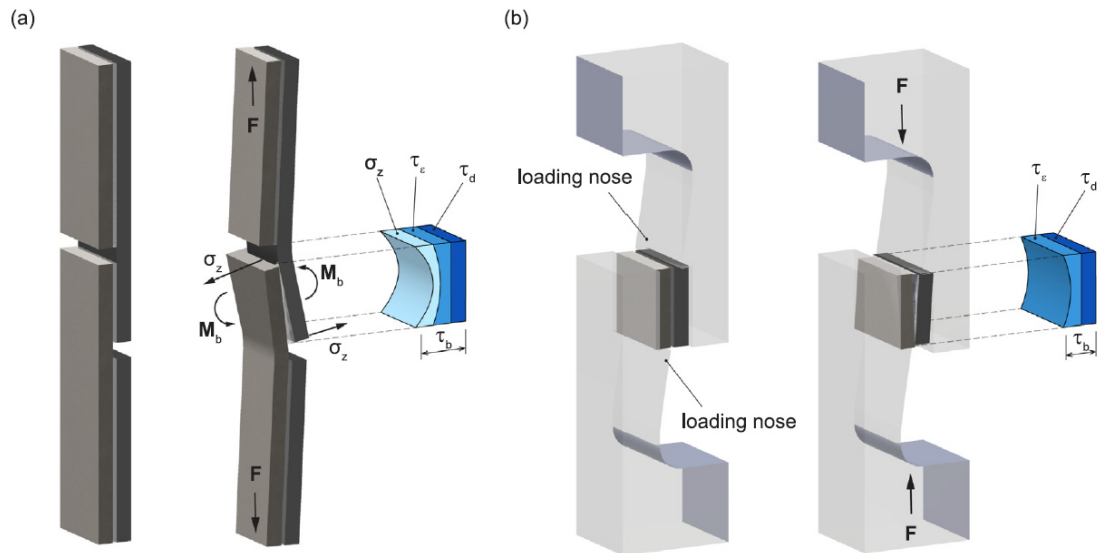


**Fig. 1.** Unloaded and loaded (a) single lap shear test specimen and (b) compression shear test specimen with stress distribution in the bonding area, where  $\tau_d$  refers to the direct shear stress parallel to the bonding surface due to the applied load,  $\tau_c$  to the combination of shear and tensile stresses parallel to the bonding surface caused by the strain of the adherands and  $\sigma_z$  to the tensile stress perpendicular to the bonding surface caused by the bending moment ( $M_b$ ) [20].

In this paper, a study assesses the use of a novel compression shear test (CST) to characterise the bonding strength of metal-composite hybrids manufactured out of steel and a unidirectional CF/PA6 composite using an automated laser-assisted tape placement process. The test results were compared with the ASTM D3165 single lap shear test [4] in terms of shear strength and failure modes. In order to assess the sensitivity of CST, different surface pre-treatments for the steel and their influence on the bonding behaviour to CF/PA6 were considered for the metal-composite hybrids.

#### 4.3.4. Materials and testing methods

##### Materials

The materials used in this study were a fully impregnated CF/PA6 unidirectional (UD) prepreg tape (Celstran<sup>®</sup> CFR-TP PA6 CF60-01, Celanese Corporation, Irving, Texas, USA) with a thickness of 0.13 mm, a width of 12 mm and a fibre volume fraction of 48% and a pickled, skinpassed low carbon steel (BlueScope BRIGHTFORM<sup>®</sup>, Australia) with a thickness of 2 mm. For the manufacturing of the hybrids, a 100  $\mu\text{m}$  thick unfilled PA6 film (Folien GmbH Monheim, Germany) was applied to the textured steel before tape placement.

##### Specimen preparation

All specimens were manufactured using a laser tape placement system from AFPT GmbH (AFPT GmbH, Germany) equipped with a near infrared diode laser to heat the incoming tape and substrate. The molten surfaces were bonded by means of a consolidation roller. The laminates manufactured were made out of 20 unidirectional plies of CF/PA6 processed at a control temperature of 280  $^{\circ}\text{C}$ , a placement rate of 100 mm/s and a consolidation cylinder pressure of 3 bar. More details on the manufacturing process can be found in [17,18]. The test specimens were cut out only from the locations where the ATP process had stabilized.

For the manufacturing of the metal-composite hybrids, firstly the laser texturing was applied to a steel substrate. A femtosecond laser from Coherent (Coherent, Inc., USA) with 275 fs pulse length, 1035 nm wavelength and 42.3 W output power was used. It was shown previously that different surface pre-treatments have an impact on the bonding behaviour of pure PA6 and steel [19]. In this paper, it is of particular interest to investigate if CST yields the identical failure modes as SLST. Therefore, two different textures, microgrooved ( $\mu\text{G}$ ) and macrogrooved (MG), were selected, as distinct failure modes were expected. The main differences between the textures were the ablated depth per scanning line, 5  $\mu\text{m}$  for  $\mu\text{G}$  and 60  $\mu\text{m}$  for MG, and the step distance between adjacent scanning lines, 4  $\mu\text{m}$  for  $\mu\text{G}$  and 600  $\mu\text{m}$  for MG. The orientations of the scanning lines and grooves were aligned with the direction of tape placement and the load axis in the mechanical tests (Fig. 2a). After the laser texturing, the steel substrate was laminated with a 100  $\mu\text{m}$  thick PA6 film according to the procedure described in [17]. Then 20 plies of CF/PA6 were placed on top of the steel substrate by means of ATP using the same processing parameters as described for the composite-only laminates. The cross section of the MG metal-composite hybrid is shown in Fig. 2b. The PA6 film, which appeared as an additional layer between the steel and the composite, filled all textures entirely. Residual stresses led to minor delamination at both edges between the CF/PA6 laminate and the PA6 film as well as between the steel substrate and the PA6 film. The latter were trimmed to ensure that the specimens cut out of the hybrid laminate would not include the parts with delamination.

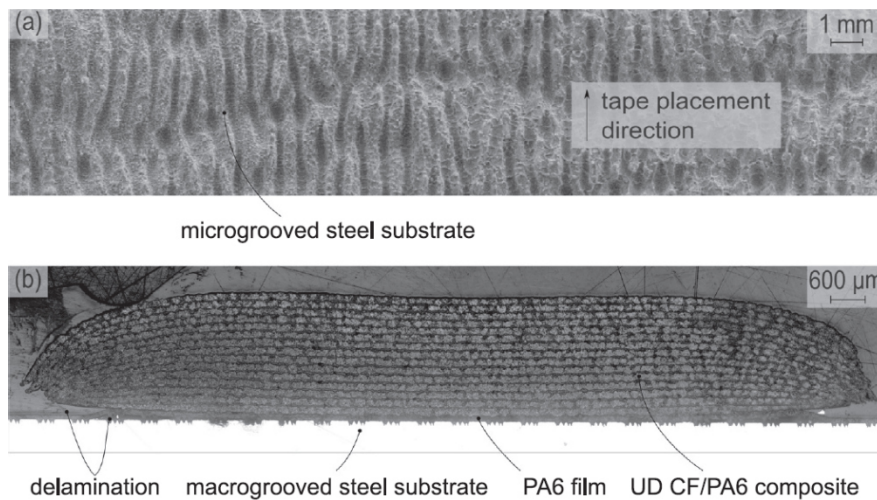


**Fig. 2.** (a) Cross section of the macrogrooved laser textured steel surface with 100  $\mu\text{m}$  PA6 film lamination and 20 plies of UD CF/PA6 and (b) SEM image of the microgrooved structure with magnification of 10 000x.

### Lap shear testing

The single lap shear test was performed according to ASTM D3165 [4] to assess the metal-composite bonding quality. In terms of consistency and comparability with the authors' previous work [17], the geometric dimensions of the specimens were 10 mm in width, 4.5 mm in thickness and an overlap length of 10 mm. The adherend length was 40 mm, resulting in a total specimen length of 70 mm.

The specimens were mounted in an Instron universal testing machine (Instron, USA) with 4 mm load application pins and tested with a crosshead speed of 13 mm/min. For each material five samples were tested successfully. A schematic drawing of the test is shown in Fig. 1a. The shear strength was calculated according to Eq. (1).

$$\sigma = \frac{F_{peak}}{l * b} \quad (1)$$

where  $\sigma$  is the shear stress,  $F_{peak}$  is the peak load at failure,  $l$  is the length and  $b$  is the width of the overlap area.

### Compression shear testing

The geometry of the CST specimens was chosen to match that of corresponding comparative test methods. The metal-composite hybrid laminates were cut to  $10 \times 10 \times 4.5 \text{ mm}^3$  (length  $\times$  width  $\times$  thickness) to provide the same bonded area as the SLST. Composite-only laminates were cut to  $6.5 \times 6 \times 2.5 \text{ mm}^3$  to match the width of the interlaminar region to the SBS test. Comparative SBS tests were attempted, however the load was observed to increase monotonically without failure and inelastic deformation was observed indicating an invalid test as reported by others [10]. The device used for the compression shear testing was designed following the proposed testing method by [15]. The original design focused on testing of curved specimens and the loading nose was mounted on a pivot so that the nose would follow the curved shear plane of the specimens. This work focuses on flat specimens; the loading nose was instead mounted on vertical linear guides and therefore moves in pure translation, ensuring pure shear loading. The specimens were inserted between the loading noses (Fig. 1b). The gap between the loading noses can be adjusted manually and was set to 0.5 mm for all specimens. Adjustable support blocks behind both loading noses are used to align the shear plane and provide gap-free sample location or preload perpendicular to the shear plane to prevent sample tilt. The specimens were aligned symmetrically with respect to the bond-line for the metal-composite hybrids, and with respect to the mid-plane for the composite-only specimens. The compression shear testing device was placed between two compression plates in a servo-hydraulic test machine MTS 810 (MTS Systems Corporation, Germany) equipped with a 25 kN load cell. Five specimens for every material configuration were tested at 1 mm/min under displacement control. The tests were performed under standardised laboratory conditions. The shear strength was calculated according to Eq. (1).

#### 4.3.5. Results and discussion

### Shear strength

Two different specimen sets, namely the microgrooved steel-CF/PA6 hybrid and the macrogrooved steel-CF/PA6 hybrid were analysed with both, CST and SLST. The UD CF/PA6 laminate was only analysed with CST as SBS tests had invalid failure.

The results obtained are shown in Fig. 3. For the metal-composite hybrids, the results of SLST and CST were in good agreement with each other. The tests yielded equivalent shear strength within scatter of one standard deviation; of about 8 MPa for the  $\mu\text{G}$  specimens and of about 19 MPa for the MG specimens. The CST results showed less scatter indicating a better repeatability. The hybrids indicated a lower shear strength for the microgrooved surface texture and a higher shear strength for the macrogrooved textured surface. This difference is due to the macroscopic texture of the MG specimens. It provided mechanical interlocking during shearing as the PA6 film filled the macroscopic texture entirely.

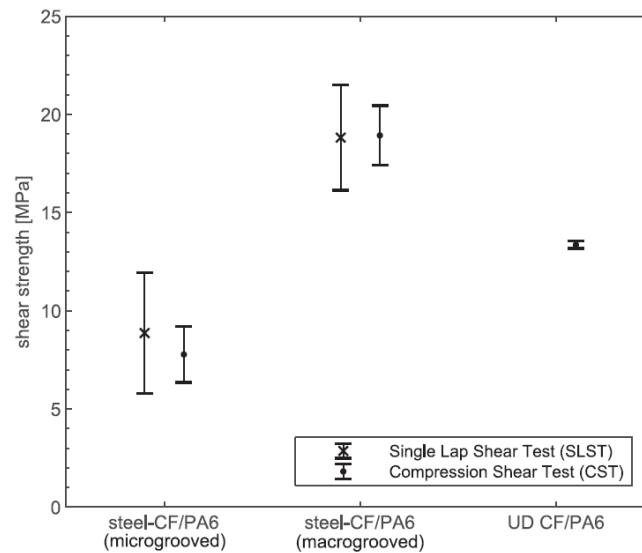


**Fig. 3.** Lap shear strength and compression shear strength of the laser textured metal-CF/PA6 hybrids and compression shear strength of the UD CF/PA6 laminate.

The obtained shear strength is 13.4 MPa for the UD CF/PA6 laminate. It should be noted that this value is provided for reference only, and the result is not directly comparable to the hybrids due to the differences in specimen geometry.

#### Failure modes

The failure modes for SLST and CST of metal-composites hybrids are compared in Fig. 4. In general, the same failure modes can be observed for the same specimen surface structure regardless of the testing method. For the specimens with the microgrooved structure, the failure mode occurred was predominantly adhesive in both tests (Fig. 4a). In this case, neither the composite nor the steel adherend failed, which implies that the bonding between the PA6 film and the microgrooved steel was of poor quality leading to the lower shear strengths.

For the specimens with the macrogrooved structure, cohesive failure through the composite was observed (Fig. 4b). Additionally, fiber bridging was observed within the crack of the composite, indicating intralaminar / cohesive failure of the composite. In this case the interface was not the weakest part of the bond interface. For the UD CF/PA6 laminate, shear fracture was observed along the length of the samples. The specimen's top view shows the crack propagation through multiple plies, indicating intra- and inter-laminar failure (Fig. 5). This is a valid failure mode for this composite system and the compression shear test method.



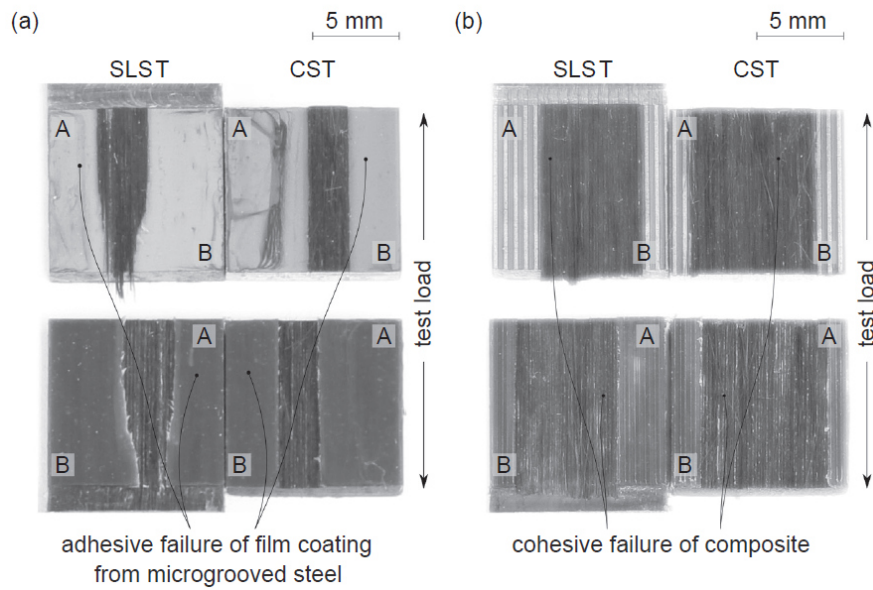


**Fig. 4.** Comparison of failure modes for metal-composite hybrids with (a) microgrooved and (b) macrogrooved structure tested using SLST and CST. A and B refer to the corresponding fracture areas.

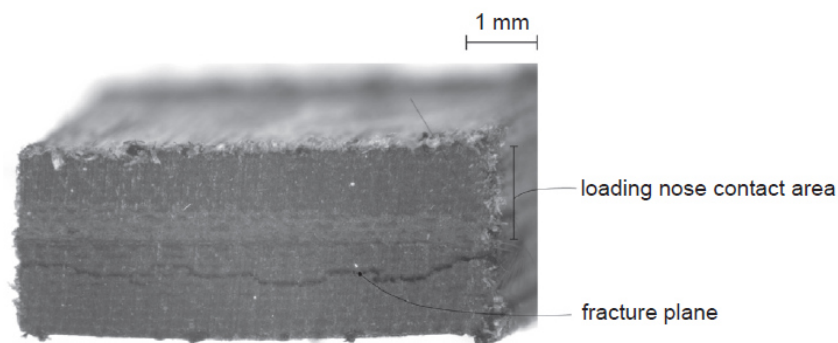


**Fig. 5.** Top view of a UD CF/PA6 specimen tested using CST.

Overall, these findings revealed that the novel CST method is sensitive to surface modifications. This is especially important, as surface modifications are central for an increased shear strength within metal composite hybrids. It was shown that CST is consistent with the well-established SLST in both, shear strength and failure mode for steel-CF/PA6 metal-composite hybrids with less sample preparation effort. CST yielded valid failure for UD CF/PA6 laminates.

#### 4.3.6. Summary and conclusion

A comparative study on the shear testing of thermoplastic based composites and metal-composite hybrids was carried out. Two different material combinations manufactured using a laser-assisted tape placement process were investigated: UD CF/PA6 laminates and steel-CF/PA6 hybrids. The results obtained according to the standardised single lap shear test (ASTM D3165) were compared with the results of a novel application of the compression shear test. The specimen preparation for the compression shear test was shown to be more efficient and less material consuming compared to SLST, which could be advantageous for further material characterisations. The main conclusions for this study are summarized below:

- SLST and CST yielded equivalent shear strengths with less scatter for CST;

- The failure modes in which the metal-composite hybrids failed are alike for the same surface pre-treatment of the metal;
- The novel CST method and SLST are sensitive to surface modifications;
- High toughness materials such as UD CF/PA6 laminates and material combinations such as metal-composite hybrids, in this case steel-CF/PA6 hybrids, can be tested with the compression shear testing device.

In summary, the compression shear test is shown to be an efficient alternative to the single lap shear test for testing high toughness composite materials and their metal-composite hybrids. Further investigation might be useful to enlarge the range of thermoplastic-based composites to further test the validity of the compression shear test.

### **Acknowledgements**

This project was conducted within the ARC Training Centre for Automated Manufacture of Advanced Composites (IC160100040), supported by the Commonwealth of Australia under the Australian Research Council's Industrial Transformation Research Program. The authors acknowledge the facilities, and the scientific and technical assistance, of the Australian Microscopy & Microanalysis Research Facility at the Centre of Advanced Microscopy and the Laser Physics Centre at the Australian National University. A. Khudiakova and M. Wolfahrt would like to thank the Austrian Competence Centre Program "COMET" sponsored by the Federal Ministry for Transport, Innovation and Technology and the Federal Ministry of Science, Research and Economy for supporting this work. The compression shear testing was performed at the Polymer Competence Center Leoben (PCCL) GmbH with contributions by the Montanuniversität Leoben (Chair of Material Science and Testing of Polymers). The PCCL is funded by the Austrian Government and the State Governments of Styria, Lower Austria and Upper Austria.

### 4.3.7. References

- [1] Stokes-Griffin CM, Compston P. The effect of processing temperature and placement rate on the short beam strength of carbon fibre-PEEK manufactured using a laser tape placement process. *Compos A Appl Sci Manuf* 2015;78:274–83.
- [2] Biron M. *Thermoplastics and Thermoplastic Composites*. William Andrew; 2018.
- [3] Dillard DA. *Advances in Structural Adhesive Bonding*. Elsevier; 2010.
- [4] ASTM D3165 Test Method for Strength Properties of Adhesives in Shear by Tension Loading of Single-Lap-Joint Laminated Assemblies. West Conshohocken, PA: ASTM International; 2014.
- [5] DIN EN 2563:1997-03, Luft- und Raumfahrt\_- Kohlenstoffaserverstärkte Kunststoffe\_- Unidirektionale Laminate; Bestimmung der scheinbaren interlaminaren Scherfestigkeit; Deutsche Fassung EN\_2563:1997. Beuth Verlag GmbH; 1997.
- [6] ASTM D2344/D2344M-00 Standard Test Method for Short-Beam Strength of Polymer Matrix Composite Materials and Their Laminates. West Conshohocken, PA: ASTM International; 2016.
- [7] Stokes-Griffin CM, Kollmannsberger A, Compston P, Drechsler K. Investigation of the effects of heating bias and placement head angle on the short beam strength of CF/PEEK laminates manufactured in a laser tape placement process. 9<sup>th</sup> Australasian Congress on Applied Mechanics, Sydney: 2017.

- [8] Comer AJ, Ray D, Obande WO, Jones D, Lyons J, Rosca I, et al. Mechanical characterisation of carbon fibre–PEEK manufactured by laser-assisted automated-tapeplacement and autoclave. *Compos A Appl Sci Manuf* 2015;69:10–20.
- [9] Botelho E. Mechanical behavior of carbon fiber reinforced polyamide composites. *Compos Sci Technol* 2003;63:1843–55.
- [10] Stokes-Griffin CM, Kollmannsberger A, Compston P, Drechsler K. The effect of processing temperature on wedge peel strength of CF/PA 6 laminates manufactured in a laser tape placement process. *Compos A Appl Sci Manuf* 2019;121:84–91.
- [11] Kotik HG, Perez Ipiña JE. Short-beam shear fatigue behavior of fiber metal laminate (Glare). *Int J Fatigue* 2017;95:236–42.
- [12] Botelho EC, Silva RA, Pardini LC, Rezende MC. A review on the development and properties of continuous fiber/epoxy/aluminum hybrid composites for aircraft structures. *Mat Res* 2006;9:247–56.
- [13] Whitney JM, Browning CE. On short-beam shear tests for composite materials. *Exp Mech* 1985;25:294–300.
- [14] Cui W, Wisnom MR, Jones M. Effect of specimen size on interlaminar shear strength of unidirectional carbon fibre-epoxy. *Compos Eng* 1994;4:299–307. [https://doi.org/10.1016/0961-9526\(94\)90080-9](https://doi.org/10.1016/0961-9526(94)90080-9).
- [15] Schneider K, Lauke B, Beckert W. Compression Shear Test (CST) – A Convenient Apparatus for the Estimation of Apparent Shear Strength of Composite Materials. *Appl Compos Mater* 2001;8:43–62.
- [16] Rosselli F, Santare MH. Comparison of the short beam shear (SBS) and interlaminar shear device (ISD) tests. *Compos A Appl Sci Manuf* 1997;28:587–94.
- [17] Stokes-Griffin CM, Kollmannsberger A, Ehard S, Compston P, Drechsler K. Manufacture of steel–CF/PA6 hybrids in a laser tape placement process: Effect of first-ply placement rate on thermal history and lap shear strength. *Compos A Appl Sci Manuf* 2018;111:42–53.
- [18] Stokes-Griffin CM, Ehard S, Kollmannsberger A, Compston P, Drechsler K. A laser tape placement process for selective reinforcement of steel with CF/PA6 composites: Effects of surface preparation and laser angle. *Mater Des* 2017;116:545–53.
- [19] Zinnecker V, Stokes-Griffin C, Madden S, Rode A, Compston P. Investigation of the effects of femtosecond laser metal surface texturing on bonding of PA 6 to steel. *Procedia Manuf* 2019;29:313–20.
- [20] Habenicht G. *Kleben: Grundlagen, Technologien, Anwendungen*. 6., aktualisierte Aufl. Berlin: Springer; 2009.

## Chapter 5. Summary and Outlook

### Summary

Additive manufacturing (AM) refers to manufacturing technologies producing 3D objects through a sequential layer-by-layer material deposition. This additive building approach makes AM more efficient in terms of material consumption compared to conventional manufacturing (CM) based on material removal. In addition, complex parts which would require the production of multiple integral parts using CM can be manufactured in one step using AM without the need for follow-up assembly. AM methods can process a wide range of materials including carbon fibre (CF) reinforced thermoplastic composites, which are of great interest to industries, such as aerospace, automotive, medical and sports where weight reduction and strength play an important role. However, the layer-wise manufacturing approach leads to the formation of interfaces between adjacent layers, and the interlayer bonding is prone to the accumulation of defects. This impairs the load-bearing capacity of AM parts and limits their application on an industrial scale. Therefore, the present research was dedicated to the comprehensive investigation of the mechanical anisotropy and the interlayer bonding in neat and CF reinforced thermoplastic parts produced by AM.

A systematic analysis was performed to investigate the dependence of the mechanical and microstructural properties of neat and carbon fibre (CF) reinforced polyamide PA1212 on the parts' orientation in the building chamber during SLS printing. For this purpose, specimens of each material were printed in twelve different directions and two different positions in the building chamber, and subsequently characterised using tensile testing. The data revealed nearly isotropic behaviour for the neat specimens, while the reinforced specimens exhibited high anisotropy. The reinforced specimens that were printed lying in the plane of the building platform with the longitudinal axis along the travel direction of the roller distributing the powder showed the highest tensile strength and tensile modulus. Light microscopy, scanning electron microscopy and X-ray tomography analysis provided overwhelming evidence for the presence of a preferable fibre orientation in the CF reinforced specimens. It could be demonstrated that 85-95% of the fibres were located in the horizontal plane, and most of them were furthermore oriented along the travel direction of the roller, which affected the tensile properties of the specimens accordingly.

The mechanical anisotropy was also investigated for parts produced by FFF. For this study, specimens from neat and CF reinforced polylactic acid (PLA) were printed with raster angles of 0°, 45° and 90° and characterised by means of tensile testing with the application of digital image correlation (DIC). The use of DIC enabled the determination of Poisson's ratio on both front and side specimen faces. Thus, the complete sets of engineering constants were successfully acquired for the two materials under investigation, which can be directly used for material modelling. Additionally, the quality of interlayer bonding between PLA/PLA, CF-PLA/CF-PLA and PLA/CF-PLA was characterised by fracture mechanics tests, namely the mode I double cantilever beam (DCB) test and the cracked round bar (CRB) test. Values of the critical energy release rate,  $G_{IC}$ , obtained by the DCB tests of PLA were approximately twice as high as those of CF-PLA. Interestingly, the crack propagation in the multi-material DCB samples did not occur in the PLA/CF-PLA interface, but instead the crack always deviated towards the CF-PLA part. This observation indicated that the PLA/CF-PLA interface was stronger than that of CF-PLA/CF-PLA. Unlike the DCB test, the CRB test enabled the determination of  $G_{IC}$  of the PLA/CF-PLA interface, which was 1.5 times smaller than  $G_{IC}$  of PLA/PLA and 1.2 times higher than  $G_{IC}$

of CF-PLA/CF-PLA. In conclusion, the CRB test was revealed to be an appropriate test method for the interlayer bonding characterisation of FFF printed samples, especially in the case of multi-material interfaces.

Fracture mechanics testing was also employed to characterise the interlayer bonding of unidirectional (UD) laminates produced from CF reinforced polyphenylene sulphide (PPS) using ATPisc. The laminates were manufactured following two different building approaches. According to the first approach, the laminates were prepared in the more conventional way by sequential layer-by-layer tape placement. In the second approach, the laminates were periodically flipped to the other side. While the latter approach resulted in almost flat laminates, the laminates produced by the former approach exhibited a curvature. The interlayer bonding of the laminates was characterised using quasi-static and fatigue mode I DCB tests. Independent of the building approach, the laminates exhibited multiple cracking and fibre bridging under both loading regimes. Additional damage processes affected the main crack growth and led to scattered results. Various data reduction methods were applied, providing a quantitative assessment of the laminate quality. It was shown that a non-linearity of the cubic root of the compliance plotted as a function of the crack length could indicate secondary damage processes occurring in specimens during testing. The damage parameter  $\varphi$  was found to decrease throughout the test, suggesting an accumulation of damage in the course of the test. Moreover,  $\varphi$  was found to be smaller for the specimens tested under fatigue loading than under quasi-static loading, implying a higher extent of damage. The delamination resistance under quasi-static loading was presented using the resistance curves, whereas that under fatigue loading was presented using approaches based on the Paris relation and a modified Hartman-Schijve equation. In addition, the 'zero fibre bridging' methodology was applied to exclude the effect of multiple cracking and fibre bridging on the determination of the fatigue delamination threshold.

In order to make the mode I DCB testing less labour intensive and decrease the risk of erroneous measurements of the crack length using a travelling microscope, a new methodology for automated crack length measurement by means of DIC was proposed. In this context, two data reduction methods were developed for the localisation of the crack tip, relying on either the high strain concentration in the vicinity of the crack tip or the crack tip opening displacement. These methods were applied to UD CF/PEEK laminates exhibiting either continuous or stick-slip crack propagation. For both propagation phenomena, the results acquired by means of DIC were consistent with those obtained visually using a travelling microscope. Moreover, both methods showed good agreement with the top surface analysis known from literature, demonstrating DIC as a suitable technique for automated crack length measurements.

Finally, the novel compression-shear test (CST) was employed to characterise the interlayer bonding of two material systems in terms of shear strength. The selected materials, namely unidirectional CF-PA6 laminates and hybrid steel/CF-PA6 composites, were manufactured by ATPisc. The CST was compared with the standardised single lap shear test (SLST). The results obtained from these two tests were in good agreement, highlighting CST to be a promising test method for interlayer shear strength in CF reinforced thermoplastic composite materials and their metal-composite hybrids. The use of CST can be especially recommended for the first phases of research to optimise manufacturing parameters, because it constitutes a less time and effort consuming testing technique than SLST.

## Outlook

The present research provides valuable new insights into the mechanical performance of parts produced by AM methods. The results obtained widen the knowledge of the capabilities and challenges of AM, and their consideration is of great importance in material modelling and safety design. Despite the considerable new findings in this field, follow-up research should be undertaken in the following areas:

- *Models for the interlayer bonding characterisation.* It is essential to develop new models to describe the interlayer bonding, including both physical processes occurring at the molecular level (e.g. inter-diffusion) and processes occurring at the global level (e.g. the accumulation of voids and residual stresses). Such models would allow a better understanding of the final mechanical properties of AM parts and provide clues for improving them.
- *Fracture toughness of SLS parts.* Further experimental investigations are needed to estimate the effect of fibre reinforcement on the fracture toughness in parts produced by SLS. It is also desirable to determine whether the cracked round bar test can be applied to SLS parts.
- *Multi-material printing.* The use of AM to produce multi-material parts was successfully demonstrated for FFF. This achievement suggests that further research should be focused not only on the processing of materials of different stiffnesses using a single AM method, but also on the combination of different AM methods. For example, FFF printing could be directly performed on SLS parts or ATPisc laminates.
- *Multiple cracking behaviour.* The ATPisc laminates that were tested in the present research showing multiple cracking have raised many questions in need of further examination. It is important to understand how to proceed with such complex fracture behaviours and estimate the real value of the threshold value of the crack growth onset. In addition, further investigations of the 'zero-bridging approach' [1] applied to the laminates with multiple cracking are required.
- *Comparison of  $G_{I_{th}}$  and  $G_{II_{th}}$ .* Further research could be dedicated to the comparison between mode I and mode II fatigue fracture of CF/PPS laminates. To date, it has been proven for carbon fibre reinforced PEEK that mode II fatigue fracture is more conservative than mode I fracture, even though quasi-static values describe mode I as more conservative [2,3]. Hence, knowing if this applies to thermoplastic matrix polymers in general, for example, due to specific damage mechanisms, or whether other factors are involved, is of particular interest.
- *DIC in other fracture modes.* It would also be interesting to apply the DIC methodology developed herein to follow crack propagation not only in mode I but also in mode II DCB tests with an extension to fatigue loading.
- *Interlayer shear strength of FFF.* The results gained from CST were promising when applied to ATPisc laminates and should be validated with regard to composites produced by FFF.

## References

- [1] Alderliesten R. Fatigue delamination of composite materials – approach to exclude large scale fibre bridging. IOP Conf. Ser.: Mater. Sci. Eng. 2018;388:12002.
- [2] Martin, R.H. and Murri, G.B. Characterization of mode I and mode II delamination growth and thresholds in AS4/PEEK composites. Composite materials: testing and design 1990;9.
- [3] Stelzer, S., R. Jones, and A. J. Brunner. "Interlaminar fatigue crack growth in carbon fiber reinforced composites." In The 19th International Conference On Composite Materials, 2013, p. 1-9.